THE UNIVERSITY *of* EDINBURGH

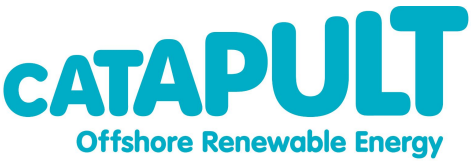

Predicting failure of dynamic offshore cables by insulation breakdown due to water treeing

A thesis submitted in partial fulfilment of the requirements
for the award of an Engineering Doctorate

David Glenn Young

Academic Supervisors:
Prof. Lars Johanning
Dr. Selda Oterkus
Dr. Quan Li

Industrial Supervisor:
Dr. Chong Ng

March 2020

IDCORE

This thesis is submitted in partial fulfilment of the requirements for the award of an Engineering Doctorate, jointly awarded by the University of Edinburgh, the University of Exeter and the University of Strathclyde. The work presented has been conducted under the industrial supervision of ORE Catapult as a project within the Industrial Doctoral Centre for Offshore Renewable Energy.

THE UNIVERSITY *of* EDINBURGH

Declaration

I declare that this thesis has been composed solely by myself and that it has not been submitted, in part or in full, in any previous application for a degree. Except where stated otherwise by reference or acknowledgement, the work presented is entirely my own.

Signed: _____

David Glenn Young

March 2020

Lay summary

The offshore wind industry has progressed from traditional fixed bottom platforms for the wind turbines to be installed on, to having floating platforms. This allows access to wind resources further offshore that were previously unavailable due to the greater water depth. Floating wind platforms introduce new challenges for offshore cables, particularly the array cables which will be required to hang from the base of the platform through the water column to the seabed. This arrangement exposes the cable to the dynamics of the marine environment it is installed in, creating concern for the failures of these dynamic cables. One particular failure mechanism of subsea cables is the degradation of the insulation layers by water treeing.

Water trees propagate due to mechanical and electrical loadings, and the move to having more dynamic installations for the cables is expected to increase the number of cables failing offshore. A primary concern with water treeing is that with current technologies they remain undetectable until they cause an unexpected failure of a cable, which may have been previously deemed healthy. This work presents a methodology which can model the propagation of a water tree to predict the time taken for it to propagate to a length which would cause failure of the dynamic cable. This ability to predict when a dynamic cable is at risk of failure allows for better planning of maintenance, as opposed to an unexpected failure. This results in the overall prediction of when the modelled dynamic cable is at risk of failure due to water treeing, and a new fatigue life estimate.

Acknowledgements

In the writing of this thesis there is a small legion of people that I owe a sincere and substantial gratitude to. To all my supervisors; Lars, Chong, Quan and Selda thank you for all of your support, guidance, advice and encouragement during this process. To my colleagues at ORE Catapult; thank you all for your patience and support, in particular Ampea, Chunjiang and Peter, for your wealth of knowledge and willingness for discussion. To all of the members of my IDCORE cohort; thank you for your friendship and sharing this process with me, I wish you all every success. To the team at JDR cables; thank you for your enthusiasm and sharing of information regarding offshore cable design and manufacture. To the team at Orcina; thank you for allowing me complimentary use of the OrcaFlex software throughout the duration of this research.

To my parents; I am lucky to have you both, truly thank you for everything. To Andy, Graham and Avril; thank you for continuing to be sources of inspiration and encouragement and for your keen willingness to ensure I remain grounded.

To all my friends; thank you for your support, proof reading, positivity and hilarity. Kristin, thank you for the excess of 10,000 emails during the past three years that became a welcomed, if not necessary, daily source of wisdom and encouragement.

This research was funded by the Energy Technologies Institute and the RCUK Energy Programme through the Industrial Doctoral Centre for Offshore Renewable Energy (Grant number EP/J500847/1) and is gratefully acknowledged.

Abstract

The offshore wind industry has progressed from traditional fixed bottom platforms for the wind turbines to be installed on, to having floating platforms. This allows access to wind resources further offshore that were previously unavailable due to the greater water depth. Floating wind platforms introduce new challenges for offshore cables, particularly the array cables which will be required to hang from the base of the platform through the water column to the seabed. This arrangement exposes the cable to the dynamics of the marine environment it is installed in, creating concern for the failures of these dynamic cables. One particular failure mechanism of subsea cables is the degradation of the insulation layers by water treeing.

Water trees propagate due to mechanical and electrical loadings, and the move to having more dynamic installations for the cables is expected to increase the number of cables failing offshore. A primary concern with water treeing is that with current technologies they remain undetectable until they cause an unexpected failure of a cable, which may have been previously deemed healthy. This work presents a methodology which can model the propagation of a water tree to predict the time taken for it to propagate to a length which would cause failure of the dynamic cable. This ability to predict when a dynamic cable is at risk of failure allows for better planning of maintenance, as opposed to an unexpected failure.

To achieve this, both the mechanical and electrical stresses the dynamic cable will be exposed to have been considered. A global model of a floating wind platform has been developed which leads to a local model of the dynamic cable's cross section to

deduce the mechanical stresses the environmental force loadings will exert on the insulation. Following this the distortions of the electric field across a dynamic cable's cross section in the presence of a water tree have been modelled to calculate the resulting stresses. Finally these two stresses are combined and a series of fatigue damage and crack propagation methods are employed, leading to the modelling of the microscale breaking of the insulation chemical bonds to predict the propagation of a water tree. This results in the overall prediction of when the modelled dynamic cable is at risk of failure due to water treeing, and a new fatigue life estimate.

List of publications

During this EngD programme, a number of conferences were presented at and publications produced, copies of which can be found in the appendix:

2018 **D G Young**, C Ng, S Oterkus, Q Li, L Johanning. *Assessing the mechanical stresses of dynamic cables for floating offshore wind applications.* Global Wind Summit (2018) Hamburg, Journal of Physics: Conference Series **1102** 012016. doi: 10.1088/1742-6596/1102/1/012016.

2018 **D G Young**, C Ng, S Oterkus, Q Li, L Johanning. *Predicting failure of dynamic cables for floating offshore wind.* RENEW 2018 3rd International Conference on Renewable Energies Offshore, Lisbon.

The following were oral presentations at conferences only:

2018 **D G Young**, C Ng, S Oterkus, Q Li, L Johanning. *An approach to assessing mechanical fatigue of dynamic subsea cables for floating offshore wind turbines.* Research at Alpha Ventus RAVE, Offshore Wind R & D Conference 2018, Bremerhaven.

The following are article publications within magazines:

2018 **D G Young**, L Johanning. *Dynamic Cables for Floating Offshore Wind - Dynamic Mechanical Stresses on Fatigue Life of Dynamic Cables.* Windtech International November/December issues 2018.

2018 **D G Young**, *Predicting Dynamic Subsea Cable Failure for Floating Offshore Wind*, Analysis & Insight reports Offshore Renewable Energy Catapult.

List of Figures

List of Tables

Contents

Chapter 1

Introduction and motivation

1.1 Introduction

In this chapter some background context is given to the research topic. The motivations and justifications for the research are given and an overview of the objective of the project follows.

1.2 Background and motivation

There is a pressing need to reduce carbon emissions and move energy production away from fossil fuel consumption to prevent the worst impacts of climate change. The warming of the earth's climate is of particular significance because most of it is extremely likely to be the result of human activity. As the world's leaders seek to develop a sustainable energy policy, many are looking to renewable energy sources as a means to reduce global carbon emissions.

The European Commission has set a target of 32% of total energy consumption to be from renewable sources by 2030 [1]. In addition to this, the UK's Climate Change Act commits the UK to reduce total carbon emissions by 80 percent of 1990 levels by 2050 [2]. In the second quarter of 2018, renewable energy accounted for 31.7 percent of the UK's electricity generation [3]. This increase from the previous year reflects increases in capacity, particularly of wind and solar photovoltaics. Specifically, offshore

wind accounted for 6.2 percent.

Technological advancements in the offshore wind industry, coupled with economies of scale, has resulted in continuously larger wind turbines offshore. To benefit from the greater wind resource available, these large turbines are moving further away from the shoreline. However, moving further from shore corresponds with an increase in water depth. Traditional fixed bottom wind turbine technologies are no longer the best option for the turbine platforms, creating the need for new floating platform wind turbines. Much work has been completed in advancing floating wind technologies, including that of the LIFES50+ consortium [4]. By the end of 2019 there was 32MW of floating offshore wind installed in UK waters [5].

Floating wind platforms will introduce new challenges for the umbilical, or array, cables that hang from the base of the platform to the seabed. This cable installation arrangement will expose the cables to the dynamic forces of the environment they would be installed in, including the actions of the waves, current flows and movement of the platform itself in response to wind/turbine interactions. Cables exposed to dynamic environmental loadings will experience dynamic mechanical stresses across their cross sections and along their length. This is a new operating consideration as traditional fixed bottom platforms have allowed cables to operate statically.

A reliable electrical infrastructure is instrumental in maximising the system availability of assets offshore. The offshore environment is a challenging one in which to minimise maintenance costs and ensure reliable operation. Some of the most costly interruptions to an offshore wind farm's availability are the failure of the subsea cables, resulting in cable failure incidents being named as one of the greatest risks to the continued lowering of the levelised cost of energy, LCOE, for offshore wind. Further to this, over 80% of offshore wind projects experience a cable related incident [6]. The average repair cost of a subsea export cable is estimated as £12.5 million, with the average repair time taking between three to five months [7]. [7] continued further and performed calculations ac-

counting for lost revenue due to the wind farm down time and arrived at a total cost of a cable failure to be £22.8 million, split approximately equally between repair costs and lost revenue. The move to floating offshore wind turbines will have the greatest impact on the array cables in an offshore wind farm, as these are the ones which will hang in the water column below the floating platform. Array cables are typically replaced rather than repaired, and if an array cable fails it results in only one turbine being offline and not the whole wind farm. To deduce the cost of an array cable failure, the cost of lost revenue can be ignored and the time taken to replace the cable can be compared to the time to repair an export cable. In April 2017 extraction and replacement of two array cables at the London Array wind farm was completed within one month [8], giving an average time on each cable of two weeks.

Offshore subsea cables fail during normal operation, and excluding third party interference, due to three main causes, all of which lead to the eventual breakdown of the cable's insulation layers and ultimate failure of the cable [9]:

- Mechanical damage
- Water ingress
- Overheating

Mechanical damage occurs most frequently when the cable is at its most vulnerable during its installation, here over tension when paying the cable out from the offshore vessel during installation or breaking the minimum bend radius can result in damage. Mechanical damage during the manufacturing process, transport and handling is also possible. GCUBE, a renewable energy insurance provider, generated a breakdown of the cause of cable related insurance claims, shown in Figure 1.1 [10].

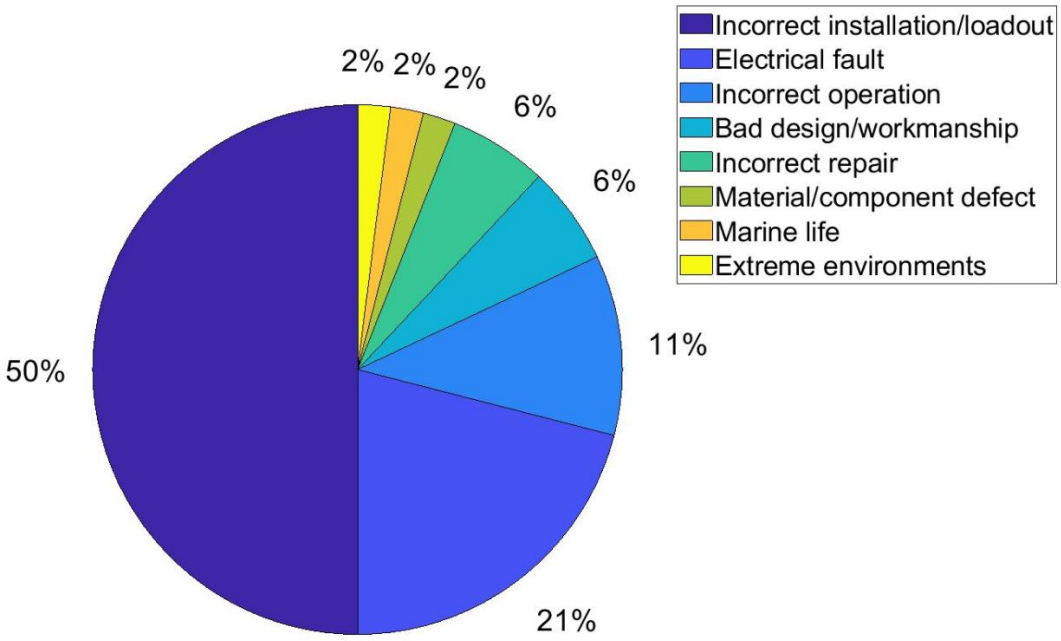

Figure 1.1: Breakdown of cable related incidents by cause

Figure 1.1 shows that cable failures are approximately evenly split between those that happen during installation and those that happen during operation. An offshore cable has an expected lifetime of twenty-five years, however insurers are already seeing a trend where cables are failing after ten years, sometimes between two and five years service unexpectedly [11]. It is thought that a reason for these unexpected faults is an insulation degradation mechanism known as water treeing.

Water trees propagate due to mechanical and electrical loads. As the industry moves to floating offshore wind and installing cables in more dynamic environments, it is expected that there will be an increase in the number of subsea cables failing. Therefore to reduce the number of unexpected cable failures offshore, this work aims to develop a model which can predict the growth of water trees within the cable's insulation layers. Predicting the growth of water trees will allow for preventative maintenance on subsea cables before a fault will occur and will give more representative fatigue lifetimes of subsea cables.

1.3 Aims, objectives and limitations

1.3.1 Aim

The aim of this project is to address the industrial research question regarding the unexpected failure of subsea cables which were otherwise deemed healthy from current cable testing methods. As this is a research project based within industry the research project must address a need of the industrial partner, ORE Catapult. ORE Catapult has completed previous testing of subsea cables focusing on water ingress and water trees within cable insulation layers under various conditions and has interests in better understanding the unexpected failures of subsea cables. As stated previously, the insulation degradation mechanism known as water treeing is thought of as a reason for these unexpected failures. This thought is due to water trees currently being undetectable by current cable monitoring and testing technologies. Therefore the aim of this research project is to develop an electrical - mechanical coupled model which can model the growth of water trees within the insulation layers of a dynamic cable, which can be then used as a tool to predict when ultimate failure of a dynamic cable will occur.

This model will account for the mechanical stresses imposed on the dynamic cable from the environment it is installed in, and the electrical stresses imposed by being energised with 66kV. The purpose of this coupled model is to provide a fatigue lifetime of dynamic cables installed for floating offshore wind. Modelling the growth of water trees, and predicting when their failure will occur, will allow for preventative maintenance on subsea cables before a fault occurs and give more representative fatigue lifetimes of subsea cables. A series of objectives to achieve this aim and address the industrial research question are listed in section 1.3.2. The limitations and constraints to the scope of the project are provided in section 1.3.3.

1.3.2 Objectives

To account for the mechanical stresses the dynamic cable would be exposed to, a number of steps and objectives are completed:

- Complete a resource assessment at site chosen for installation of floating offshore wind platform.
- Develop load cases from the resource assessment.
- Build a global model of the floating offshore wind platform with attached dynamic cable, and apply the developed loadcases.
- Build a local model of the dynamic cable and apply global model outputs.
- Generate stress time histories from the local model of the dynamic cable.

To account for the electric stresses the dynamic cable would experience, the following objectives are listed:

- Generate a 2D cross section model of a dynamic cable's insulation layer.
- Apply 66kV across the insulation thickness for varying water tree length.
- Record electric field distortions and concentration magnitudes.

Finally, to deduce the fatigue life of the cable with respect to its insulation layers, the following are completed:

- Using the mechanical stress time histories only, complete a Palmgren Miner damage accumulate method to deduce fatigue life of the insulation.
- Complete a fatigue crack growth analysis using the combined mechanical and electrical field distortion stresses.
- Complete a water tree propagation analysis by means of energy accumulation and monomer chemical bond breaking.
- Calculate and compare results and estimated fatigue lives.

1.3.3 Limitations of work

To complete this work a number of simplifications and assumptions were made which limit the results. This work aims to predict the failure of subsea cables by water tree degradation, and therefore only the stresses experienced by the insulation layer of the cable are considered. This work assumes that the floating turbine is operational 100% of its life and is never switched off, ensuring the dynamic cable is always energised. Further to this it assumes the cable is always energised to its 66kV rated value. This would not be applicable in practice as there will be occasions where the turbine will be turned off to allow for maintenance work or repairs. The cable modelled in this work specifically is a 66kV dynamic cable that has been updated and edited from a historic oil and gas project. It is a quad layer galvanised steel armoured cable with outer and inner polyethylene sheaths. The three cores have an outer PVC sheath, cross-linked polyethylene insulation layer, an inner polyethylene sheath and copper cores.

The modelling of the armour wire layers has been simplified to thin walled tubes based on work completed by [12], which is based on the assumption that the cable armouring wires remain within stick state and do not slide over one another. The stiffnesses of the dynamic cable are a key property which determine much of the dynamics of the cable when installed to the floating offshore platform. For this work the cable stiffnesses have been assumed as a property solely of the armouring layers, and the stiffnesses are calculated based on work completed by Raoff [13] and Chen [14] for bending and axial stiffness respectively. These stiffness calculations account for the helical structure of the armouring wire, which for this work the helical angle has been assumed to be 18°. Ideally, stiffness would be provided from the cable manufacturer based on experimental work, which accounts for the helical structure and movements of the armouring layers. These assumptions based on numerical work and assuming the cable remains within stick state, and simplifying the armouring layers to thin walled tubes are limitations of the work.

The cable modelled is assumed to be a dry type cable, therefore there is no water tree retardant material within the XLPE, it is assumed pure uniform XLPE. This decision was taken as it simplifies the water tree propagation due to monomer chemical bond breaking process as the impact of the water tree retarding material on this process can be neglected. In future dynamic cables may not be dry type and will have water tree retarding material within the XLPE, impacting water tree propagation.

Vortex induced vibration of the cable has not been considered as it has been assumed that the cable damping would prevent vortex induced vibration. Furthermore, as the cable is quad armoured it would be torque balanced.

The cable modelled is based on a historical oil and gas dynamic cable. The floating offshore wind platform chosen is therefore a tension leg platform due to it being akin to oil and gas operations and being installed in similar water depths. Therefore the MIT/NREL reference 5MW tension leg platform has been included in this work.

Thermal effects are not considered in this work; the cold water site chosen coupled with a constant flow of water due to the dynamic arrangement of the cable was assumed an appropriate cooling mechanism. Micro jetting of water molecules in an electric field within the water trees was not considered, the water trees are considered to propagate only as a mechanism of the Maxwell stress generated by the electric field distortions and the mechanical stress induced by the marine environment. To this effect, the chemical impacts of free radicals released during polymer rupture is not considered, nor is the hydrophilic actions of the exposed carbonyl groups.

1.4 Methodology

The methodology to achieve the listed objectives and overall aim is described accordingly and presented as a work flow in Figure 1.2. To complete a resource assessment at the proposed installation site and develop the corresponding environmental load cases,

the tidal current, wind and wave conditions at the site need to be recorded. Data from an Acoustic Doppler Current Profiler (ADCP) deployed at the site is analysed to determine the water depth, current velocity, current profile and direction. A wave buoy is deployed at the same site, or one an appropriately short distance away from the AWAC. Data collected from the wave buoy is binned according to its significant wave height and wave period, and analysed to develop a spectrum of wave conditions at the installation site. Wind velocity and direction data at the site are traditionally recorded using an anemometer and wind vane respectively, however if this information is unavailable, appropriate hindcast data will suffice. From this assessment of the offshore environment, the load cases to simulate in the global model of the floating offshore wind turbine are developed. For this work, the load cases developed have been based upon the DNVGL standard DNVGL-ST-0019 for floating wind turbine structures.

The global model of the floating offshore wind turbine is constructed using OrcaFlex to model the hydrodynamics of the platform and cable, coupled with FAST (with turbulent wind input files generated from TurbSim) to model the global loading on the turbine. For this work the floating platform and turbine are based on the NREL 5MW reference turbine and tension leg platform. Inputs into this model, including the reference turbine, are the developed environmental load cases, the mechanical properties of the dynamic cable to be assessed and the appropriate hydrodynamic coefficients. The outputs from this global model which are then used as input to the local model are the force and bend moment responses of the dynamic cable at various points along its length.

To generate the stress time histories on the cable's insulation layers, a local model of the dynamic cables cross section is built. This local model is an ANSYS finite element model of the cable's cross section, which discretises the cross section into elements with their own set degrees of freedom. The global load histories generated from the global model are applied and the stress time histories of the insulation layer's elements are extracted. Within this work, to reduce the computational expense, a linear superposition of the global loads onto dynamic cable is completed in a quasi dynamic analysis

as opposed to a complete transient dynamic analysis.

To calculate the stresses on the insulation layer caused by the electric field, another finite element model of the cable's cross section is built with ANSYS Maxwell, however differing lengths of water tree are included in the cross section. The presence of the water tree is used to model the distortion of the electric field at the tip of the water tree. This process is repeated iteratively, and the electric field concentrations calculated. These electric field concentrations are then converted to Maxwell stresses, and a stress time history related to the frequency of the applied voltage is generated.

To calculate the fatigue life of the insulation layer of a dynamic cable, a traditional damage accumulation assessment by Palmgren-Miners rule is completed. The stres-life method by rainflow counting and linear damage accumulation is well accepted for analysing high cycle fatigue loadings. To model the water tree as a fatigue crack propagation mechanism, Paris Law is employed which assumes linear crack propagation within the Paris regime for differing stress intensity factors and has been demonstrated to be an appropriate method for modelling cracks within XLPE. The local model and electric field model stresses can be combined into an effective stress intensity factor and the propagation calculated. Finally the water tree propagation is considered in terms of microscopic fracture of chemical bonds within the insulation monomers to rupture the overall polymer chain. The breaking of bonds is considered by accumulation of energy imparted on the water tree tip. Using this rupture of the polymer chains as a propagation mechanism, the time taken to propagate the water tree to a point of insulation failure is modelled, producing a new fatigue life estimate of the dynamic cable due to water treeing.

Figure 1.2 shows a work flow of the methodology for this thesis, grouped into the respective chapter where each section is discussed.

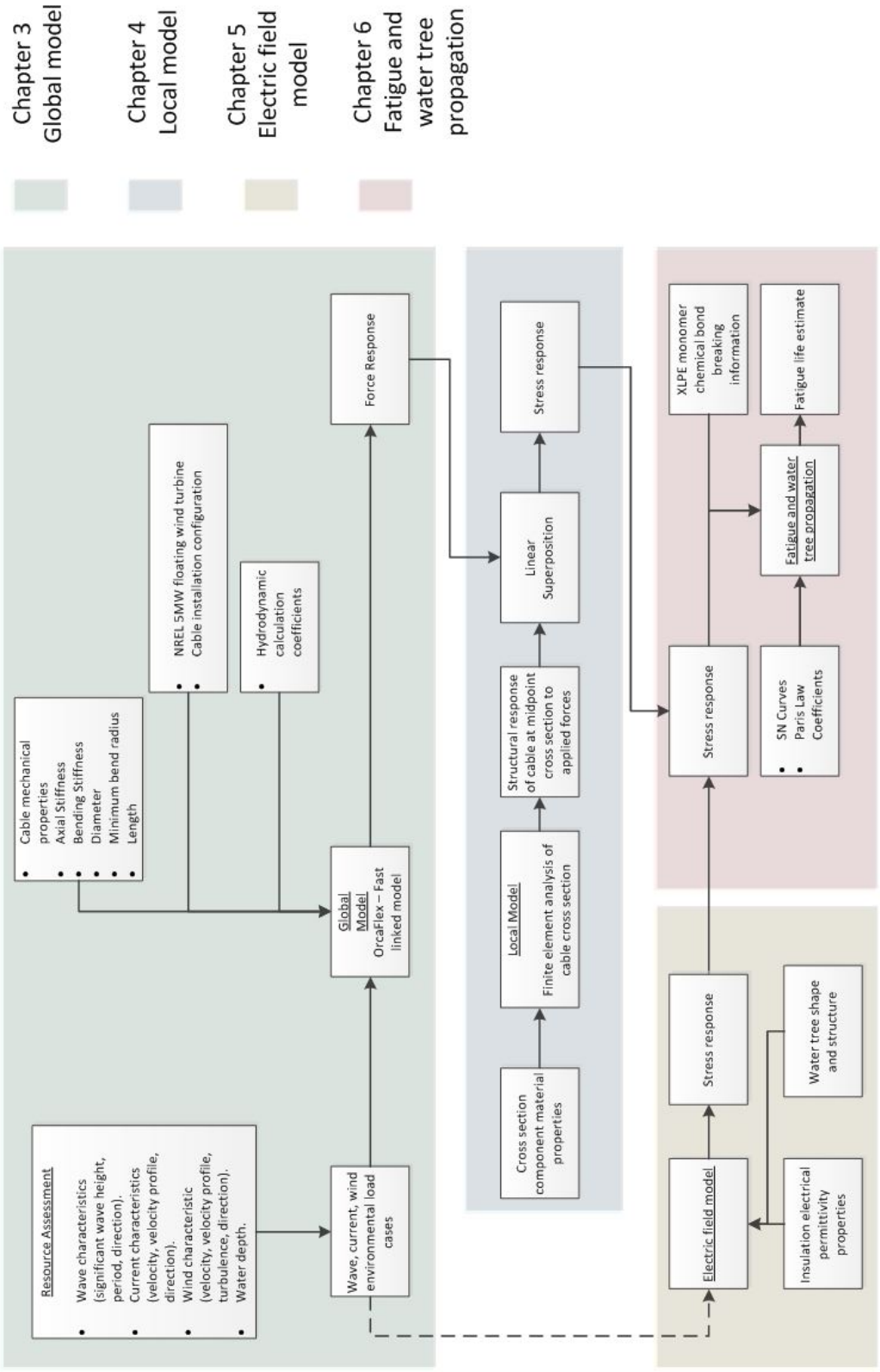

Figure 1.2: Overview of the methodology developed, grouped by thesis chapter.

1.5 Original Contribution

Fatigue analysis of dynamic cables is a complex problem. The nature of the loading, the complicated behaviour of the cable materials and the differing component interactions means there is considerable uncertainty in the results obtained from fatigue analyses. When considering cable testing, a cable's mechanical performance is tested independently of its electrical performance, rarely are the two tested simultaneously.

This work addresses this mechanical and electrical independence by developing a methodology that combines them both in a fatigue analysis to model water tree propagation. Prior to this work, there had been analysis on the factors that impact water tree propagation and their potential shapes, but prediction of their propagation by combined electrical and mechanical factors was lacking. The microscopic failure of the insulation monomers has been shown to be a key propagation prediction mechanism, these have been addressed and suggestions have been made on how to further improve this prediction in future.

In summary, this thesis makes a novel contribution to the prediction of failure by water treeing of dynamic subsea cables installed for floating offshore wind has been made.

1.6 Thesis structure

In this section an overview of the structure of the thesis to follow is given. The purpose of which is to give a guideline to the work presented to demonstrate the methodology laid out in Section 1.4 and Figure 1.2. Chapter 2 reviews the literature on the subject of water treeing within subsea cable's insulation and the work already completed. It serves to give relevant background to the work to provide a context of where this research fits.

Chapter 3 presents the work completed for the global model, highlighted in green in Figure 1.2. This chapter discusses the work undertaken to produce the force loadings on the dynamic cable, by completing a resource assessment of the offshore site, building of

the global model within OrcaFlex, the dynamic cable properties and the hydrodynamic calculation coefficients.

Chapter 4 presents the work completed for the local model of the dyanmic cable's cross section, highlighted in blue in Figure 1.2. This chapter discusses the work undertaken to produce the time history of von Mises stress the dynamic cable's cross section will experience by building a finite element model of the cross section and completing a linear superposition of the global force loadings.

Chapter 5 presents the work completed for the electric field model, highlighted in yellow in Figure 1.2. This chapter discusses the work undertaken to produce the time history of Maxwell stress at the tip of the water tree, by finite element analysis modelling of the electric field concentrations at the tip of water trees of differing lengths.

Chapter 6 presents the work completed to combine the von Mises and Maxwell stresses to calculate the corresponding fatigue lifetime of the dynamic cable's insulation by water tree propagation, highlighted in red in Figure 1.2. This chapter discusses the steps undertaken to complete a linear damage accumulation assessment of the insulation, a crack propagation technique by Paris Law to model the water tree propagation and a technique involving bond breaking of the monomer bonds of the insulation to propagate the water tree.

Finally chapter 7 gives some discussion to the results including their academic and industrial relevance. From this, chapter 8 draws conclusions from the work presented and offers a proposed series of future works.

Chapter 2

Literature Review

2.1 Offshore wind turbines

The first offshore wind farm in the UK was the Blyth Offshore Wind Farm, commissioned in December 2000 [15]. Like most offshore wind farms the Blyth Offshore Wind Farm's foundation structure is fixed bottom, in Blyth's case the offshore turbines sat upon grounded monopiles. Foundations for offshore wind turbines can be divided into two groups: fixed or floating [16]. Limited by water depth further offshore where fixed bottom foundations are too costly, the wind resource remained unexploited, driving research into and development of floating offshore wind platforms. Resulting from this effort the world's first floating wind farm Hywind Scotland was commissioned in 2017 [17]. An introduction to these two main configurations of offshore wind turbines is provided.

2.1.1 Fixed bottom offshore wind turbines

At offshore locations where the water depth is relatively shallow (<50-60m) and the bathymetry seabed allows, the use of traditional fixed bottom foundations to install offshore wind farms is commonplace. Fixed bottom foundations consist of monopiles or jackets which are directly embedded into the seabed to provide a stable base on which the wind turbine is installed. Figure 2.1 [16] provides an overview of the different fixed bottom foundations available.

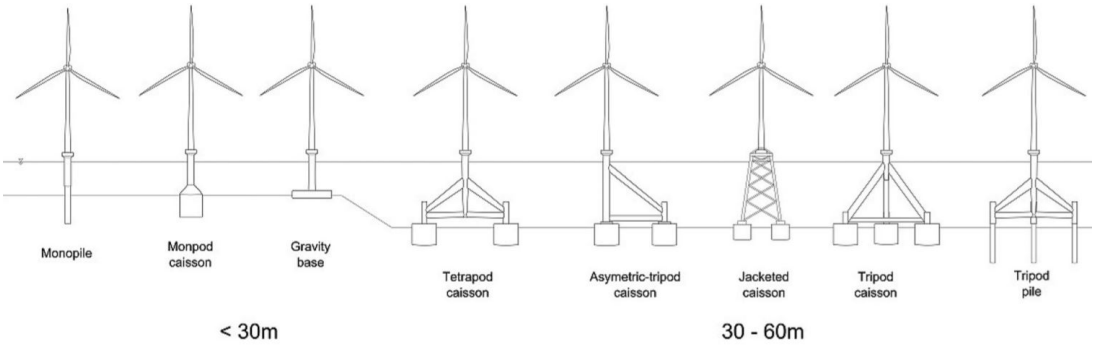

Figure 2.1: Different types of fixed bottom foundation [16]

2.1.2 Floating offshore wind turbines

Floating offshore wind turbines provide the opportunity to exploit the wind resource in deep water sites, where the installation of a fixed bottom foundation is not feasible. It's not true to think that deep water sites are always further offshore, locations such as Japan, Norway and the West coast of the US all have waters deeper than 60m a few kilometres from the shoreline. The main configurations for floating offshore wind platforms are the spar buoy, barge, semi-submersible and tension leg platform (TLP). Table 2.1 lists some of the more developed projects according to their different typology and country of origin. It can be seen that the majority of the listed typologies are semi-submersibles (Ideol's being the only barge).

Semi-submersible/Barge	Tension leg platform	Spar buoy
Windfloat (USA)	Gicon* /PelaStar (Germany/USA)	Hywind (Norway)
Fukushima (Japan)	SBM Offshore (Netherlands)	TetraSpar (Denmark)
Ideol *(France)	TLPWIND (Spain)	Fukushima Advanced Spar (Japan)
DCNS *(France)		Toda Spar (Japan)
NAUTILUS (Spain)		
VolturnUS *(USA)		
Tri-Floater (Netherlands)		
OO-Star *(Norway)		
Cobra *(Spain)		

Table 2.1: Developed floating wind turbine systems (*Uses concrete) [18]

2.1.2.1 Spar buoy

The spar buoy typology consists of a single upright floating cylindrical spar buoy moored by chains or cables to the sea bed. The buoy is characterised by its thin shape and large draft. In the Hywind example the substructure is a steel cylinder ballasted with water, rock and iron ore so that the entire structure floats upright. It is moored by a conventional three line catenary mooring system. Figure 2.3 shows a schematic of a spar buoy system.

2.1.2.2 Barge

The barge typology consists of a flat bottomed platform with a small draft and large water plane area. It is moored with catenary lines. Ideol is developing a barge typology based on the damping pool concept. In this case the centre of the barge is hollow to damp the motions of the platform. Figure 2.3 shows a schematic of a barge system, however it should be noted that the figure shows a generalised barge and lacks the central opening of Ideol's design. Figure 2.2 shows Ideol's damping pool design specifically.

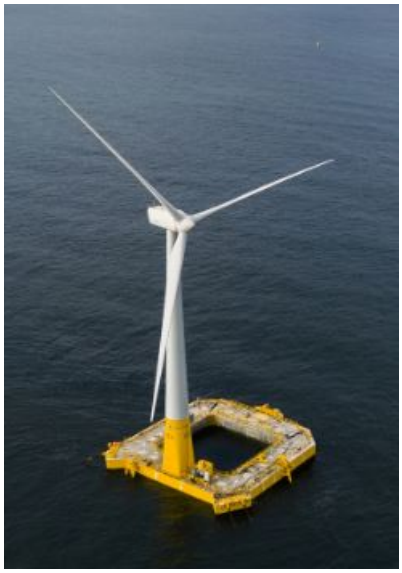

Figure 2.2: Ideol's damping pool barge configuration [19]

2.1.2.3 Semi-submersible

The semi-submersible typology consists of an upper deck above the water level that the turbine sits on, supported by vertical columns which are connected below the water surface. They have a medium draft and are moored by catenary lines. WindFloat is a semi-submersible typology that utilises "water entrapment plates" fitted to the base of the three vertical columns, with a static and dynamic ballast system for stability. Figure 2.3 shows a schematic of a semi-submersible system, however it should be noted that for WindFloat specifically the turbine sits upon one of the vertical columns, and not in the centre as depicted in the image.

2.1.2.4 Tension leg platform

The TLP typology consists of an overly buoyant platform held in position by a vertically tensioned mooring system. TLP's are characterised by their high stiffness in heave, roll and pitch and are adapted from original TLP concepts from the oil and gas industry. The tendons act as both a stabilising and a station keeping system, and they are particularly suited to water depths ranging from 250m to 1000m. Figure 2.3 shows a schematic of a TLP system.

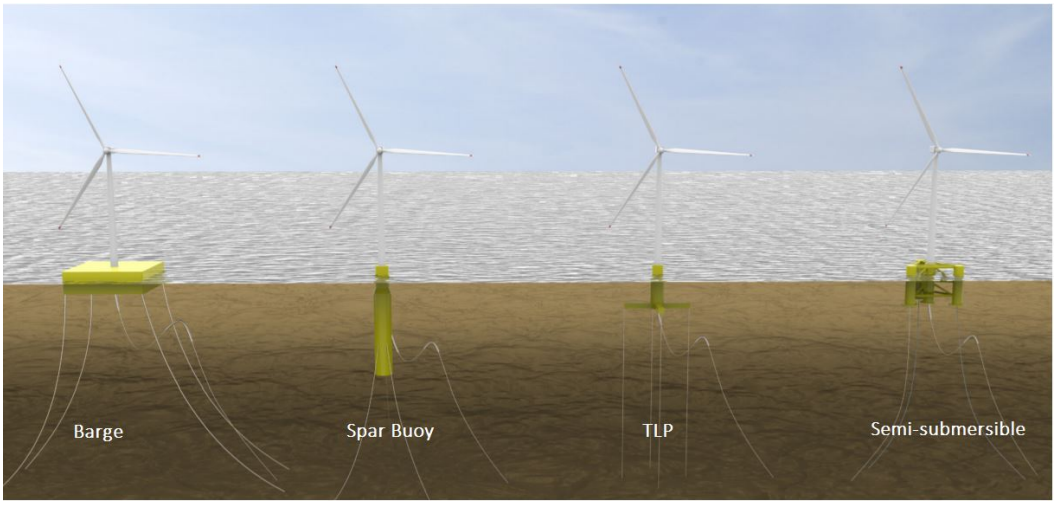

Figure 2.3: Floating wind typologies (left to right: barge, spar buoy, TLP, semi-submersible) [18]

2.1.3 Design standards of offshore wind turbines

There are a number of standards for offshore wind turbines, delivered from the International Electrotechnical Commission (IEC) and certification bodies. Standards establish best practice engineering design methods and support wind farm owners, insurers and financiers to assess their risk. As this work was not a design project of an offshore wind turbine, the standards are included in this literature review for completeness and reference. DNV-GL standards however were used to produce the load cases of the offshore environment, as well as Germanischer Lloyd regulations for wind velocity calculations.

IEC 61400 was published as an international standard regarding wind turbines with IEC 61400-3 [20] specifically referring to the design requirements of offshore wind turbines. DNVGL-ST-0126 [21] standard provides guidance for the design of support structures for offshore wind turbines. DNVGL-ST-0119 [22] - Design of floating wind turbine structures (which superseded the previous DNV-OS-J103) was used for the design of the environmental load cases, supplementary to DNVGL-ST-0437 - Loads and site conditions for on and offshore wind turbines [23]. Germanischer Llyod's "Guideline for the Certification of Wind Turbines, 2005" [24] provides guidance on calculation of wind velocities at differing turbine heights.

2.2 Offshore infrastructure

The electrical infrastructure for an offshore wind farm includes the array cables arranged in strings that connect the turbines to one another, the offshore substation, and the export cable to shore. The substation typically houses the transformers, switch gears and auxiliary equipment such as back up power systems.

A reliable electrical infrastructure is essential in maximising the system availability of assets offshore. If a failure of this infrastructure was to occur, not only are the costs associated with repair incurred but also the costs of lost revenue by losing availability of the asset. The offshore environment is a challenging one to minimise maintenance

costs and deliver reliable operation. Despite subsea cables costing approximately 5-10% of the initial investment cost of an offshore wind farm [6], they account for most of the unavailability of offshore wind farms. These subsea cables can be grouped as either the inter array cables or the much larger export cable. Figure 2.4 shows a typical offshore electrical infrastructure for a fixed bottom wind farm.

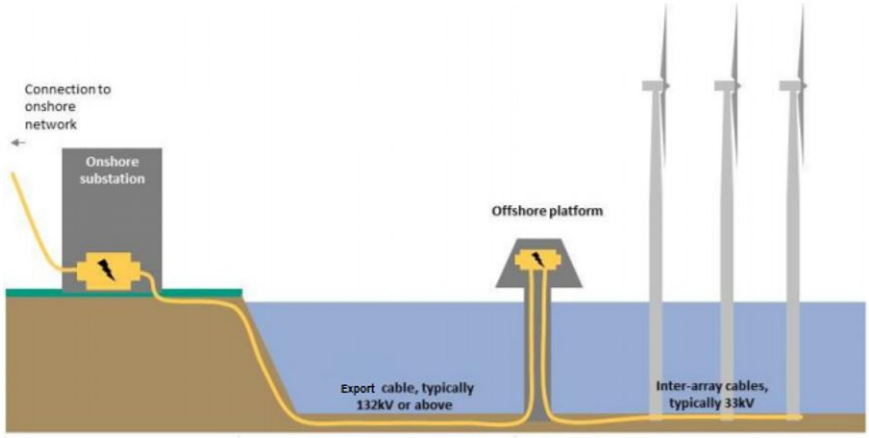

Figure 2.4: Offshore electrical infrastructure for a typical fixed bottom wind farm [25]

With the advent of floating offshore wind, the offshore electrical infrastructure has been adapted and updated accordingly, the key difference being the new configuration of the subsea cable installation. Without the fixed foundations of the turbines and substations for the cables to run through, they are instead installed exposed to the water column and the dynamics of the marine environment. This new cable is different to a static cable and is designed for its dynamic operation, and is hence known as a dynamic cable. Further to these dynamic array cables, there is ongoing work to develop up to 250kV export cables [26]. The dynamic cable installation for the Fukushima Floating Wind Farm Demonstration Project is shown in Figure 2.5 for the purpose of visualising these differences.

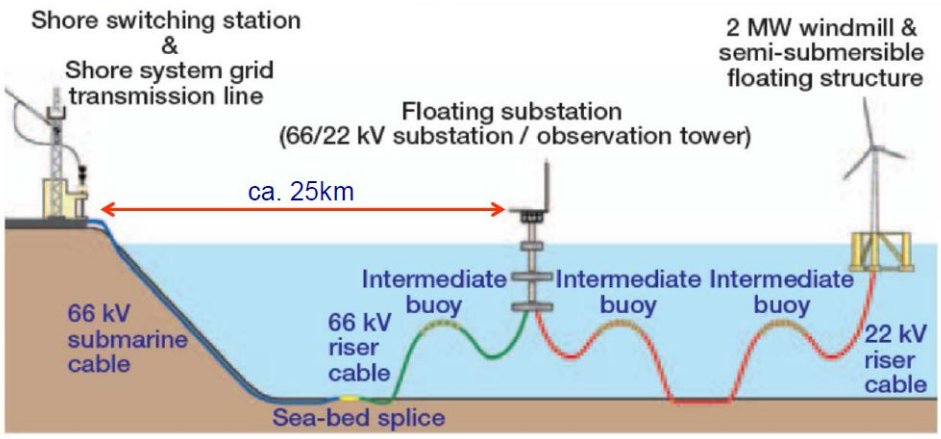

Figure 2.5: Offshore electrical infrastructure for Fukushima Floating Offshore Wind Farm Demonstration Project [27]

2.2.1 Subsea cables

Subsea cables for offshore wind can have varying degrees of complexity in their design. While no two cables are identical, they follow a general structure of a metallic copper (or aluminium) core, metallic screens, an insulation layer, protective armouring layers and an outer PVC sheath. Figure 2.6 shows a labelled picture of a 36kV inter array cable for offshore wind.

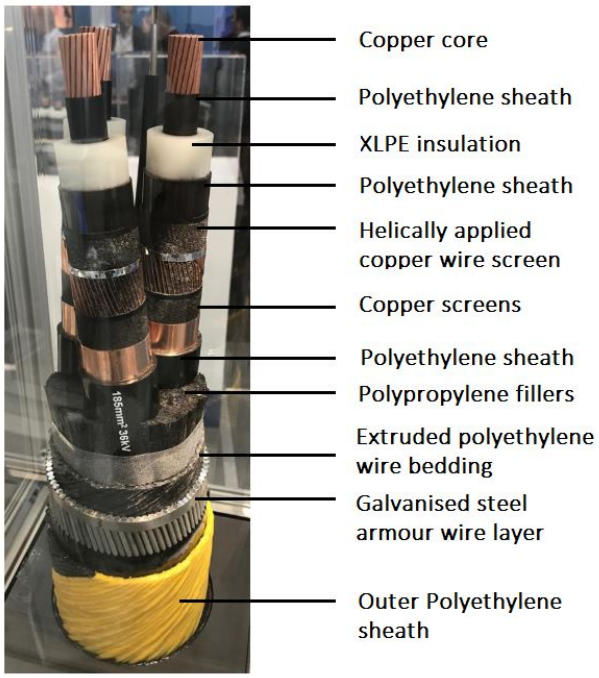

Figure 2.6: Labelled picture of a 36kV offshore array cable used in static applications.

While the general make up of a dynamic cable may appear similar to that of a static cable as presented in Figure 2.6, there are key differences in their design. Dynamic cables can be designed to have more than one steel wire armouring layer, depending upon their operation conditions, to protect them them from external influences. Materials with low fatigue lives such as lead screens are removed and replaced with polyethylene screens. For static cables their weight is designed for seabed stability, however for dynamic cables their weight and stiffness may need to be engineered to suit dynamic application. Dynamic cables must be able to withstand extreme loading, and the floating section must not kink or come into contact with the seabed.

2.3 Offshore wind industry overview

Aukland et al. as part of 4C Offshore [28] have analysed the offshore wind market as having a global total of 26.1GW installed with an additional 16.9GW of capacity under construction but yet to be fully installed. The UK remains the global leader with 9GW currently installed. However this is soon expected to be superseded by China as the country is experiencing a surge in offshore wind expansion. In fact, by 2029 China is predicted to have 99.4GW of offshore wind installed, almost half of the then predicted global total of 223.5GW. This prediction is based upon 4C Offshore's project opportunity pipeline, and Figure 2.7 illustrates this prediction by country.

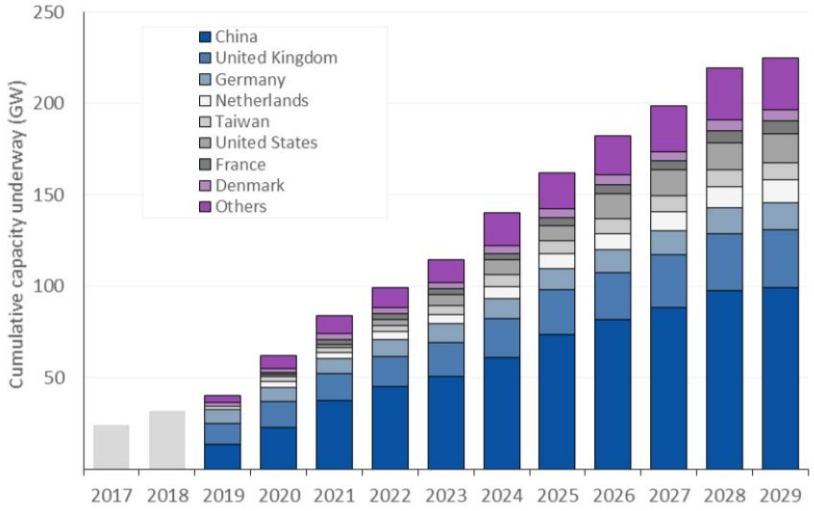

Figure 2.7: Offshore wind industry market prediction by 2029 [28]

Markatselis et al. [5] predict that by 2030 the global capacity of floating offshore wind will lie between 7GW-13GW, based upon a low or high uptake case scenario. It is not made clear if this 13GW is additional or incorporated within the 223.5GW predicted by [28], regardless it is clear that the market is predicting growth in both fixed and floating offshore wind farms. Figure 2.8 illustrates by country the market share of the high case scenario of floating offshore wind capacity by 2030.

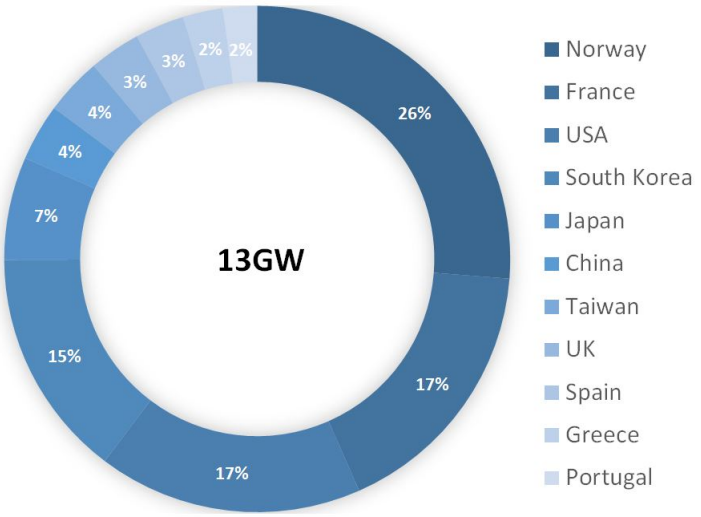

Figure 2.8: Floating offshore wind installed capacity prediction by 2030

2.3.1 Subsea cable industry overview

Aukland and Langdon [29] estimate that there are 17,000km of offshore wind array and export cables installed globally. With the predicted expansion of the offshore wind market, so too must the subsea cable market expand to meet this global demand with predictions of 53,000km of offshore wind array and export cables by 2027.

Tuğçe [30] predicts between 2019-2024 within Europe 28,730km of subsea cable is to be installed where in 2024, annual demand reaches 11,400km of subsea cable in Europe. It should be noted that this number accounts for interconnector type cables which are excluded for offshore wind. If array and export cables for offshore wind are considered individually, daily installation rates of 0.96km/day and 1.19km/day respectively are predicted.

Looking at UK subsea cables specifically, data for installed offshore wind farm export and array cables was collected for 31 UK wind farms. This information came from a collection of 4C Offshore cable reports [31], Ofgem [32], national grid annual national electricity transmission system performance reports [33], and ORE Catapults in-house subsea cable trend tool [34]. This historic data is plotted in Figures 2.9 and 2.10 for export and array cables from 2003-2017 respectively.

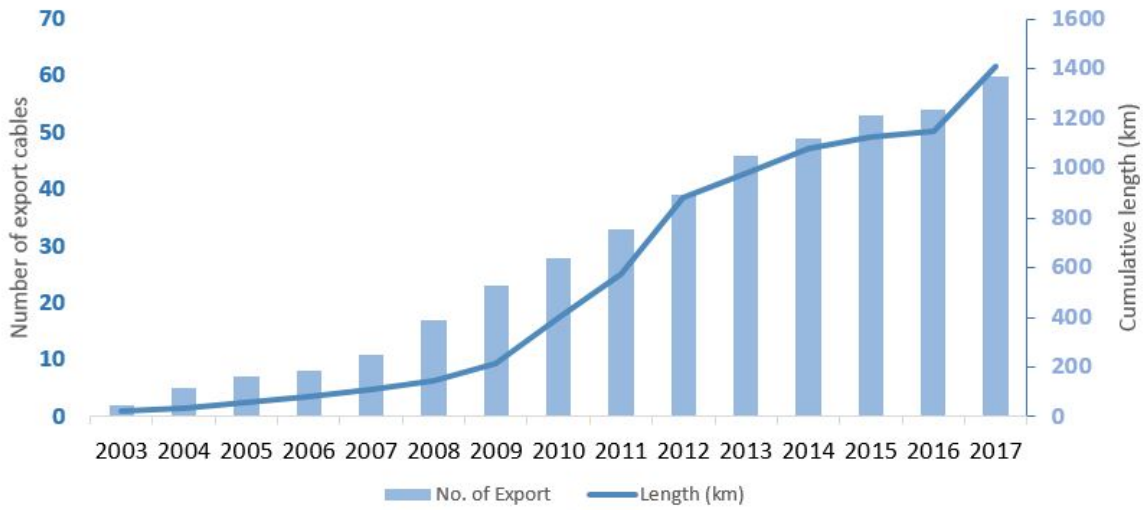

Figure 2.9: Export cable length (km) installed in the UK 2003-2017

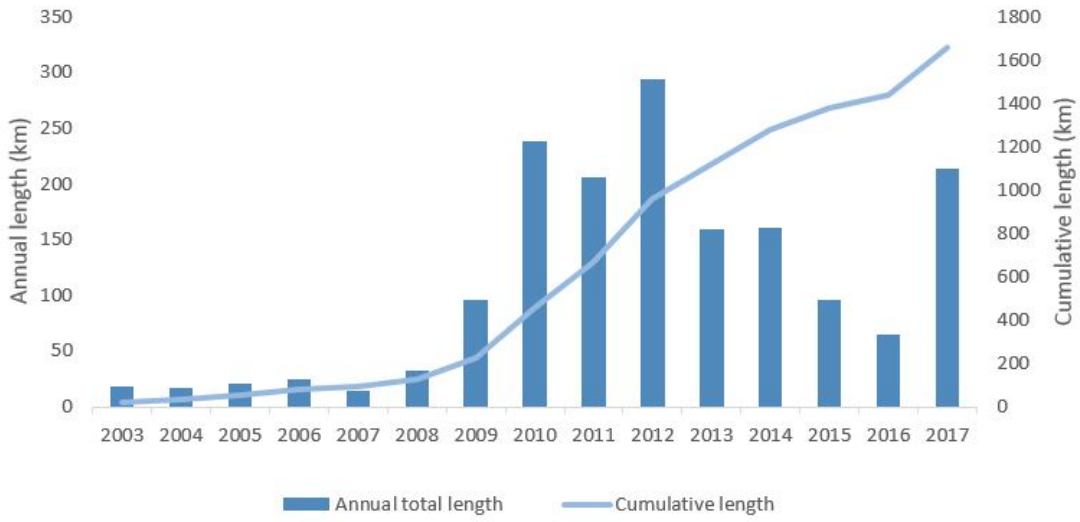

Figure 2.10: Array cable length (km) installed in the UK 2003-2017

Both Figures 2.9 and 2.10 show that there has been an increase in the length of the array and export cables installed in UK waters from 2003-2017. Furthermore [29] states that while there are greater lengths of cable being installed offshore, they are being installed in deeper waters and further from the shoreline, illustrated in Figure 2.11. With floating offshore wind moving to deeper waters, it is expected that subsea cables will continue this trend towards having more cables offshore and in deeper waters.

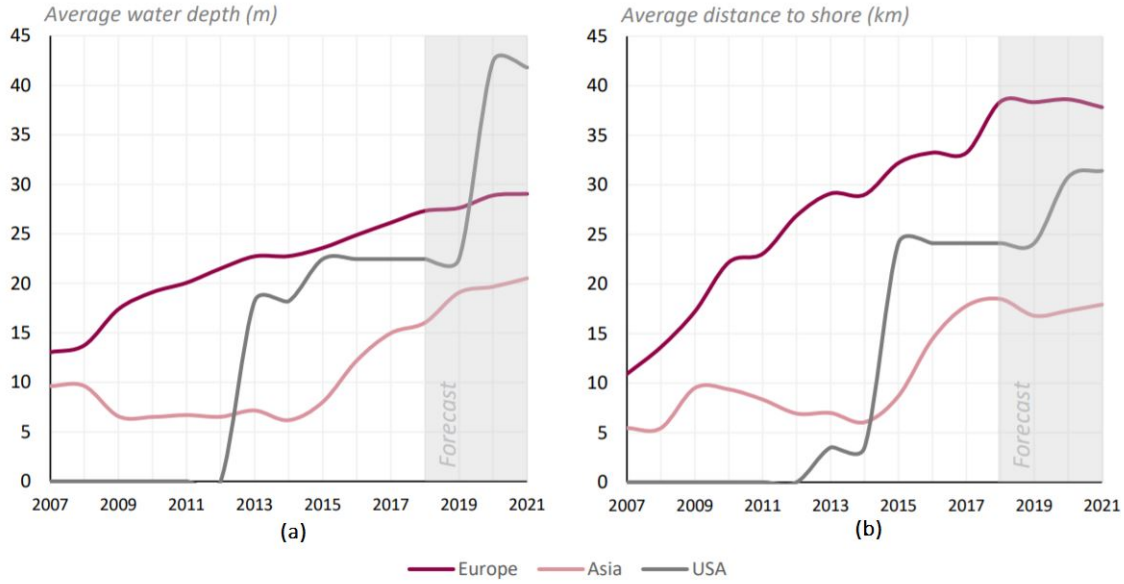

Figure 2.11: Subsea cable installation water depth trend (a), and subsea cable instllation distance from shore (b) [29]

2.3.1.1 Subsea cable failure

To understand the need to predict a failure mechanism of subsea cables, it is first necessary to gain an understanding of the frequency of subsea cable failures and the associated costs. As stated previously within Chapter 1, subsea cables fail due to mechanical damage, water ingress or overheating, all of which lead to the eventual breakdown of the insulation. Gcube [10] estimates that cable failure is split approximately 50/50 between installation and operational cable failures (shown in Figure 1.1 in Chapter 1). Data for the previous decade has been collated on export cable failures. Export cable failures are recorded in more detail due to the loss of availability of the offshore wind farm, and their time of repair therefore having greater pressures. Array cable failures however result in a small number of the turbines of the wind farm losing availability so their impact is

less significant, and they are typically replaced rather than repaired. A timeline of the number of cable faults per year is presented in Figure 2.12 where the number of failures per year can be seen. In total there have been 43 cable failures by the end of 2017 in UK waters. Its important to emphasise that this presents on export cable failures only and does not include array cables.

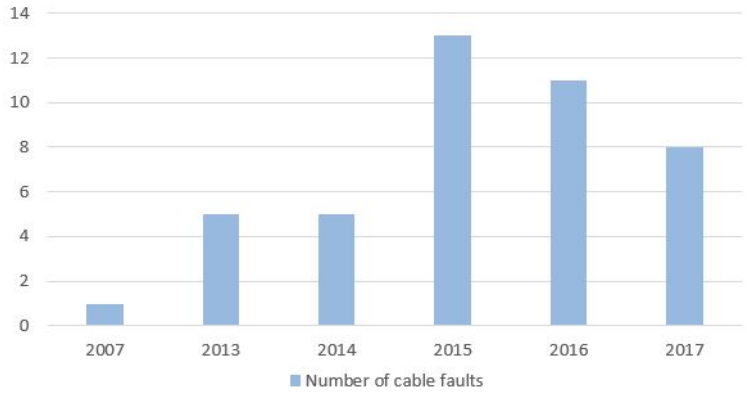

Figure 2.12: UK Export cable failures from 2007-2017

To understand the cost of a subsea cable failure, the Offshore Wind Programme Board [7] presented the publicly disclosed costs listed in Table 2.2. This shows the average cable repair cost of £12.5m and an average export cable repair time of 3-5 months. Furthermore if lost revenue due to unavailability is accounted for, and based on the assumption of 40% load factor, £140/MWhr sell price, the total cost of the seven failures listed in Table 2.2 is estimated as £160m, approximately equal between repair and lost revenue [7].

Table 2.2: Publicly disclosed cable repair costs [7]

Repair	Cost	Source
Guernsey-Jersey (2012)	£8m	BBC News
Guernsey Jersey (2015, pre-emptive)	£5.3m	Owners' annual report
Moyle (2011-2012), 2 repairs	£15.5m (average)	Owners' annual report
Gwynt y Mor (2015)	£10.2	Ofgem (income adjustment claim)
Gywnt y Mor (2015-2016)	£14.2m	Ofgem (income adjustment claim)
Thanet (2015)	£11.7m	Ofgem (income adjustment claim)

It should be noted that if a cable failure can be predicted before hand and planned for accordingly, the cost of the repair approximately halves, as shown in Table 2.2.

Using the total number of export cable failures of 43 in Figure 2.12, and total cumulative length of 1400km in Figure 2.9 over the ten year period gives an average cable failure rate of 0.003 failures/km/year. This failure rate is in accordance with Warnock et al [35] who calculated an average cable failure rate of AC systems currently opertational in Europe as 0.003 failure/km/year. Furthermore [35] illustrated failure rates for particular wind farms, Figure 2.13.

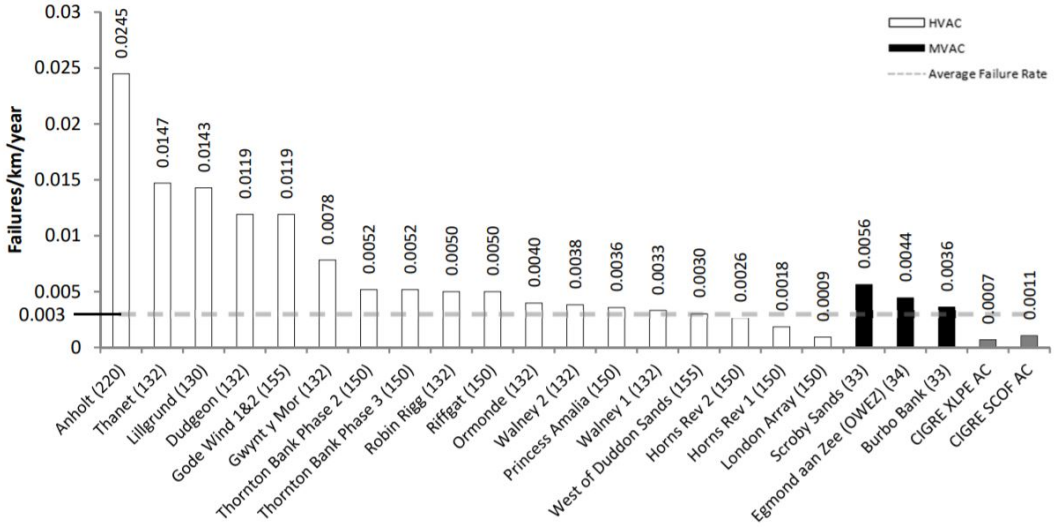

Figure 2.13: Failure rate of alternating current (AC) European offshore wind farm transmission connections until March 2018

In both [35] and [36] Warnock argues that previous cable failure rates published by CIGRE [37], [38] should be treated with caution, as they underestimate subsea cable failure rate. In particular the failure rates published for cross linked polyethylene cables, XLPE, are significantly lower than their findings. This is particularly important to note as XLPE insulation cables are vulnerable to water treeing.

To determine if this cable failure rate holds for the estimated offshore wind expansion, the classic bathtub curve can be examined. The bathtub curve shows that at the beginning of a project's life there can be an expected high rate of failures to reflect its

infancy, known as infant mortalities, where lessons are being learned. After this the curve plateaus as the lessons have been learned and a relatively constant and lower failure rate is observed during the project lifetime, impacted by random failures. Finally towards the end of the project lifetime a higher failure rate can be expected due to component wear out. This is shown in Figure 2.14.

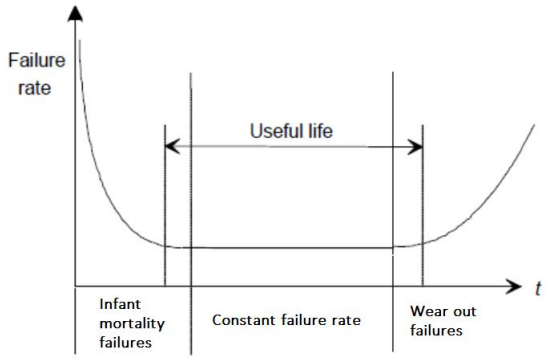

Figure 2.14: Bathtub curve representing failure rate evolution in a components lifetime

Steisdal and Madsen [39] investigated the reliability of offshore wind components and determined that the classic bathtub curve may not always be applicable. Figure 2.15 shows this adapted failure rate curve, accounting for infant mortality, random failure, wear out failure and premature mortality failure to determine the overall failure curve for offshore wind components. Warnock [36] suggests that this adapted failure curve may hold for subsea cable failure rates.

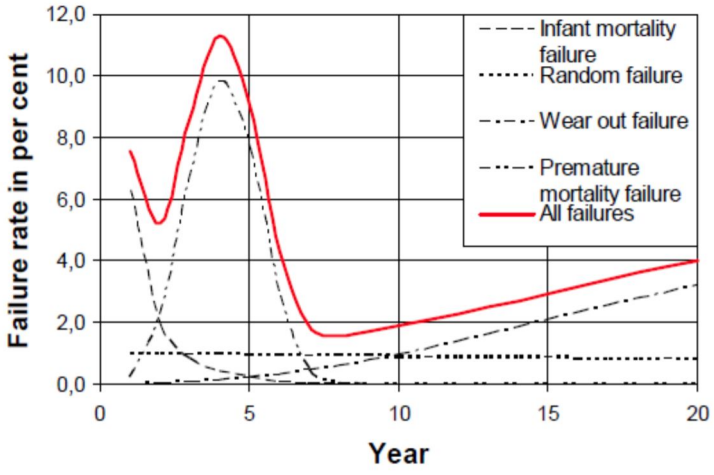

Figure 2.15: Adapted failure rate curve [39]

2.4 Cable insulation materials

It has been stated that the failure modes of subsea cables lead to the eventual breakdown of the cable insulation layer, leading to ultimate failure of the subsea cable. For offshore wind subsea cables, the insulation tends to be either XLPE or ethylene propylene rubber, EPR. XLPE was first introduced as a cable dielectric in the 1960's, serving as a catalyst to replace existing oil filled paper insulated cables and to be the insulation material of choice for future subsea cable installations. The move to replace the oil filled paper insulation was, while a reliable technology, because of concerns regarding the environmental suitability of it due to possible leaks of the cable fluid [40]. Further to this, oil impregnated paper cables suffered from high dielectric losses and high operational costs [41].

Ethylene propylene rubber is a generic term that refers to a range of polymers consisting of a blend of ethylene and propylene copolymers. EPR is a suitable insulation material for subsea cables due to its high dielectric strength properties, flexibility, superior thermal expansion properties and low sensitivity to water treeing. However the loss factor of EPR insulated cables is twenty times higher than XLPE cables, furthermore XLPE cables exhibit a 70% higher impulse strength than EPR cables [41]. While failure rates of comparing EPR cable to XLPE cables was not found for subsea cables connecting to wind farms, [41] did compare the two for 20kV underground cables, Figure 2.16 which clearly shows XLPE insulation cables having a much lower failure rate than EPR insulation cables. Therefore XLPE has since gained wide acceptance as the cable insulation material of choice. For example, Chen [42] notes that more than 90% of Japans underground cables are XLPE insulated [43].

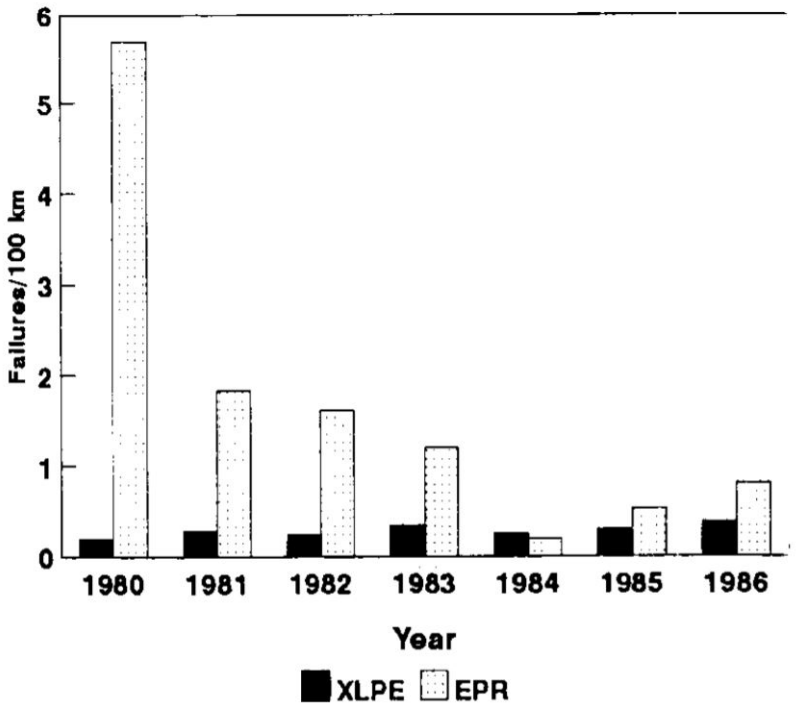

Figure 2.16: Failure rate of 20kV XLPE and EPR cables [41]

Thermoset compounds are fabricated from polymer resins that are irreversibly cured to a plastic or polymer. XLPE is a form of thermoset polymer, where the polyethylene chains are linked together by a process known as cross-linking. This cross linking prevents the polymer from separating or melting at high temperatures. XLPE has less dielectric losses than EPR, is resistant to heat deformation and the cross-linking within the polymer increases its mechanical strength. This increase in mechanical strength increases XLPE's resistance to abrasion, increases its impact and ultimate tensile strength and stress crack resistance. In general, the greater the level of cross-linking the greater the mechanical strength. However Pruitt [44] and Gencur [45] claim that very high levels of cross-linking in XLPE used for hip and knee replacement surgeries actually decreases the mechanical strength of the XLPE including its ductility, elastic modulus, fracture toughness and crack propagation resistance. For traditional static installations of subsea cables, the mechanical properties remained secondary to its superior dielectric properties making it a desirable dielectric to have, with approximately 50% of cables in service today in some countries having been installed in the 1970s [46]. When these new XLPE subsea cables were intially installed it was envisioned they would have a service

life of 25 years. Unfortunately after approximately 5 years [11], water trees began to appear leading to cable faults [47]. This highlighted the concerning weakness of XLPE with its susceptibility to water treeing.

2.4.1 Chemistry of XLPE

A thermoplastic polymer, like polyethylene, refers to a material that softens upon heating, and re-stiffens by cooling. Conversely, a thermoset, or thermosetting plastic, material like XLPE is one that is irreversibly hardened by the curing of the of the polymer resin. Curing here refers to the chemical process where a polymer is hardened by the cross-linking of the polymer chains. In short, the thermoplastic polyethylene is cured to produce the thermoset XLPE.

Ethylene is a gaseous hydrocarbon of two carbons and four hydrogens, where the two carbons are held with a sigma and pi double bond between the two carbon atoms. Valence shell electron pair repulsion theory predicts the bond angles and spatial positions of the carbon and hydrogen atoms as shown in Figure 2.17.

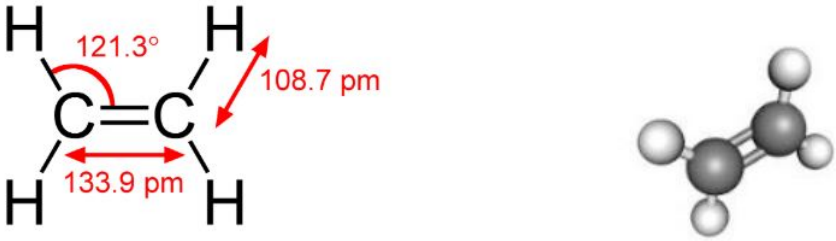

(a) Bond structure of ethylene (b) Monomer unit of polyethylene

Figure 2.17: Bond angle and length of ethylene molecule, [48] and 3D monomer structure [49]

Using Figure 2.17 the atomic diameter of ethylene is approximately 2.12Å, assuming the carbon and hydrogen atoms remain co planar, typically the covalent radius of the C=C bond is used instead which in this case is 1.34Å. By contrast the atomic diameter of ethane, which only has the sigma (which is free to rotate) C-C bond which has a covalent radius of 1.54Å, giving atomic radius of 2.2Å. The C-C bond is longer than the C=C bond due to the bond electrons attracting the positive nuclei more strongly and

pulling the atoms closer together. When producing the polyethylene from the gaseous ethylene monomers, the pi bond is broken and enables an ethylene molecule to join with others to form a chain where all the carbon atoms are linked. These chains are three dimensional with the hydrogens bonded and arranged along a central zig-zag spine of carbon atoms. Furthermore these chains of polyethylene are all of varying length.

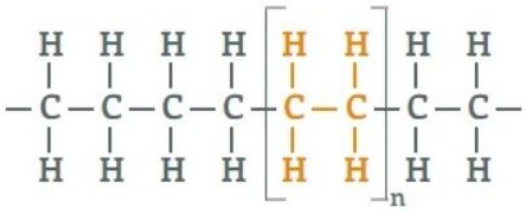

Figure 2.18: Chain of polyethylene with highlighted repeating monomer unit. There can be n number of monomers within a single chain.

Cross-linking of polyethylene leads to the production of insoluble polymers, where the chains are joined together to form a three-dimensional structure [50]. Polyethylene can be crosslinked by addition of a peroxide under heat and pressure, or by irradiation with electrons or gamma rays, both of which are free radical processes [51] [50]. In the cross-linking process carbon atoms of the same or a different polymer chain are joined together. The bonds can be between two carbon atoms or a chemical bridge linking more than two carbon atoms.

(a) Simplified non cross-linked polyethylene (b) Simplified cross-linked polyethylene

Figure 2.19: Non cross-linked and cross-linked polyethylene

The kinetic diameter of a monomer of ethylene is 3.9Å. The kinetic diameter of a molecule gives an indication of its size, as a measure of the likelihood that the gaseous ethylene molecule will collide with another ethylene molecule in the polymerisation process. Kinetic diameter is not the same as the atomic diameter, as this defines the size of the ethylene's electron shell and is typically much smaller. Therefore during the cross-

linking process the carbons in the ethylene monomers of the polyethylene chains with the free radicals will have this "sphere of influence" to form the cross linking. Therefore the estimate of a monomers size for polyethylene is taken as the kinetic diameter of ethylene.

2.5 Water trees

Water treeing in subsea cables is a fault phenomenon that is difficult to detect. Water trees grow very slowly within a cables insulation, leading to unexpected faults years later. They cause permanent damage and their presence drastically reduces the service life of a subsea cable; sometimes reducing a cables expected lifespan of 25-30 years to five. They have a minute electrical signature, making them extremely difficult to detect. It is understood that there are two main classifications of water trees, distinguished by their initiation and propagation. They are known as "Vented Trees" and "Bow-Tie Trees" [47] [52].

Vented water trees are defined as those which initiate due to a defect at the interface between two mediums. These can occur on the outer surface of the XLPE, growing inwards across the cross section of the XLPE insulation towards the inner core. Likewise they can initiate at the inner conductor screen side of the insulation and propagate towards the outer surface of the XLPE. Water trees which originate from the inner surfaces are often caused by defects in the manufacturing of the conductor, whereas water trees which originate on the outer surfaces are more typically caused by external damage and age [47]. Vented water trees propagate across the cross section of the insulation in a humid environment to a length (<60% of insulation thickness[47]) that can cause a cable fault. It should be noted that XLPE cables at higher voltages can break down without the water tree crossing the entire insulation thickness [53]. [54] goes further and reveals that the length of the longest water tree is more closely related to electrical breakdown, than the density of water treeing or degree of ageing.

Bow-Tie trees are those which originate within the dieletric XLPE thickness itself, due to the presence of impurities or defects during the manufacturing process. They grow within the insulation in two opposite directions. Figure 2.20 illustrates a schematic of vented and bow-tie trees.

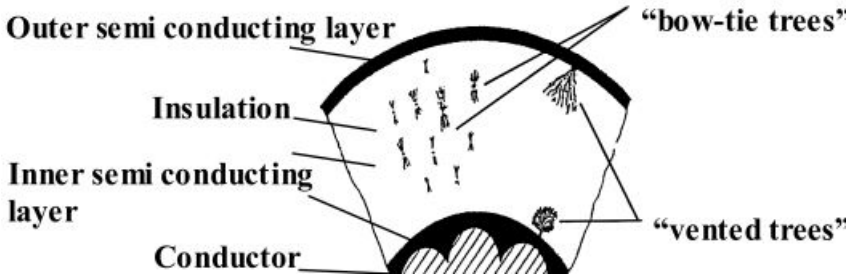

Figure 2.20: Schematic of Vented and Bow-Tie Trees [52]

Eventually the electric field built up at the tip of the water tree can increase to a point that it evolves to becomes an electrical tree. Once initiated electrical trees grow rapidly, weakening the XLPE insulation to the point where it can no longer withstand the applied voltage [55]. Electrical trees are bigger and more distinct than water trees, being visible to the naked eye. They propagate through the mechanism of partial discharge (PD). PD can occur across the insulation where the strength of the electric field exceeds the break down strength of that section of the insulation. Due to a concentration of an electric field at the tip of the water trees, if the voltage stress increases above the corona inception voltage for the moisture within the tree, PD can start. This PD activity generates heat and allows the newly evolved electrical tree to "bore" through the insulation quickly. It should be noted however that a water tree is not required to evolve to an electrical tree to cause failure of a cable's insulation.

2.5.1 Water tree propagation

Water trees propagate by the build up of an electric field at the tips of the water tree branches. This concentration of electric field generates a frequency dependent Maxwell stress along a fixed direction [47] [54] [56] [57]. Furthermore, micro-jetting of the water can occur where water is exposed to time varying electric fields, propelling droplets of water in a fixed direction [47]. This is a phenomenon that is taken advantage of in

electrospraying for DNA characterization purposes [58]. As outer vented water trees grow towards the cable core they will experience increasing build up of electric field concentration at their tips, further encouraging propagation. Vented trees that grow from the inner interfaces of the cable will experience a lessening electric field as they propagate further from the core causing their growth to slow and sometimes ultimately stop. This is why vented trees which grow from the outer surfaces are most damaging and lead to the most faults. Bow-tie trees grow along electric field lines and rarely lead to insulation breakdown. They only grow to a comparatively small size, due to a lack of free moisture. This is supported by water trees not developing in laboratory tests of insufficient moisture ($< 60\%$) [59].

2.5.1.1 Factors Affecting Water Tree Propagation

There are a number of factors which influence the propagation of water trees. Moisture content, voltage stress, voltage polarity, frequency, ageing time and temperature all play a role. [60] investigated the possible influence of salinity and acidic level effects on XLPE. They found that a lower pH did increase propagation of water trees, however the applicability of these findings are questionable to subsea power cables as this scenario was for acid rain prone areas of Malaysia on underground XLPE cables. Further to this [61] found that inorganic ions dissolved in water will diffused into XLPE. Not all ions diffuse at the same rate, but as salt concentration increases, so will the intake of water by the XLPE. This is of importance to subsea cables, as in practice these cables will be in a higher salinty than what they have been tested in within laboratories. Crucially, it was found that increasing the level of cross-linking of the XLPE decreases the diffusion of ions.

[62] showed that increasing temperature increases water tree propagation. A number of reasons are given such as that increasing temperature increases the kinetic energy of the water molecules, while also decreasing the crystallinity of XLPE. Cable service time also increases the likelihood of failure by water treeing [63]. [64] found that in general

water trees did not form in accelerated ageing of cables with DC voltages and tended to form more readily with AC voltages.

Electric field strength is the primary factor leading to water tree growth, i.e. a stronger electrical field results in longer tree branches. It should be noted that when a water surface is subjected to a time-varying electric field it propels water droplets in micro-jets. It is thought that these micro jets can potentially propagate the water tree.

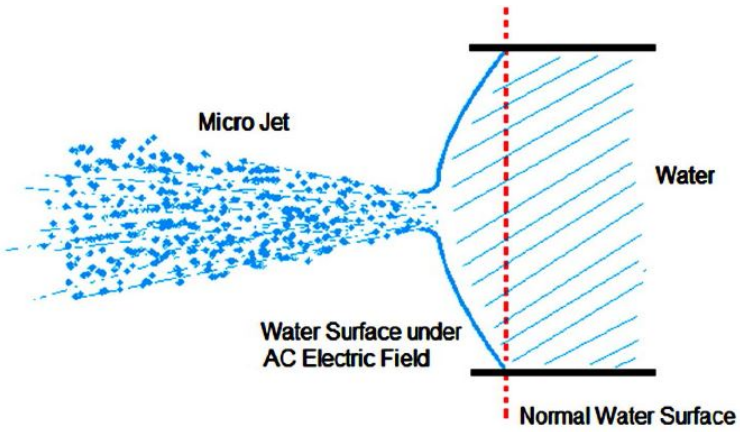

Figure 2.21: Water surface ejecting micro-jets under AC field [47]

2.5.2 Water tree shape

The geometric structure of water trees is found to be dependent on several factors such as magnitude of electric stress, caused by higher voltages, frequency and water content. [54] envisioned water trees to consist of several ellipsoidal cavities connected by a series of collapsible channels as shown in Figure 2.22.

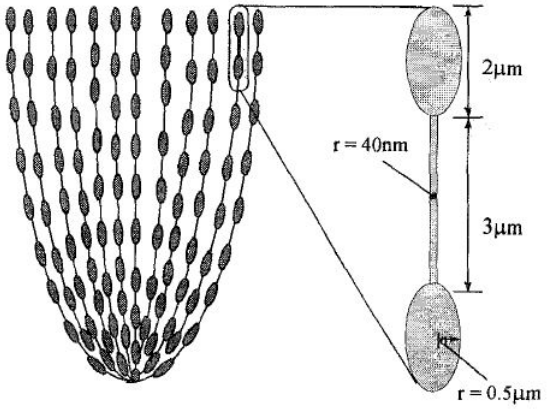

Figure 2.22: A simplified sketch of a water tree showing ellipsoidal shaped cavities interconnected by small channels. [54]

When a voltage above a certain threshold is applied the water droplets align with the electric field and are driven into the channels, opening them and allowing water to penetrate deeper into the insulation. When the voltage is disconnected the channels collapse and force water out, causing the channels in the water trees to become invisible.

2.5.2.1 Factors Affecting Water Tree Shape

Water trees have a small cross sectional area with a rather arbitrary structure. It is due to this very small cross sectional area that water tree branches have a high resistance. Likewise this small cross section in the overall cable area gives a very low capacitance value for water trees. Laboratory testing has confirmed the variability of water tree branches as they still grow in a wide range of branch numbers and length in identical conditions [65]. Discussed previously is that a higher applied voltage creates a stronger electrical field at the tip of the water tree branch.

Previously it was thought that the frequency of the electric field was a dominant factor in determining water tree shape, however [47] has found that the number of zero-crossing of the field is the dominant factor. This is in agreement with [66] which went further still in that it is the number of consecutive voltage zero-crossings that impacts the shape of water trees growth. If there are many zero crossings the water tree cross section will

branch out to a greater extent and become more "hand-shaped". In contrast, if there are less zero-crossings the tree will become more "ball-shaped". This is true even if the applied voltage is combined of two different waves of different frequencies. Figure 2.23 illustrates an overall schematic of these two shapes, while Figure 2.24 shows the differing shapes a water tree can have.

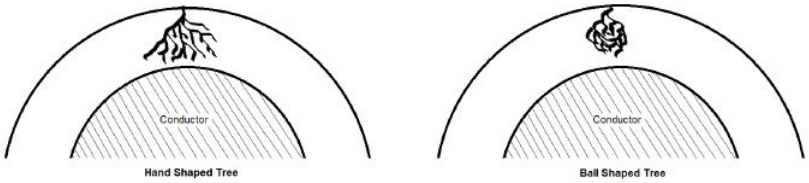

Figure 2.23: Specific Shape of Water Tree [47]

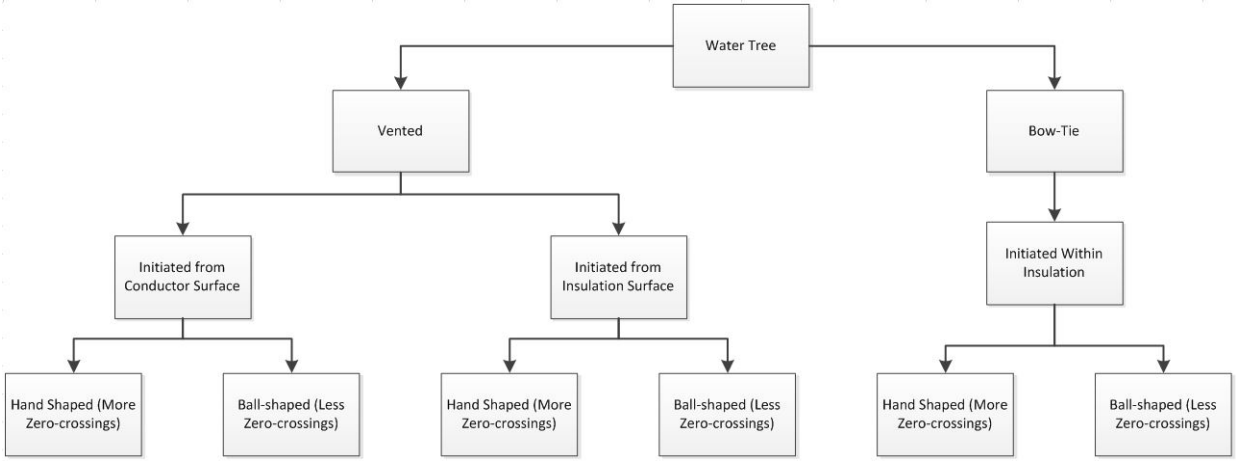

Figure 2.24: General types of water tree [47]

2.5.2.2 Water Tree Diagnosis and Detection

Water trees can be thought of as a single line to ground fault (SLGF), however they have a considerably higher impedance than these faults. Furthermore if the service voltage is low, a water tree fault might not occur regardless if it has crossed the entire length of the insulation. As discussed before water trees exist as a network of branches; strings of ellipsoidal shapes or "pearls". Maxwell forces can open and close these channels, cutting off conductive pathways. Therefore, this generates a challenge with the detection and identification of high impedance faults. Due to their small cross section water trees are also low current faults. These type of faults do not draw enough current to be detected

by traditional overcurrent means [67]. Although the currents are small, in the 0-50 ampere range [68], the voltages can be high. These high voltages mean that during cable testing, the test voltage is limited to a lower voltage to avoid corona effects phenomena [69]. Normally a corona discharge can happen spontaneously in high voltage systems unless the maximum voltage is reduced to limit the electric field. It happens when the fluid surrounding an electrical charged conductor, like a subsea cable, ionizes.

A method to assess water tree degraded XLPE is loss factor measurements in the frequency domain, known as Frequency Domain Spectroscopy (FDS). FDS measurements are conducted by producing an AC voltage across the insulation which has a varying frequency. One should then record the current response and measure the phase angle difference between the voltage and current waveforms. From this the tan δ, known as the loss factor, can be calculated in addition to the real and imaginary components of the capacitance [70].

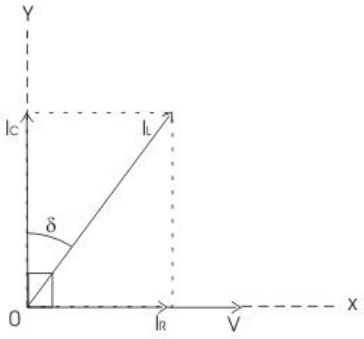

Figure 2.25: Loss Factor Phase Angle Diagram [71]

Figure 2.25 shows the current lagging the voltage with the current split into its resistive and capacitive components. In a perfect capacitor the voltage and current are phase shifted 90 degrees with the current being entirely capacitive. Impurities or water trees increase the resistance in the cable, and thus a resistive current occurs in the cable. Therefore the phase shift angle will no longer be exactly 90 degrees. Therefore the more resistance the larger the tan δ will be. Tan δ can be related to the real and imaginary parts of the capacitance and permittivity (the ability of the XLPE to resist the applied

electric field) according to the following equation:

$$tan\delta = \frac{I_R}{I_C} = \frac{C^{"}}{C'} = \frac{\epsilon^{"}}{\epsilon'} \tag{2.1}$$

Where I_R and I_C are the resistive and capacitive currents, $C^{"}$ and $\epsilon^{"}$ are the imaginary components of the capacitance and the permittivity respectively. C' and ϵ' are the real components of the capacitance and permittivity respectively. Tan δ is measured in radians.

Once tanδ is calculated, it's magnitude can be used to give an indication of the levels of degradation of the XLPE, it cannot indicate where the water trees are along the length of the cable nor what length they are. Tan δ values will increase in proportion to the ageing time of cables as well as intensifying with the increment in applied voltage or stress voltage [69]. An advantage of this type of system is that it can reveal the level of degradation, so it could be utilised as a spot check condition monitoring method to see if the cable remains in the same health. This might be useful to determine what other tests are needed in the future. Furthermore the lower voltage does not encourage water trees propagation during testing to accelerate. However, this method does not provide information on where a fault is should one occur.

Partial discharge (PD) tests are a common tool for the investigation of cable insulations. PD works under the premise of time domain reflectometry (TDR). TDR allows for the identification of partial discharges along the cable, indicating a potential fault at that point. It is based on the time difference arrival of an electrical pulse and its reflection at the opposite end of the cable [72]. Figure 2.26 is a schematic of the pulse reflections in PD testing.

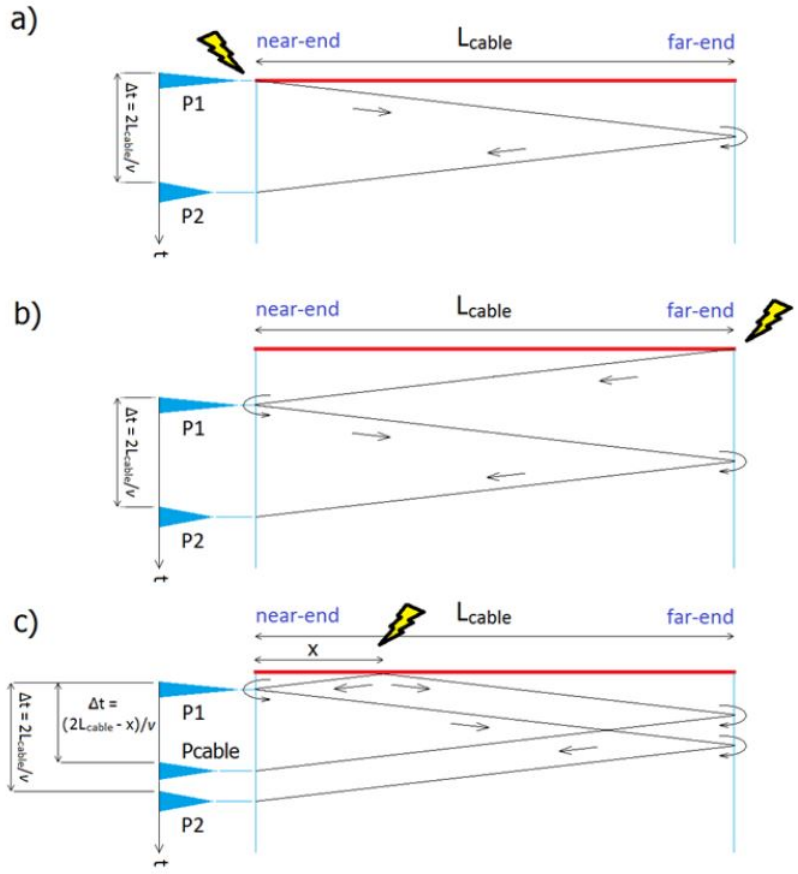

Figure 2.26: a) shows a TDR of a near-end PD pulse. b) shows a TDR of a far-end PD pulse. c) shows a TDR of a pulse originated at a distance "x" from near-end. [72]

A TDR system sends a very short pulse down the cable. When the pulse reaches a change in impedance such as at a fault or joint a portion of the pulse is reflected back at that point [73]. The distance from the sending end is then calculated from the time difference between the sent and the reflected pulses and the velocity of propagation of the cable. PD testing is therefore better suited for short cable lengths, as there is sufficient energy in the input pulse for the reflected pulse to be detected over the full length of the cable. In longer cables there may be insufficient energy in the pulse to allow the reflection to overcome the attenuation of the full length of the cable. To have a pulse with large enough energy for longer cables one would need to increase the voltage of the applied pulse, however as found before this larger voltage will further damage the cable and encourage water trees to grow in other sections of the cable which may not have faulted until many years later. The magnitude of the reflection is a function of both

the magnitude of the change of impedance and the distance to the feature [73]. Due to this attenuation of the pulse magnitude and on-line background noise, the accuracy of this method is reduced [74]. It should be noted that when a PD pulse travels a distance greater than approximately 50m the high frequency components are filtered. This results in the wave becoming more symmetrical, but also looses that information. PD testing may not detect water trees as they do not partially discharge, instead it may force a water tree to partially discharge by accelerating its propagation to a length that can evolve into an electrical tree which does PD. Obviously this testing is not ideal as it further damages the cable.

A newer variation of the PD pulse TDR is to use a two-sensor method. Two sensors are installed at different points along the length of the cable and pulses are analysed to determine which one is faster and stronger. This work is currently under investigation as previous work has shown a large number of errors in the location reported due to attenuation of the pulses in long cables [74].

It is becoming increasingly evident that the attenuation of the pulse for PD detection in long cables is a considerable limitation of this method. This therefore reduces its applicability in on-line cable testing and noisy environments. [75] recognised this shortcoming and deduced that PD testing should also provide information about the type of fault in addition to accurate locations. To this end phase resolved partial discharge (PRPD) was analysed to give more information about the type of fault. Using this same technique, noise patterns can be identified by recognising their characteristic pattern. However during on-line testing PRPD proves very difficult to apply appropriate filter techniques to remove the background noise and classify pulses according to the sources involved. [76] attempted to discriminate between noise and PD by grouping the discharges into different clusters based on the comparison of signal energies associated with particular wavelet-decomposition levels, and applying specific noise rejection filters. Each pulse is characterised by frequency and time of the signal and classification is based on the comparison of the two pulses. An advantage of this dual sensor method

is that it gives information to locate the position of the fault, however the work is currently in its infancy.

A different way of detecting water trees in XLPE is by means of the residual charge method. This is based on the polarisation and depolarisation processess. DC voltage is applied to water tree damaged XLPE cables which allows a build up of charge in the spaces of the water trees. Following this an AC voltage is applied to release these trapped charges, known as residual charges [53]. There is a rapid charging and depolarisation of the water trees, meaning that a pulse voltage may be used in place of a DC then AC voltage. Having a pulse charge is expected to increase reliability of this method due to being able to conduct many pulses in the same time period as conventional testing, but allowing then for the averaging out of the response signals. [53] used this method of sequence pulse signal's to detect current signals related to water tree degradation.

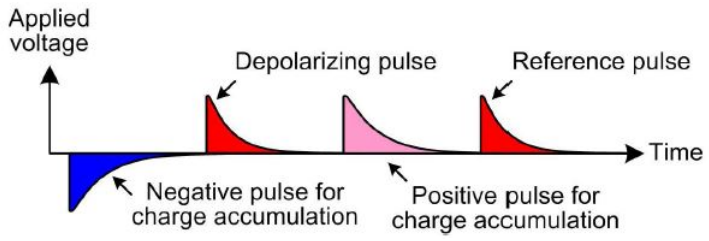

Figure 2.27: Sequence of applied pulses [53]

The initial negative pulse is applied for charge accumulation in water trees. A shorter width positive pulse is applied to depolarise the residual charges. A third pulse of the same size as the initial pulse but of opposite polarity is applied. Finally, a reference pulse is applied with the same pulse voltage and pulse width as the second depolarising pulse. This paper found that bow-tie trees charge relatively easily, and the charge remains within them, however depolarisation is more difficult to achieve with pulse voltages. Furthermore their results suggest that the effect of charge accumulation with pulse voltage is not the main factor affecting small current signals. They did however find that the residual charge magnitude increases with an increase in pulse voltage for charge accumulation and the depolarising pulse voltages. Again this method gives

information of the level of degradation of XLPE cables by water trees, but does not provide much information on their location.

With High Impedance Faults (HIF) a fault current typically flows in an arc, an arc fault being when a high power discharge of electricity occurs between two conductors. This translates as heat and can melt or burn the XLPE insulation. An arc fault is what typically leads to the ultimate failure of the cable. The gap between the two conductors will not conduct until the applied voltage is above a certain breakdown point. In a water tree failure, the two conductors are the cable core and the water filled tip of the water tree. Arc faults are low current faults but can have very large voltage.

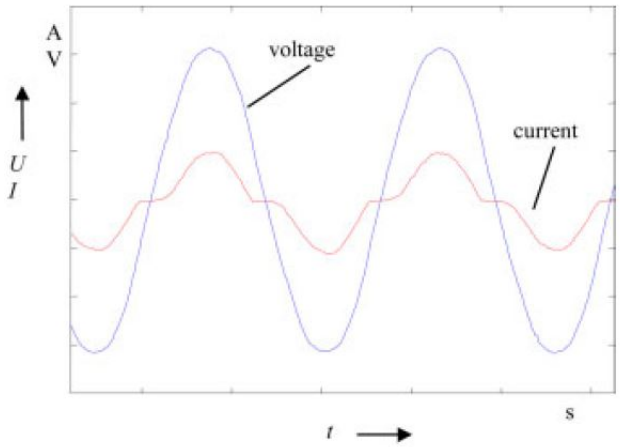

Figure 2.28: Electrical Arc Voltage and Current Shape [77]

Currents due to HIFs are lower than over current thresholds so phase or residual over current devices do not activate. A solution to this is to try and detect the harmonics in time-frequency domain of changes in phase current waveforms caused by faults. A difficulty with this method is that it can be very difficult to distinguish between two critical harmonic components that can discriminate between one disturbance and another. So far [78] have used this method for fault classification purposes but not location detection.

A hybrid high frequency pulse and pattern recognition method for water tree detection and estimation in long cables was proposed by [56]. By using finite element analysis

on the physical structure of the water tree in the XLPE, [56] estimates the capacitance of a water tree to range from 10pF to 50nF. This was confirmed using a COMSOL numerical model. It was proposed that for long cables high radio frequency pulses are a reliable method instead of traditional low frequency pulses. This is an unusual technique as a subsea cable can in one mind be thought of as a very large capacitor, with the high frequency components of a voltage being filtered out along the length of the cable. However they have argued that a high frequency pulse is a benefit in that it lowers the impedance of the water tree fault, making it easier to detect and locate using the same principles as TDR. The authors comment that this technique will compliment traditional partial discharge and low frequency travelling wave methods. This is because these methods excel in diagnosing short cable lengths whereas this new high frequency method is limited to longer cable lengths and lower water tree capacitances.

2.5.3 Water Trees in cables under mechanical stress

A key topic of interest in this research project is whether mechanical stress will influence the likelihood of a cable experiencing an electrical fault at that same location, both in the immediate and longer term. It has been found that static tensile strains do accelerate the formation of water trees [79], thought to be because tensile strains can increase the quantity of elongated microvoids in the XLPE insulation, whereas compressive static strains have the opposite effect. Water can condense in these elongated microvoids, resulting in field enhancement at the tip of the voids, resulting in Maxwell forces, and thus water trees initiate and propagate.

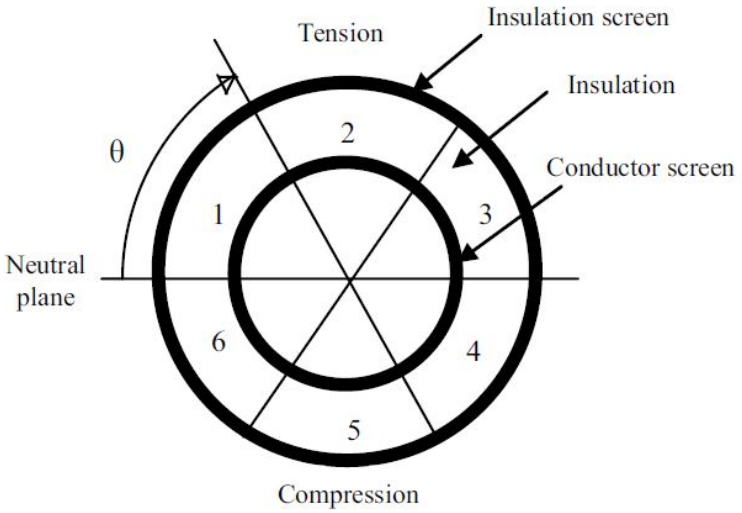

Figure 2.29: Cable Cross Section Showing Division into Tension and Compression Sectors [79]

During the installation process, and for array cables suspended in the water column during operation, the cables are subject to dynamic loading. The dynamic loading is due to wave and current action while also being impacted by the heave and yaw of the offshore wind turbine platforms. This is a factor of particular interest as offshore wind moves closer to the next generation of floating offshore wind turbines. How the cables have been installed will also determine potential "hot spots" for strain and therefore what impact this might have on future electrical faults. It is known that crazing of polymers can lead to cracks at stresses below what is necessary to cause bulk shear yield [80]. Crazes are plastically deformed regions of polymer with voids and polymer fibrils. They initiate when stress causes mircovoids at points of high mechanical stress concentration. The primary mechanical loads on the cable are axial tension and bending of the cable.

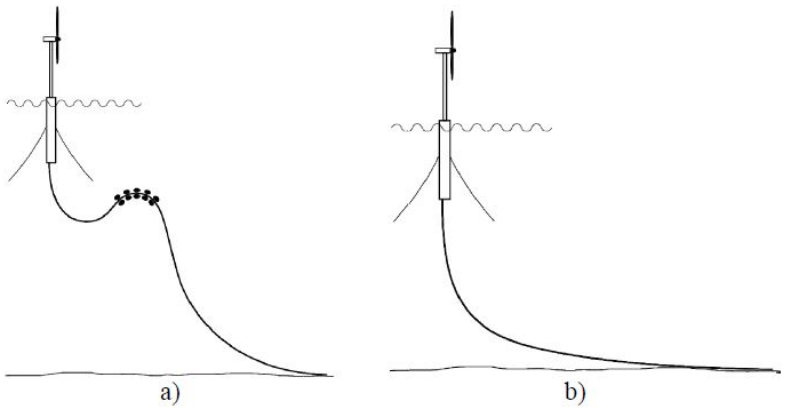

Figure 2.30: Typical Cable Installation Configurations for the Dynamic parts of the Cable. a)Lazy Wave Installation b) Catenary Installation [81]

[81] dynamically bent cables to induce a maximum strain of 1%. The cables were accelerated aged for three months in a wet environment. In all experimental results, interestingly only bow-tie trees were observed. A possible reason for this is that vented trees require a longer initiation time than bow-tie trees [80] so perhaps in this scenario the cables were not aged long enough. A significantly higher number of bow tie trees were found in the strained cable, compared to a unstrained reference cable. Some bow tie trees did form in the compressive sections and these were approximately the same length as those formed in the tensile sections. However, the results did show that there was a greater density of bow tie trees in the tensile strained sectors than the compressive sections.

[79] subjected XLPE cables to a range of static tensile and compressive stresses by bending the cable around cylinders of differing diameters. Both vented and bow-tie water trees occurred during the accelerated ageing tests.

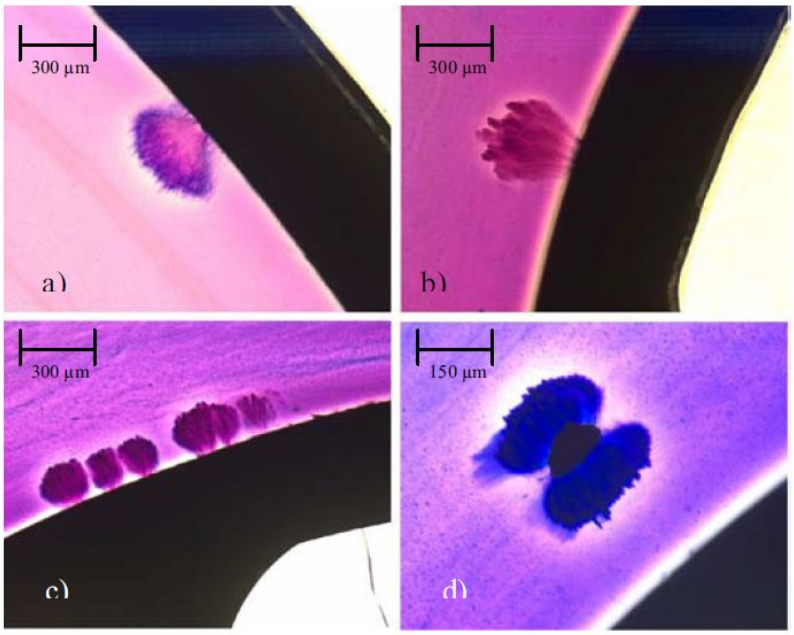

Figure 2.31: a) Vented Tree at Insulation Screen b) Vented tree at Condustor Screen c)Several Smaller Vented Trees Initiated Clsoe Together at Conductor Screen d)Bow-tie Tree [79]

It should be noted that during bending the side of the cable experiencing tensile strain will still experience compression. This is because the insulation is pressed against the incompressible copper conductor, opposing the effect caused by the axial strain. This would therefore result in tensile strain being greatest at the insulation screen side. One could therefore expect the majority of the observed trees to initiate from this screen, however the opposite is true. An explanation to this was provided in that the electric field at the conductor screen is approximately 60% higher than the electric field at the insulator screen. As previously established electric field strength is a key factor in water tree initiation and propagation. Crucially those vented trees which did originate at the insulator screen were roughly double the length of those originated at the conductor screen. Bow-tie trees formed in the most sharply bent sections of the cable with 75% located in tension sectors. [80] conducted a similar cable ageing investigation and found that 88% of all observed vented water trees initiated in mechanically stressed zones, and that not only did the number of trees increase in this region, but also their length, agreeing with what was found in previous studies. These results seem to suggest that mechanical stress is crucial in the initiation or water trees, but it is the electric field

which dominates their propagation.

2.6 Fully dynamic simulation

2.6.1 OrcaFlex

For this work the proprietary marine dynamics software OrcaFlex by Orcina Ltd was used. This software is a three dimensional non-linear time domain finite element program. It splits the length of the cable into user defined lengths and employs a lumped mass approach to solve the cable's dynamic behaviour.

Shown in Figure 2.32 the cable is represented as a series of lines, or "elements", connected by a node at each end. The line elements hold the axial and torsional characteristics while other properties such as mass, buoyancy, weight etc. are held by the nodes. Forces and moments are applied to the cable at the nodes, and line segments are weightless and straight with the axial and torsional spring damping characteristics. The segment ends hold a rotational damping term that is used to model the cable bending.

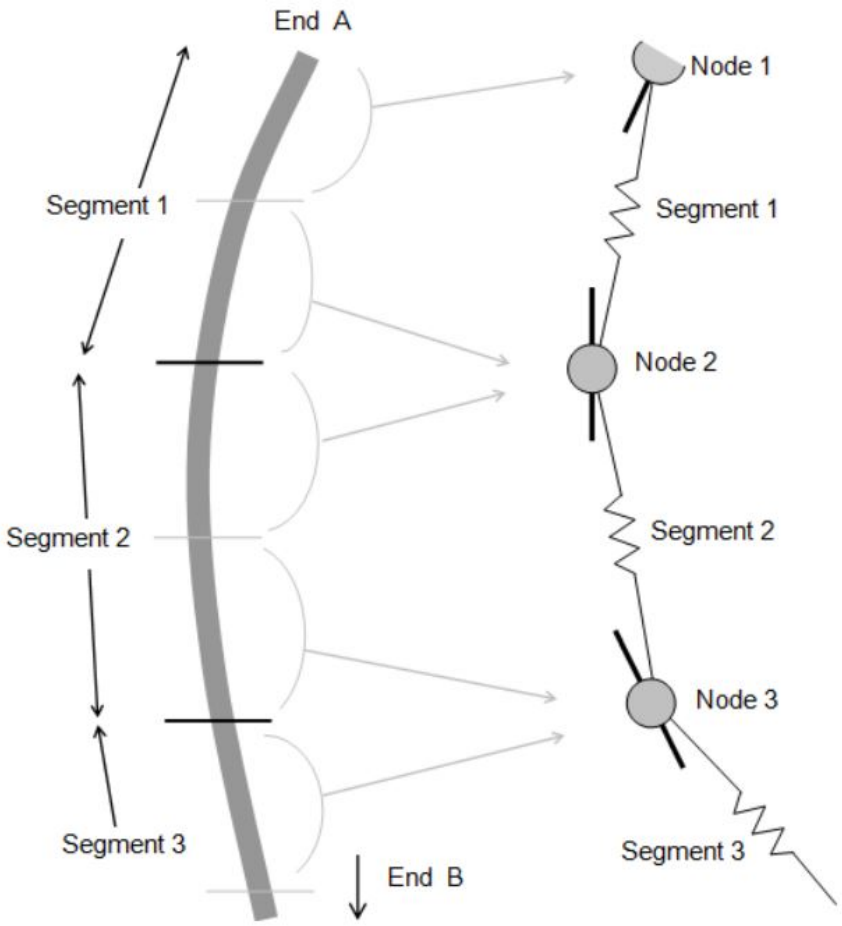

Figure 2.32: Orcina's lumped mass model, showing how lines are discretised into nodes and elements [82]

.

2.6.2 Marine condition calculations

The waves within OrcaFlex can be applied using linear Airy wave theory, in a JONSWAP spectrum [83]. To confirm if the waves are deep water waves, the following condition needs to be met:

$$Z > 0.5\lambda \tag{2.2}$$

Where Z is the water depth, and λ is the wavelength.

The wavelength can be calculated using equation 2.3.

$$\lambda = \frac{g}{2\pi}T^2 \tag{2.3}$$

Where g is gravity and T is wave period.

Using the calculated λ the wave number can be calculated using equation 2.4.

$$k = \frac{2\pi}{\lambda} \tag{2.4}$$

Where k is the wavenumber.

2.6.3 FASTLink

FASTlink is a FAST-OrcaFlex interface package that was used for this work [84]. All hydrodynamics and mooring loads on the cable are solved using OrcaFlex, while the NREL 5MW reference turbine, tower, floating platform structural dynamics, aerodynamics control and electrical drive dynamics are computed using FAST; the fatigue, aerodynamics, structures and turbulence code.

FAST is an aeroelastic simulator which is used to predict fatigue and extreme loadings on three blade horizontal axis wind turbines.

2.6.4 NREL tension leg platform model

This work incorporated the MIT/NREL reference 5MW turbine installed on a tension leg platform [84]. This model was used to simulate the motions of the platform and the cable when exposed to the marine environment, and to investigate their impact on the dynamic cable stresses. This is a platform of 18m waterline diameter with a draft of 47.89m. It has four 27m long pontoons with two mooring lines attached to each pontoon end. The turbine hub sits at a height of 90m asl, with a hub radius of 1.499m. The rotor radius is 62.94m and there are three blades.

2.6.5 Hydrodynamic structural response of the dynamic cable

Within OrcaFlex the hydrodynamic loadings on the cable and the floating platform, with its associated mooring tendons, are calculated using an extended version of the

Morison's equation. Morison's equation takes into account the inertia force of the wave water particle accelerations and the drag force relative to the water particle velocity. For moving objects in a dynamic analysis, the same is applied but adapted to account for the movement of the body. This extended version of Morison's equation is:

$$\boldsymbol{F_f} = (M\boldsymbol{a_f} + C_a M\boldsymbol{a_r}) + \frac{1}{2}\rho C_d A_d \boldsymbol{v_r}|\boldsymbol{v_r}| \tag{2.5}$$

Where $\boldsymbol{F_f}$ is the fluid force, M is the mass of fluid displaced by the body, $\boldsymbol{a_f}$ is fluid acceleration relative to Earth, C_a is the added mass coefficient, $\boldsymbol{a_r}$ is the fluid acceleration relative to the body, ρ is water density, $\boldsymbol{v_r}$ is fluid velocity relative to the body, C_d is the body drag coefficient and A_d is the drag area. The term in brackets at the beginning is the inertia force, while the later term is the drag force. The first part of the inertia term is known as the Froude-Krylov term while the second is the added mass.

The Froude-Krylov term is the force on the moving body caused by the water moving in to fill the empty space left when the body moves. The water will have an associated mass and an acceleration and will therefore generate a force. The added mass term is the result of the distortion of the water by the presence of the moving body.

2.7 Polymer fatigue

The fatigue of polymer materials, similar to metallic materials, is commonly characterised by the stress-life (SN) behaviour or the SN curve [85]. The mechanisms of fatigue and fatigue crack growth are applied from generic approaches established for metals, and the stress-life curves and fatigue data for polymers appear remarkably similar to that found for metals. This suggests that there is a common macroscopic mechanism of crack initiation and growth for polymers and metals.

Sauer and Richardson [86] state that true mechanical fatigue failure of a polymer,

involving initiation and growth of a fatigue crack under continued cyclic loading occurs generally between one quarter and one-half of the yield strength of the polymer. Polymers are susceptible to thermal fatigue, however it would be unlikely that their mechanical applications would involve high loading frequencies or high stress levels, as at these conditions thermal increases would cause the polymer to melt after a few cycles. Crawford and Benham [87] demonstrate this effectively by illustrating thermal failures in polymers of low stress amplitude and high frequency, and conversely low frequency but high stress amplitude.

The mechanism of fatigue crack initiation and propagation within polymers is reviewed by Hertzberg and Manson [88]. Figure 2.33 shows the crack (or craze) initiation limit for Polymethyl methacrylate (PMMA) as well as the failure line. Comparing the time periods, of the crack imitation to the fracture time period, it becomes clear that the lifetime of the polymer is determined by the duration of the crack's propagation. This is a key assumption of the fracture mechanics method.

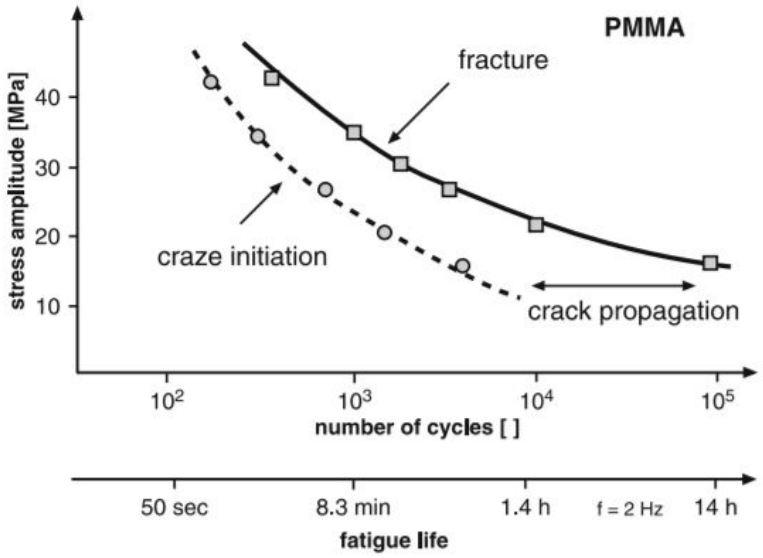

Figure 2.33: SN Curve for PMMA [88]

Other reviews of polymer fatigue by [89], [90] and [91] in addition to Hertzberg and

Manson, all agree on the general macroscopic mechanism of polymer fatigue. The mechanism being largely similar to metals that failure of polymers begins by the initiation of a crack at a surface craze, defect or stress concentration point.

2.7.1 Linear elastic fracture mechanics

2.7.1.1 Paris law

Paris Law is a fatigue crack growth fracture mechanic method which describes the relationship between cyclic crack growth rate $\frac{da}{dN}$ and stress intensity range ΔK. The relationship is associated with P.C. Paris and is described as:

$$\frac{da}{dN} = C\Delta K^m \tag{2.6}$$

Where C is a Paris Law constant for the material and m is the slope of the log-log plot. The stress intensity factor, K, is defined as a function of the crack length, a, the applied far field stress σ, and a geometry function Y which usually approximates to 1.12:

$$K = Y\sigma\sqrt{\pi a} \tag{2.7}$$

Combining equations 6.6 and 2.7 produces:

$$\frac{da}{dN} = C\Delta K^m = C(Y\Delta\sigma\sqrt{\pi a})^m \tag{2.8}$$

Figure 2.34 shows a general Paris Law plot highlighting the three distinct regions, with region two being where Paris Law holds. Figure 2.35 shows a Paris Law graph for XLPE specifically, taken from [44].

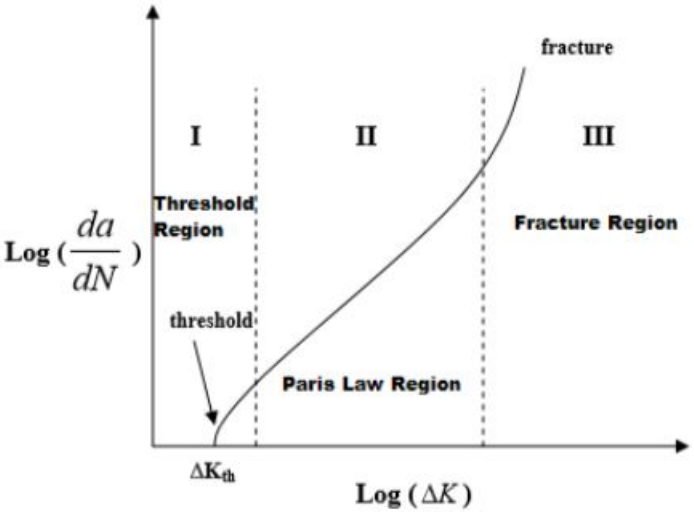

Figure 2.34: Paris Law plot, showing the three distinct regions of crack initiation, linear propagation and finally uncontrolled propagation.

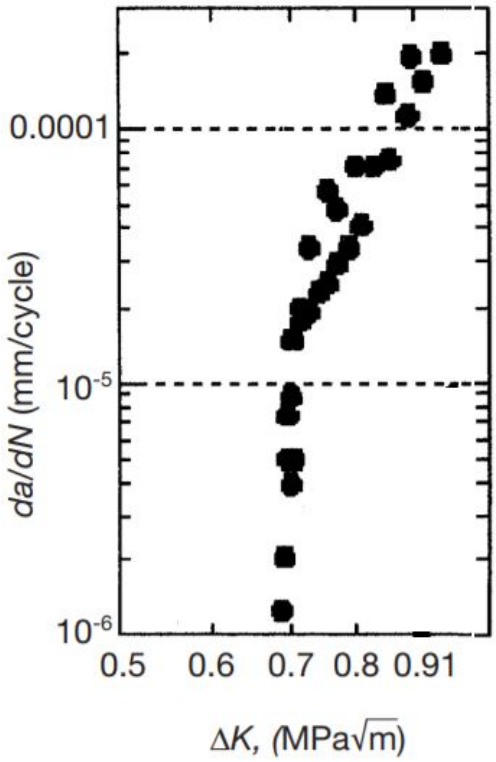

Figure 2.35: Plot of crack propagation rate as a function of stress intensity factor for XLPE adapted from [44]

2.7.2 Combining different stresses

To combine the mechanical stress induced by the installed environment, and the Maxwell stress from the electric field distortions, the stress intensity factors for each individual stress can be calculated and combined. There are three primary modes of fatigue crack propagation:

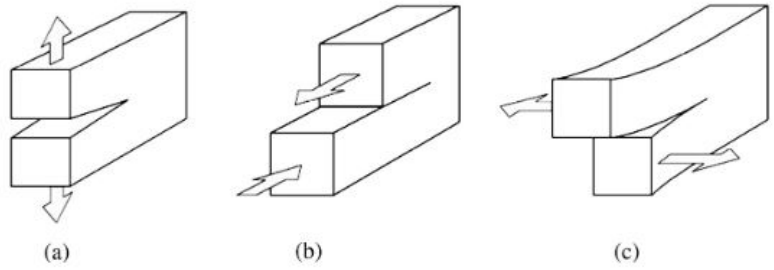

Figure 2.36: The three general fracture modes (a) Mode I, (b) Mode II, (c) Mode III [92]

Mode I is known as the opening mode, II as the shearing mode and III as the tearing mode. To use Equation 6.6 an effective combined stress intensity factor at the water tree tip is calculated. The effective stress intensity factor, $K_{effective}$ is calculated by [93]:

$$K_{effective} = [K_I^2 + K_{II}^2]^{\frac{1}{2}} \tag{2.9}$$

Where K_I is the stress intensity factor calculated from the stresses acting in Mode I, while K_{II} is calculated from the stresses acting in Mode II. Fodil [94] completed work comparing six alternative formulas for calculation of $K_{effective}$, and found the result to be "virtually identical" regardless of the formula used. Due to this the most simplistic is shown in Equation 6.7.

2.7.3 Stress counting

The stress life method estimates fatigue life of a material for a given stress level in terms of the number of cycles to failure. This relationship between stress level and number of cycles to failure is determined experimentally. Due to the statistical nature of fatigue a vast number of test specimens are required. In a rotational bending test the specimen is

subjected to constant stress amplitude cycles below that of the ultimate tensile stress, and the number of cycles to failure is recorded. This is repeated for differing stress levels and the results recorded in an SN curve.

SN curves show the number of cycles that a stress amplitude would need to act to cause a material to fail. In practice stress amplitudes are not constant in a stress time history and a complex stress loading history of differing amplitudes is commonplace. Consequently stress cycle counting methods are employed to represent a variable amplitude stress time history. The rainflow counting method is one of the most common and accepted methods for this task. The outcome of the rainflow count is to convert the variable stress time history so it can be treated as a series of constant amplitude stress cycles, defined by their range and mean value. To complete a rainflow count the algorithm requires the stress history to be filtered so that only the peaks and valleys remain, furthermore it is required that it be reordered so that the stress history starts and ends with the highest stress peak, or lowest stress valley.

Once the stress have been counted, the total damage accumulated by the varying stress levels can be deduced.

2.7.4 Damage Accumulation

The most widely recognised damage accumulation rule is the Palmgren-Miner rule, which states that the accumulated damage of a batch of stress cycles is the number of cycles that occurred divided by the number of cycles that would cause the material the failure. Failure is assumed when the accumulated damage (damage sum) equals 1.

$$D = \sum_{i=1}^{k} \frac{n_i}{N_i} \tag{2.10}$$

Where for k different stress levels and the average number of cycles to failure at the i^{th} stress S_i, N_i is the total number of cycles of S_i to failure and n_i is the number of cycles of S_i that occur. No fatigue damage limit has been included for this work, and

therefore all fatigue ranges contribute to the damage.

Damage accumulation has been shown to be both over and under conservative [95] when applied to spectrum loading, so large safety factors need to be considered. The Palmgren-Miner rule can be used with a Goodmans diagram to characterise uni-axial fatigue behaviour for any R value. R value being the ratio of stress cycles minimum and maximum values.

Fatigue is not only a consideration of the range of the cyclic stress, but the mean stress in that cycle also plays a role on the fatigue behaviour. The stress cycles will vary throughout the time history in both amplitude and mean. Figure 2.37 shows how the Goodman line balances between its boundaries of when the mean stress is equal to that of the ultimate tensile strength (x-axis) so the stress amplitude must be zero, and the second when the mean stress is zero, so the stress amplitude has a maximum of the fatigue limit stress amplitude (y-axis). In between these boundaries there is an infinite number of combinations of mean and stress range. Below the Goodman line infinite life is assumed; if a stress cycle exists above the line infinite life is not possible. Figure 2.37 also shows the Gerber correction parabola line, however the Goodman correction is more conservative and so has been chosen for this work. Goodman's correction can be written as Equation 2.11:

$$\sigma_{\mathrm{a}} = \sigma_{\mathrm{fat}} \times \left(1 - \frac{\sigma_{\mathrm{m}}}{\sigma_{\mathrm{ts}}}\right) \tag{2.11}$$

Where σ_a is the alternating stress in Pa, σ_{fat} is the fatigue limit, or endurance limit, from the SN curve in Pa, σ_m is the mean stress of the stress time history cycle in Pa and σ_{ts} is the ultimate tensile strength of the material in Pa.

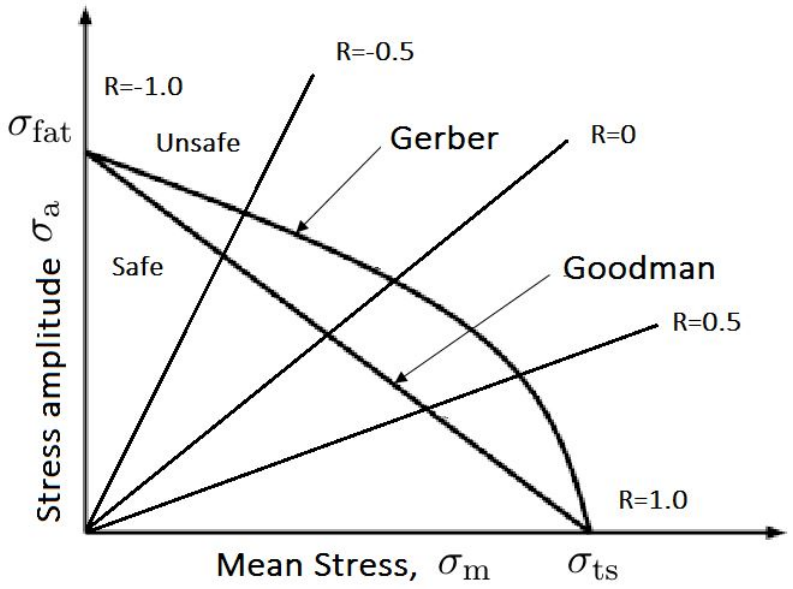

Figure 2.37: Goodman and Gerber correction diagram for differing R values

The Goodman correction calculates an effective alternating stress, accounting for this mean stress, allowing for use of an SN-curve with a fixed stress ratio of -1. The effective stress σ_{eff} is calculated and used to read from the SN curve the number of cycles to failure:

$$\sigma_{eff} = \sigma_a \left[\frac{\sigma_{ts}}{\sigma_{ts} - \sigma_m} \right] \tag{2.12}$$

2.7.5 Kinetic theory of fracture

Regel and Leksovski [96] state that from the standpoint of the kinetic theory, fracture is a process that develops within a body under loading and is not an event that occurs when a critical stress is reached. The elementary events in a fracture process are the breaking of interatomic bonds. For a polymer like XLPE these bonds can be both chemical and inter-molecular. Successive breakages of these bonds lead to the eventual macroscopic failure of the specimen; to the formation and propagation of cavities and

cracks and eventual ultimate failure.

Mathematically the theory is most common presented as Equation 2.13 in which τ is the time to failure, σ is the applied stress, T is the absolute temperature, k is the Boltzmann constant, τ_0 is the period of atomic vibration, U_0 is the activation energy of the fracture process, and $\gamma\sigma$ is the induced decrease in activation energy due to the applied mechanical load. In short, fracture can be thought of as a series of successive rupturing of bonds of the material at the atomic level.

$$\tau = \tau_0 \exp\left(-\frac{U_0 - \gamma\sigma}{kT}\right) \tag{2.13}$$

2.7.6 New surface energy and crack propagation

Lake and Thomas [97] considered crack propagation under stress within a rubber polymer as the energy per unit area required to produce new surface (T_0). This energy can be calculated approximately by considering the energy requirement to rupture a polymer chain lying across the path of the crack propagation. This energy, similar to the kinetic theory of fracture, is calculated from the strength of the chemical bonds of the polymer monomers, where secondary forces are ignored.

T_0 is substantially greater than the energy required simply to rupture a bond lying across the crack plane. The polymer will consists of a number of flexible long-chain molecule crosslinked at intervals. The plane ahead of the crack tip will have multiple of these chains, where multiple crosslinks will cross the crack propagation path. For the crack to propagate these chains must be broken. This is illustrated in Figure 2.38.

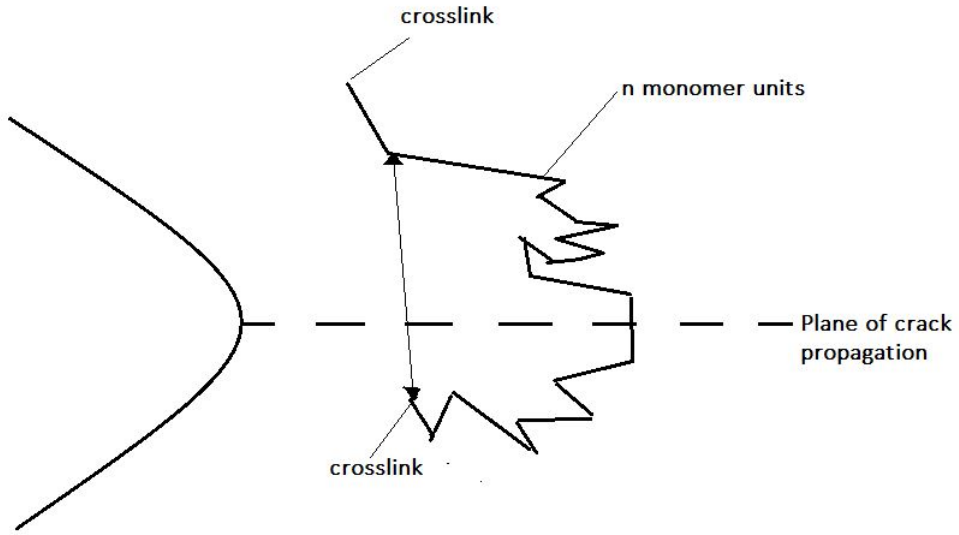

Figure 2.38: Schematic showing a polymer chain lying across the plane of crack propagation

In Figure 2.38 the polymer chain consists of n monomer units and has a displacement length L between the points where it is crosslinked. As forces and stresses are transmitted via the crosslinks, to break a single bond in a polymer chain it is necessary to subject all other bonds within the chain to virtually the breaking force. Therefore the energy required to do this, T_0, is larger than the disassociation energy of a single bond lying across the crack propagation plane. If the energy required to rupture one monomer unit (which contains several bonds) is U, then the energy required to rupture a polymer chain is nU, noting only one of the monomer units will in fact be ruptured. This allows for crack propagation of one monomer length or diameter.

To calculate initial approximations of T_0 a number of assumptions are made. Firstly it is observed that separate to the rupturing chain, neighbouring chains can significantly deform without breaking. The energy losses in these deformations are ignored. Secondly, a perfectly uniform network of polymer chains is assumed where each chain contains the same number of monomer units (n), the same displacement length L, and N is the number of polymer chains per unit volume of the polymer.

$$T_0 = \frac{1}{2}LNnU \tag{2.14}$$

Chapter 3

Global model

3.1 Chapter introduction

In this chapter the forces of the marine environment on the dynamic cable are considered. The cable dynamics are governed by the environment they are operating in, and the platform they are attached to. A global model of a tension leg platform has been built, using OrcaFlex coupled with FAST, with a dynamic cable attached to it. The global model has been used to model the dynamics of the whole floating wind platform system.

A resource assessment of the wind, waves and current for a site off the North East coast of England was completed to derive the environmental load cases for the global model. These inputs are then applied in turn to the global model of the floating wind platform, and the force response along the dynamic cables length are investigated.

To conclude this chapter, the force response time histories along the cable are extracted at specific points of interest along the length of the dynamic cable. These force time histories are then used as inputs to the Local model chapter to deduce the mechanical stress time histories across the dynamic cables cross section.

3.2 Resource assessment

This section of the chapter discusses the work completed to derive the environmental input load cases for the global model. The DNV standard for floating wind turbine structures [22] has been used as guidance in formulating the environmental load cases for this work. The environmental specifications required are the significant wave height, zero-upcrossing period and mean wave direction, ten minute mean wind speed at a specified reference height, the wind shear, and the misalignment between wind and wave directions. Finally current speeds and directions are included if deemed relevant.

Marine data was obtained from a site off the North East coast of England. The wave data was collected from a wave buoy placed at a site in ninety metres water depth for a period of one year, only stopping because the buoy broke it's mooring during a storm event on the 26th January 2012 and was not redeployed. Current data was collected from a nearby site in fifty six metres water depth by an acoustic wave and current profiler, AWAC, for a period of six months. Table 3.1 gives some details on these collection sites. This wave and current data was collated from a previous in-house commercial project, however a copy can now be found online at Marine Data Exchange [98] logged under Blyth NaREC Offshore Demonstration Site, Oceanographic Monitoring, Raw Data. Wind speed data correlated to wave height was obtained from two locations based in the central North Sea from the NEXT study, an extension of the North European Storm Study, NESS [99]. Figure 3.1 gives some context to the site and the data collection point locations.

Table 3.1: Marine data collection sites

Site	1	2	3	4
Data source	AWAC	Wave buoy	NEXT model	Next model
Location coordinates	55 08.890N, 01 17.5967W	55 14.313N, 01 05.715W	55.850N 0.911W	55.391N, 0.263E
Operational period	11/02/2011 - 03/08/2011	21/01/2011 - 26/01/2012	January-December 1977-1979 & 1989-1994	January-December 1977-1979 & 1989 - 1994
Water depth	56m	90m	-	-

Figure 3.1: Locations of the AWAC,1,the wave buoy, 2, and the NEXT model locations, 3 and 4

3.2.1 Wave resource

The wave buoy data was analysed for the site and a wave rose was plotted, Figure 3.2. From the wave rose it can be seen that the vast majority of the waves come from between 0-30 degrees, with North being 0 degrees. Therefore for the global model the waves are assumed to be coming from 15 degrees. Furthermore, the direction of these waves suggests that they are swell waves, benefiting from the longer fetch to the North East.

To understand the wave characteristics at the site, a spectrum of significant wave height and zero crossing period was plotted in Figure 3.3, with the probability of each wave condition plotted. As an example from Figure 3.3 it can be deduced that the most common wave condition is a wave height of 0.5-1m with a period of 3.5-4.0s.

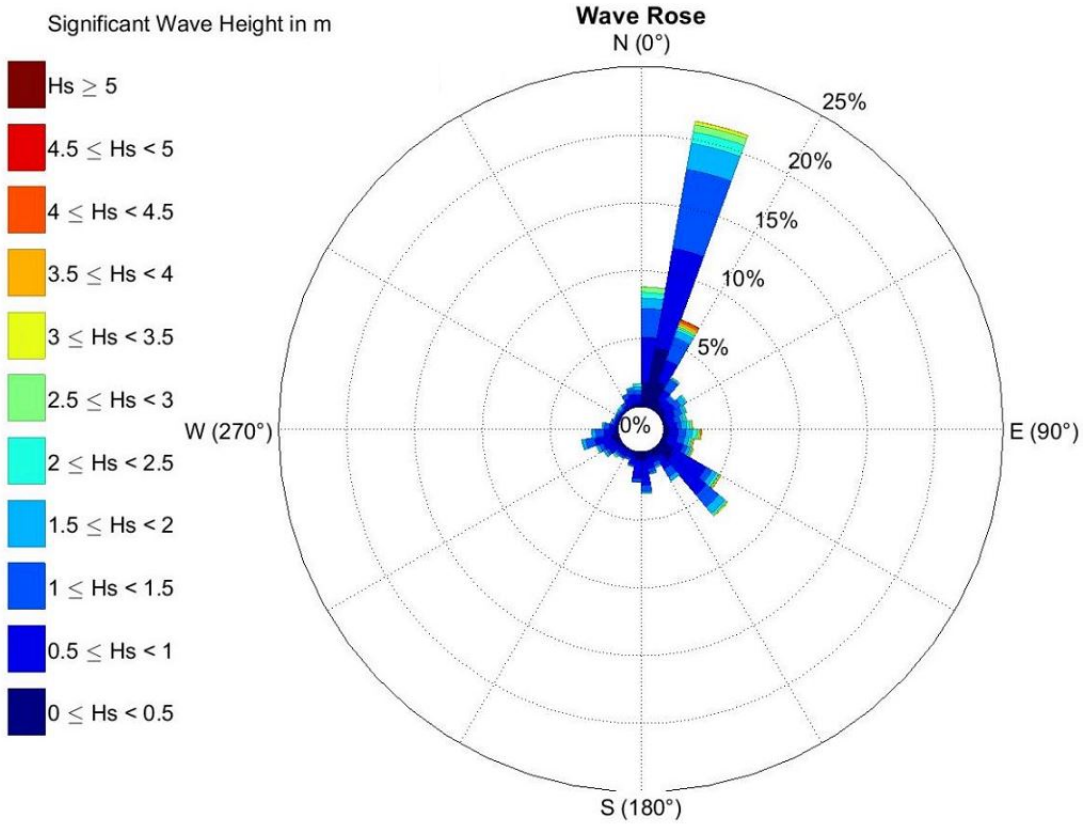

Figure 3.2: Wave direction and height

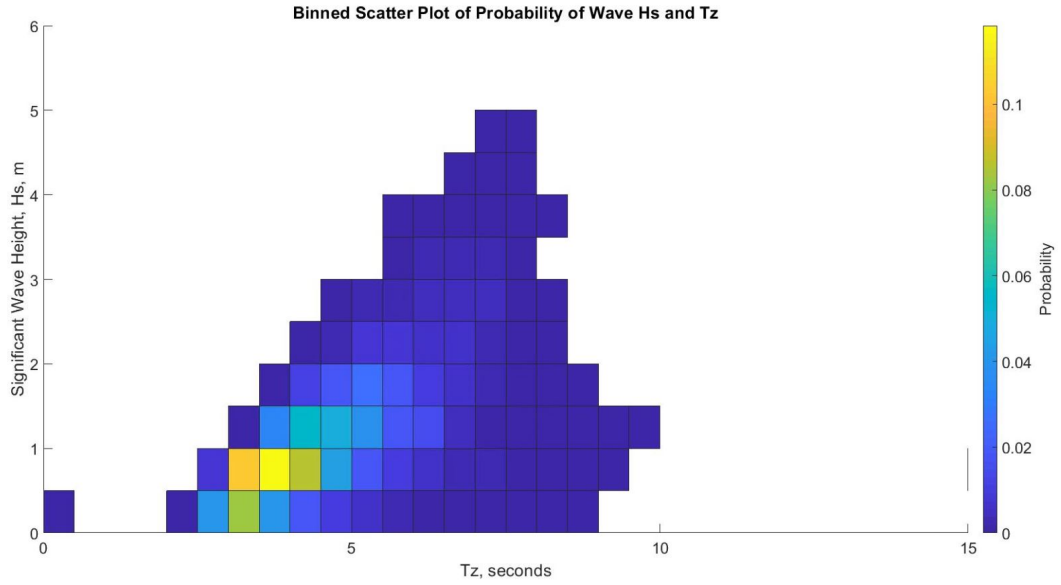

Figure 3.3: Binned scatter plot of significant wave height and period

3.2.2 Current resource

Similar to Figure 3.2, a rose of current directions from the AWAC was plotted in Figure 3.4. From this it can be quickly deduced that the tidal current at the site is bi-directional, travelling up and down the coast of North East England. The two directions assumed for these works of the current resource are 165° and 345°. The tidal cycle around the British Isles is semidiurnal. Pheonix [100] demonstrates that in a tidal cycle in the British Isles, the current velocity accelerates to its maximum, decelerates to zero and then changes direction, Figure 3.5.

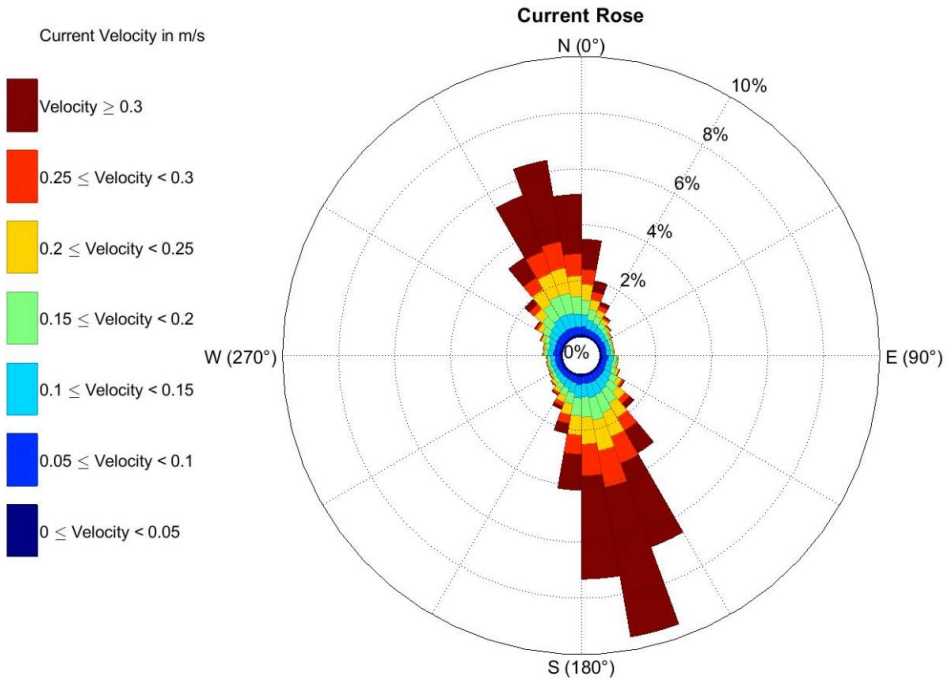

Figure 3.4: Current velocity and direction

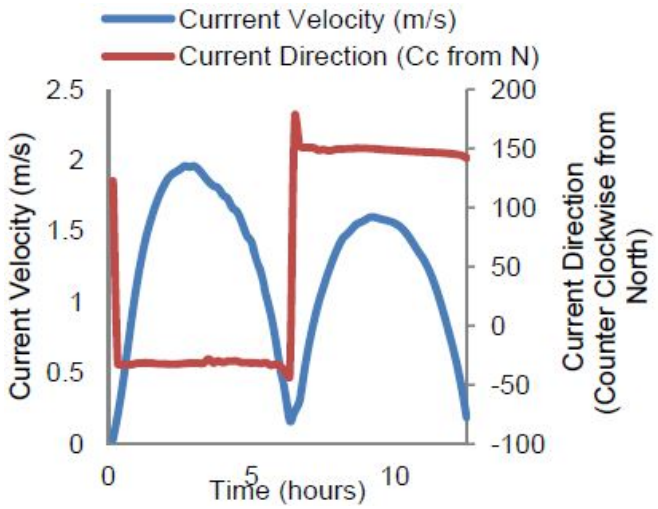

Figure 3.5: Variation in speed and direction over a tidal cycle [100]

The AWAC was placed in fifty six metre water depth, and this data was extrapolated to a depth more appropriate for a floating offshore wind turbine. The "deep offshore" environment begins at water depths greater than fifty metres. Phase 2 of the Fukushima floating offshore wind farm demonstration project is in water depths of one hundred and fifty metres. The dynamic cable modelled in this work, however, is based upon a historic oil and gas project in depths typically greater than that of Fukushima. Furthermore, this dynamic cable is much more complicated than would be anticipated for floating offshore wind applications, with such complexity unlikely to be cost effective for offshore wind. Due to this, a compromise was made with the water depth, making it applicable to floating offshore wind but also more appropriate for the design of the dynamic cable. For this a water depth of two hundred metres was chosen, and the current data from the AWAC fitted and extrapolated.

In Figure 3.6 the current data was plotted, fitted to a curve, and extrapolated. Using the power law Equation 3.1 two power factors were compared. Many researchers advocate for the seventh power law equation, however others have claimed a ninth power law fits more closely for current shear profiles [101]. When comparing the two, the ninth

power law did fit the extrapolated real fitted data better.

$$\frac{U}{U_0} = (\frac{Z}{D})^{\frac{1}{n}} \tag{3.1}$$

Where U_0 is the current velocity in ms^{-1} at the surface, Z in m is the distance above the seabed, D is the water depth to the nth power.

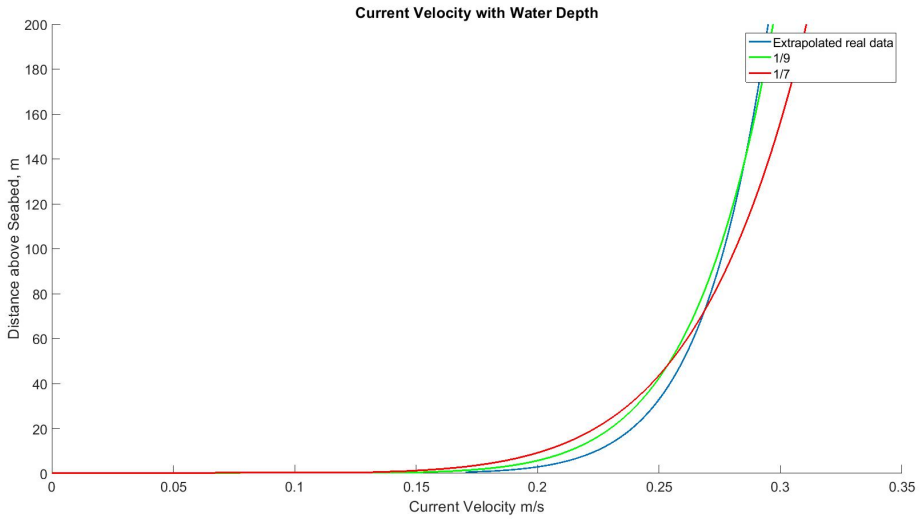

Figure 3.6: Current velocity with water depth

3.2.3 Wind resource

A disadvantage of the site data was that no specific wind measurements were taken on the same dates the wave buoy and AWAC were deployed. However wind speed data correlated to wave height was obtained from locations based in the central North Sea from the NEXT study, an extension of the North European Storm Study, NESS [99]. NESS was initiated to produce a hind cast database of winds, waves and currents for the North European continental shelf. Figure 3.7 illustrates the locations of the NEXT grid points and sub-regions. From this it can be seen that the wave buoy and AWAC were deployed in the central North Sea grid area, marked within the pale blue boxed region. The wind data collection site closest to the wave buoy and AWAC within the central North Sea region is the site numbered 15138 and so the wind data from this location has been chosen for this work. Figure 3.8 shows the significant wave height to mean wind speed spectrum for the site labelled 15138.

The NEXT model collected data from January through December in 1977-1979 and again 1989-1994, totalling seven years of data collection.

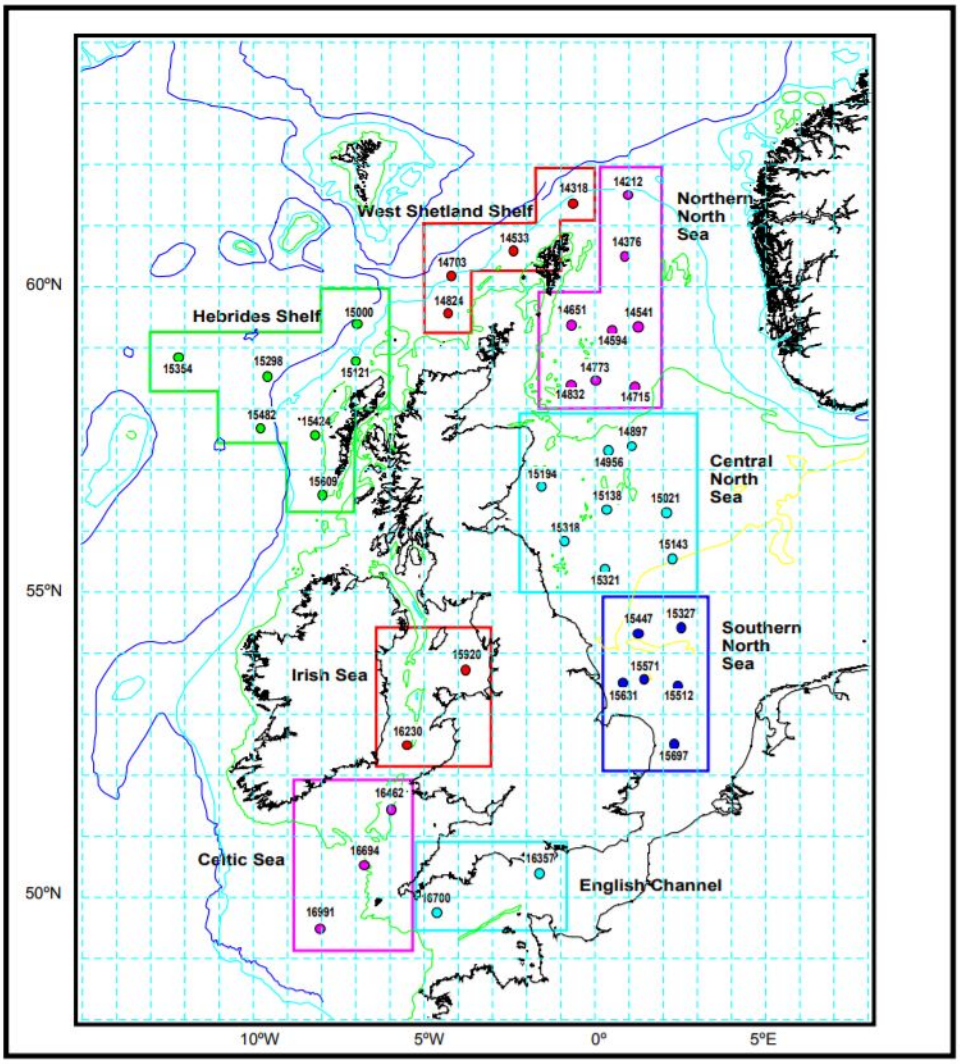

Figure 3.7: Chart showing location of NEXT grid points and sub-regions

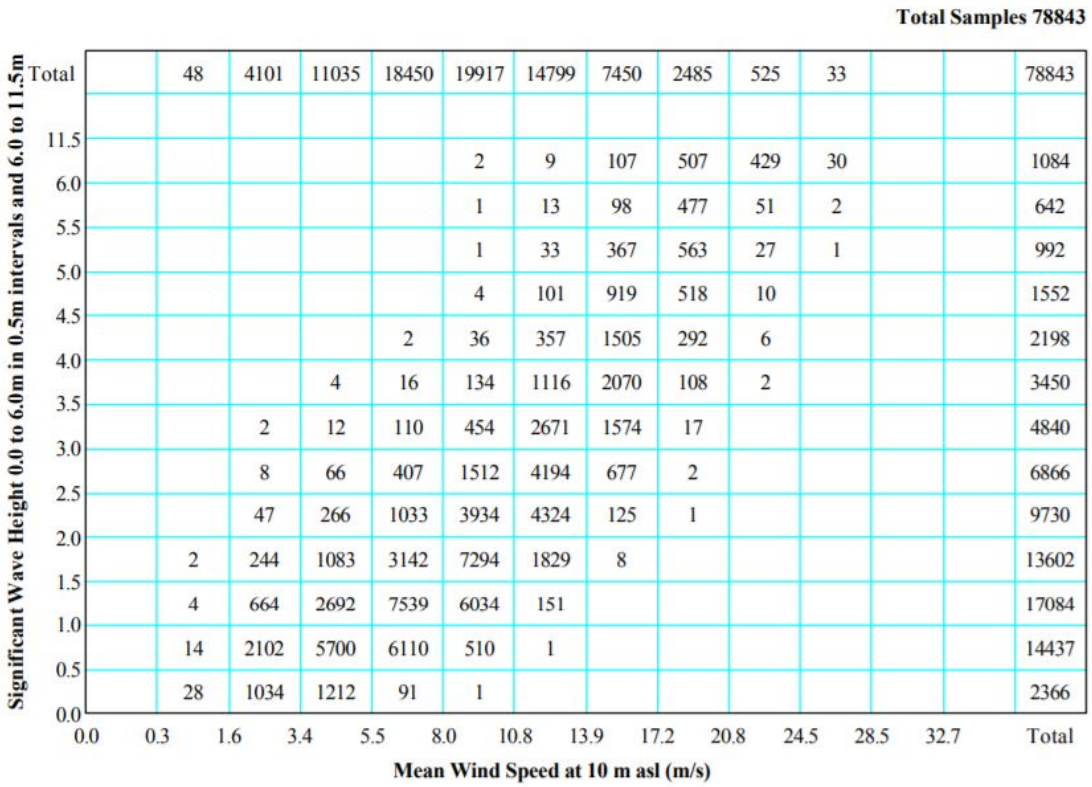

Figure 3.8: Binned signification wave height to mean wind speed from site 15138 [99]

To use wind data near the wave data site it was necessary to assume that the wind and wave resources at the wave buoy and the NESS model site were the same, and that there was a correlation between the wave height and the wind speed. The NEXT data sites present wave height binned with a corresponding wind speed 10m above sea level. When this spectrum of wave height by wind speed is replotted with a line graph fitted to the data, Figure 3.9 is obtained. This line was then used to estimate the wind speed for the wave heights recorded by the wave buoy. Table 3.2 shows the wind velocities ten metres above sea level, asl, calculated for the significant wave heights captured by the wave buoy.

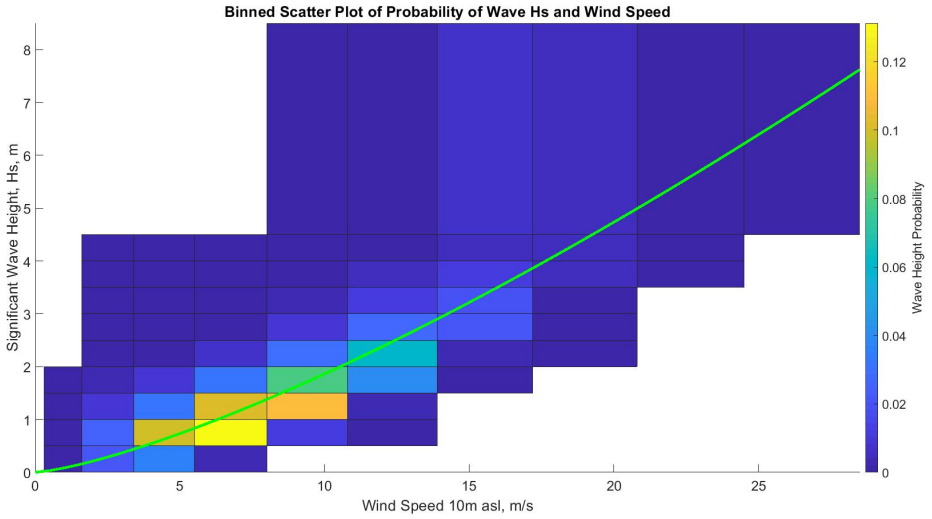

Figure 3.9: Binned scatter plot of probability of wave height and wind speed

Table 3.2: Significant wave height and corresponding wind velocity

Significant wave height H_s (m)	Wind velocity 10m asl (ms^{-1})	Wind velocity at hub height (ms^{-1})
0.25	2.2	3.0
0.75	5.1	6.9
1.25	7.4	10.1
1.75	9.5	12.9
2.25	11.5	15.6
2.75	13.4	18.2
3.25	15.1	20.5
3.75	16.8	22.9
4.25	18.5	25.2
4.75	20.1	27.3

This model includes a tension legged floating wind platform incorporating the NREL 5MW turbine. This turbine has a hub height of 90m, therefore by using the equations laid out in the guidelines for the certification of offshore wind turbines [24] the wind

speed at the hub height was calculated using Equation 3.2. These calculated wind velocities at hub height are included in Table 3.2.

$$V_z = V_{hub}(\frac{h}{h_{hub}})^{\gamma} \tag{3.2}$$

Where V_z is the wind velocity at height h in ms^{-1}, h is the height above the still water line in m, h_{hub} is the hub height above the still water line in m, and γ is the power law exponent, where [24] assumed γ is equal to 0.14 for all wind velocities, i.e calculating the wind shear profile using the seventh power law.

Mean wind directions were also obtained from the NESS model and shown below.

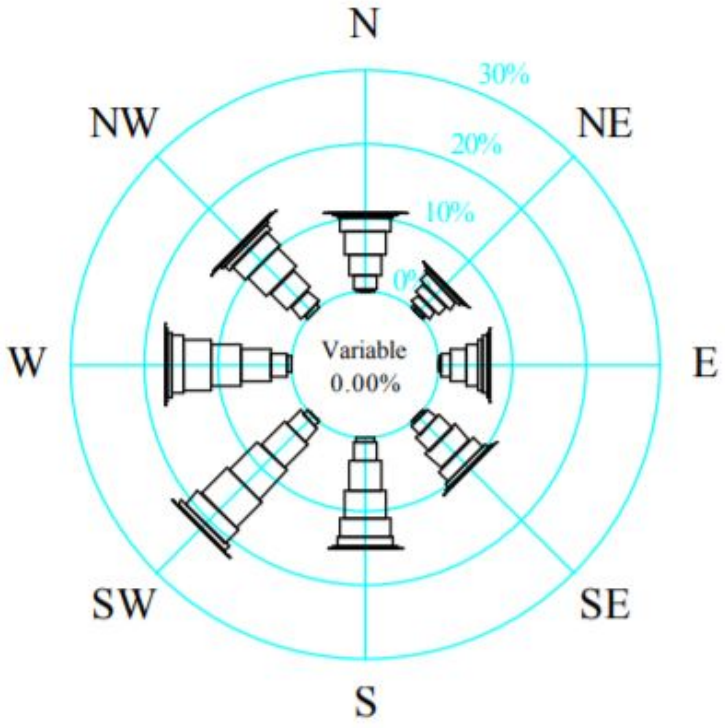

Figure 3.10: Mean wind directions [99]

3.2.3.1 Wind flow field modelling

Using the mean wind velocities calculated in Table 3.2, TurbSim was used to generate the turbulent wind profiles, for use in the global FAST-OrcaFlex coupled model. TurbSim is a turbulence simulator which provides numerical simulations of the wind containing coherent turbulent structures.

Figures 3.9 and 3.8 show the wind data collected for seven years, however actual wind profiles are complex with turbulent eddies. Flow field simulators enable these effects to be simulated to generate a more realistic wind profile, while maintaing the average wind speed calculated from Equation 3.2 for use in the global model.

In this work the IEC Kaimal spectral model defined in [102] (edition 2), [103] (edition 3) and explained in the TurbSim user guide [104], which assumes neutral atmospheric stability (no temperature inversions) is used. The IEC Kaimal model was chosen as this is typically used for offshore conditions. The spectra of the three wind components, K = u, v, w are given by:

$$S_k(f) = \frac{4\sigma_k^2 L_k/\bar{u}_{hub}}{(1+6fL_k/\bar{u}_{hub})^{\frac{5}{3}}} \tag{3.3}$$

Where f is the cyclic frequency and L_k is an integral scale parameter. The IEC 61400-1 standard defines L_k as:

$$L_k = \begin{cases} 8.10\Lambda_u, & K = u \\ 2.70\lambda_u, & K = v \\ 0.66\Lambda_u, & K = w \end{cases} \tag{3.4}$$

Where the turbulence scale parameter Λ_u is:

$$\Lambda_u = \begin{cases} 0.7.\min(30\text{m}, \text{Hub height}), & \text{Edition 2} \\ 0.7.\min(60\text{m}, \text{Hub height}), & \text{Edition 3} \end{cases} \tag{3.5}$$

In Equation 3.5 the function "$\min(x_1, x_2)$", indicates the minimum value of x_1 and x_2. The turbulence scale parameter Λ_u is defined as the wavelength where the non-dimensional, longitudinal power spectral density is equal to 0.05. Thus wavelength is defined as $\Lambda_u = \frac{V_{hub}}{f_0}$ where $f_0 S_1(f_0)/\sigma_1^2 = 0.05$ [102]. The relationship between the standard deviations is given as follows:

$$\begin{aligned} \sigma_v &= 0.8\sigma_u \\ \sigma_w &= 0.5\sigma_u \end{aligned} \tag{3.6}$$

This is used to produce a turbulent air flow field as shown in Figure 3.11 and Figure 3.12.

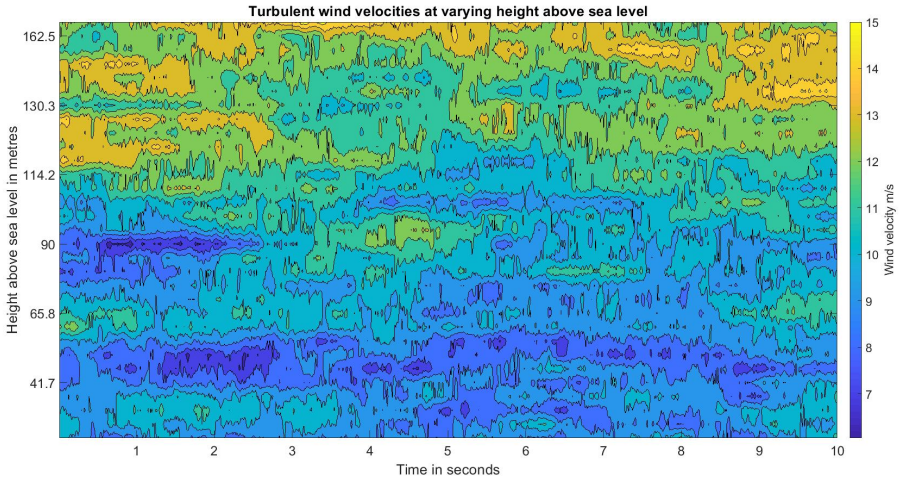

Figure 3.11: Axial variation of wind velocity when the wind velocity at 10m asl is 7.4ms^{-1}

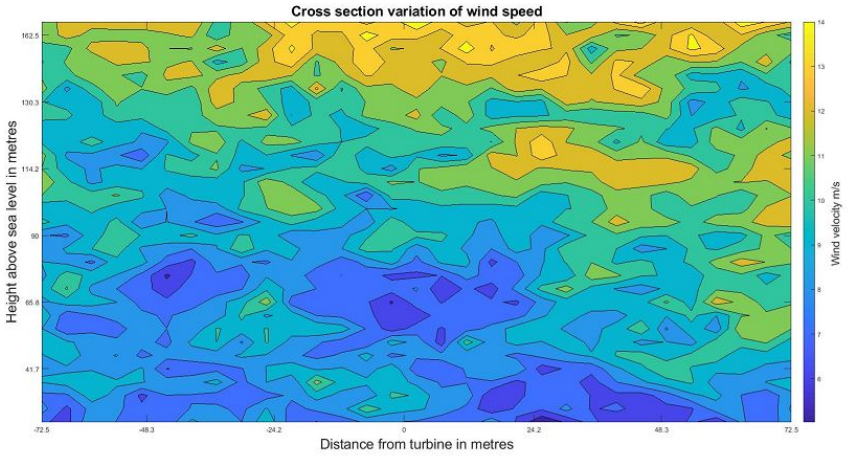

Figure 3.12: Lateral variation of wind velocity when the wind velocity at 10m asl is 7.4ms^{-1}

Figure 3.11 shows the first ten seconds of the wind field through a plane at the centre of the rotor. Figure 3.12 shows a snapshot in time of the wind profile to either side of the rotor.

Typically wind speed will be greater at increased heights above the sea level, roughly following a shear profile. However, while Figures 3.11 and 3.12 show this to be the general case, there are instances where the wind speed is greater at lower heights. This is reflective of the random nature of turbulence, creating instances where the wind speed variation differs from what would typically be expected.

3.3 Environmental load cases

In DNVGL-ST-0019 [22] some proposed design load cases are given that have been used as a template for this work. Table 3.3 gives details on design load case 2.6 from DNVGL-ST-0019, supplementary to DNVGL-ST-0437 [23], which provides a number of proposed design load cases by combining various environmental conditions.

Table 3.3: Proposed floater design load case

Design situation	Design load case	Wind condition	Sea state condition	Wind/wave directionality	Current
Power Production + occurrence fault	2.6	Normal turbulent model	Normal sea state	Multiple misaligned directions	Normal current model

Using the standard load cases laid out in Table 3.3, and the assessment of the wind, wave and current resource at the site, a table of load cases was derived. Figure 3.13 gives some clarity on the directions of each environmental load case for quick assimilation.

Table 3.4: Proposed global model environmental load case inputs

Load Case	Mean wind velocity	Significant wave height	Wave period	Wave direction	Wind/wave direction misalignment	Current
1	Table 3.2 (2.2 - $20.1 ms^{-1}$)	Table 3.2 (0.25 - 4.75m)	See Figure 3.3 (0.25 - 9.75s)	15°	0	Bi-directional sinusoidal max $0.3 ms^{-1}$
2				15°	-90°	
3				15°	+90°	
4				15°	180°	

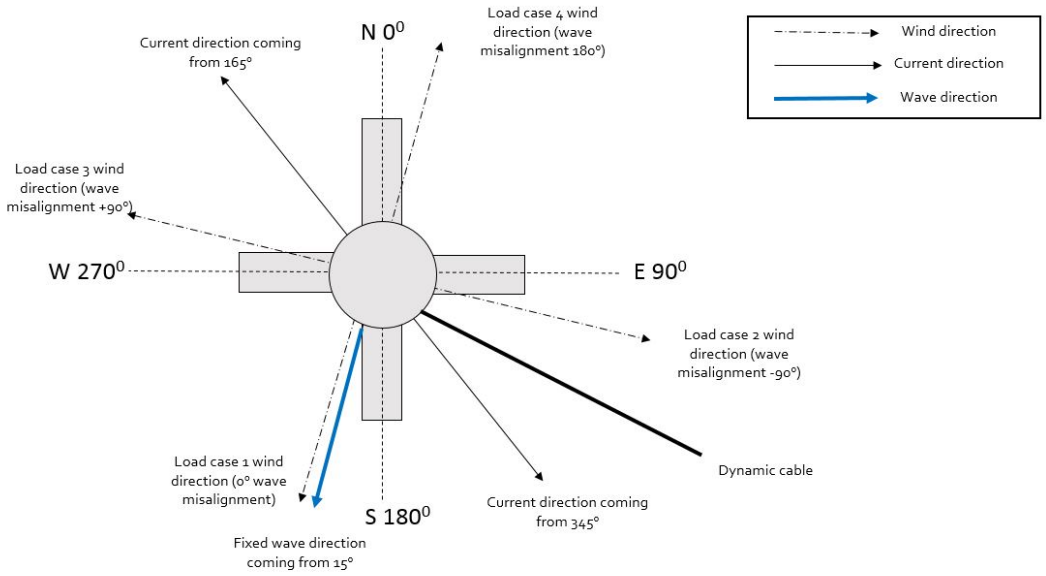

Figure 3.13: Top view of the tension leg platform with wave, current and wave/wind misalignment directions indicated

3.3.1 Current considerations

According to DNVGL-ST-0019, a normal current model is included in the global model if deemed necessary. The wind and waves are named as the dominate environmental loadings. For this work an initial bi-directional current model was included for Load Case 1 in Table 3.4, ramping from 0.3ms^{-1} towards 345°, to 0.3ms^{-1} towards 165° with a H_s of 0.75m and a period of 3.75s. In Load Case 1 the wind and waves are aligned with one another so as to have a control with only the current directions varying.

To see the impact of the current on the displacement of the platform, and therefore the tension in the dynamic cable at the hang off point, the surge and sway of the platform for the maximum current velocity in each direction was compared, illustrated in Figure 3.14. The tensions of the dynamic cable are then compared to the platform displacements, shown in Figure 3.15, with the ultimate goal of determining the impact of the current and if it is necessary to be included in the model. It should be noted here that positive surge is in the South direction in Figure 3.13 while positive sway is in the East direction. Table 3.5 shows the tensions for each Load Case and current direction.

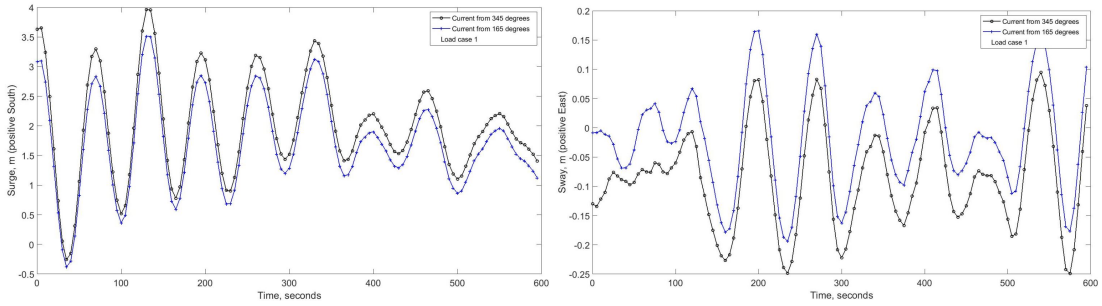

(a) Platform surge (b) Platform sway

Figure 3.14: The surge and sway of the floating platform when Load case 1 conditions are applied with a H_s of 0.75m and a period of 3.75s for each current direction

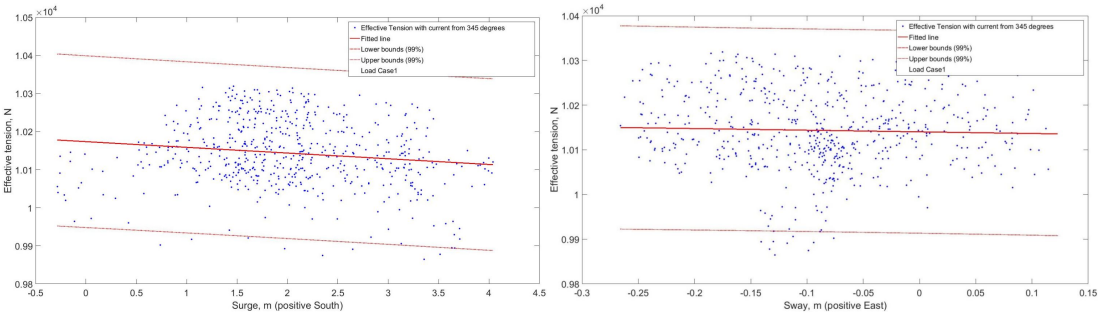

(a) Cable tension with surge for 345 current (b) Cable tension with sway for 345 current

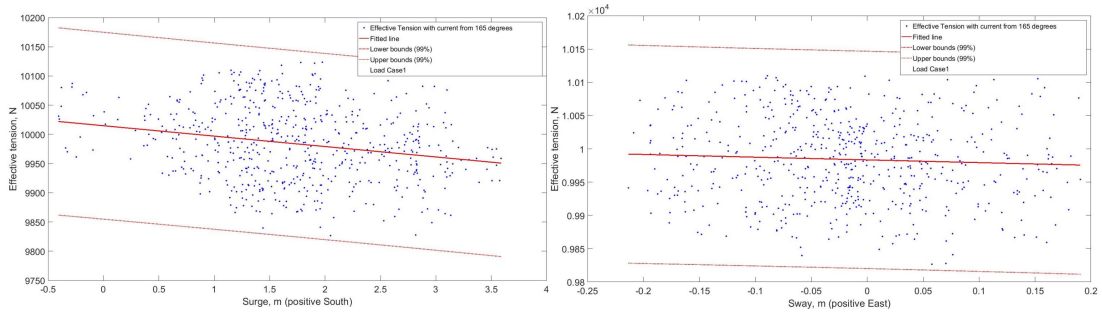

(c) Cable tension with surge for 165 current (d) Cable tension with sway for 165 current

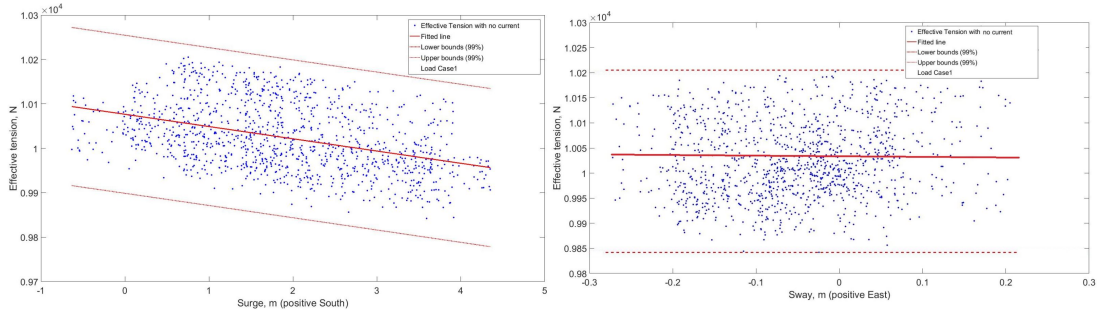

(e) Cable tension with surge for no current (f) Cable tension with sway for no current

Figure 3.15: The cable tension vs. the surge and sway of the floating platform when Load case 1 conditions are applied with a H_s of 0.75m and a period of 3.75s for each current direction

Table 3.5: Table of cable tensions for each Load Case with each different current direction

	Current direction	Max Tension	Mean Tension	Tension Range
	degrees	kN	kN	N
Load Case 1	345	10.328	10.144	473.84
	165	10.128	9.984	316.93
	No current	10.212	10.025	370.44
Load Case 2	345	10.248	10.159	292.87
	165	10.097	10.035	123.98
	No current	10.115	10.048	147.44
Load Case 3	345	10.252	10.169	266.19
	165	10.116	10.057	119.67
	No current	10.127	10.060	132.57
Load Case 4	345	10.321	10.189	319.45
	165	10.215	10.098	224.68
	No current	10.211	10.084	257.06

From Figure 3.14 it can be seen that a current from 345° and 165° produces a similar shape profile of the surge and sway of the platform. When the current is from 345° the sway and surge are larger than from 165°. This corresponds to when the current is more aligned with the wind and wave directions. There is some instances at the beginning of the simulation when the surge is negative, as in the platform moves to the North. This is unexpected and is contributed to some run up errors in the simulation. The initial 30 seconds of the simulation were discarded to avoid these transients however this suggests that more time would need to be discarded.

Considering Figure 3.15 it can be quickly deduced that cable tension increases with

negative surge, when the platform moves North. This is to be expected as the cable trajectory illustrated in Figure 3.13 would result in the cable being pulled in this direction, however when the platform surges South (positive surge) this moves the platform more inline with the cable's trajectory, and as such the tension does not increase as much. The greatest cable tensions are observed when the current comes from 345°. The smallest tensions are observed when the current is from 165°. In fact when there is no applied current there are greater recorded cable tensions than the 165° case, this suggests the current counteracts the actions of the wind and waves somewhat, to reduce their positive surge, however not enough to have a great enough impact that results in more movement North. In short it stabilises the platforms displacements somewhat, and the tensions in the cable are reduced.

When considering the sway, the gradients of the plot are more flat, showing not a huge difference in positive or negative sway. However looking at Figure 3.13 it would be expected that a Westerly movement of the platform (negative sway) would result in greater tensions in the cable due to its trajectory towards the South East. Furthermore the magnitudes of the sway in either direction is less that 30cm, so not much impact on the tension would be reasonable. In short the platform is most surging in the direction of the waves and wind.

Looking at Table 3.5 it can be consistently seen that the greatest maximum and mean effective tension on the cable is found when the current is applied from 345° for all Load Cases. Furthermore the greatest range in tension is found when the current is applied from 345°. The overall greatest mean tension is found when Load Case 4 is applied, when the current and wind are acting towards the North. This matches earlier explanations that surging to the North would increase cable tension the most. It can be seen from Table 3.5 that having a current from 345° increases cable tension, whereas a current from 165° decreases the cable tension when compared to a case with no applied current. The impact of this is not enormous, for all Load Cases a current from 345° increases mean cable tension by 1% when compared to the no current case. The ranges

however in cable tension when a current is applied from 345° is much larger than that with no current, for instance in Load Case 3 it is doubled. This is of interest as the tension ranges are a concern when considering fatigue.

This small percentage difference is in agreement with DNVGL-ST-0019, that current may not be deemed necessary. However the large differences in range are of concern and as such for the most conservative result a constant maximum current is assumed from the 345° direction. Table 3.4 is updated accordingly with this information and presented in Table 3.6.

3.3.2 Installation configuration

As evidenced in Section 3.3.1, the installation configuration of the floating wind platform and the dynamic cable plays a fundamental role in the tensions, and therefore the stresses, which the dynamic cable experiences. This is shown when the platform moves over the cable trajectory, it decreases the tensions at the cable hang off point. The impact of this configuration, and a subsequent optimisation, however is not the focus of this work, and therefore the configuration laid out in Figure 3.13 is the final chosen configuration for the duration of this work.

Table 3.6: Final global model environmental load case inputs

Load Case	Significant wave height	Wave period	Wave direction	Mean wind Velocity	Wind/wave direction misalignment	Current velocity	Current direction
1	Table 3.2 (0.25 - 4.75m)	See Figure 3.3 (0.25 - 9.75s)	15°	Table 3.2 (2.2 - 20.1 ms^{-1})	0	0.3ms^{-1}	345°
2					+90°		345°
3					- 90°		345°
4					180°		345°

3.4 The dynamic cable

The dynamic cable modelled in this work is based on a cable manufactured by JDR Cable System [105], from a historical oil and gas application. Figure 3.16 shows a schematic of the cable. Table 3.7 gives some of the cables mechanical parameters used in the model.

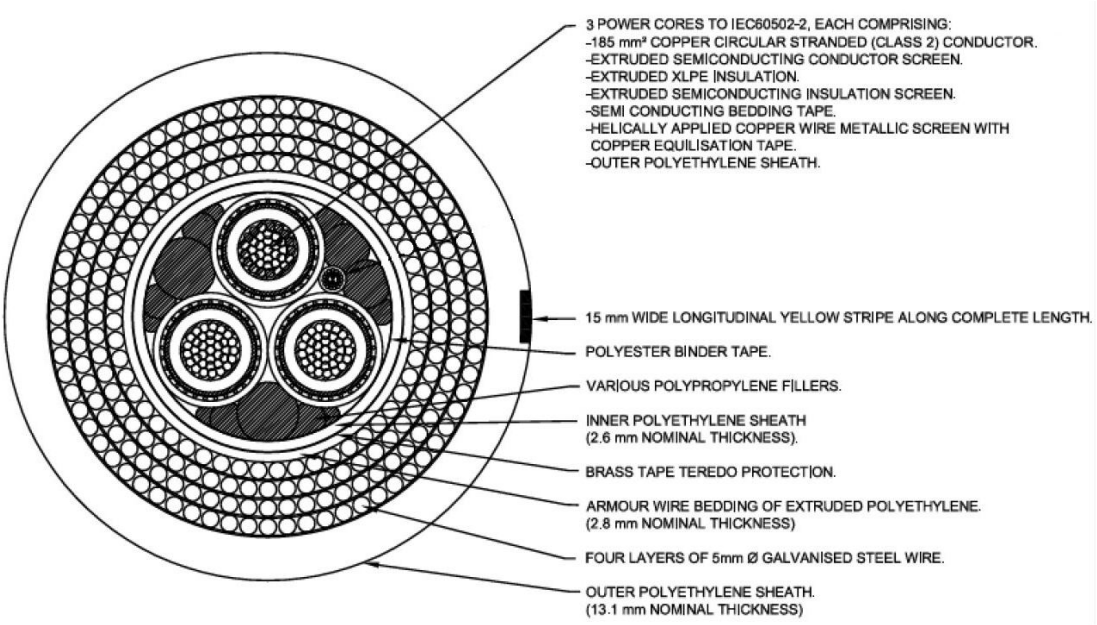

Figure 3.16: Schematic overview of the dynamic cable [105]

Table 3.7: Mechanical parameters of the dynamic cable

Mechanical property	
Outer diameter	164mm
Outer sheath material	Extruded polyethylene
Cable armouring	Galvanised steel wire
Minimum bend radius	2000mm
Safe working load	250kN
Diameter to weight ratio	4.27m/Te

In an effort to save offshore cabling costs, there has been a move in the offshore wind industry towards having 66kV inter array cables and away from the traditional 33kV cables. This is to allow for a greater power to be carried in a single cable string,

therefore allowing more and larger rated turbines to be attached to the same string, thus reducing the length of cabling offshore. This reduction of the number of cables offshore has a cost benefit, however it is important to note that in the first instance a 66kV cable is larger than a 33kV cable and would therefore cost more initially. Table 3.8 lists the offshore wind projects employing 66kV cables as of November 2018.

As stated previously, the cable presented in Figure 3.16 is from a lower voltage oil and gas project. It was desired that this work would model the stresses for a 66kV cable to align with the industry direction. OREC benefits from having access to technical specifications of 66kV power cores from previous testing within the high voltage laboratory. This information gives details of the XLPE insulation thickness required for a 150mm^2 core cross sectional area. This information is commercially sensitive so cannot be presented in its entirety. It is noted here due to the final cable modelled being an adjusted version of the schematic presented in Figure 3.16 to allow for this insulation thickness and core cross sectional area variation. In terms of design layout the cable has remained unchanged i.e having the same number of armouring layers and cores. It should be noted that while this cable was designed for oil and gas and may not prove cost effective for floating offshore wind, it serves as an available example that could be adjusted for this work.

Finally [106] states that the allowable current rating for a 150mm^2 three cored submarine cable with steel wire armour and XLPE insulation is 375A.

Table 3.8: List of current 66kV projects [107]

Project	Location
Blyth Offshore Demonstrator Wind Farm Project	U.K
East Anglia ONE	U.K
Nissum Bredning Vind	Denmark
Aberdeen Bay Offshore Wind Farm	U.K
Windfloat Atlantic Portugal	Portugal
Moray East	U.K
Borssele 1 & 2	Netherlands

3.4.1 Cable stiffness

A key parameter that determines the dynamics of a cable is how stiff it is. Normally the manufacturer would supply this information, however due to the commercial sensitivities of this work this information was not supplied. Instead axial and bending stiffness were calculated using equations 3.7 and 3.8 respectively.

$$K_a = \sum_{i=1}^{n} A_i E_i \cos\alpha_i (\cos^2\alpha_i - v\sin^2\alpha_i) + \sum_{j=1}^{m} A_j E_j \tag{3.7}$$

Where $A_i E_i$ is the axial stiffness of the helical components, α_i is the lay angle of the helical components, n is the number of helical components, $A_j E_j$ is the axial stiffness of any straight component and m is the number of straight components. The radius reduction ratio is the relationship between the radius reduction and the axial elongation

of the helical tendon, represented by v. The bending stiffness K_b is defined by:

$$K_b = I \sum_{i=1}^{N} \lambda_i E_i \tag{3.8}$$

Where, denoting the cable outside diameter by d_o,

$$I = \frac{\pi}{4} \frac{\pi (d_o - d_i)^4}{64} \tag{3.9}$$

N is the number of layers of helical wires and λ_i is denoted by Equation 3.10

$$\lambda_i = \frac{I_{ni}}{I_o} \tag{3.10}$$

Where I_{ni} is the second moment of area of each layer and I_o is given by Equation 3.11

$$I_o = \sum_{i=1}^{N} I_n i \tag{3.11}$$

The E_i is the Young's modulus for each individual layer i for no slip, defined by:

$$\frac{E_i^{\text{no-slip}}}{E_i^{\text{full-slip}}} = 3.998 - 7.916K_1 + 7.238K_1^2 - 2.321K_1^3 \tag{3.12}$$

Where $K_1 = \frac{E_i^{\text{full slip}}}{E_{\text{steel}}}$ and lies between $0.35 \leqslant K_1 \leqslant 1.0$, E_{steel} is 210 GPa and $E_i^{full-slip}$ is defined by:

$$\frac{E_i^{\text{full sip}}}{E_{\text{steel}}} = -0.26442 - 2.004046H_i + 6.5735H_i^2 - 3.3058H_i^3 \tag{3.13}$$

Where H_i is the Hruska's parameter, lies between $0.70 \leqslant H_i \leqslant 1.0$ and is defined by:

$$H_i = \cos^4 \alpha_i \tag{3.14}$$

Where α_i is the lay angle of the helical wires in the armouring layers, which for this work is taken as 18°.

3.4.1.1 Cable stiffness assumptions

A number of assumptions were made to perform the analysis of the dynamic cables. The cable stiffness was assumed to be a characteristic of the cable armouring layers. Similar to [12] the armouring layers were simplified to thin walled tubes. This was based on the assumption that the cable armouring layers remain in stick state and that the individual armour wires do not slide over one another during normal operation. This assumption of the cable armouring wires remaining in stick state results in a larger bending stiffness calculated than what would be experienced in practise. This larger estimate is accepted, as the larger stiffness would reduce the dynamics of the cable, but would also result in a higher stress calculated across the cable cross section, allowing for a more conservative estimate of damage than the cross section would experience. Further to this, the magnitude of the bending stiffness calculated using Equations 3.8 to 3.11 coincide with those calculated in [13]. Martindale (2017) [108] deduced experimentally the stiffness of a single armour layer dynamic cable, shown in Figure 3.17. Using Figure 3.17 for a 185mm^2 cable in stick state, the EI value can be estimated as 50kNm^2. This is considerably smaller than that calculated using Equation 3.8 [13], however this could be [108] testing results being for a cable with less than four armouring layers, such as in this case. It is for these reasons that the larger value calculated is chosen. The bending stiffness and other parameters of the cable are presented in Table 3.9.

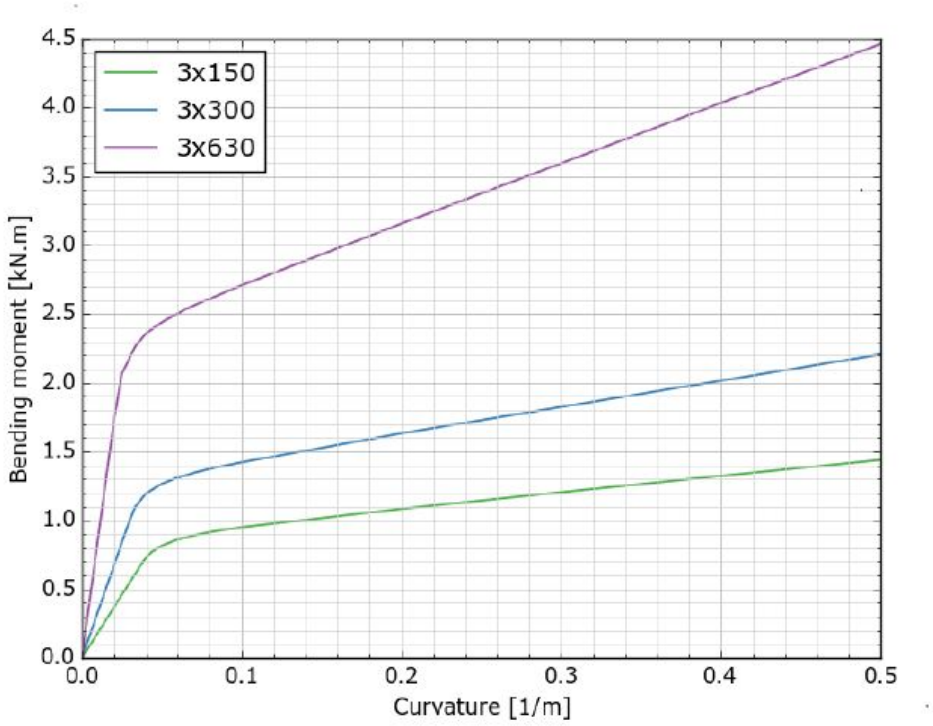

Figure 3.17: Example array cable moment-curvature relations for 3x150mm^2, 3x300mm^2 and 3x630mm^2 cables [108].

3.4.2 Cable length

A sea depth of 200m was chosen for the analysis. This depth was chosen because as the dynamic cable being modelled is from oil and gas applications, it would have been more likely to be installed in depths of this magnitude. Using the recommendation laid out in [109] to install a "lazy s" configuration gives a cable length of 280m using Equation 3.15

$$L_o = \sqrt[z]{1 + 2\frac{H}{wZ}} \tag{3.15}$$

Where Z is the maximum water depth, w is the submerged weight of 1m length of cable and H is the maximum expected bottom tension, taken in this case to be 15kN.

3.5 Global model

To understand the mechanical stresses that a dynamic cable would experience, the entire floating wind turbine system has been analysed. The dynamics of the cable and therefore the stresses it experiences are dominated by the movements of the platform, and the marine environment it is installed in. The motions of the floating platform itself are in reaction to the marine environment and the actions of the turbine. This work coupled the actions of the wind on the turbine, with the action of the waves and currents on the platform, platform tendons and the dynamic cable.

Inputs into this global model are the environmental loadings and the properties of the cable to be modelled, as explored earlier in this chapter. Table 3.6 details the environmental load case inputs to the global model. Table 3.9 gives details on the modelled cable.

Table 3.9: Characterisation data for modelled dynamic cable

	Unit	Four armoured cable	Buoyancy section
Length	m	100 (section 1) 100(section 3)	80
Outside diameter	mm	164	164
Bending stiffness	kNm^2	500	500
Axial stiffness	MN	150	150
Torsional stiffness	kNm^2	600	600
Minimum bend radius	m	2	2
Allowable tension	kN	250	250
Mass per unit length	kg/m	36	10

3.5.1 Fully dynamic simulation

To estimate the force loadings on the dynamic cable in response to the wind and marine environment's actions on the motions of the floating platform, the software OrcaFlex was

used. An introduction to OrcaFlex and the lumped mass model it utilises is provided in the literature review. For this work the cable was split into 0.5m length elements.

OrcaFlex was coupled with FAST via FASTLink, where FAST computes the actions of the wind on the turbine, and OrcaFlex calculates the marine loadings on the dynamic cable. The waves applied within OrcaFlex were linear Airy waves in a JONSWAP spectrum. The current conditions from Table 3.6 are applied from the stated direction for that loadcase in a shear profile according to the power law, Equation 3.1, with an exponent of 9.

The wind directions and velocities are input into FAST. The directions applied are as stated in Table 3.6. The wind velocities are applied using Equation 3.2 with a shear profile according to the seventh power law. Turbidity in the wind is accounted for in FAST using the turbulent wind profiles for each applied wind velocity generated by TurbSim according to Section 3.2.3.1. More details on FASTLink can be found within the literature review.

This work incorporated the MIT/NREL 5MW reference turbine installed on a tension leg platform. Figure 3.18 shows a wire frame illustration of the floating platform installation with the dynamic cable attached and installed in a "lazy-s" configuration, modelled in OrcaFlex. If desired more details regarding the NREL tension leg platform can be found in the literature review.

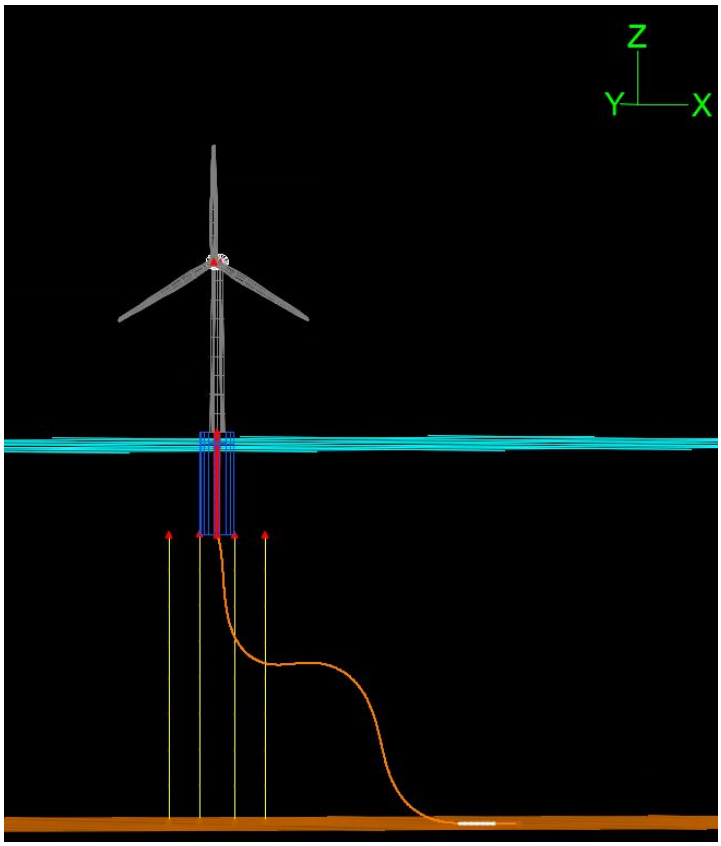

Figure 3.18: Global model of the tension leg platform and the NREL 5MW turbine, with the 66kV cable installed in a "Lazy s" configuration.

3.5.2 Morison's equation

Within OrcaFlex the hydrodynamic loadings on the cable and the floating platform, with its associated mooring tendons, are calculated using an extended version of the Morison's equation. Details of the extened Morsion's equation that OrcaFlex utilises can be found in the literature review, however for ease of reference the equation is reproduced here:

$$\boldsymbol{F_f} = (M\boldsymbol{a_f} + C_a M\boldsymbol{a_r}) + \frac{1}{2}\rho C_d A_d \boldsymbol{v_r}|\boldsymbol{v_r}| \tag{3.16}$$

Choosing suitable drag, C_d, and inertia coefficients, C_a and C_m, is crucial when calculating wave loadings using Morison's equation. The drag and inertia coefficients are dependent on time, Reynolds number, Re, relative motion of the fluid, history of the

motion, relative roughness of the cable, cable shape etc. C_a and C_d can be determined by experimentally averaged values. However they can be approximated and plotted as functions of Re, K, and β where K is the Keulegan-Carpenter number and β is the Stokes parameter. The Reynolds number within OrcaFlex has been set to be calculated accounting for the flow direction and the angle of the flow relative to the cable segment.

$$Re = \frac{|v_r|d}{\Upsilon \cos \alpha_f} \tag{3.17}$$

Where Re is the Reynolds number, d is the cable diameter, v_r is the relative fluid velocity, α_f is the angle between the relative flow direction and the normal of the cable line and Υ is the fluid kinematic viscosity. OrcaFlex notes that when the relative flow approaches to being axial to the cable line, the Re value becomes arbitrarily large.

$$K = \frac{U_f T_{flow}}{d} \tag{3.18}$$

Where K is the Keulegan-Carpenter number, U_f is the fluid velocity and T_{flow} is the period of the flow.

$$\beta = \frac{Re}{K} \tag{3.19}$$

Where β is the Stokes parameter. Figure 3.19 shows how Re, K and β relate to the C_d.

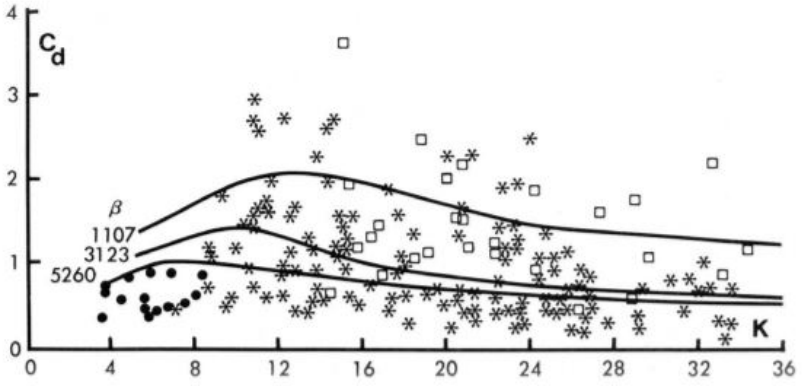

Figure 3.19: Drag coefficients from field data and plotted in [110]

From OrcaFlex the Re along the length of the cable can be extracted. Choosing a point in the water column as an example, 150m water depth, the average Reynolds number over the whole simulation on the node of the cable at this depth is 37943. Using the equation for the Keulegan-Carpenter number, Equation 3.18, the K value is calculated as approximately 12. Figure 3.20 shows the flow velocities at 150m depth to allow for this calculation. Using Equation 3.19 the Stokes parameter value is calculated as 3162. Finally using Figure 3.19 the C_d is found to be approximately 1.2.

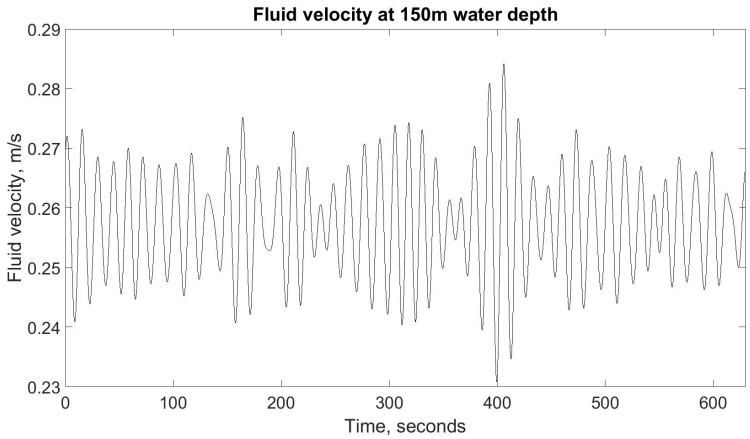

Figure 3.20: Fluid velocity at 150m water depth, Load case 1 H_s 4.75, T_z 7.75s

A further approximation stated in [110] by Sarpkaya is that the inertia coefficients used for Morison's equation can be written as:

$$C_m = (1 + C_a) \tag{3.20}$$

Where C_m is the inertia coefficient and C_a is the added mass coefficient. This is the same approximation that is set within OrcaFlex for this work. In [110] a table of added mass coefficients for finite cylinders is given, Table 3.10. Using the data presented in this table, the cable radius given in Table 3.9, and a cable segment of 0.5m in OrcaFlex, gives a value for $l/(2c)$ of 3. This gives a C_a value of 1 according to strip theory. Using Equation 3.20 this give a C_m value of 2.

Table 3.10: Added mass coefficients for finite cylinders [110]

Cylinder(length = l, radius = c)		
Added mass C_a / $(\pi\rho l c^2)$		
$l/(2c)$	Strip theory	Experiment
1.2	1	0.62
2.5	1	0.78
5.0	1	0.90
9.0	1	0.96

Giving further credence to these coefficient assumptions is the data collected by Zhang et al. in [111]. Here, recommended values of C_m when using linear wave theory is also given as 2, shown in Table 3.11. Recommended values for C_d when using Airy waves range between 1-1.4. Therefore similar to [111] a mid point value of 1.2 is accepted for the C_d coefficient as previously calculated.

Table 3.11: Recommended values of C_d and C_m [111]

Wave theory	C_d	C_m	Note	Reference
Airy linear wave	1.0-1.4	2	Recommended design values based on statistical analysis of published data	[112]
Stoke 3^{rd} Order	1.34	1.6	Mean values for oscillatory flow for 2-3 in cylinders.	[113]
Stokes 5^{th} Order	0.8-1.0	2	Recommended design values based on statistical analysis of published data	[112]

3.5.2.1 Flow/Cable line angle considerations

Whenever the α_f angle approaches 90° the Re becomes arbitrarily large according to Equation 3.17. Figure 3.21 shows how the Reynolds number changes along the length

of the cable. Here it can be seen that in the Lazy S configuration, when the cable is more axially in line with the flow, there is an increase in Reynolds number as expected.

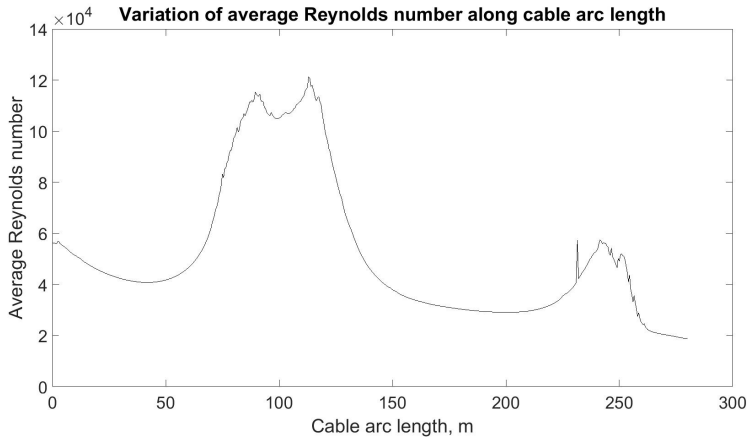

Figure 3.21: Variation of average Reynolds number along the cable arc length, Load case 1 H_s 4.75, T_z 7.75s

At 113m, where the average flow velocity is 0.28 ms^{-1}, the peak average Re is observed as approximately 12 x10^4. Using Equations 3.18 and 3.19 and Figure 3.19 the C_d is estimated as 0.6. This estimation matches work conducted by [114] on the drag coefficients of inclined cylinders. Here C_d was found to vary from 0.6 to 1.2 for Reynolds numbers in the order of magnitude x10^4 when the angle of inclination varied between 0 to 90°. Within OrcaFlex the C_d can be set to vary with Reynolds number to account for this change in the cable angle.

To generate lift, a turn of the flow is required. A rotating cylinder would generate lift by inducing vortex-like flow around itself. For this work the cable has been assumed to not be rotating, and vortices are not considered. It should also be noted that as vortices are not considered here, vortex induced vibration is therefore also out of the scope of this work. Table 3.12 shows the final Morisons's coefficients chosen for this work.

Table 3.12: Chosen Morison's equation coefficients for the global model simulations

Morison's Coefficient	Value
C_d	0.6-1.2
C_m	2
C_a	1
C_l	0

3.5.3 Global model force response

For a dynamic cable the structural response is considered in terms of the axial forces and bend moments. From OrcaFlex the forces and moments in the six degrees of freedom are extracted. A node at a desired location along the length of the cable is chosen. Here, as the lines are modelled as a lumped mass model, the F_x, F_y, F_z, M_x, M_y and M_z can be extracted at a chosen node. Figure 3.22 shows the forces and moments that the cable experiences across its length, during a ten minute simulation of Load Case 1 with a significant wave height of 4.75 metres and a period of 7.75 seconds.

From Figure 3.22 points of interest along the length of the cable are chosen. From the nodes at these locations on the dynamic cable line, the time histories of the F_x, F_y, F_z, M_x, M_y and M_z can be extracted across the 600 second simulation. This time history of forces and bend moments is what is then used as inputs to the local model.

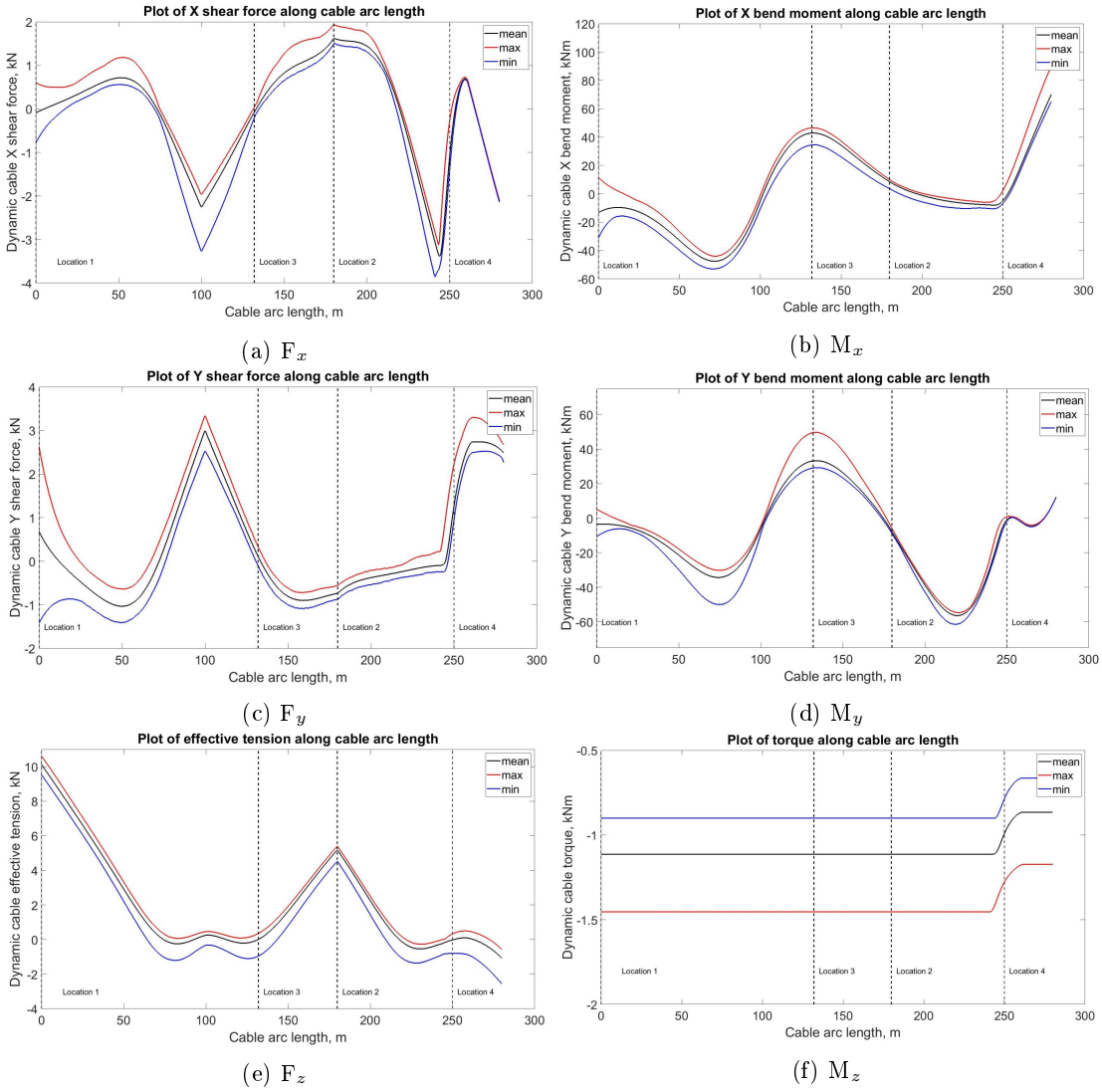

Figure 3.22: Force and moment results for Load Case 1, H_s 4.75m, T_z 7.75s

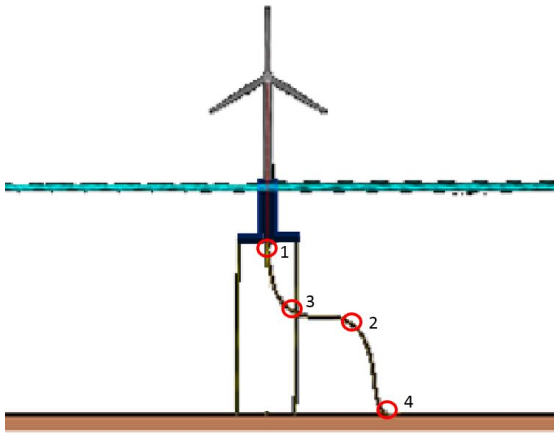

Figure 3.23: Locations identified on dynamic cable

In Figure 3.22 the simulated mean, minimum and maximum of each of F_x, F_y, F_z, M_x, M_y and M_z are plotted along the length of the dynamic cable. Looking at Figure 3.22 (e), it can be seen that the greatest tension, or F_z, in the cable is observed at the hang off point from the floating platform, i.e at a cable arc length of 0m. This point is chosen as Location 1 for further analysis, denoted by the dashed line in all Figures at cable arc length 0 and labelled as such. Continuing with (e), it can be seen that a secondary peak in cable tension is observed at 180m; this is due to the lazy s configuration the cable is installed in, which induces a second hang off point along the cable at the end of the buoyant section. This is chosen as Location 2. These peaks in tension on the cable arc length match work previously completed by [115]. Moving to Figure 3.22 (b) and (d) it can be seen that the bending moments in the M_x, M_y peak at 132m. This is chosen as Location 3 as bending of the cable is thought of as a particular concern. At 250m is where the cable touches down at the seabed, this is chosen as Location 4. These four chosen locations and their lengths along the cable are listed in Table 3.13. Figure 3.23 provides context on where these locations are on the cable's length.

Table 3.13: Marked locations on Figure 3.22 and length they are on the dynamic cable

Location	Length along cable, m
1	0
2	180
3	132
4	250

At the locations listed in Table 3.22 the time history of the F_x, F_y, F_z, M_x, M_y and M_z the cable experiences can be extracted. The minimum, mean and maximum of each of the force/moments is listed in Tables 3.14 to 3.5.3 for each of the environmental Load cases.

Table 3.14: Table of results for Load Case 1

Load Case 1												
Force/Moment (kN/kNm)	Location 1			Location 2			Location 3			Location 4		
	Max	Mean	Min	Max	Mean	Min	Max	Mean	Min	Max	Mean	Min
F_x	8.814	0.952	0.000	1.843	1.624	1.494	0.163	0.053	0.000	1.277	0.928	0.394
F_y	2.695	0.565	0.000	0.872	0.734	0.586	0.346	0.099	0.000	2.156	1.390	1.013
F_z	10.87	9.666	4.866	5.389	5.119	4.536	0.962	0.108	0.000	0.813	0.092	0.000
M_x	31.11	11.71	0.000	9.973	8.491	4.491	46.75	43.21	38.93	7.101	5.241	0.001
M_y	127.0	15.76	0.000	9.462	8.294	6.392	48.79	33.25	28.30	1.613	0.514	0.000
M_z	2.112	1.102	0.500	1.351	1.126	0.901	1.351	1.126	0.901	1.191	0.991	0.781

Table 3.15: Table of results for Load Case 2

Load Case 2												
Force/Moment (kN/kNm)	Location 1			Location 2			Location 3			Location 4		
	Max	Mean	Min	Max	Mean	Min	Max	Mean	Min	Max	Mean	Min
F_x	0.7313	0.111	0.000	1.840	1.635	1.480	0.156	0.055	0.000	1.267	0.932	0.542
F_y	2.964	0.5818	0.000	0.903	0.723	0.550	0.336	0.096	0.000	2.036	1.409	0.986
F_z	11.87	10.15	8.492	5.436	5.129	4.600	0.871	0.099	0.000	0.758	0.079	0.000
M_x	33.07	12.03	0.000	10.13	8.197	4.428	46.94	42.23	37.42	7.279	4.683	0.000
M_y	9.753	3.756	0.000	9.279	8.040	6.189	45.00	34.02	28.96	1.596	0.534	0.000
M_z	1.356	1.137	0.898	1.356	1.137	0.898	1.356	1.137	0.899	1.197	1.002	0.789

Table 3.16: Table of results for Load Case 3

Load Case 3												
Force/Moment (kN/kNm)	Location 1			Location 2			Location 3			Location 4		
	Max	Mean	Min	Max	Mean	Min	Max	Mean	Min	Max	Mean	Min
F_x	1.006	0.117	0.000	1.782	1.637	1.530	0.139	0.055	0.000	1.364	0.946	0.623
F_y	2.706	0.594	0.000	0.855	0.723	0.587	0.330	0.093	0.000	1.860	1.414	1.008
F_z	11.20	10.17	9.197	5.468	5.151	4.820	0.5182	0.114	0.000	0.498	0.079	0.000
M_x	32.56	12.27	0.000	9.056	7.832	3.857	44.58	41.49	37.71	4.836	3.837	0.000
M_y	12.62	3.949	0.000	8.789	7.842	5.887	43.69	34.17	30.32	2.016	0.611	0.000
M_z	1.486	1.197	1.079	1.486	1.197	1.079	1.486	1.197	1.079	1.351	1.064	0.965

Table 3.17: Table of results for Load Case 4

Load Case 4												
Force/Moment (kN/kNm)	Location 1			Location 2			Location 3			Location 4		
	Max	Mean	Min	Max	Mean	Min	Max	Mean	Min	Max	Mean	Min
F_x	0.901	0.424	0.000	2.067	1.944	1.549	0.125	0.039	0.000	1.207	0.041	0.000
F_y	5.118	1.016	0.000	0.835	0.562	0.386	0.419	0.111	0.000	1.874	1.417	1.146
F_z	11.00	10.10	9.011	5.351	4.539	4.328	0.889	0.634	0.000	1.350	1.163	0.000
M_x	47.93	10.64	0.000	8.832	0.447	0.000	43.99	24.08	16.38	16.64	12.74	0.000
M_y	7.594	2.965	0.000	10.13	8.711	5.930	53.56	50.24	31.11	1.462	0.449	0.000
M_z	1.746	1.491	1.129	1.746	1.491	1.129	1.746	1.491	1.129	1.622	1.392	1.002

3.5.3.1 Load case selection

This section aims to review each of the applied load cases to select the one that produces the greatest force and bend moment outputs for further analysis within the further chapters.

When looking at Tables 3.14 to 3.5.3 the initial impression is that they are relatively similar to one another for the differing environmental load cases applied. However when the average force and moment responses are examined it becomes immediately clear that two load cases consistently produce the greatest forces and moments on the dynamic cable; Load Case 1 and Load Case 3.

These two load cases are the two that would move the platform furtherest from the dynamic cable's trajectory, Figure 3.13. In fact when Load Case 1 does not have the greater average force or moment result at any location on the cable's length, then Load Case 3 will produce the greatest average result and vice-versa, bar six results. Figure 3.18 shows a tiled plot for quick assimilation of which load case produces the greatest force or moment at a particular location on the cable's length.

Table 3.18: Colour tiled table showing which Load Case produces the greatest average force or moment at the corresponding location on the cable's length

Force/	Location			
moment	1	2	3	4
F_x	**LC1**	**LC4**	**LC2**	**LC3**
F_y	**LC3**	**LC1**	**LC1**	**LC3**
F_z	**LC3**	**LC3**	**LC3**	**LC1**
M_x	**LC3**	**LC1**	**LC1**	**LC1**
M_y	**LC1**	**LC1**	**LC3**	**LC3**
M_z	**LC4**	**LC4**	**LC4**	**LC4**

From Table 3.12 Load Cases 1 and 3's dominance can be quickly deduced. However it should be noted from Figures 3.14 to 3.5.3 the difference between them (and indeed all of the load cases) is minimal and either load case could be chosen. There is however one exception to this. The largest M_y value is found when Load Case 1 is applied at Location 1. The maximum value here is 127 kNm, with an average of 15.76 kNm. This maximum value and average value are considerably larger than the M_y values calculated for any of the other load cases at Location 1. For comparison, Load case 3 produces a maximum value of 12.62 kNm and an average of 3.949 kNm.

For the above reasoning, Load Case 1 has been chosen as the applied environmental load condition for further analysis. Load Case 1 is where the wave and wind are aligned with one another, and are also most aligned with the current direction, a misalignment of 30° respectively. Moving forward, the force/moment response of the cable generated from Load Case 1 will be used as the inputs to the local model of the dynamic cable's cross section. Table 3.19 gives a further breakdown of the Load Case 1, where the mean force/moment response at each location is shown for each of the wave height conditions within Load Case 1.

Table 3.19: Detailed mean force/moment response of the cable at differing locations for each significant wave height of Load Case 1

Load Case 1																								
Significant wave height	Location 1						Location 2						Location 3						Location 4					
H_z (m)	F_x	F_y	F_z	M_x	M_y	M_z	F_x	F_y	F_z	M_x	M_y	M_z	F_x	F_y	F_z	M_x	M_y	M_z	F_x	F_y	F_z	M_x	M_y	M_z
0.25	0.1015	0.5217	10.16	11.34	3.630	1.174	1.637	0.730	5.109	8.112	8.053	1.174	0.0534	0.1004	0.0767	42.34	34.11	1.174	0.908	1.453	0.090	4.650	0.461	1.036
0.75	0.0969	0.5413	10.14	11.54	3.436	1.133	1.627	0.736	5.105	8.468	8.300	1.133	0.0524	0.1020	0.104	43.18	33.44	1.113	0.911	1.408	0.098	5.228	0.471	0.997
1.25	0.0954	0.5584	10.13	11.66	3.272	1.092	1.618	0.741	5.096	8.823	8.529	1.092	0.0515	0.1043	0.108	44.07	32.87	1.092	0.911	1.388	0.099	5.970	0.464	0.957
1.75	0.1016	0.5643	10.14	11.80	3.389	1.111	1.623	0.734	5.110	8.607	8.373	1.111	0.0527	0.1001	0.111	43.49	33.16	1.111	0.919	1.389	0.094	5.490	0.485	0.976
2.25	0.1060	0.5830	10.14	12.06	3.474	1.120	1.623	0.733	5.121	8.511	8.300	1.120	0.0534	0.0972	0.104	43.24	33.21	1.120	0.929	1.387	0.083	5.289	0.509	0.986
2.75	0.1131	0.6141	10.14	12.46	3.532	1.123	1.621	0.733	5.134	8.475	8.274	1.123	0.0537	0.0948	0.113	43.15	33.08	1.123	0.942	1.371	0.082	5.157	0.550	0.991
3.25	0.1229	0.6519	10.14	12.88	3.593	1.123	1.618	0.732	5.146	8.470	8.264	1.123	0.0537	0.0932	0.124	43.13	32.93	1.123	0.958	1.351	0.084	5.072	0.596	0.992
3.75	0.1341	0.6849	10.14	13.25	3.679	1.119	1.615	0.732	5.157	8.479	8.261	1.119	0.0536	0.0920	0.134	43.12	32.78	1.119	0.972	1.331	0.088	5.018	0.640	0.991
4.25	0.1489	0.7270	10.13	13.65	3.805	1.112	1.612	0.731	5.167	8.506	8.263	1.112	0.0534	0.0923	0.147	43.12	32.64	1.112	0.988	1.309	0.093	4.959	0.691	0.985
4.75	0.1641	0.7660	10.13	13.98	3.940	1.104	1.609	0.730	5.176	8.538	8.269	1.104	0.0533	0.0928	0.157	43.15	32.52	1.104	1.002	1.289	0.099	4.933	0.733	0.979

3.5.3.2 Load Case 1 analysis

Looking at Table 3.19, it can be seen that the greatest magnitude of forces on the cable are experienced at Location 1 at the hangoff point, and the greatest bend moments at Location 3. The average force/moment responses with differing significant wave heights are plotted in Figures 3.24 and 3.25 for Locations 1 and 3 respectively. From Figure 3.24 it can be seen at the hang off point that there is a general increase in F_x, F_y, M_x and M_y with increasing significant wave height. The tension in the cable at the hang off point, F_z, remains fairly constant, suggesting that the main contributor to the tension at Location 1 in the cable is its own weight. The M_z torque varies by generally decreasing with increasing significant wave height, however a sharp decrease is observed at a significant wave height of 1.25, coinciding with a sharp decrease in F_y at this wave height.

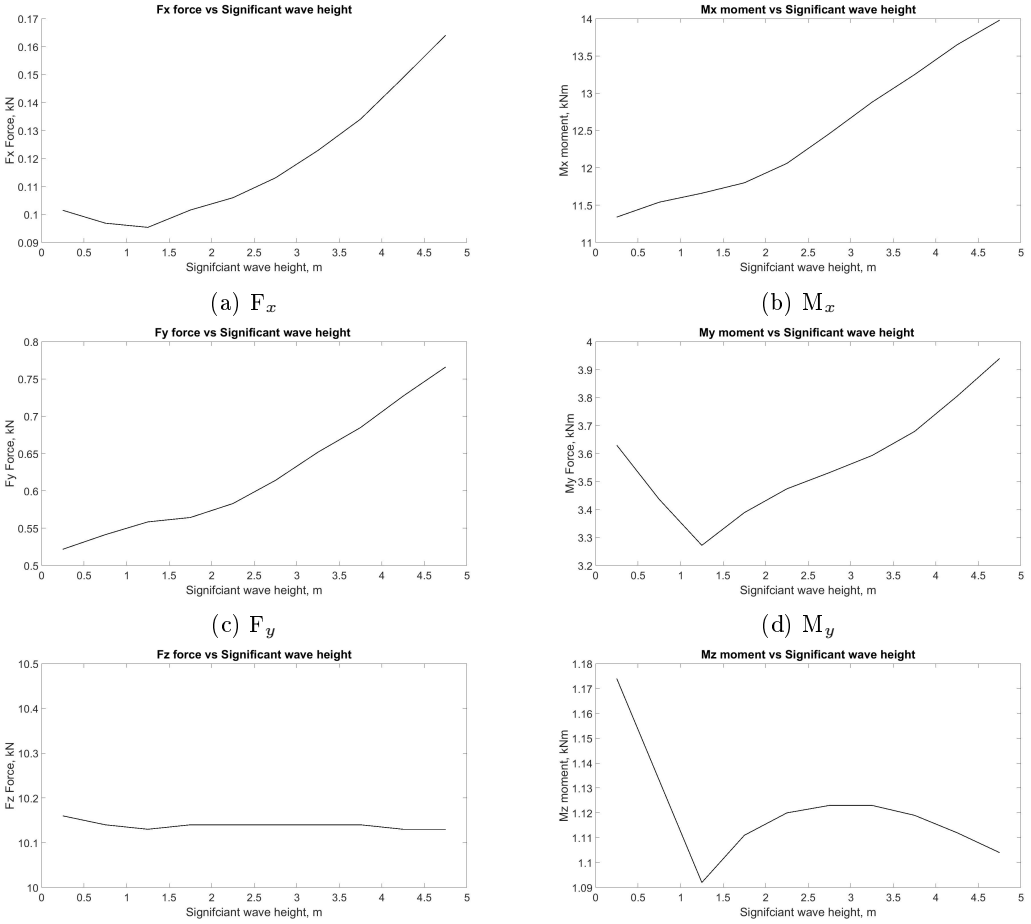

(a) F_x (b) M_x

(c) F_y (d) M_y

(e) F_z (f) M_z

Figure 3.24: Force/moment results for Load Case 1 with varying H_s, at Location 1 (hang off).

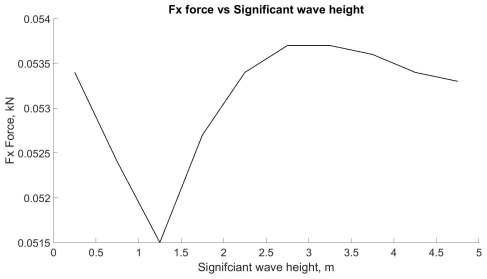

(a) F_x

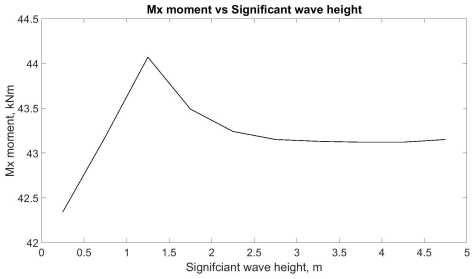

(b) M_x

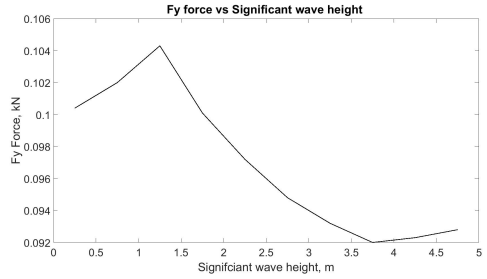

(c) F_y

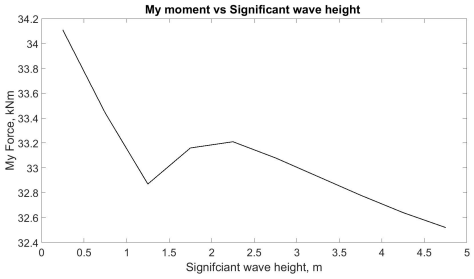

(d) M_y

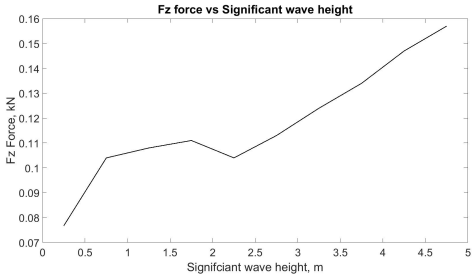

(e) F_z

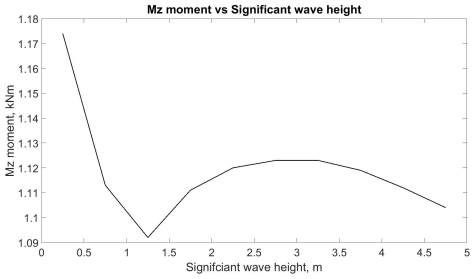

(f) M_z

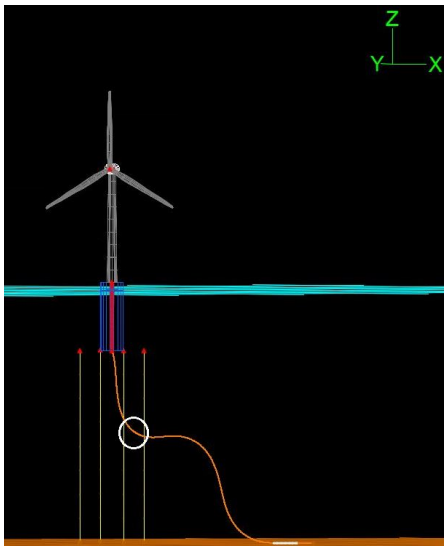

(g) Location 3 circled

Figure 3.25: Force/moment results for Load Case 1 with varying H_s, at Location 3, identified in (g).

From Figure 3.25 it is immediately deduced that the magnitude of the forces are

smaller than those at Location 1, whereas the bend moments are much larger. Again, peak values are observed at a significant wave height of 1.25m. Interestingly, at significant wave heights of 1.25m the surge of the floating platform peaks, resulting in larger forces and moments at this wave height on the cable at Location 3. Within this global model the wave heights were prescribed to wind velocities according to Figure 3.9 and shown in Table 3.2. The rated wind speed of the 5MW wind turbine in the global model is 10m/s and a wave height of 1.25m corresponds to a wind speed of 10.1m/s at the hub height, i.e rated wind speed.

The axial force on a wind turbine is dependent on the axial induction factor of the blade section. As this wind turbine is a pitch regulated turbine, the turbine changes the pitching of the blades to regulate power output. From cut in wind speed to rated wind speed the thrust force increases, however after rated wind speed the blades pitch to shed power to avoid overloading. Therefore after rated wind speed, the thrust force on the turbine decreases. This maximum thrust force observed at rated wind speed, and consequent wave height of 1.25 metres, causes the floating platform to surge to its maximum. It is this increase in platform surge which causes the peaks in the corresponding forces and moments the dynamic cable is subjected to. For instance a greater surge of the platform causes greater bending at Location 3. These peaks are not as readily observed at Location 1, as the forces here are dominated by the tension in the cable, which is a product of the cables weight at the hangoff point. Figure 3.26 compares the surge for a wave height of 1.25m to the maximum recorded wave height of 4.75m, at the same wave period of 7.75s and confirms this maximum surge at 1.25m significant wave height.

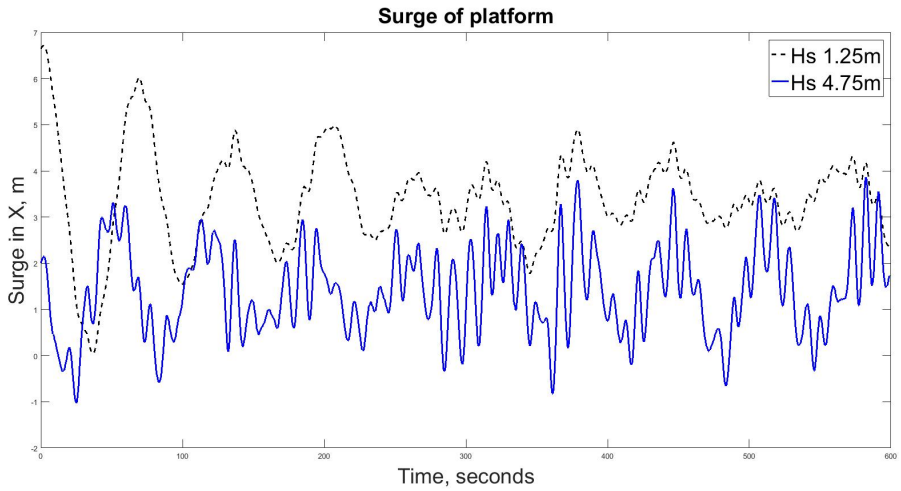

Figure 3.26: Platform surge at 1.25m wave height compared to 4.75m wave height with T_z of 7.75s

The output force and bend moment time histories of the dynamic cable's responses at the four locations along its length are now used as inputs to the Local model to allow for generation of stress time histories across the dynamic cable's insulation cross section.

3.6 Chapter summary

Within this chapter a global model of a floating offshore wind turbine and platform with its attached dynamic cable was constructed. The floating platform was that of a tension leg platform with the NREL 5W reference turbine installed on top. The dynamic cable was based upon a dynamic cable from a historic oil and gas installation. Four environmental Load Cases were developed based upon DNVGL-ST-0019 and applied to the global model. The force and bend moment outputs from the global model at four points along the dynamic cable's length were extracted. The four points being; the hang off point at the base of the turbine platform, the beginning of the Lazy-S bend configuration, the end of the Lazy-S bend configuration and the cable touch down point on the seabed. These force and moment outputs at each location on the cable were compared in Section 3.5.3 to determine which environmental load case generates the greatest forces and moments on the dynamic cable which will be considered for further

analysis. Load Case 1 was determined to generate the greatest force and bend moments; Load Case 1 being when the wind and waves are aligned from the same direction, 15°, and the current comes from 345°.

A peak in force and bend moment output was observed at a significant wave height of 1.25m. This is explained due to the wind velocity being correlated to significant wave height, and a wave height of 1.25m corresponds to the rated wind speed of the NREL 5MW reference turbine. Here the thrust force on the turbine will be greatest, causing the platform to surge to its maximum, and a corresponding peak in bend moment and force experienced by the dynamic cable.

The overall output from the global model chapter which is used moving forward, are the ten minute time histories of forces and bend moments extracted from each location on the cable's length during Load Case 1. The forces extracted are the tension and shear forces the cable experiences, F_z, F_x, and F_y, while the bend moments are M_z, M_x and M_y. These serve as inputs to the local model chapter to determine what stress the applied forces and moments induce on the cross section of the dynamic cable.

Chapter 4

Local Model

4.1 Chapter introduction

This chapter discusses the steps taken to build the local model of the cable cross section and how the stress responses of the insulation layers were derived.

The local model refers to the finite element analysis model of the cross section of the dynamic cable. The local model uses the F_x, F_y, F_z, M_x, M_y and M_z force response output from the global model at a chosen location and applies them to the FEA. Applying the six degrees of freedom allows for calculation of plane and shear stresses across individual cable components, and can be combined to produce the von Mises stress. The final output from the local model is a stress time history of a component of a dynamic cable's cross section configuration. For this work, the insulation layer is the component of interest. These stress time histories are then used as inputs for the fatigue and water tree propagation chapter.

4.2 Cross section material properties

To complete the finite element analysis of the dynamic cable's cross section, the material properties of the cross section need to be known. The materials that constitute the cross section are the insulation cross linked polyethylene, XLPE, the galvanised steel wire armouring, the copper conductor, the polyvinyl chloride, PVC, sheaths and the polyethylene sheaths. All materials within the local model were assumed isotropic. Table 4.1 gives an overview of the material properties used for this work, while Figure 4.1 illustrates the cross section layout of the dynamic cable modelled.

Table 4.1: Cable cross section material properties

Material	Density kgm^{-3}	Youngs Modulus (Pa)	Poisson's Ratio	Tensile Ultimate strength (Pa)
Copper	8600	1.17×10^{11}	0.33	200×10^{6}
Polyethylene	940	8×10^{8}	0.46	1×10^{7}
PVC	1400	3×10^{9}	0.4	1.5×10^{7}
Steel	7850	2×10^{11}	0.3	4.6×10^{8}
XLPE	924	3.5×10^{9}	0.4	1.7×10^{7}

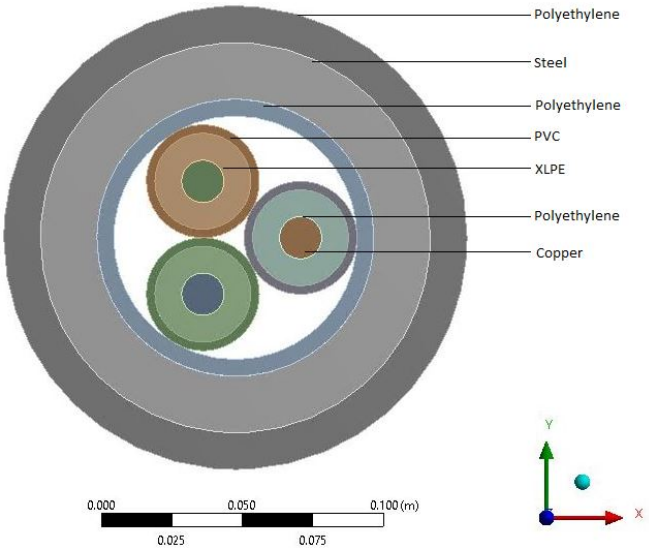

Figure 4.1: Labelled cross section of the modelled dynamic cable

4.3 Finite element analysis

A finite element analysis, FEA, of the cable cross section was constructed using ANSYS Mechanical software. This proved an effective method to determine the interactions between different components of the dynamic cable's cross section. Similar works on dynamic umbilical cables [116], [117] both used an alternative FEA software called UFlex2D. This is a custom built software for umbilical cross sections. For this work, however, ANSYS was used for its ease of coupling with OrcaFlex.

4.3.1 3D cable FEA modelling

A 0.5 metre 3D length of the dynamic cable was built within ANSYS. A length of 0.5m was chosen as this was the same length as the sections of the lumped mass model of the cable within the global model. This 3D model consists of two equal lengths of 0.25 metres glued together at their centre. The purpose of this is to allow for a flat surface of the cable cross section exactly at its midpoint. Figure 4.2 illustrates these two equi-length 3D sections of the cable glued together, shown by the two differing colours. Figure 4.3 illustrates the flat cross section that can be achieved using this technique at the exact midpoint of the 0.5m length. This was done to allow for extraction of results at the cross section at the exact mid point of the cable length. As this is a 3D model, and therefore 3D elements are used in the model, the key benefit of using the glueing technique is that it allows for a flat surface that can be further refined and modelled in a 2D sub-model. If this technique is not used then sub modelling on at flat 2D surface at the midpoint would not be achievable.

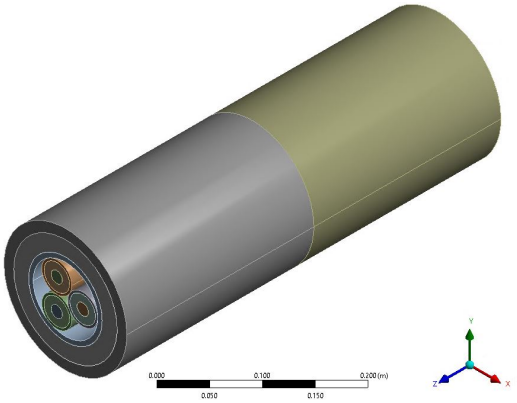

Figure 4.2: 3D model of 0.5m length of the dynamic cable

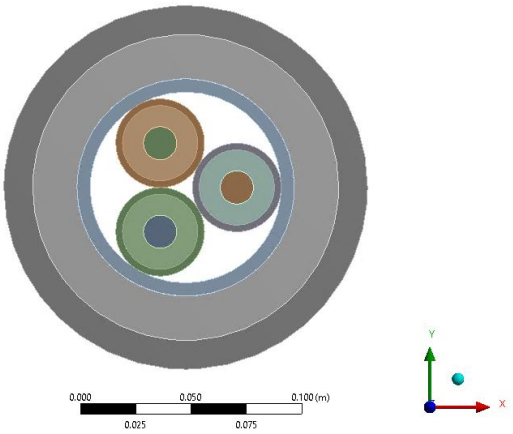

Figure 4.3: Modelled cross section of the dynamic cable

For this 3D model, the helical armouring wire layers and the helical copper cores have been simplified to thin walled tubes and a solid core respectively. This simplification is based on work completed by [12], which is based on the assumption that the armour and core helical wires remain within stick state and do not slide over one another. It should be noted that the stiffness of the cable in the global model was calculated numerically based on work by Raoff [13] and Chen [14], which does account for the helical structure of the armouring wires, where the helical lay angle was assumed to be 18°. For clarity, these stiffnesses calculated for use in the global model accounting for the armouring helical structure assumed the cable's armour wires remain in stick state. Therefore this same assumption of remaining in stick state is carried to the local model.

The force and bend moment outputs from the global model are applied and solved. A submodel of this is then created focusing on the cable's flat midsection with a much greater refinement of the mesh and with an emphasis on the cable insulation layers.

4.3.2 2D cross section sub model

A 2D sub model of the flat surface at the mid point of 0.5m cable length was constructed within ANSYS. This 2D sub model is a greater refined model with a focus on the insu-

lation layer, as this is the component of interest of the cable's cross section for this work.

Submodelling uses two separate models, the previous generated 3D model of the cable 0.5m length segment, and the 2D model of the face of the cable's cross section at its midpoint. The initial 3D model is used to transform the applied loads from the global model to local deformations, the sub model in turn then includes the local geometric details with the more refined mesh density. The sub modelling algorithm then interpolates deformations from the initial 3D model to the sub model's boundaries and solves for stress states on the sub model. As the sub model includes the geometric details from the initial 3D model, material properties including stiffness are ensured.

4.3.2.1 2D sub model mesh quality

Figure 4.4 shows the mesh refinement at the flat 2D surface cut at the midpoint of the FEA model. It can be seen that there is a great refinement in the submodel at the insulation layers of the dynamic cable. Figure 4.5 shows the quality of the elements generated in the mesh. Here it can be seen that the vast majority of the elements have a quality of 0.959, with an overall mesh element quality of 0.91395. A mesh element quality of 0.7-0.95 is considered "very good", with 0.95-1.00 being considered "excellent.

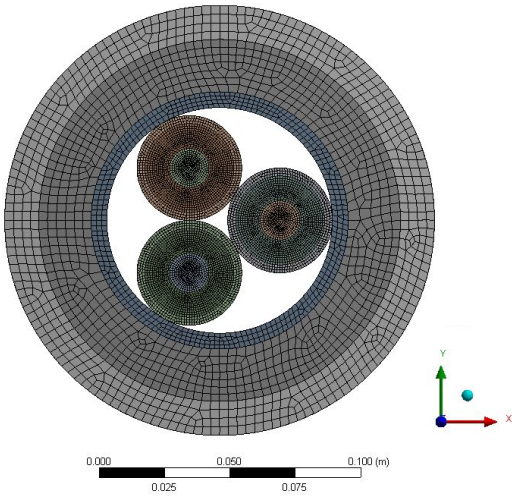

Figure 4.4: Submodel mesh refinement of cross section at cable midpoint

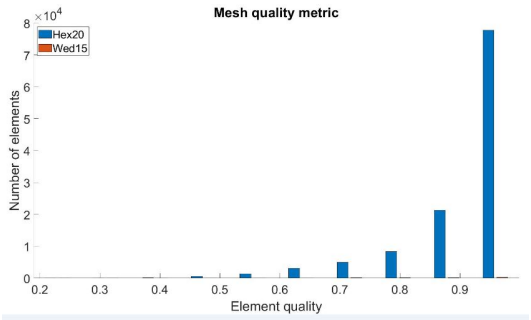

Figure 4.5: Mesh element quality metric

When Figures 4.4 and 4.5 are combined and the mesh is replotted according to quality, as shown in Figure 4.6, it can be seen that the majority of the elements of the insulation layers fall into the "excellent" category. As the insulation layers are the focus of this work, this mesh and FEA is accepted to be of an appropriate quality.

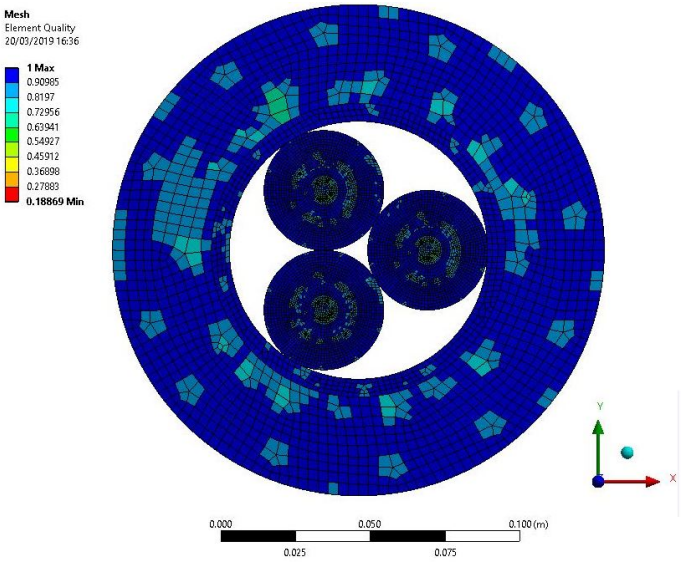

Figure 4.6: Plot of submodel mesh by element quality

4.4 Linear superposition

This section explains the work undertaken to complete a linear superposition of the forces and moments calculated in the global model onto the local mechanical FEA model. It was initially envisioned that the forces and moments calculated from the global model would be applied to the FEA of the dynamic cable in a transient dynamic analysis. This however proved excessively computationally expensive, so a linear superposition of the forces from the global model to the local FEA model was completed within Matlab.

Mechanical stresses initially modelled by the FEA created in ANSYS were superimposed to a dynamic model within Matlab. The purpose of this was to allow for calculation of the stress time histories much more quickly than completing a transient dynamic analysis within ANSYS. The local model of the cable cross section was created within ANSYS by having a 0.5m length of cable split into two equal length sections, illustrated in Figure 4.2 and described in Section 4.3.

The boundary conditions applied were that one end of the cable length was fixed in all degrees of freedom, while the other end had uniform loads applied in six degrees of freedom individually. Each degree of freedom was applied individually in a static structural analysis, and the response of the cable or the stress distributions across the cable's cross section mid point were extracted.

Table 4.2: Inputs for the static structural stress analysis

Force / Moment	Applied excitation (kN/kNm)
F_x	1
F_y	1
F_z	1
M_x	1
M_y	1
M_z	1

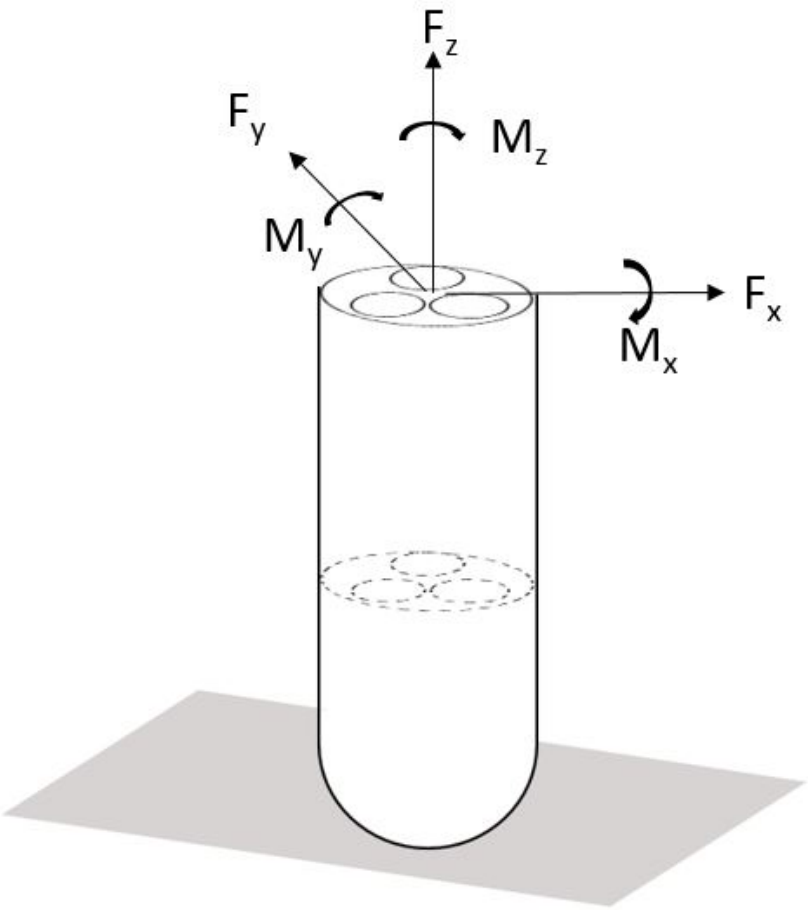

Figure 4.7: Application of Table 4.2 inputs on cable free end

For each excitation applied the shear and normal stresses were extracted across

the flat 2D cross section at the midpoint. The stress tensor for each applied force or moment was extracted for every element across the 2D cross section and the cable midpoint, according to Equation 4.1

$$\sigma = \begin{bmatrix} \sigma_{xx} & \sigma_{xy} & \sigma_{xz} \\ \sigma_{yx} & \sigma_{yy} & \sigma_{yz} \\ \sigma_{zx} & \sigma_{zy} & \sigma_{zz} \end{bmatrix} \tag{4.1}$$

Where σ_{xx}, σ_{yy} and σ_{zz} are the calculated normal stresses, and all others are shear stresses. In some instances in the literature to denote shear stresses, σ is replaced with τ as illustrated in Figure 4.8. It should be noted that the order of the subscript is arbitrary and that $\sigma_{xy} = \sigma_{yx}$ as per Equation 4.2. This results in six components of the stress tensor and not nine; three normal stresses and three shear stresses.

$$\begin{aligned} \sigma_{xy} &= \sigma_{yx} \\ \sigma_{yz} &= \sigma_{zy} \\ \sigma_{zx} &= \sigma_{xz} \end{aligned} \tag{4.2}$$

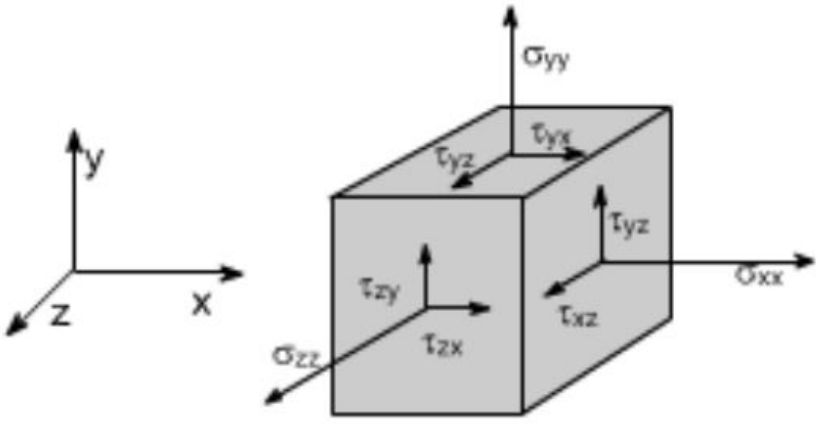

Figure 4.8: Normal and shear stress components indicated on a single cube element

In the F_x and F_y load cases, when these shear forces are applied at the free end of the cable as shown in Figure 4.7, they generate a moment at the beam cross section mid point, i.e an M_y and M_x. As the local model was a 3D model, but it was desired

to understand the stresses across the 2D cross section at the cable mid point, these generated moments need to be accounted for and corrected.

To get the combined effect of the six components of the stress tensor by linear superposition, the stresses induced by the unit forces and moments were added together. The bend moments induced by the forces applied at the cable free end need to be corrected according to Equation 4.3. For example, the σ_{xx} stress at the mid-point is a function of the stress induced at the midpoint by the F_x force applied at the cable free end plus the additional stress induced by the bend moment generated by this force. Note that when the induced moment is clockwise, when looking from the origin to the force arrow head in Figure 4.7, the moment is positive, whereas if anticlockwise the moment is negative.

$$\begin{aligned} \sigma_{xx}(midpoint) &= \sigma_{xx}(F_x) - 0.25\sigma_{xx}(M_y(F_x)) \\ \sigma_{yy}(midpoint) &= \sigma_{yy}(F_y) + 0.25\sigma_{yy}(M_x(F_y)) \end{aligned} \tag{4.3}$$

Where $\sigma_{xx}(midpoint)$ represents the stress at the midpoint, $\sigma_{xx}(F_x)$ represents the stress generated by the F_x force applied at the cable free end and $\sigma_{xx}(M_y(F_x))$ represents the stress induced by the bend moment generated by this force.

With this correction applied, any of the normal or shear stresses can be investigated at the midpoint. The von Mises stress is a representation of the effective stress produced by a combination of the tensile, compression, bending and shear loading, such as in this case. The von Mises stress criterion provides a viable general value of the distortional energy stored in an isotropic material before it will begin to fail at a value known as the yield strength, σ_y. The von Mises stress, σ_v, can be used to predict yielding of an isotropic material which is subjected to complex loadings, such as a dynamic cable. For this the von Mises stress across the 2D cross section at the midpoint was calculated

using Equation 4.4.

$$\sigma_v = \sqrt{0.5[(\sigma_{xx} - \sigma_{yy})^2 + (\sigma_{yy} - \sigma_{zz})^2 + (\sigma_{zz} - \sigma_{xx})^2] + 3(\sigma_{xy}^2 + \sigma_{yz}^2 + \sigma_{zx}^2)} \quad (4.4)$$

Using Equation 4.4, the von Mises stress for each element was calculated and plotted, illustrated in Figure 4.9. To deduce if the results of the linear superposition aligned with what was calculated within ANSYS, a verification was completed where the loads presented in Table 4.3 were simultaneously applied to the cable free end.

Table 4.3: Inputs for linear superposition verification

Force (kN)/Moment(kNm)	Value
F_x	6.40
F_y	-0.51
F_z	0.03
M_x	0.46
M_y	19.12
M_z	-1.72

Looking at Figures 4.9 and 4.10, it can be quickly deduced that the distribution of the von Mises stress across the cross section match.

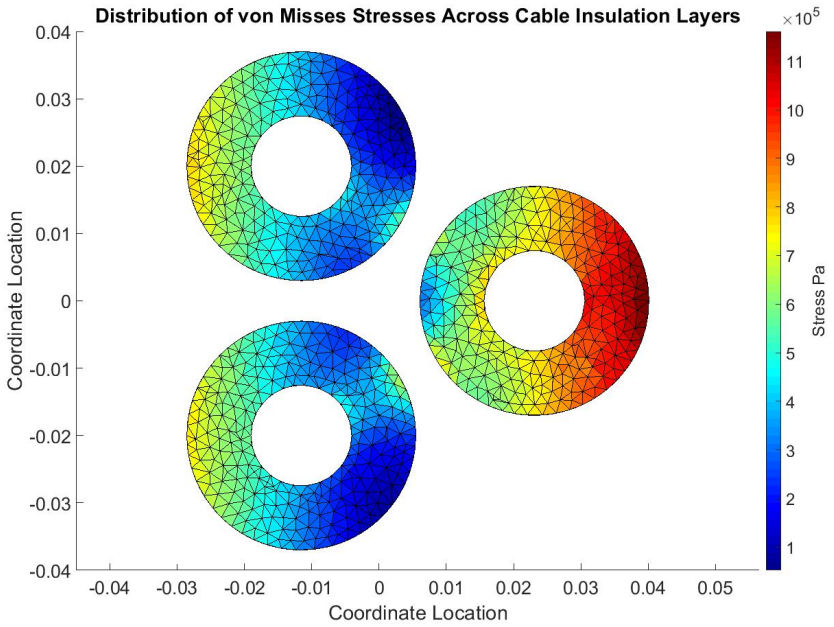

Figure 4.9: Matlab linear superposition von Mises stress distribution across cable's cross section insulation layers

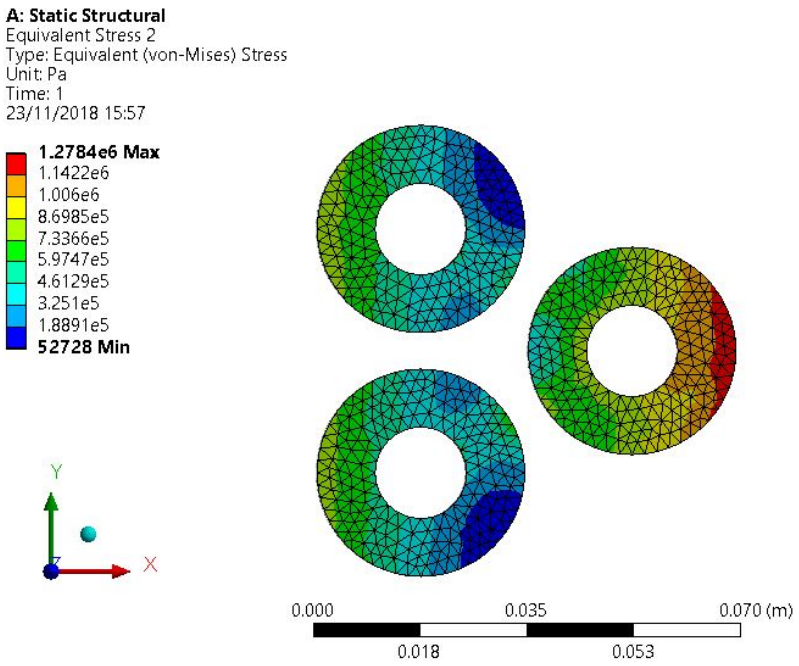

Figure 4.10: ANSYS von Mises stress distribution across cable's cross section insulation layers

When comparing the calculated stresses, the maximum von Mises stress the Matlab linear superposition calculates is 1.21MPa, whereas the ANSYS model calculates the maximum as 1.28MPa. This is an under prediction of 5.5% with an explanation provided in how the model in ANSYS is constructed using the Boolean operations.

4.4.1 ANSYS Boolean operations

The ANSYS local model was constructed using Boolean operations where the two cable lengths were "glued" together at their ends to form the overall cable volume as shown in Figure 4.2 and described in Section 4.3. The benefit of this over having one continuous cable length was that it allowed for a flat 2D plane exactly at the mid point, allowing for extraction of stress results at that face.

When using the Boolean operations within ANSYS, when volumes are glued together they maintain their individuality, i.e they are not added, and therefore do not share nodes. They instead are joined using constraint equations and become connected at their intersection. Figure 4.11 illustrates this for the gluing of two cuboid volumes, taken from the ANSYS Modeling and Meshing Guide user manual [118].

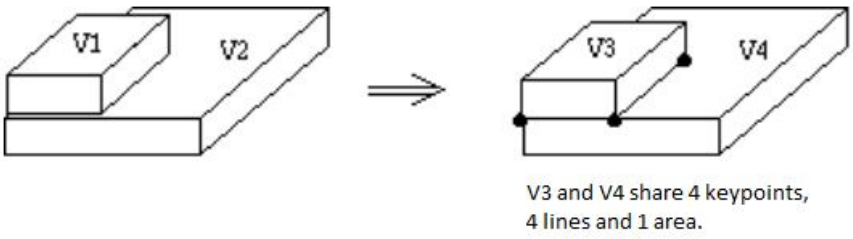

Figure 4.11: ANSYS Boolean operations glueing two volumes

From Figure 4.11 it can be seen that the two volumes share an area. This shared area is what serves as the face at the cable length midpoint intersection from which the stresses are extracted. This sharing of an area, while the two glued volumes maintain their individuality, results in some interactions that would otherwise not be accounted for within the linear superposition within Matlab. Figure 4.12 displays the percentage

difference between the ANSYS model and the linear superposition across the cable's insulation layers.

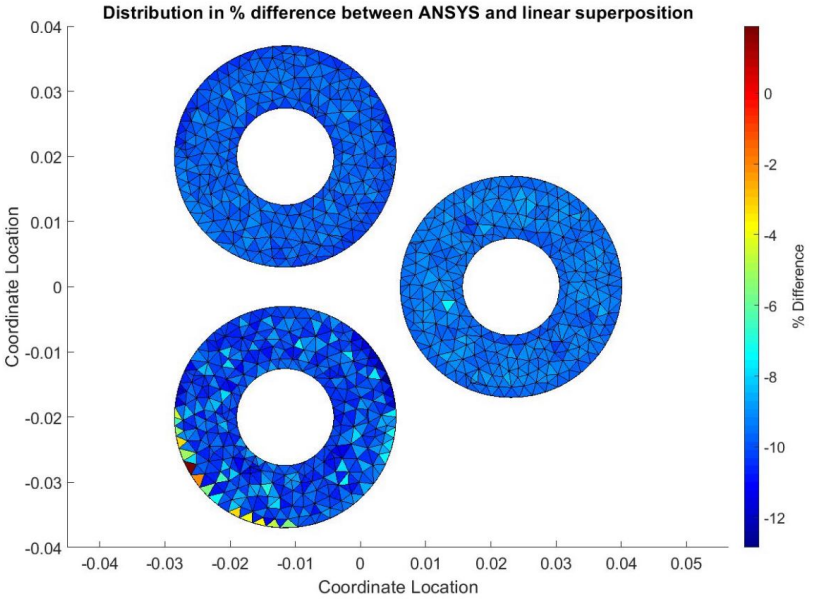

Figure 4.12: % difference distribution between ANSYS model and linear superposition

From Figure 4.12 it can be seen that there is the same general under prediction by the linear superposition compared to the ANSYS model. The average % difference between the two is an under prediction of 9.6%. The greatest % difference is a 12.8% under prediction.

An average percentage difference of 9.6% has been accepted as reasonable to allow for use of the linear superposition within Matlab of the dynamic analysis to drastically reduce computational expense. Further backing this decision is that the overall distribution spread of the stress in Figures 4.9 and 4.10 match very closely between the two.

4.5 Stress response

Using the previously discussed local model by linear superposition, time histories of the shear and planar stresses experienced by any mesh element of the insulation layers cross section can be extracted. A stress based approach to fatigue was used as the stresses exerted upon the cross section are lower than the design yield stresses of the cable insulation material, cross linked polyethylene (XLPE). These shear and planar stresses were combined to calculate the von Mises stress across the cross section according to Equation 4.4. The von Mises stress is used as it allows comparison between a three dimensional stress condition and an experimentally determined uniaxial stress yield limit.

Figure 4.13 shows example plots at every location of the stress time histories extracted from the element of the insulation cross section that experienced the greatest von Mises stress. From the global model the first thirty seconds of the simulation were discarded to remove any possible transients.

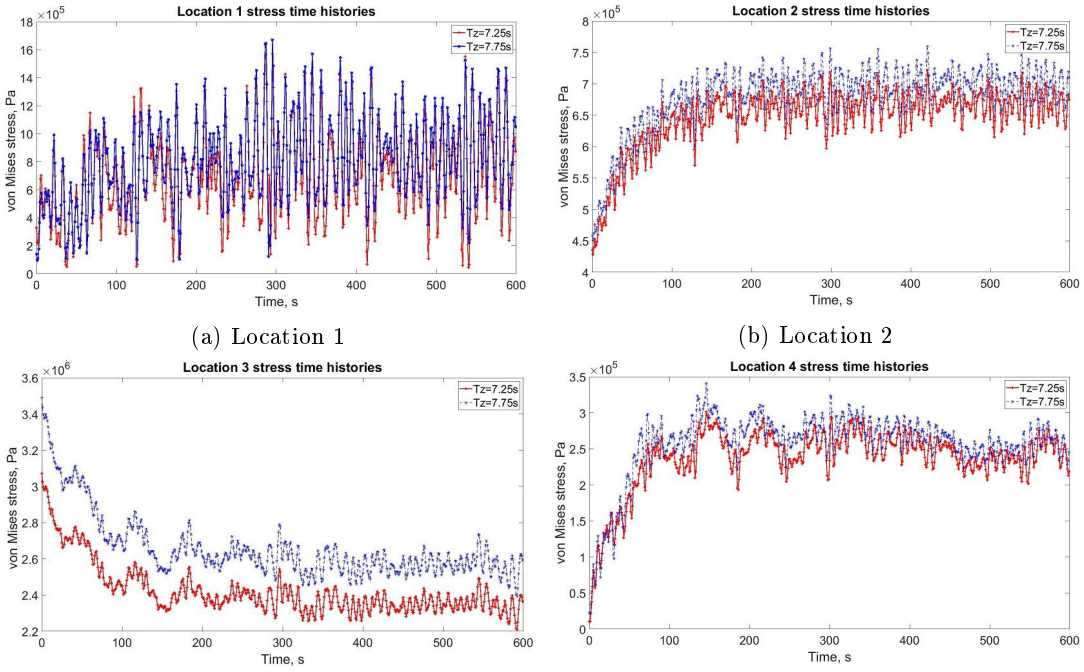

(a) Location 1

(b) Location 2

(c) Location 3

(d) Location 4

Figure 4.13: Stress time history calculated at Location's 1 to 4 on the cable's insulations cross section during Load case 1, H_s 4.75m for differing wave periods.

In Figure 4.13 (a) the stress time histories at the cable hang off point are plotted for differing wave periods (constant wave height of 4.75m). It can be seen that the time histories for each wave period follow the same general profile. This is repeated for locations 2, 3 and 4 and shown in Figure 4.13 (b),(c) and (d) respectively. In (b), (c) and (d) it can be seen that similar to (a) the different wave periods follow the same general stress profile. In addition these plots allow for the clearer visualisation of the impact of the platform moving from its stationary position to its equilibrium position for the applied load case. This is evidenced in the first 200 seconds of the simulation plots where the greatest change in stress is shown; i.e the platform moving from stationary to equilibrium position and thus the induced stress on the cable.

These stress time histories as shown in Figure 4.13 are generated for every element of the insulation's cross section, on every location identified, for every applied load case. They are then used as the "mechanical stress" inputs to the fatigue and water tree propagation chapter.

In Table 4.4 the minimum, mean, and maximum von Mises stress across the cable's insulation cross section is shown for each of the wave heights recorded at the offshore site. The wave periods were grouped within their respective wave heights, and the minimum, mean, and maximum values shown are of these collective wave periods.

In Table 4.4 it can be seen that with increasing significant wave height, there is a general trend of increasing von Mises stress at all of the different locations chosen along the cable's length. The greatest von Mises strengths are consistently calculated at Location 3, where the cable experiences the greatest level of bending. The second greatest stresses are found at Location 1, at the hang off point where the cable experiences the greatest level of tensions. This is not to suggest that bending the cable produces a greater stress than applying tension. It is important to consider that the bend moment outputs from the global model were an order of magnitude larger than the tension forces, shown in the force output section of Chapter 3. Furthermore, following the spike

in force output from the global model at a wave height of 1.25m, a spike in the produced stress is also seen at this wave height. This was due to the waves being correlated to a wind speed that is the rated wind speed of the floating turbine at this wave height, and thus the thrust force of the turbine was at its greatest causing the floating platform to surge. Location 1 at the hang off point, however, does not show this spike; this is because the surging of the platform would not cause the same level of bending in the cable at this location, unlike the other locations. Figure 4.14 shows how stress varies with significant wave height at each location.

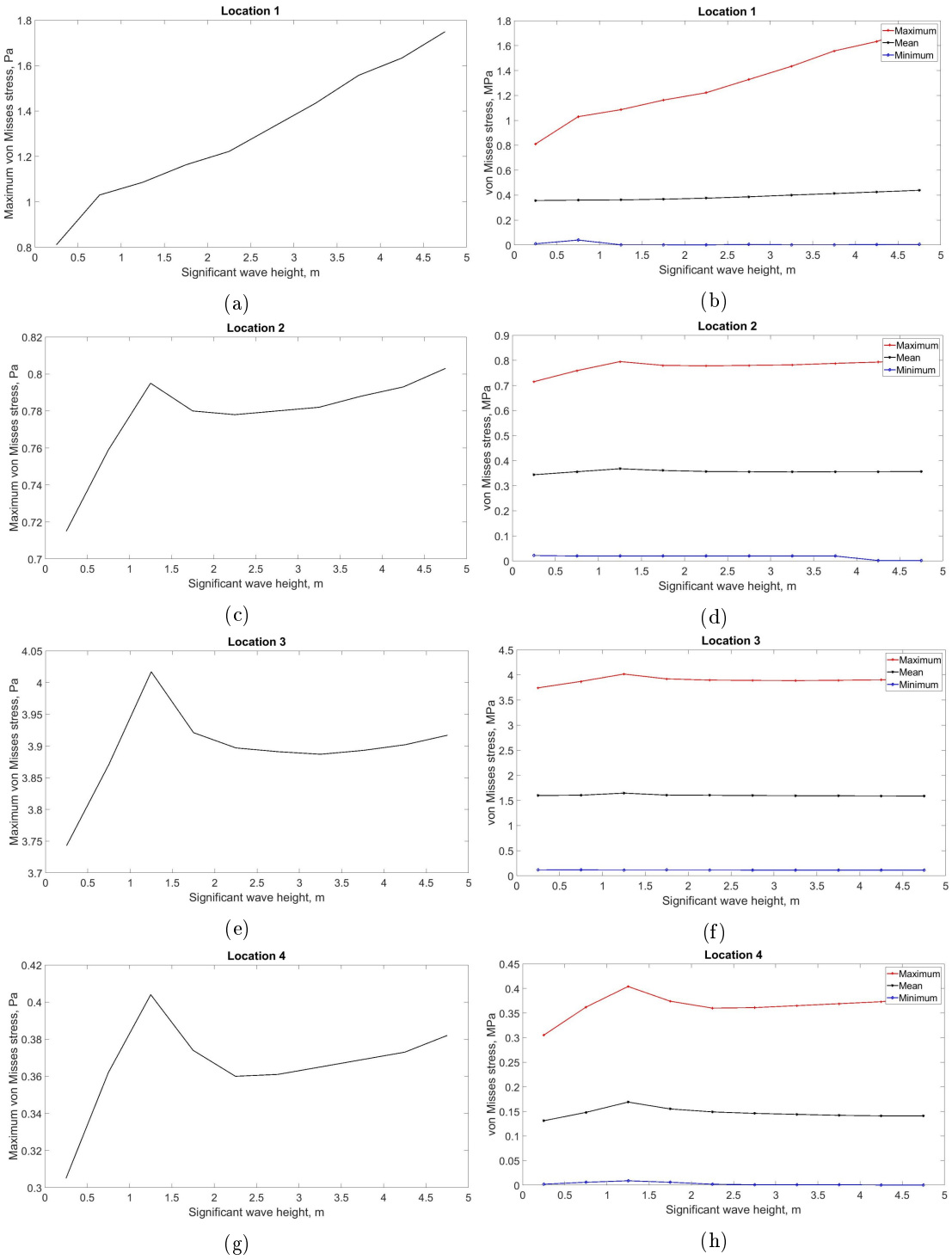

Figure 4.14: Maximum, mean and minimum calculated von Mises stress on the insulation layer at each location for varying significant wave heights. Maximum von Mises stress is replotted for visualisation of stress peak at 1.25m significant wave height

Table 4.4: Minimum, mean and maximum calculated von Mises stress (MPa) on the insulation cross section layer at differing locations on the cable length and varying wave height

Load Case 1													
Significant wave height H_s	Probability	Location 1			Location 2			Location 3			Location 4		
		min	mean	max	min	mean	max	min	mean	max	min	mean	max
0.25	0.204	0.010	0.357	0.811	0.022	0.344	0.715	0.116	1.597	3.743	0.002	0.131	0.305
0.75	0.403	0.04	0.360	1.030	0.020	0.356	0.759	0.117	1.605	3.871	0.006	0.148	0.362
1.25	0.224	0.002	0.362	1.086	0.020	0.368	0.795	0.115	1.646	4.017	0.009	0.169	0.404
1.75	0.097	0.002	0.368	1.163	0.020	0.361	0.780	0.116	1.607	3.921	0.006	0.155	0.374
2.25	0.037	0.001	0.376	1.222	0.020	0.357	0.778	0.115	1.602	3.897	0.002	0.149	0.360
2.75	0.019	0.005	0.387	1.328	0.020	0.356	0.780	0.114	1.598	3.891	0.0009	0.146	0.361
3.25	0.009	0.002	0.401	1.434	0.020	0.355	0.782	0.113	1.595	3.887	0.001	0.144	0.365
3.75	0.004	0.002	0.413	1.557	0.020	0.356	0.788	0.113	1.592	3.893	0.001	0.142	0.369
4.25	0.003	0.004	0.426	1.633	0.002	0.356	0.793	0.112	1.590	3.902	0.0004	0.141	0.373
4.75	0.0004	0.005	0.439	1.749	0.002	0.357	0.803	0.113	1.588	3.917	0.0003	0.141	0.382

4.6 Chapter summary

Within this chapter a local model of the dynamic cable's cross section was constructed. The local model was a finite element analysis of the cable cross section built using ANSYS Mechanical software. This local model was used to allow application of the F_x, F_y, F_z, M_x, M_y and M_z force/moment response output from the global model to determine the stress exerted on the insulation layers of the cross section.

To save on computation expense a linear superposition of the FEA local model was completed within Matlab as opposed to completing a transient dynamic analysis with ANSYS as described in Section 4.4. Using this model the three planar and three shear stress time histories were calculated for every element of the insulation layer's cross section. These six components of the stress tensor were combined to calculate the von Mises stress time history of every element of the insulation layer's cross section. The generated von Mises stress time history is then known as the "mechanical stress" as a result of the marine environment impact on the dynamic cable, and serves as an input to Chapter 6 to determine the damage to the cable's insulation layer and the water tree propagation.

Chapter 5

Electric field model

5.1 Chapter introduction

This chapter discusses the work completed to produce a time history of stresses due to the distortion of the electric field within the cables XLPE insulation. The propagation of a water tree across the insulation thickness is examined and the electric field distortions modelled and recorded. This distortion is used to determine how the electric field changes across the insulation thickness. The electric field strength at different points along the insulation thickness is converted to a mechanical stress by means of Maxwell stress calculations. As the Maxwell stress will alternate with the electric field in an alternating current, AC, system a sinusoidal shape is used as the basis of the time history. Different stress histories have been plotted to quantify this, depending on how far along the insulation the water tree has propagated.

5.2 Electric field modelling

One of the fundamental concepts within electromagnetism is the idea of charge, a physical property of matter, that can be either positive or negative, and causes that matter to experience a force when exposed to an electromagnetic field. Around a point of charge exists an electric field. The presence of this electric field means work is needed to be applied to either move another point of charge away from, or towards, this point of charge. This work required to move a point of charge between two points of differing electric

potential is known as the potential difference, i.e. the voltage. The moving point of charge is then known as the current, and a moving current induces a magnetic field. To summarise, a charge produces an electric field, which therefore also produces a potential difference. The moving charge is the current, which produces a magnetic field. It is important to note these two field types are not distinct from one another and co-exist.

When the XLPE insulation encompasses the cable core, the surrounding electric field distributes evenly as a function of the insulation thickness, assuming the insulation is perfect and uniform. If the cable core, insulation and surrounding screen is considered as a capacitor, introducing the dielectric XLPE which has its own relative permittivity will increase the capacitance. The capacitance can be written as a function of the dielectric permittivity, the area of plates, or in this case the core outer surface and the insulation screen surface, and the distance between them, which in this case is the thickness of the XLPE insulation, Equation 5.1

$$C = \varepsilon_r \varepsilon_0 \frac{A}{d} \tag{5.1}$$

Where C is the capacitance in Farads, A is the area m^2, d is the distance between them in m, ε_0 is the permittivity of a vacuum 8.85x10^{-12} Fm^{-1}, and ε_r is the dielectric constant or the relative permittivity. Further to this the capacitance can be written as the ratio of the charge to the voltage, Equation 5.2.

$$C = \frac{Q}{V} \tag{5.2}$$

Where Q is the charge in Coulombs, and V is the voltage in Volts.

When considering Coulombs Law, Equation 5.3 shows how electric field strength can be written as a function of charge and the distance from the charge source.

$$E = \frac{Q}{4\pi\varepsilon_0\varepsilon_r r^2} \tag{5.3}$$

Where E is the electric field in Vm^{-1} and r is the radius in m.

The voltage of the core in the model has been set to 66kV. The relative permitivites of the XLPE insulation and a water tree is shown in Table 5.2 [70, 119, 120]. ANSYS Maxwell software has been used to create a FEA of the cable core's insulation layer. The thickness of the insulation layers is the same as what was created during the FEA for the local model chapter, and meshed accordingly.

5.2.1 ANSYS Maxwell FEA

Meshing of the FEA is different within ANSYS Maxwell compared to ANSYS Mechanical, previously discussed in Chapter 4. Within Maxwell, meshing is a much more automatic process that begins with a very coarse mesh, and runs through a refinement convergence study to reach the desired % error between two consecutive convergence passes.

In this study, a % error between convergence passes was set as 1% with a minimum number of two passes with an 80% refinement between passes. With this the user can ascertain the mesh quality from the mesh refinement study, and should in theory always be able to get a model which is mesh-independent. Table 5.1 shows that only one pass was required, however two were completed due to the minimum set requirements, increasing the number of elements from 1320400 to 2376788 for a final % error of 0.051%.

Table 5.1: Mesh refinement pass results

Pass	Number of elements	% error
1	1320400	0.25491
2	2376788	0.051169

Figure 5.1 shows how the electric field strength distributes radially across the thickness of the XLPE insulation layer, while Figure 5.2 illustrates graphically the magnitude

of the electric field moving further from the core. Figure 5.2 illustrates that the electric field seen at the conductor screen side of the insulation is more than double that seen at the insulation screen side of the XLPE.

Table 5.2: Parameters for electrical field model

	XLPE	Water tree	Cable core (copper)
Relative permittivity (ε_r)	2.3	10	1
Conductivity γ (Sm^{-1})	1 x 10^{-17}	1 x 10^{-8}	9.33 x 10^{6}

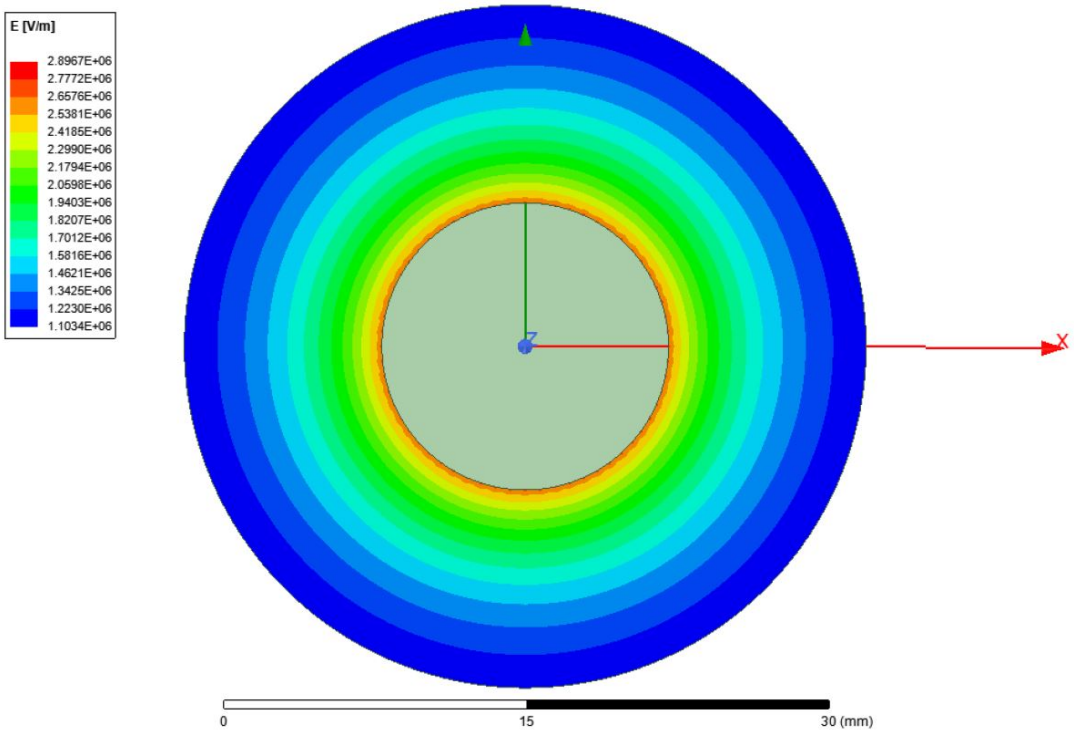

Figure 5.1: Distribution of the electric field across a uniform XLPE insulation layer

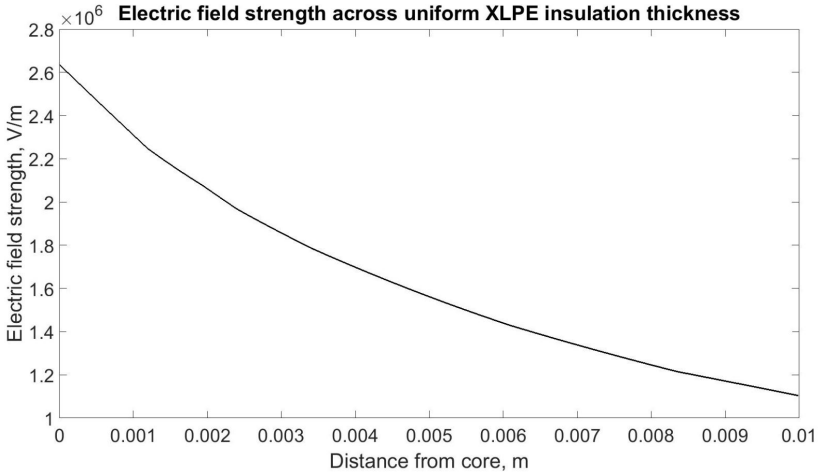

Figure 5.2: Magnitude of the electric field strength across a uniform XLPE insulation

5.2.2 Electric field distortion

When a water tree grows, it can be thought of as a typical water filled crack within the homogenous XLPE following a "pearl and chain" propagation structure, "pearl and chain" referring to a series of ellipsoidal voids connected by a narrow channel crack. Using the Kinetic Theory of Fracture [96] as a standpoint, where fracture is a process that a body under stress undergoes whereby interatomic or chemical bonds of the XLPE polymer are broken causing rupture of the bonds and the polymer chain; successive ruptures of these bonds lead to the macroscopic failure of the XLPE resulting in the formation of cracks and micro voids or cavities [96] such as the "pearl and string" arrangement [54]. A FEA model of this ellipsoidal void and string was created with the sizing of the water tree head void taken from [120] and shown in Table 5.3. Figure 5.3 shows the FEA mesh of the water tree model. Here it can be seen that a refinement of the mesh was generated at the boundary of the water tree, with particular focus on the tip of the ellipsoidal void. The presence of a water filled water tree within the XLPE insulation causes distortion of the electric field as shown in Figure 5.4.

Two dimensional models of the water tree in the XLPE cross section were used for the simulation of the electric fields. Electric field lines are perpendicular to equipotential lines and direct radially outwards from the core to the outer insulation screen for

a positive core polarity. For a negative polarity the electric field lines remain perpendicular and radial but direct inwards to the core. Therefore 2D models are accepted as appropriate for analysis of the electric field distributions [121]. Further to this, when modelling the electric field distribution in the presence of water trees, the water tree is to be in line with the electric field. This assumption is made as water trees propagate parallel to the direction of the electric field.

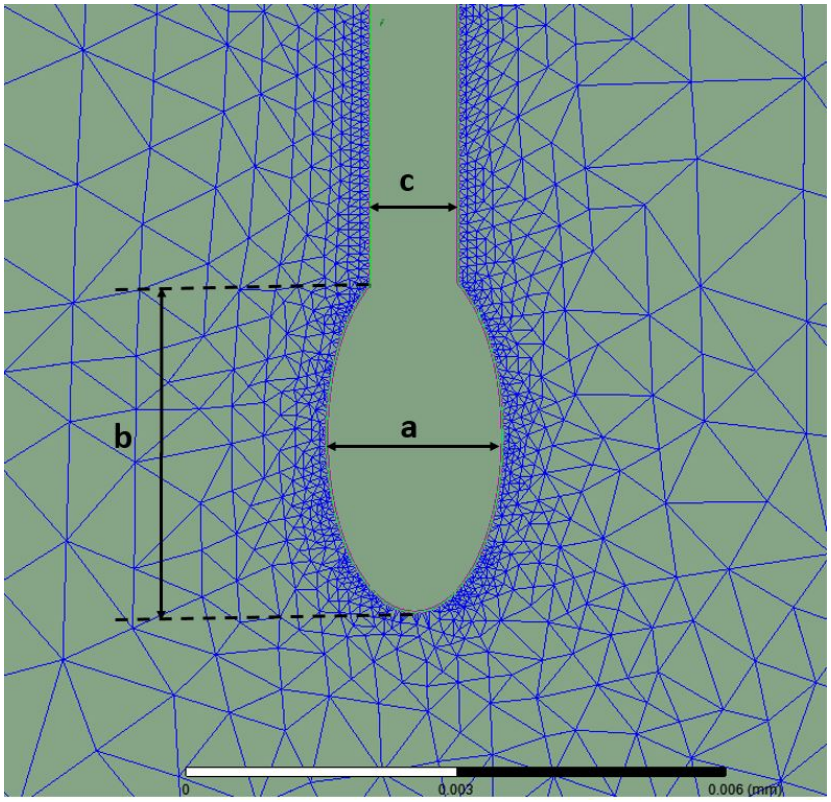

Figure 5.3: FEA mesh of a tip of a water tree crack with ellipsoidal head

Table 5.3: Dimensions of the water tree model

	Length (μm)
a	2
b	4
c	1

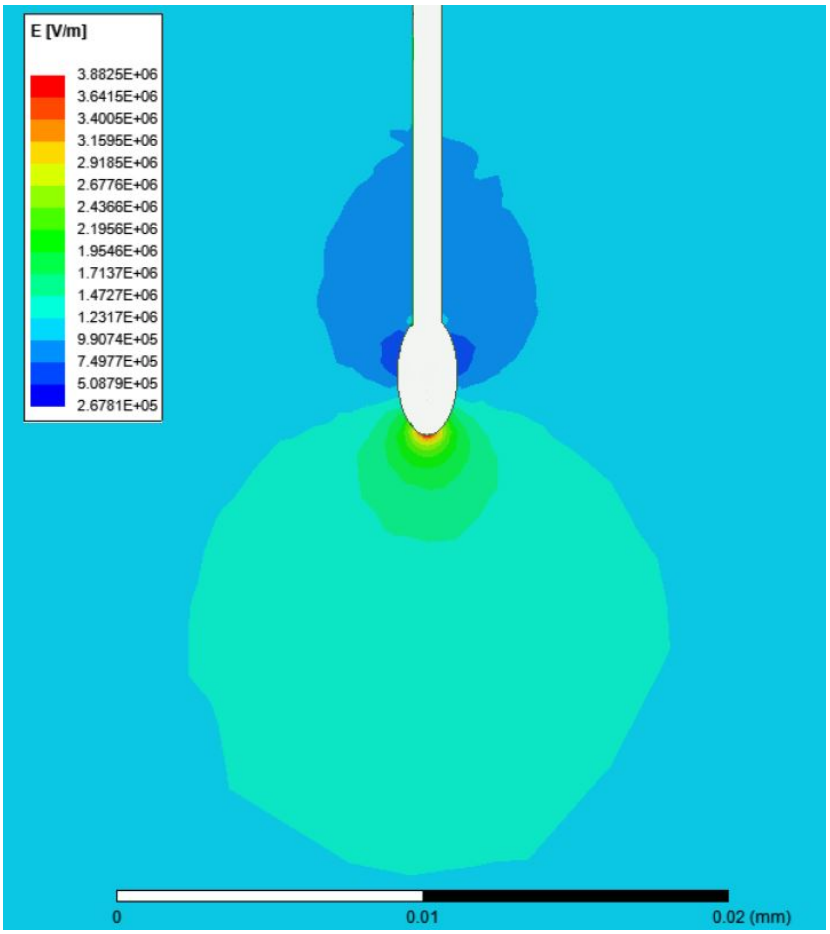

Figure 5.4: Electric field distortion due to presence of the water tree at 1mm length across XLPE cross section

The presence of the water tree causes distortion of the electric field distribution across the cross section of the XLPE insulation. It can be seen that the electric field concentrates at the tip of the ellipsoidal micro void or, if considered from a macroscopic stand point, the tip of the water tree crack, i.e the point closest to the cable core. It is because of the tip concentration that the mesh was refined at this position in Figure 5.3, to allow for capture of this information. Figure 5.4 shows that this electric field concentration at the tip occurs over a distance of a few micrometres, 3μm. Figure 5.5 shows graphically the spike in electric field strength that occurs at the tip of the water tree that has propagated 1mm across the insulation thickness. This spike is similar to [121] where results found a spike in electric field strength at the tip of water trees.

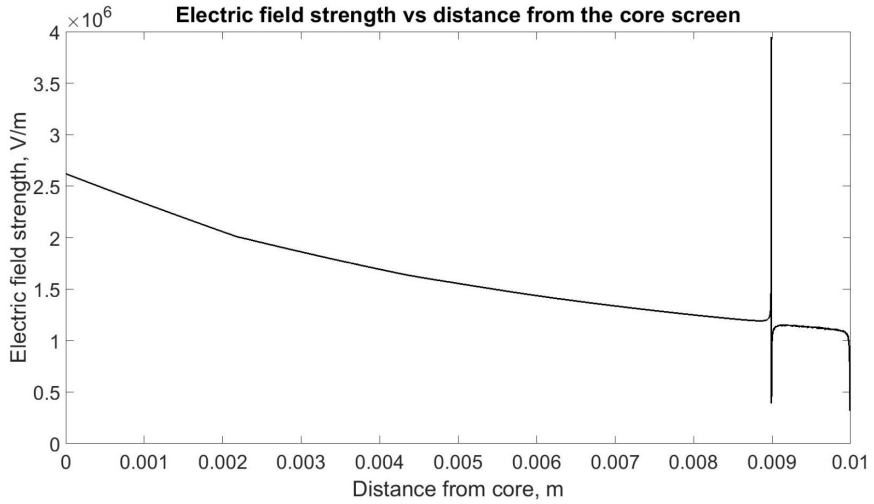

Figure 5.5: Electric field distortion due to presence of the water tree at 1mm length across XLPE cross section

The spike in electric field strength is even greater than the electric field strength recorded at the conductor screen side closest to the core. This can be explained by the concentration of the electric field at this point. When water molecules are present inside the water tree they act as a conductor within the originally uniform electric field. As water is a polar molecule, the charged ends of the dipole move within the ellipsoid head of the water tree, polarising it until the electric field lines are perpendicular to the surface of the water tree tip. This is illustrated schematically in Figure 5.6 where two example water molecules are shown to have their dipoles aligned with the electric field lines and concentrating at the tip of the ellipsoid head.

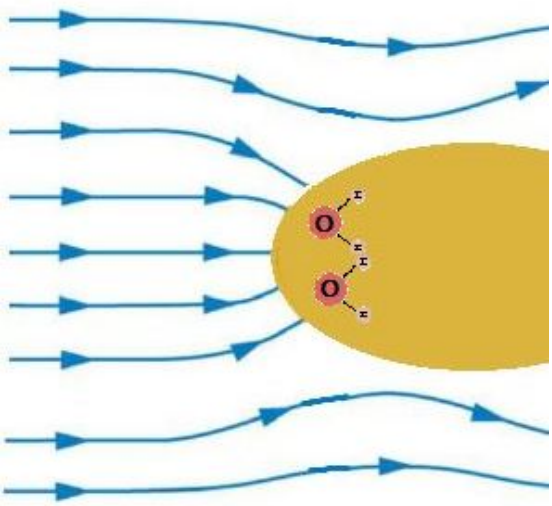

Figure 5.6: Polarisation of water filled ellipsoid head within a uniform electric field [122]

It should be noted that no net electric field exists within the water tree void itself. This is because the water molecule dipoles can move freely in response to a moving electric field until it is balanced. Like charged ends of the dipole repel until they are distributed accordingly on the surface of the microvoid and the net electric field within the conductor decreases and becomes zero. This can be related to Equation 5.3, where the net value of Q will be reduced to zero by the movement of the water dipoles. This is confirmed when Figure 5.4 is replotted but this time including the electric field within the water tree. The exact zero cannot be seen due to the plots resolution, but the obvious decrease is visible with the dark blue colouring, Figure 5.7. It is for this reason that the decrease in electric field strength is seen immediately after the spike in Figure 5.5, as this distance is measured through the ellipsoidal head of the water tree and through its length.

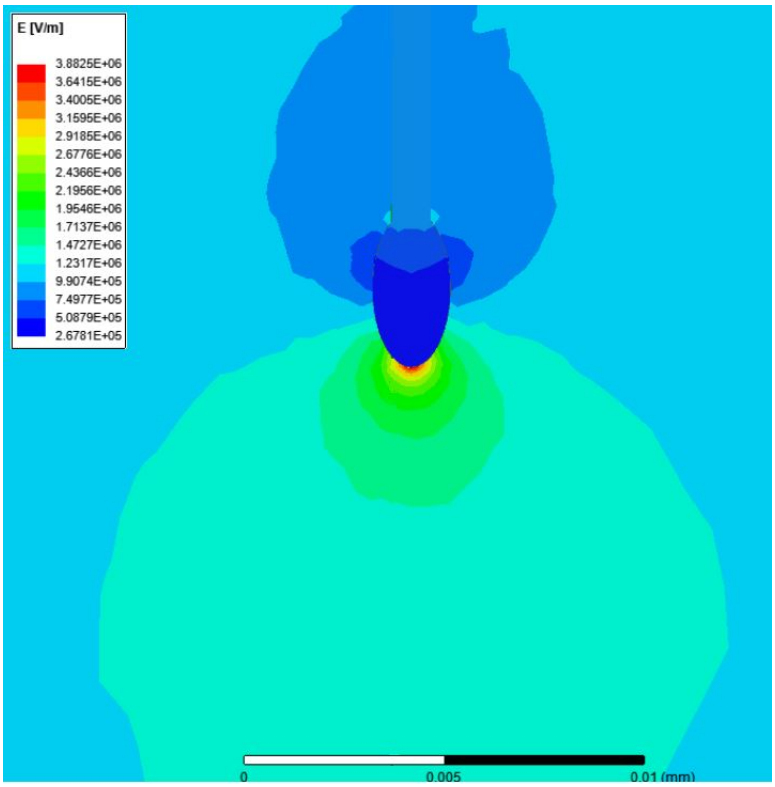

Figure 5.7: Electric field strength within the water tree head tip is shown to be zero

5.2.3 Water molecule propulsion

When a conductor is exposed to an electric field, charged ions within the conductor repel each other until they are evenly distributed on the conductor's surface. For a water tree the dipoles of the water molecules align and distribute accordingly on the surface of the water tree/XLPE boundary, as discussed previously. When the water molecules are exposed to the electric field and they distribute on the surface, they are in fact propelled in micro-jets. For an AC system the water molecules will be rotating their dipole alignment in accordance with the frequency of the voltage. This will mean that the water molecules will be constantly rotating and propelling against the XLPE interface. This propulsion will have an impact force on the XLPE polymer chains. This propulsion direction alignment may also explain why differing lengths of water trees have been observed when testing of differing pulse polarities, as depending on the pulse polarity, it will be the smaller hydrogen or larger oxygen atoms that will be leading the water micro jet propulsion. Furthermore it may help explain why increasing the

frequency of the AC system also increases the length of the water trees.

This water molecule micro-jetting and resulting impact force on the XLPE has not been modelled for this work. It is currently unknown if the increased water tree length with increasing frequency is a factor of the water micro-jetting or of the generated Maxwell stress. The magnitude of the effect of the water micro jetting has yet to be considered, however it is envisioned that it will form part of future works.

5.3 Electric field strength at water tree tip

The process of modelling the electric field strength at the tip of a water tree can be repeated iteratively for different lengths of propagation across the insulation thickness. This has been repeated from an initial water tree length of 0.5mm to 9.5mm. The results are plotted in Figure 5.8 and are compared to the electric field strength across the insulation where there are no water tree distortions.

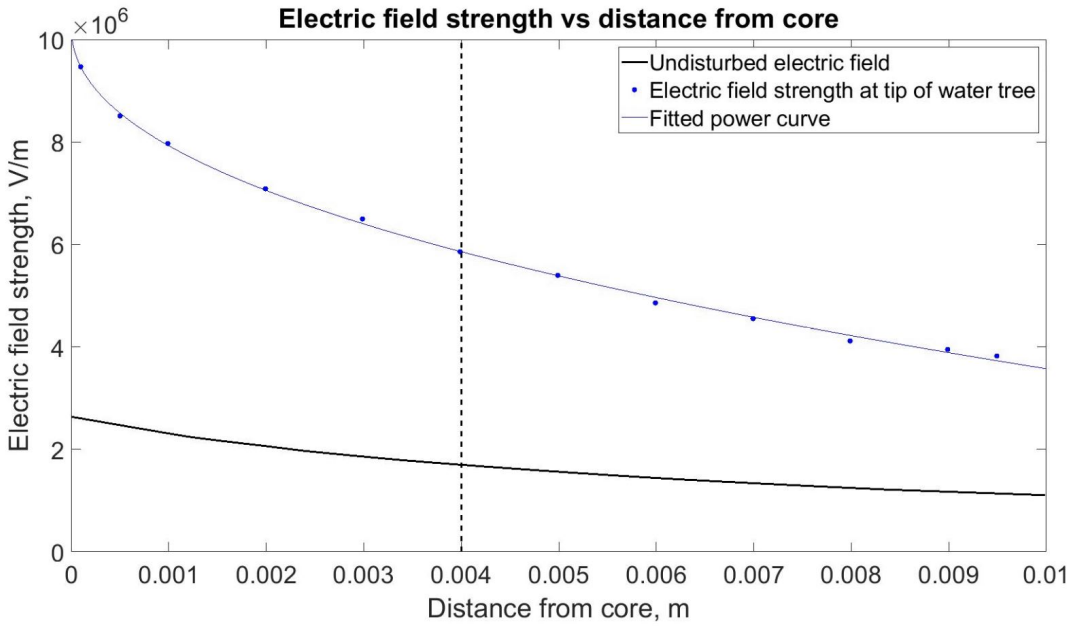

Figure 5.8: Electric field strength at the ellipsoidal tip of the water tree compared to electric field strength with no water tree

The peak electric field strengths are plotted in Figure 5.8 with a power curve fitted to the data. The fitted curve is of the equation $y = ax^b + c$ where a, b and c are -5.42 x10^7, 0.45 and 1.03 x10^7 respectively. The R^2 value of the curve fitted to the data is 0.9988, indicating this fit can account for 99.88% of total variation in the data about the average.

From Figure 5.8 it can be seen that the electric field at the tip of a water tree is much larger than what would be experienced if no water tree was present. In fact, a water tree ellipsoid at 9.5mm from the core would have a peak electric field strength already greater than what would be experienced at the conductor screen side of the

XLPE for an undisturbed cross section of insulation. As previously explained this peak happens over a very short distance, a few μm, before dissipating to normal undistorted conditions, seen in Figure 5.7. It is because of this small area that the peak in electric field strength, and therefore the water tree itself, cannot currently be detected using conventional methods. See literature review for current detection methods that try to detect water trees by forcing them to partial discharge.

At the tip of the water tree the electric field strength increases as the water tree propagates towards the core, i.e a reducing r from the core. Using Figure 5.8, the electric field strength can be written as a function of the radius, r. Equation 5.4 shows the electric field strength at the tip of a water tree as a function of the radius.

$$E = -5.42 \times 10^7 r^{0.45} + 1.03 \times 10^7 \tag{5.4}$$

A vertical dashed line at 0.004m from the core has been included in Figure 5.8. This line indicates when the vented water tree has propagated 60% across the insulation when growing from the insulator screen towards the core. It is at this point of propagation that a water tree has been recorded to cause failures of the cable by means of an arc fault [120]. An arc fault is a high power discharge between two conductors of differing voltages, i.e the cable core and the water tree tip. Water trees do not partial discharge like electrical trees, so standard tan delta testing of the cable would not indicate their presence. At this level of degradation of the cable insulation however tan delta testing may cause the water tree to accelerate and evolve into an electrical tree, which does partially discharge. Here corona discharges can occur unless care is taken to limit the electric field strength. This 60% propagation length may indicate a limit to the electric field strength the XLPE insulation can support.

5.4 Generating stress time histories

When an AC electric field is applied a Maxwell force will occur and impose a cyclic mechanical stress on the XLPE insulation [123, 120]. Under a continually alternating AC electric field, and therefore a continually alternating Maxwell stress, fatigue of the XLPE polymer chains will occur as with any alternating stress of suitable amplitude. The alternating stress can cause rupture or fracture of a weak point within the XLPE polymer chain. When these polymer chains rupture they expose the carbonyl and carboxyl hydrophilic groups at the end of the chain. Therefore when a large number of chains are broken a region of hydrophilic groups can be formed, drawing water molecules in and propagating the water tree. It is these carbonyl and carboxyl groups that dye to allow for the identification of water trees in cable forensic analysis. A useful schematic of this fatigue process of the polymer chains can be found in [120] and presented in Figure 5.9.

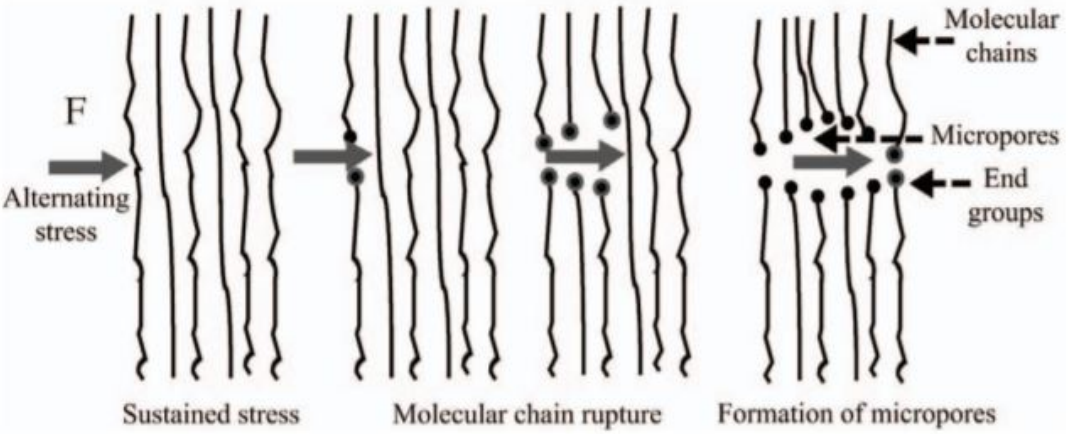

Figure 5.9: Maxwell stress causing fatigue fracture of XLPE polymer chains [120]

The Maxwell stress is defined in equation 5.5 [124]:

$$F = \frac{\varepsilon_0}{2}(\varepsilon_r - 1)\nabla E^2 \tag{5.5}$$

Where F represents the Maxwell stress in Pa, ε_0 is the permittivity of a vacuum in Fm^{-1}, ε_r is the relative permittivity of the dielectric material, XLPE, and E is the

electric field strength in Vm^{-1}.

The electric field strength is a function of the radius from the core r, the angle of field direction θ and the z direction along the cable axis. This can be shown mathematically in Equation 5.6.

$$F = \frac{\varepsilon_0}{2}(\varepsilon_r - 1)\begin{bmatrix} \frac{d}{dr}E^2 \\ \frac{d}{d\theta}E^2 \\ \frac{d}{dz}E^2 \end{bmatrix} \tag{5.6}$$

As stated previously a 2D model of the cable cross section has been accepted as water trees grow in line with the electric field. Further, the core is assumed uniform throughout the cable's length so the electric field would remain uniform as a function of z along the cable axis.

The direction of the electric field θ has been shown in Figure 5.1 to be uniform in all radial directions from the core. Finally Figure 5.1 obeys Coulombs' Law and shows that the electric field strength changes as a function of r, the radius distance from the core. With these considerations in mind Equation 5.6 can be rewritten as in Equation 5.7.

$$F = \frac{\varepsilon_0}{2}(\varepsilon_r - 1)\begin{bmatrix} \frac{d}{dr}E^2 \\ 0 \\ 0 \end{bmatrix} \tag{5.7}$$

5.4.1 Maxwell stress and electric field strength

Once the electric field strength at the tip of the water tree ellipsoidal head is known, the Maxwell stress at the water tree head can be calculated using Equation 5.5. For the geometry presented Figure 5.10 shows how the Maxwell stress at the tip of water tree

changes with distance from the core, in effect showing the Maxwell stress at the tip for the length of the water tree ellipsoidal head.

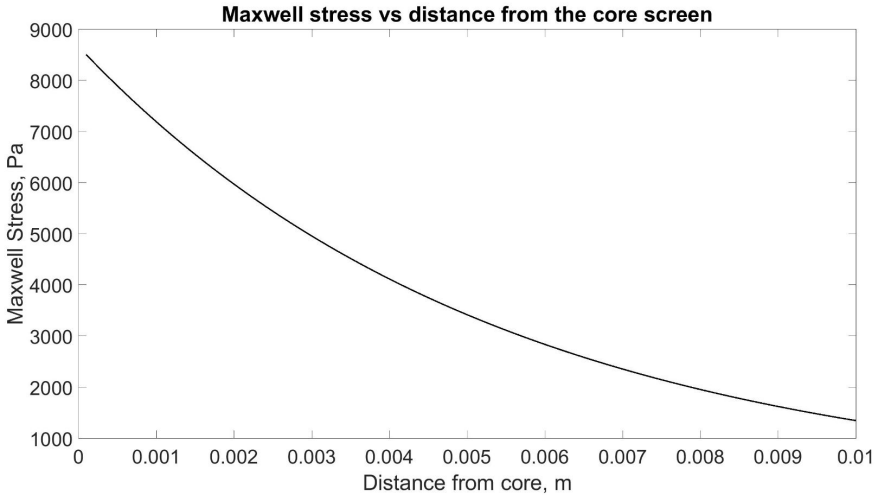

Figure 5.10: Variation of Maxwell stress at the water tree tip across the thickness of the insulation

From Figure 5.10 it can be seen that as the water tree propagates towards the cable core, the Maxwell stress experienced at the tip increases. As the water tree reaches the cable core screen side the Maxwell stress rapidly increases, however it is expected a water tree would have already caused a cable fault by arcing before it would reach this length.

As this is an AC system, the electric field direction will be alternating with the frequency of the system. As the electric field direction is alternating, so too shall the Maxwell stress. It is this alternating frequency that generates a time history of the Maxwell stress. Assuming a frequency of 50 Hertz, and a classic sinusoidal profile for the voltage, a time history of the alternating Maxwell stress can be calculated. Figure 5.11 shows a plot of this alternating Maxwell stress as a function of the radius distance the water tree tip is from the cable core.

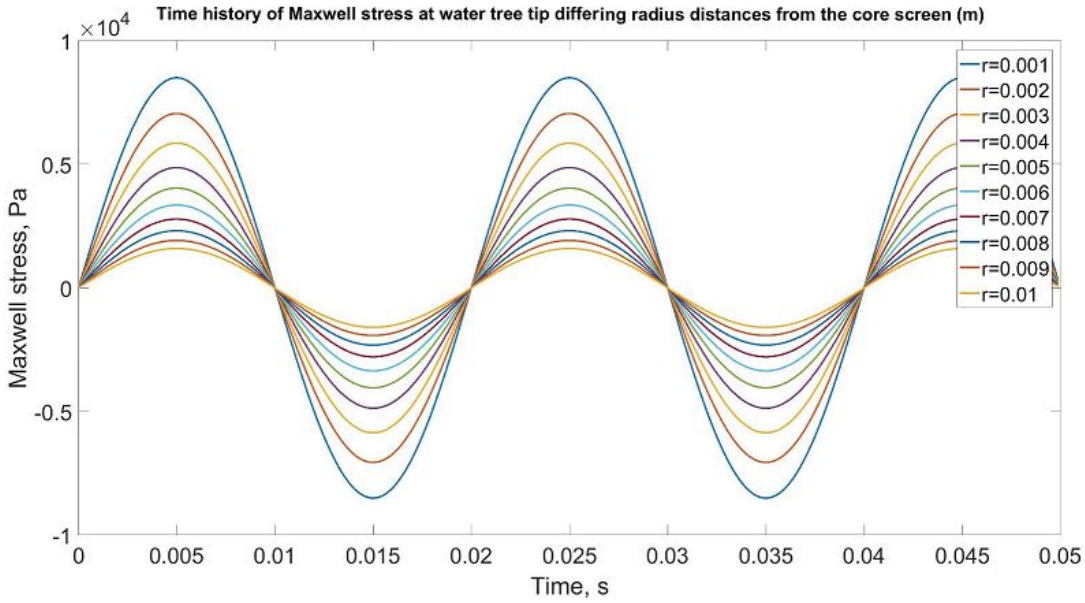

Figure 5.11: Time history of the Maxwell stress at differing points along the insulation thickness

From Figure 5.11 it can be seen that with increasing radius distance from the cable core, the amplitude of the Maxwell stress decreases. It should be noted that the experienced Maxwell stress at the tip of the water tree ellipsoid head would be these stress time histories, but also all of the intermediates not plotted as it propagates across the XLPE insulation thickness. The 50Hz frequency time history will remain constant, but the amplitude of the Maxwell stress will increase with increasing water tree length. These results are in agreement with similar simulations conducted by [125] and [120].

5.4.2 Maxwell stress and aspect ratio

Wang [125] showed that varying the aspect ratio of the water tree head greatly impacts the stress concentration at the tip of the water tree head, i.e. longer and thinner water trees or "cracks" generate much larger stresses due to greater electric field concentration at the tip, similar to a stress concentration factor. Similarly, Salleh [121] showed how the concentration factor for different shaped water trees impacts the electric field strength. This result is reproduced in Figure 5.12 [125] where theoretical aspect ratios of water trees were examined to produce unrealistically large Maxwell stresses. In Wang's work the average background electric field strength in the insulation was set to 2MV/m, which

when looking at Figure 5.1 is the same average background electric field strength used here, or approximately the background electric field strength at a distance of 0.004mm from the conductor screen in a uniform insulation layer. This is a particular advantage as it allows comparison of aspect ratio at the radius distance that water tree failure has been assumed to occur for this work.

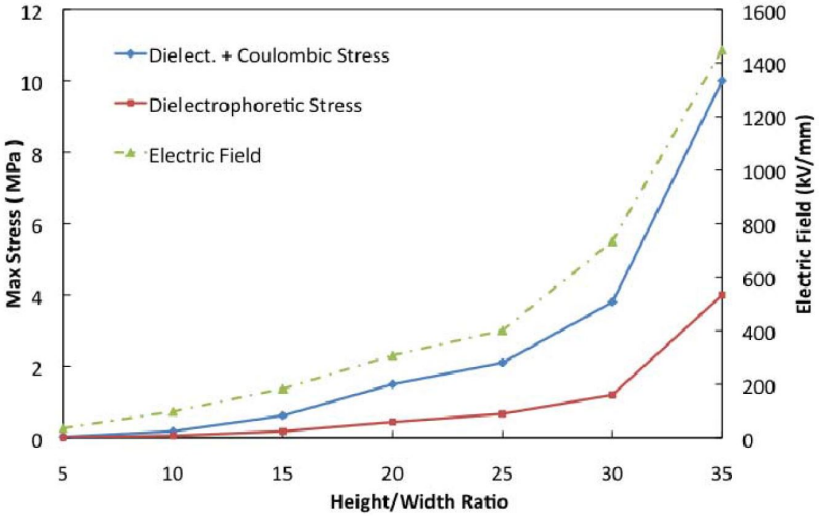

Figure 5.12: Increase in stress and electric field at tips of of spheroidal defects with increasing aspect ratio [125]

Figure 5.12 illustrates that Maxwell stresses greater than the yield strength (8MPa) of the XLPE insulation can be generated by the electric field. However the electric field strength required to generate this stress is greater than 1000 kV/mm as shown in Figure 5.12. This electric field strength is considerably greater than the 22 kV/mm dielectric strength of the XLPE insulation. Above its electric field strength the insulation will have broken down, and electric trees driven by partial discharges would have degraded the insulation. Therefore the electric field strength of the XLPE serves as the limiting factor for the maximum Maxwell stress which can be generated at the tip of the water tree. Using Figure 5.12 the electric field strength can be written as a function of aspect ratio:

$$E = 0.008 R_a^{3.4} \tag{5.8}$$

Where R_a is the aspect ratio of the water tree head. Using the electric field strength of the XLPE as a limitation the maximum aspect ratio at the tip of a water tree, at a length assumed to cause insulation failure, is 2.3. From the dimensions laid out in Table 5.3, the aspect ratio of the water tree heads used to model electric field distortions for this work is 2. This confirms that the assumed failures at this length are due to water treeing and not due to exceeding the break down strength of the XLPE leading to partial discharge and electrical treeing.

This work illustrates that the cyclic Maxwell stress at the tip of the water tree is not only a function of distance from core, i.e the water tree length, but also the head's shape. The theoretical maximum cycling Maxwell Stress at the water tree tip, according to Equation 5.7, at any length of water tree is plotted in Figure 5.13, where the distorted electric field strength is 22kV/mm.

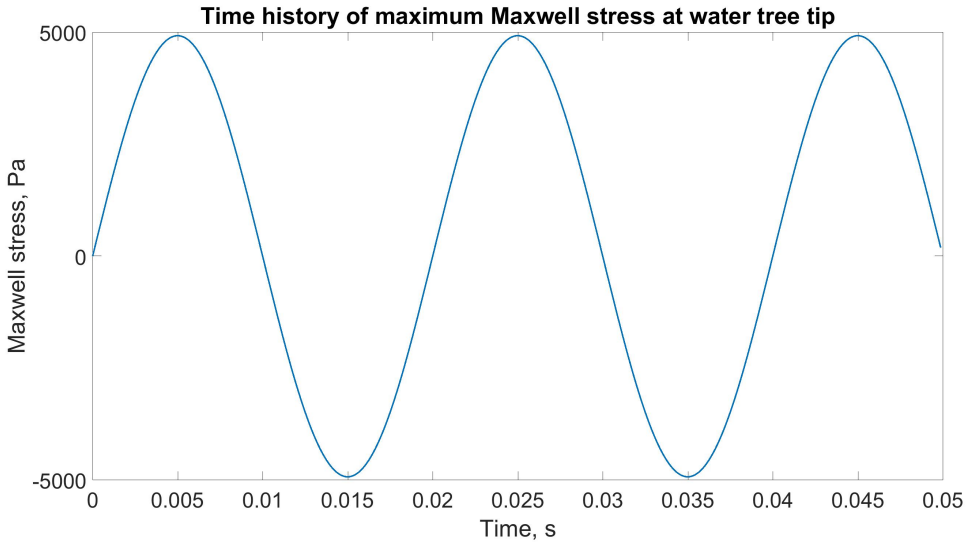

Figure 5.13: Maximum cyclic Maxwell stress at the tip of a water tree

This theoretical maximum of 4.9kPa matches Wang's [125], who predicts a maximum stress of 4.6kPa for an aspect ratio of 2.3 according to Figure 5.12. Figure 5.14 shows how the Maxwell stress at the water tree head for a water tree 4mm from the cable core varies with differing aspect ratios.

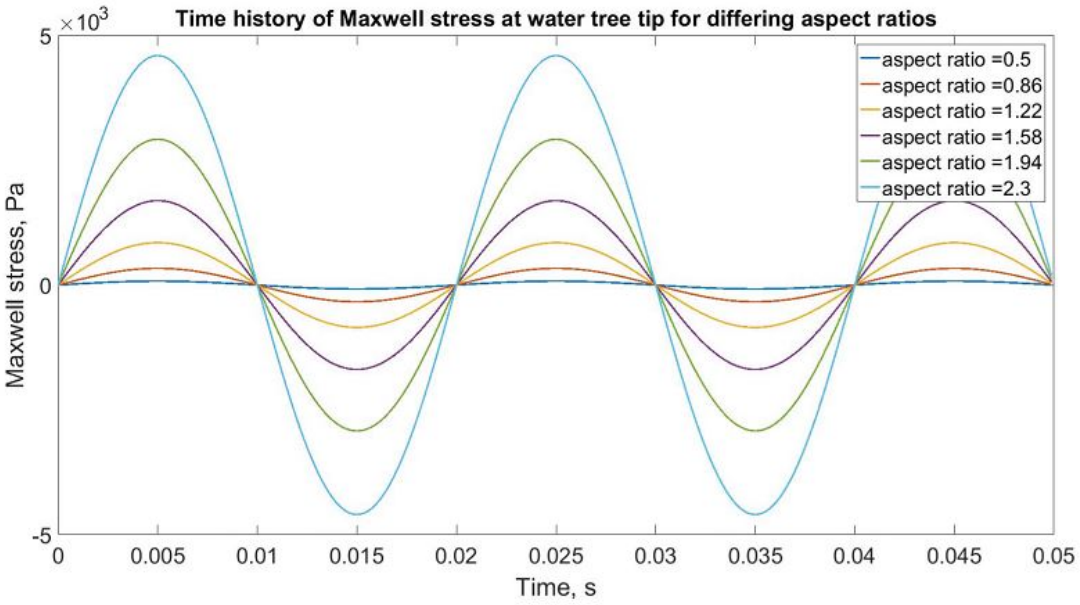

Figure 5.14: Maximum cyclic Maxwell stress at the tip of a water tree

Figure 5.14 shows that varying the aspect ratio of the water tree head can have a significant impact on the resulting Maxwell stress. Furthermore this aspect ratio of the water tree can of course change during the lifetime of the water tree as it propagates. With this changing aspect ratio it is therefore possible that a maximum Maxwell stress can be experienced at any length of the water tree, depending on its aspect ratio. This most conservative case is what is shown in Figure 5.13, where the Maxwell stress is constantly at its maximum, regardless of water tree length, and limited only by the XLPE electrical breakdown strength. In contrast Figure 5.11 illustrates Maxwell stress for a constant aspect ratio of 2, and varying by the tips distance from the cable core. Moving forward this work will assume an aspect ratio of water tree head of 2, but will also include a case of the most conservative maximum Maxwell stress for comparison purposes.

This Maxwell stress is an additional stress that will act at the tip of the water tree as it propagates in the direction of the electric field. This stress time history due to the distorted electric field, is added to the previously calculated mechanical stresses across the insulation cross section due to the dynamics of the cable in response to the environment it is installed in. The next chapter discusses how these two stress types can be combined to produce an estimate for the propagation time of water trees, and

thus a fatigue life estimate of the dynamic cable.

5.5 Chapter summary

This chapter described the work completed to produce a time history of stresses due to the distortion of the electric field within the XLPE cable insulation layer. A finite element model of the insulation layer's cross section was built using ANSYS Maxwell software. An iterative approach was taken to calculate the distortion of the electric field at the tip of a water tree head for varying lengths of water tree. This electric field distortion was then converted to a Maxwell stress by means of Maxwell equations. The electric field distortion, and thus Maxwell stress, was shown to peak at the water tree head and to increase in magnitude with increasing water tree length, i.e. when the tip of the water tree is closer to the dynamic cable's core. This Maxwell stress was shown to be considerably smaller than the previously calculated mechanical stress, but acts over a much more concentrated area at the water tree head. The Maxwell stress follows the same sinusoidal shape and frequency of the operating voltage.

The aspect ratio of the water tree head was shown to act as a stress concentrator and can produce large electric field distortions, limited by the dielectric breakdown strength of the XLPE insulation, 22MV/m. The Maxwell stress was shown to vary with varying water tree head aspect ratios and a theoretical maximum Maxwell stress based on this is provided.

The outputs of the electric field model are the Maxwell stress time histories at the tip of the water tree head. Two scenarios are considered moving forward to Chapter 6; one where the aspect ratio of the water tree head is a constant value of 2 and secondly, the more conservative theoretical maximum Maxwell stress at the tip of the water tree head. This Maxwell stress time history is in addition to the previously calculated mechanical stress time history and is used as an input to Chapter 6 to determine the water tree propagation.

Chapter 6

Fatigue and water tree propagation

6.1 Chapter introduction

This chapter discusses the work completed to model the propagation of a water tree and the subsequent fatigue life of a dynamic cable. An initial assessment of the cable insulation's fatigue life was completed using classic damage accumulation by means of the Palmgren-Miners rule. This analysis focused solely on the mechanical stress as an aggressor for the accumulated damage.

The mechanical stress time history generated as a result of the work completed in Chapter 4, and the Maxwell stress time history completed in Chapter 5, were combined. This combined stress time history is applied to a Paris Law crack propagation model. Paris Law coefficients have been selected from literature, and the propagation of the water tree as a water filled crack has been modelled.

Finally, the water tree propagation was considered on a microscale, with XLPE monomer chemical bond breaking due to the Maxwell stress serving as the water tree propagation mechanism. The time required for the water tree to propagate to a length of potential failure is used as a new estimate of fatigue life of a dynamic cable.

6.2 Damage accumulation

In Chapter 3 the load cases giving rise to the damage of the dynamic cable were analysed, with the outcome being the selection of an environmental load case for analysis, Load Case 1. Following this in Chapter 4 the resulting dynamic mechanical stress time histories were extracted from the cable's cross section at different locations along the dynamic cable's length. The extracted stress time histories were in six degrees of freedom and combined to produce a time history of effective von Mises stress, σ_v.

A number of cycles of differing amplitudes were accounted for and included in the overall accumulated fatigue damage of the XLPE insulation, by means of a rainflow counting procedure. Rainflow counting is a technique that allows for the counting of all stress cycles within a variable amplitude stress loading time history. For this work an algorithm was adapted based on the work completed by [126], allowing for stress time histories such as that displayed in Figure 6.1 to be processed, where the output is the range of each stress cycle and its corresponding mean stress value. Having a stress amplitude (half of the range) then allows for the use of the SN curve, shown in Figure 6.2, to deduce the number of cycles to fatigue failure. Finally the number of stress cycles in the time history are counted and Equation 6.1 is used to deduce the accumulated damage.

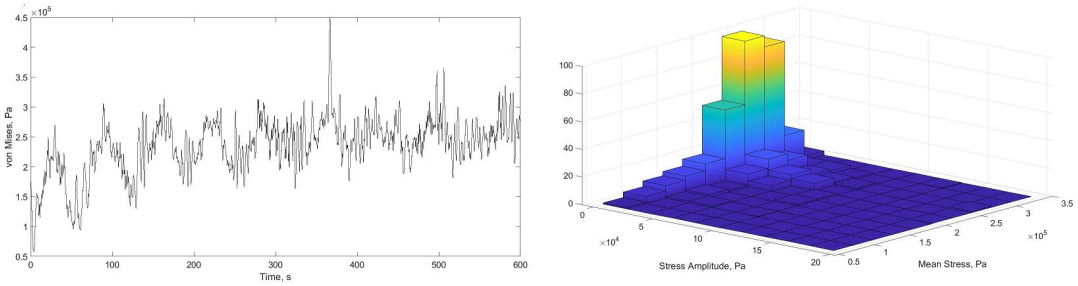

(a) von Mises stress (b) Rainflow count

Figure 6.1: An example von Mises stress and corresponding rainflow count for a cross sectional element during Load Case 1, H_s 4.75m T_z 7.75s at Location 1

Accumulated fatigue damage was calculated using the Palmgren-Miner linear dam-

age rule, Equation 6.1. Further details on the Palmgren-Miner rule can be found within the literature review.

$$D = \sum_{i=1}^{k} \frac{n_i}{N_i} \tag{6.1}$$

Where for k different stress levels and the average number of cycles to failure at the i^{th} stress S_i, N_i is the total number of cycles of S_i to failure and n_i is the number of cycles of S_i that occur. No fatigue damage limit has been included for this work, and therefore all fatigue ranges contribute to the damage.

6.2.1 Goodman correction

Fatigue is not only a consideration of the amplitude of the cyclic stress, but the mean stress in that cycle also plays a role on the fatigue behaviour. Goodman's correction allows for incorporating the mean stress into the analysis according to Equation 6.2 as explained in the literature review. The Goodman correction calculates an effective alternating stress, accounting for this mean stress, allowing for use of an SN-curve with a fixed stress ratio of -1. The effective stress σ_{eff} is calculated and used to read from the SN curve the number of cycles to failure:

$$\sigma_{eff} = \sigma_a \left[\frac{\sigma_{ts}}{\sigma_{ts} - \sigma_m} \right] \tag{6.2}$$

6.2.2 SN Curve

The extracted stress time history can be used to determine the fatigue damage on the dynamic cable's insulation. An example of readily available information on fatigue behaviour of XLPE in terms of the applied cyclic stress and the number of cycles to failure is an S-N curve graph. An S-N curve for XLPE has been found from literature in

[125] and is reproduced in Figure 6.2. This S-N curve has a stress ratio, R, of 0.1, where R is ratio of the minimum applied stress to the maximum applied stress, Equation 6.3.

$$R = \frac{\sigma_{\min}}{\sigma_{\max}} \tag{6.3}$$

Where $\sigma_{\max}$ is the maximum stress in Pa and $\sigma_{\min}$ is the minimum stress applied in Pa.

SN curves are commonly plotted for a constant specific R value. Using Equation 6.3 and the amplitude ratio allows converting of SN curves plotted in one form to another. The amplitude ratio is defined as:

$$A = \frac{\sigma_a}{\sigma_m} \tag{6.4}$$

Where σ_a is the stress amplitude in Pa of a cycle, and σ_m is the mean stress applied in Pa of that cycle, and A and R are related to one another as:

$$R = \frac{1 - A}{1 + A} \tag{6.5}$$

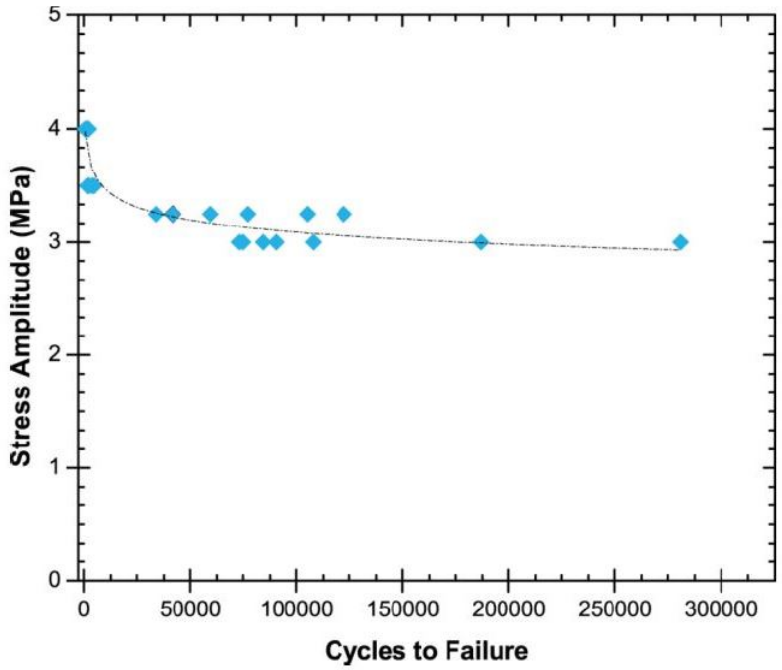

Figure 6.2: SN-curve for XLPE in air at 5Hz with R = 0.1

[125]

The SN curve shown in Figure 6.2 is converted to that of an R value of -1 using Equations 6.3, 6.4, 6.5 and 6.2 and extended to a long number of fatigue cycles of $1x10^8$ is replotted in Figure 6.3.

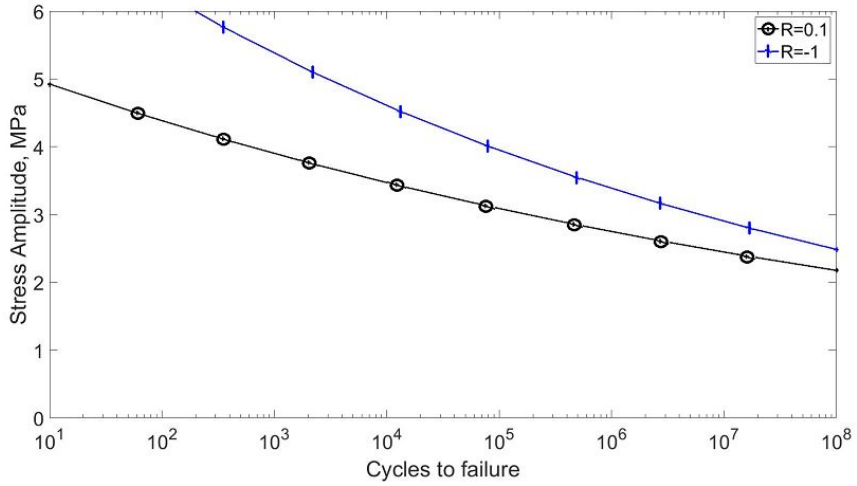

Figure 6.3: Semi log scale replotting of Figure 6.2 with extended fatigue cycles, and differing R values shown

This SN curve and the mechanical stress time histories generated in Chapter 4,

corrected to account for the mean stress using Goodmans, are used to deduce the accumulated fatigue damage using Equation 6.1 on the elements of the insulation cross section.

6.2.3 Accumulated damage cross section distribution

Using the methods described in the previous sections, the accumulated damage across the insulation's cross section due to mechanical stress has been calculated. In Figures 6.4 to 6.7 the accumulated fatigue damage is calculated for each element of the insulation cross section and plotted for each of the investigated locations along the cable length.

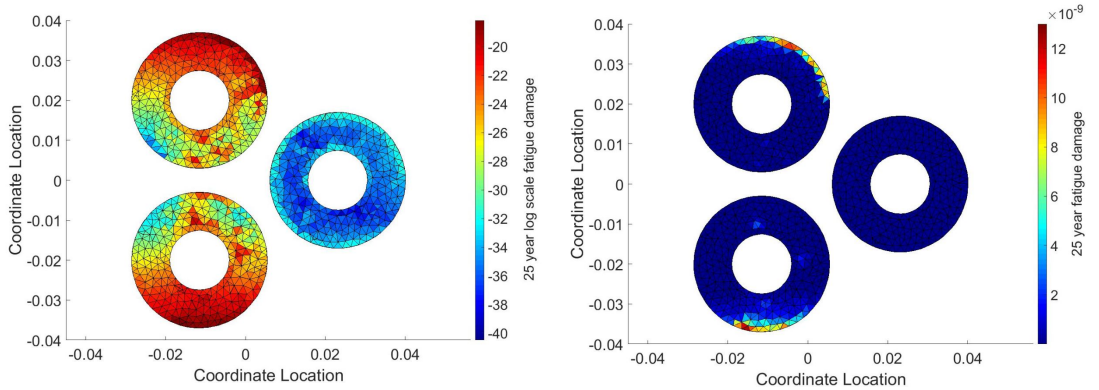

(a) Log Scale (b) Most damaged

Figure 6.4: Accumulated fatigue damage across the insulation cross section at Location 1. a) displays the logscale damage for visualisation, while b) highlights the most damaged element locations (non log), for a sea state of H_s 4.75m and T_z 7.75s.

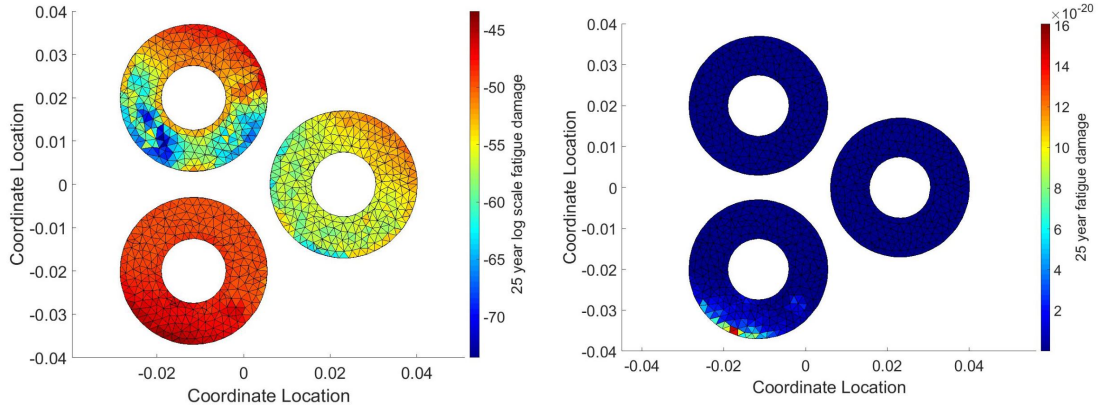

(a) Log Scale (b) Most damaged

Figure 6.5: Accumulated fatigue damage across the insulation cross section at Location 2. a) displays the logscale damage for visualisation, while b) highlights the most damaged element locations (non log), for a sea state of H_s 4.75m and T_z 7.75s.

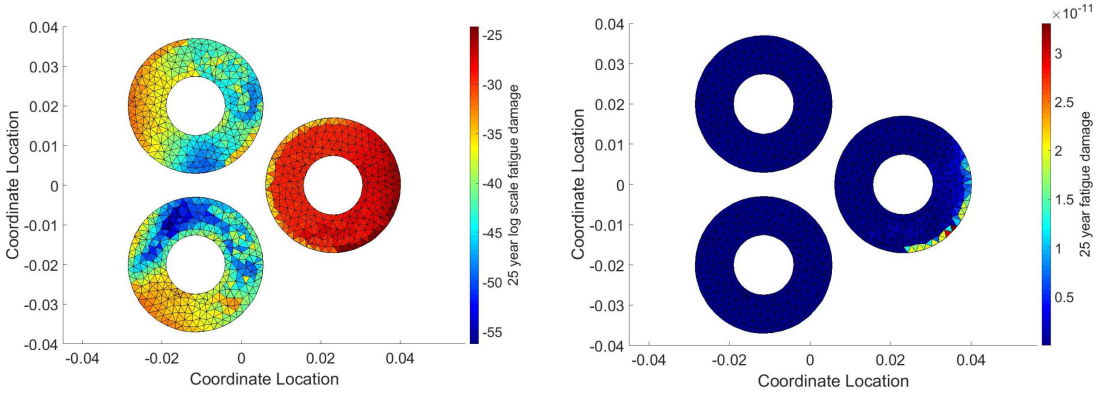

(a) Log Scale (b) Most damaged

Figure 6.6: Accumulated fatigue damage across the insulation cross section at Location 3. a) displays the logscale damage for visualisation, while b) highlights the most damaged element locations (non log), for a sea state of H_s 4.75m and T_z 7.75s.

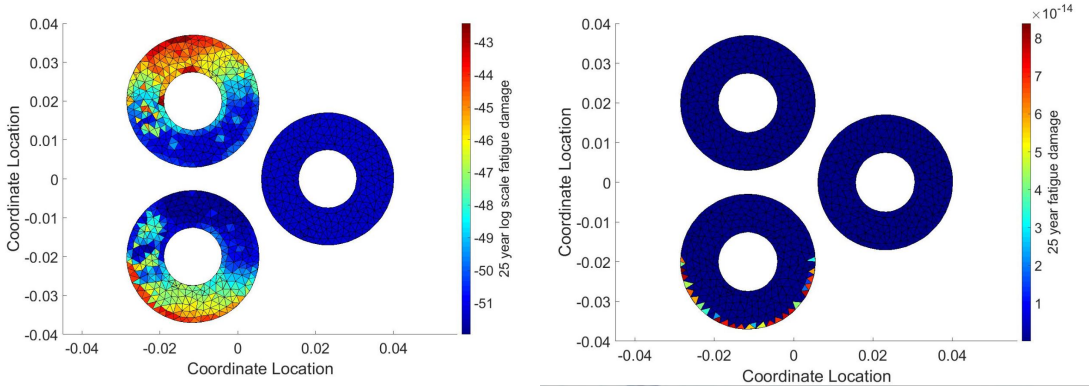

(a) Log Scale (b) Most damaged

Figure 6.7: Accumulated fatigue damage across the insulation cross section at Location 4. a) displays the logscale damage for visualisation, while b) highlights the most damaged element locations (non log), for a sea state of H_s 4.75m and T_z 7.75s.

From Figures 6.4 to 6.7 it can be seen that the accumulated fatigue damage is greatest at Locations 1 and 3. This corresponds to the hang off point where the axial tension is greatest, and a point of the lazy wave configuration where the cable is most bent, see Figure 6.8. In both instances it is seen that the most damaged elements are at the external edges of the insulation layer. These locations of most accumulated damage will serve as initiation points of the vented water treeing. In all instances it can be seen that the accumulated fatigue damage is very small, even after the expected life span of a dynamic cable of 25 years. Table 6.1 shows the accumulated damage on the insulation layers after one year at each location, accounting for the % occurrence of each wave

condition.

From this, the locations of greatest risk of failure on the cable length are identified. Furthermore it shows that the most damaged areas of the insulation cross section are the outside edges. This is of importance as it allows for the assumption that water tree growth will initiate here, i.e. vented water trees that grow towards the core. Further analysis on the estimated fatigue lifetimes of the cable insulation layers for these two most damaged locations, Locations 1 and 3, on the cable follows.

Table 6.1: Accumulated damage at each cable location, accounting for each wave conditions % occurrence

Location	Damage
1	3.64E-11
2	4.35E-21
3	2.26E-11
4	1.08E-16

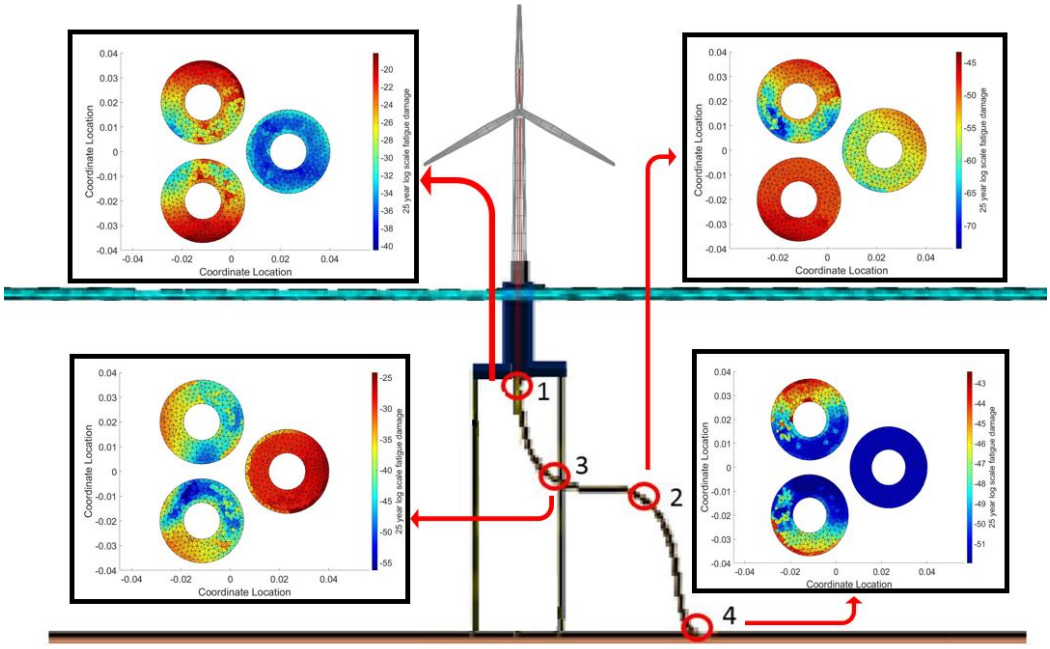

Figure 6.8: Accumulated damage distributions at each location on the dynamic cables length

6.2.4 Fatigue life assessment

In this section the fatigue life, in years, of the cables insulation layers at Locations 1 and 3, due to the mechanical stress caused by the different environmental wave conditions at the site, is investigated. Figure 6.9 shows the accumulated fatigue and corresponding lifetime estimate at Location 1 for both the steady wave condition and then adjusted for the probability of that wave condition occurring, based on Figure 3.3. This is repeated for Location 3 in Figure 6.10.

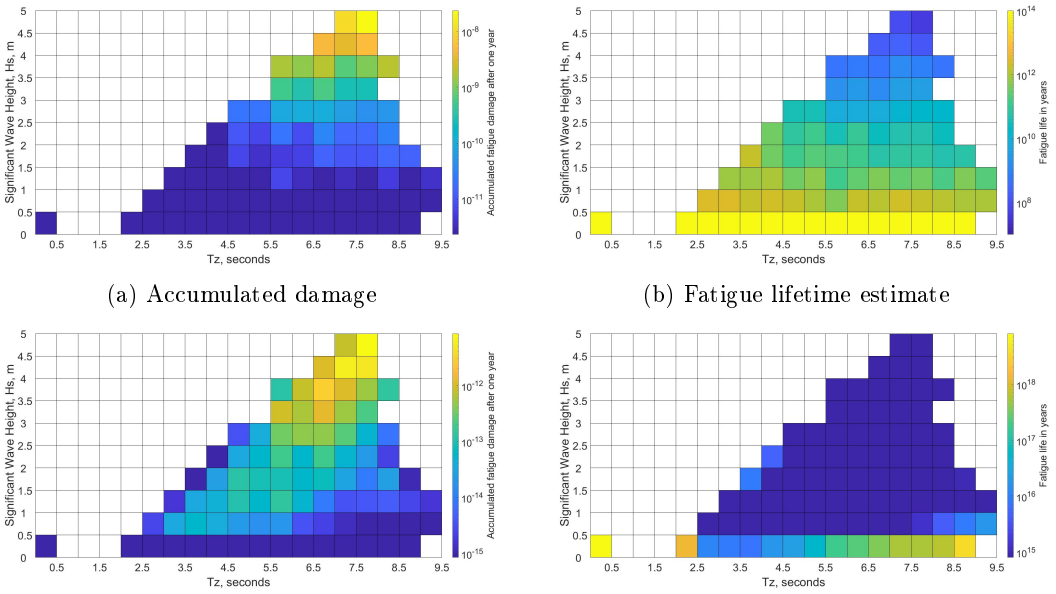

(a) Accumulated damage

(b) Fatigue lifetime estimate

(c) Adjusted accumulated damage

(d) Adjusted fatigue lifetime estimate

Figure 6.9: Spectrum of accumulated fatigue damage on the cable's insulation cross section for differing wave conditions (a), and corresponding fatigue lifetime estimates (b) at Location 1. (c) shows the adjusted accumulated fatigue damage when the probability of each wave condition occurring is included, while (d) shows the adjusted fatigue lifetime estimates.

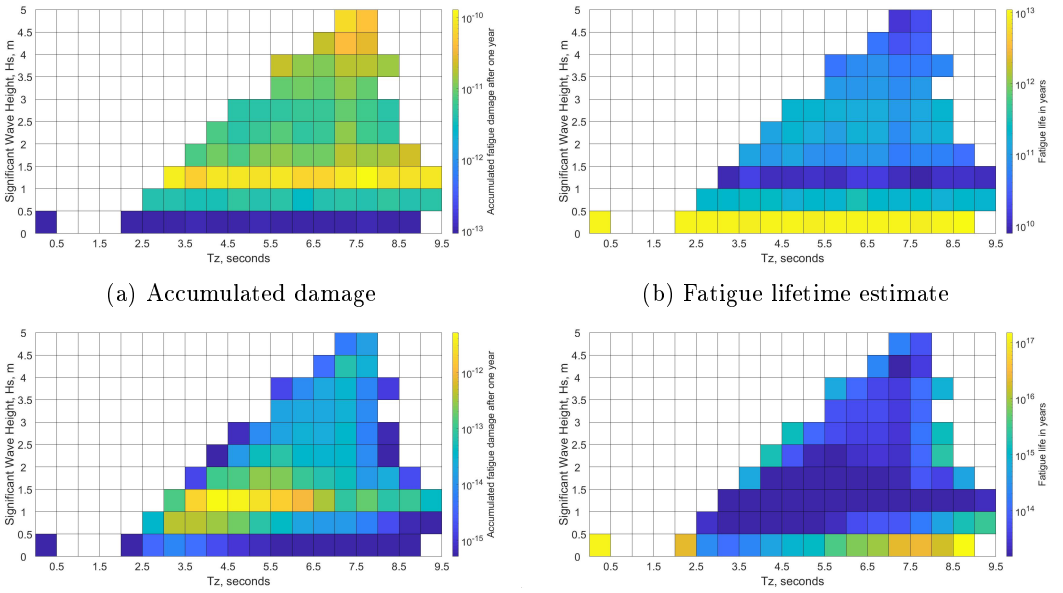

(a) Accumulated damage

(b) Fatigue lifetime estimate

(c) Adjusted accumulated damage

(d) Adjusted fatigue lifetime estimate

Figure 6.10: Spectrum of accumulated fatigue damage on the cable's insulation cross section for differing wave conditions (a), and corresponding fatigue lifetime estimates (b) at Location 3. (c) shows the adjusted accumulated fatigue damage when the probability of each wave condition occurring is included, while (d) shows the adjusted fatigue lifetime estimates.

Looking at Figure 6.9 it can be seen that the damage on the cable's insulation at Location 1 increases with increasing wave height and period. This is because at this location the forces and moments the cable is subjected to are governed by the surge and sway of the floating platform, so whether the platform moves in positive X or negative Y, it will increase the tension on the cable at the hang off point. For clarity, positive X is taken as South (180°) and positive Y is East (90°) in Figure 3.13. The damage at Location 1 is governed by the tension in the cable, which is a factor of the cables weight.

Looking at Figure 6.10 it can be seen that the greatest damages occur with waves having a height of 1.25m. The damage at Location 3 is dominated by the level of the bending of the cable. As previously explained this is due to the wave heights being related to wind speed, and at this wave height the wind speed is at the rated speed of the wind turbine. At this wave height the platform surge is greatest, which causes the greatest level of bending of the cable at Location 3, and therefore the greatest level of damage.

For both locations it's immediately apparent from the results that the insulation will not fail within the lifetime of the cable, giving way to the extremely large fatigue lifetimes.

At Location 1 on the cable length the fatigue life is calculated as $7x10^{11}$ years, whereas Location 3 is calculated as $1x10^{12}$ years. One concern with this is that the mechanism of water treeing can be thought of as similar to a crack propagation. The water tree, or crack, only needs to propagate 60% of the insulation thickness to cause an arc fault and ultimate failure of the dynamic cable. In using the Palmgren-Miners rule which utilises an SN curve, cracks and crazes within the XLPE insulation would not be recorded as a failure; it would only be recorded as a failure when the XLPE sample broke. Therefore while these results show that the insulation would not fail within the operational life of the dynamic cable, using the definition of an SN curve failure, it does not account for cracks and crazes forming within the insulation. This suggests that typical fatigue life estimate techniques would not suffice for the measurement of a dynamic cable's insulation fatigue lifetime. For this reason, a crack propagation method has been investigated to calculate the lifetime required for a crack to propagate across the insulation thickness. The areas of greatest accumulated damage calculated using Palmgren-Miners rule are assumed to serve as the initiation points of the crack, or water tree. The mechanical stress time histories extracted from these most damaged locations are used as the stress time histories to propagate the water tree as a fracture of the XLPE insulation.

6.3 Paris law

Paris Law is a fatigue crack growth fracture mechanic method which describes the relationship between cyclic crack growth rate $\frac{da}{dN}$ and stress intensity range ΔK. Details of Paris Law can be found within the literature review, however the general Equation is reproduced here:

$$\frac{da}{dN} = C\Delta K^m \tag{6.6}$$

Where C and m are Paris Law constants for the material in question.

The Paris Law constants C and m can only be determined experimentally. For this work the coefficients are taken from the plots produced by Pruitt [44] (see literature review) where fatigue crack propagation in hip and knee replacements made of XLPE material are a particular issue. Pruitt also showed that an increased level of cross linking in XLPE makes the material more brittle, reducing its fracture toughness, making fatigue crack propagation an even greater concern. The constants C and m are shown in Table 6.2:

	XLPE
C	0.0004
Slope, m	9.07
$\Delta K_{threshold}$, (MPa $\sqrt{m}$)	0.69

Table 6.2: Paris law constants reproduced from [44]

6.3.1 Contribution of mechanical and Maxwell stresses

In Chapter 4 the planar and shear mechanical stresses calculated were combined to produce the von Mises stress across the elements of the dynamic cable's cross section. This calculation allows for the simplification of a multi-axial fatigue problem into one where a single stress can be used to determine if the XLPE insulation will yield or fracture. The von Mises stress is used as it holds valid for ductile materials, which the

XLPE insulation is, as opposed to the Maximum principal stress theory which is valid for brittle materials. A further simplification that is necessary is to therefore assume a directionality that the von Mises stress acts, so as the fracture mode can be determined. This work aims to model the propagation of a water tree across the insulation thickness, so the crack opening mode, i.e. Mode-I is assumed for the mechanical von Mises stress.

In Chapter 5 the electric field strength distortions in the presence of a water tree across the XLPE insulation thickness was modelled. The Electrostatic pressure was converted to a Maxwell stress that acts at the surface tip of the water tree. This stress acts parallel to the electric field, so in this case would cause fracture of the XLPE by Mode-II.

6.3.2 Combining mechanical and Maxwell stresses

To combine the mechanical stress induced by the installed environment, and the Maxwell stress from the electric field distortions, the stress intensity factors for each individual stress can be calculated and combined. Traditionally, to use Equation 6.6 an equivalent combined stress intensity factor at the water tree tip is calculated. The equivalent stress intensity factor, K_{eq} can be calculated by [93]:

$$K_{eq} = [K_I^2 + K_{II}^2]^{\frac{1}{2}} \tag{6.7}$$

Where K_I is the stress intensity factor calculated from the stress ranges imposed by the mechanical loading and K_{II} is the stress intensity factor calculated from the stress ranges imposed by the Maxwell stress. With the effective stress intensity factor calculated from the combined mechanical and Maxwell stresses the fatigue crack propagation can be deduced.

However, in Table 6.2 the value for $\Delta K_{threshold}$ is taken from literature as 0.69 MPa $\sqrt{m}$. which only holds for Mode-I fracture. Work completed by Campbell and Ritchie [127], on mixed Mode-I and Mode-II fracture, found that for large cracks compared to microstructural dimensions, the pure Mode-I threshold when defined in terms of strain

energy release rate, $\Delta G_{threshold}$, is a conservative, lower -bound estimate of the mixed mode fatigue crack growth threshold. Equation 6.8 shows how $\Delta G_{threshold}$ is directly related to $\Delta K_{threshold}$:

$$\Delta G_{threshold} = (\Delta K^2_{I,threshold} + \Delta K^2_{II,threshold})/E' \tag{6.8}$$

Where E' is Young's modulus for plane stress, or for plane strain, $E' = E/(1-\nu)$ where ν is the Poisson's ratio.

Campbell and Ritchie conclude that for "continuum sized" cracks, i.e. large when compared to microstructural dimensions, pure Mode I threshold, defined in terms of ΔG, is appropriate for mixed mode fatigue-crack growth threshold. Therefore using Equation 6.8 the $\Delta K_{eq,threshold}$ is written as:

$$\Delta K_{eq,threshold} = (\Delta G_{I,threshold} E')^{\frac{1}{2}} \tag{6.9}$$

Therefore, the $\Delta K_{threshold}$ value of 0.69 MPa $\sqrt{m}$, is used as the equivalent stress intensity factor threshold for this work. To allow for this assumption, the initial crack that needs to be present to firstly distort the electric field is assumed to be of an appropriate length to ensure the crack is propagating within the Paris regime. It is assumed this length is larger than the microstructure dimensions, so Equation 6.9 may be utilised. Four differing lengths of initial crack length are assumed for this work; 0.5mm, 1mm, 1.5mm and 2mm.

Furthermore, the frequencies of the mechanical stresses, contributing to Mode I fracture, and the Maxwell stresses contributing to Mode II fracture, differ. The frequency of the mechanical stresses are related to the environment the floating offshore wind platform is installed in, for example the wave periods. The Maxwell stresses are denoted by the electric field frequency. To address this, a simplification is made where a set time period of ten minutes is selected. During this time the stresses are treated individually and the water tree propagation for each scenario is calculated and summed together. This

propagation with both stresses is added to update the initial crack length before the next ten minute iteration begins. It should be noted that the stress intensity factor threshold for both was the $\Delta K_{eq,threshold}$ value denoted by Equation 6.9.

6.3.3 Stress intensity factor order

A key considering with crack propagation is that the stress intensity factor at the tip of the crack is a factor of the applied stress and the length of the crack itself, meaning that the same externally applied stress can produce a different intensity factor for different crack lengths. The stress time history will be split into its cycle ranges and cycle means post rainflow counting, this is of concern as they will no longer be in the order that they appear in the model. However an important property of stress intensity factors is that they are additive, meaning that the stress intensity factor for a complex stress time history can be derived from the addition of each cycle individually. To illustrate this, three test examples of 5 individual stress intensity factors in different orders are outlined in Table 6.3. The crack propagation for each test order is shown in Figure 6.11, where it is confirmed that at the end of each test the crack propagates to the same final length.

Table 6.3: Different test orders of stress intensity factors

$\Delta K(MPa\sqrt{m})$	Test 1	Test 2	Test 3
ΔK_1	0.1	0.1	0.5
ΔK_2	0.3	0.2	0.4
ΔK_3	0.4	0.3	0.3
ΔK_4	0.5	0.4	0.2
ΔK_5	0.2	0.5	0.1

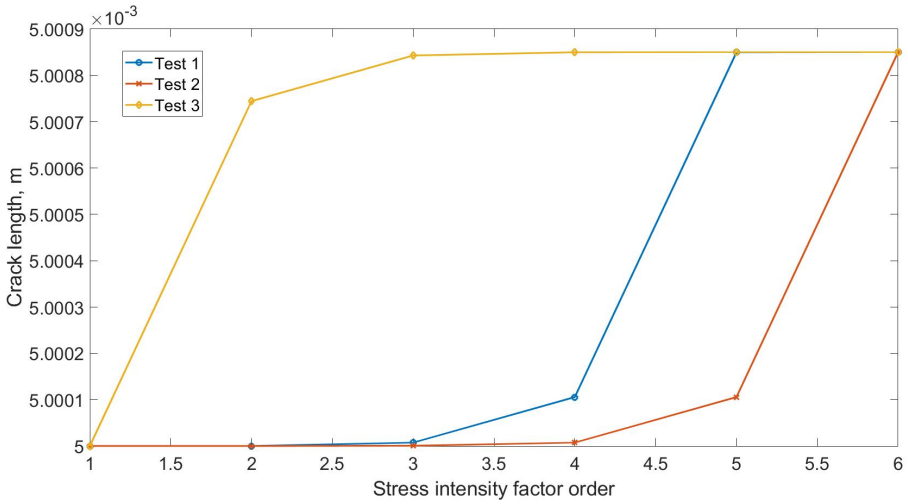

Figure 6.11: Crack propagation for each stress intensity factor stress order

6.3.4 Water tree propagation

The most damaging wave condition at Location 1 can be identified from Figure 6.9, which is a H_s of 4.75m and a T_z of 7.75s; for Location 3 Figure 6.10 is used to show a H_s of 1.25m and a T_z of 7.75s is the most damaging. Using this stress time history generated by the most damaging environment, and the maximum possible Maxwell stress time history illustrated in Figure 5.10, the rate of crack propagation $\frac{da}{dN}$ is calculated by the steps laid out in Section 6.3.2 and Equation 6.6

When using Paris Law it is necessary to assume an initial crack length to ensure that the crack is outside of the initiation phase of crack growth and is propagating within the Paris Law regime. For this work an initial crack or "defect" length is assumed to vary from 0.5mm to 2mm. From the stress time history extracted from the most damaging wave conditions described above, the largest observed $\Delta\sigma$ is 1.6MPa. Using the equations that $\frac{da}{dN} = C\Delta K^m = C(Y\Delta\sigma\sqrt{\pi a})^m$, the largest ΔK that can be produced is 0.14 MPa$\sqrt{m}$, assuming a Y value of 1.12 and an initial defect length, a, of 2mm. This ΔK value is below the assumed $\Delta K_{threshold}$ value of 0.69 MPa$\sqrt{m}$. This means that the maximum ΔK value that can be produced is not large enough to propagate the water tree crack as it is below the minimum threshold value. In fact, continuing with the 1.6MPa $\Delta\sigma$ value the initial defect crack length would need to be

47mm, also known as the critical crack length. As the maximum $\Delta\sigma$ value obtained for the Maxwell stresses is considerably smaller than the value obtained for the mechanical stresses, only the mechanical stresses are included in the above example calculation.

This result suggests that a water tree would not propagate, even with an initial defect length of 2mm. This does not match what is found both in field lifetime of power cables [11], and experimental analysis of the degradation of the XLPE insulation with respect to water tree growth [81], [128]. In these examples water trees are shown to grow parallel to electric field lines, and to propagate in static conditions i.e when only electrical field distortion induced stresses are present. These results do not reflect the governance of the electric field on water tree propagation. Possible reasoning for this is that the Maxwell stresses are not far field stresses as applied in Paris Law, but instead act locally at the water tree tip. Furthermore, the magnitude of the Maxwell stresses are not large enough to propagate a crack or fatigue the XLPE by traditional macroscale means, indicating that the action of the water tree propagation is a microscale issue of the Maxwell stresses acting at the molecular polymer level, and that a macroscopic approach using Paris Law is not applicable. This presumption is explored further in the following section.

6.4 Energy accumulation at tip of water tree

Water tree propagation in the XLPE insulation can be thought of in terms of the kinetic theory of fracture, where the beginnings of the polymer fracture process is the breaking of the chemical or the interatomic bonds. With a consequent number of bonds breaking, a monomer within the XLPE polymer chain will break, causing rupture of the polymer chain. This consecutive rupturing of the polymer chains is how the water tree propagates.

Tao [120] proposed that each rupture of a polymer monomer requires the accumulation of many stress cycles, where one stress cycle is considered as one accumulation of energy. After N cycles of energy, the accumulated energy at the tip of the water tree exceeds the yield stength of the XLPE and a molecular chain is fractured. This energy accumulation is shown in Equation 6.10:

$$0.5\mathrm{V}_0\varepsilon_0\nabla\left(\varepsilon_r - 1\right)E^2 > \sigma_{yield}V_0 \tag{6.10}$$

Where V_0 is the volume of XLPE the energy delivered by the cyclic Maxwell stress is accumulating, and σ_{yield} is the yield stress of the XLPE (8MPa).

6.4.1 Polymer monomer bond breaking

To break a monomer within the polymer chain lying across the path of the crack, the energy supplied will need to exceed the yield strength of the material, or alternatively can be thought of as the energy needed to break the chemical bonds. This is similar to the work completed by Lake and Thomas [97], where the energy required to propagate a crack is the energy per unit area required to produce a new surface, similarly calculated from the strength of the chemical bonds of the monomer, neglecting secondary forces.

This energy required for new surface, T_0, remains relatively constant, suggesting it is a property of the primary bond strength. T_0 however is considerably larger than the average disassociation energy of the C-C bonds within a polymer monomer. For

example, T_0 for the polymer isoprene is 50Jm^{-2}, whereas the average C-C bond disassociation energy is 5x10^{-15}Jm^{-2}, and if the average cross sectional area of a monomer unit is 2.5x10^{-19} m^2, calculating T_0 on this basis produces a considerably smaller value of 2Jm^{-2}.

The reason for this discrepancy is based around the mechanical structure and cross linking of the polymer chains. Forces the polymer is subjected to, or energy, are transmitted via the cross links, so to mechanically break a particular bond all the bonds within a particular polymer chain need to be subjected to this breaking force. If the energy required to break one monomer unit (which contains several bonds) is taken as $E_{monomer}$ and in the polymer chain are n monomers, then the energy required to fracture the chain will be approximately $nE_{monomer}$, noting that only one monomer unit will be broken, thus propagating the crack, or water tree, one monomer length. The kinetic diameter of an ethylene monomer is taken as 390pm. The differences between isoprene and ethylene coming from their differing chemical structure, isoprene having a C=C double bond in its repeating unit shortening the C-H bonds and the C-C bond, while also having more carbon atoms in the monomer backbone. Figure 6.12 shows the two chemical structures for comparison.

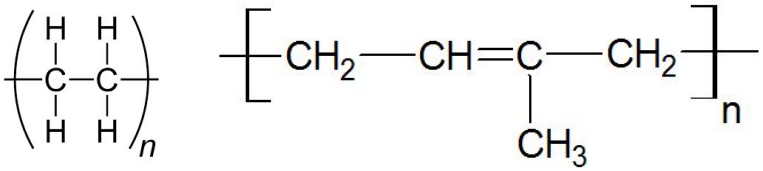

(a) Polyethylene (b) Isoprene

Figure 6.12: Chemical structure of polyethylene compared to polyisoprene

With this information considering crack propagation in terms of bond breaking energy requirements, Equation 6.10 can be used to estimate the energy needed to break one monomer of the XLPE insulation. After breaking a single monomer, the crack will propagate one monomer diameter, which for polyethylene is taken as 390pm.

6.4.1.1 Water tree propagation and fatigue life estimation

To consider the water tree propagating with regards to the Maxwell stresses as a microscale application, some information is needed to allow for use of Equation 6.10, shown in Table 6.4. The water tree growth is considered in ten minute lengths to match the time length of the mechanical stresses produced from the Local model. The Maxwell and mechanical stress time histories have different frequencies, so the water tree growth per ten minutes is calculated for both, these propagations are summed, and added to the water tree length for calculation of the next ten minutes, and repeated. The far field mechanical stresses propagation of the water tree remains calculated by Paris Law.

Table 6.4: Table of information for calculation of energy accumulation for a ten minute duration by the Maxwell Stress at water tree tip.

Variable	Value
Frequency	50 Hz
Stress cycles per 10 min	30000
Maxwell stress cycle amplitude	4.93 kPa
Monomer diameter	390 pm
No. monomers broke per 10 min	18
Water tree propagation per 10 min	7.02 nm

When the Maxwell stresses are considered as a microscale application of monomer bond breaking, the water tree propagates more readily. Furthermore the increasing crack length, a, allows for greater stress intensity factors to be calculated by the mechanical stresses, further accelerating the propagation. Figure 6.13 shows the water tree propagation for the combined mechanical and electrical stress for multiple initial defect size scenarios. As expected, a larger initial defect size results in a shorter time for a water tree to propagate to a cable failure length.

Figure 6.14 shows water tree propagation for combined mechanical and electrical stress,

assuming a constant water tree head aspect ratio of 2. Again it can be seen here that a larger initial defect size results in a quicker rate of water tree propagation.

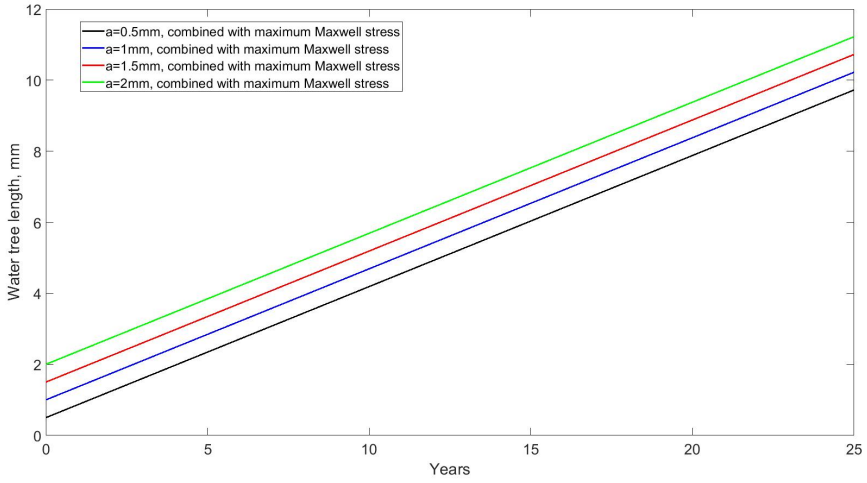

Figure 6.13: Water tree length at Location 1, after years operation in Load case 1, H_s 4.75m and T_z 7.75s with most damaging Maxwell stress applied, for varying initial defect sizes.

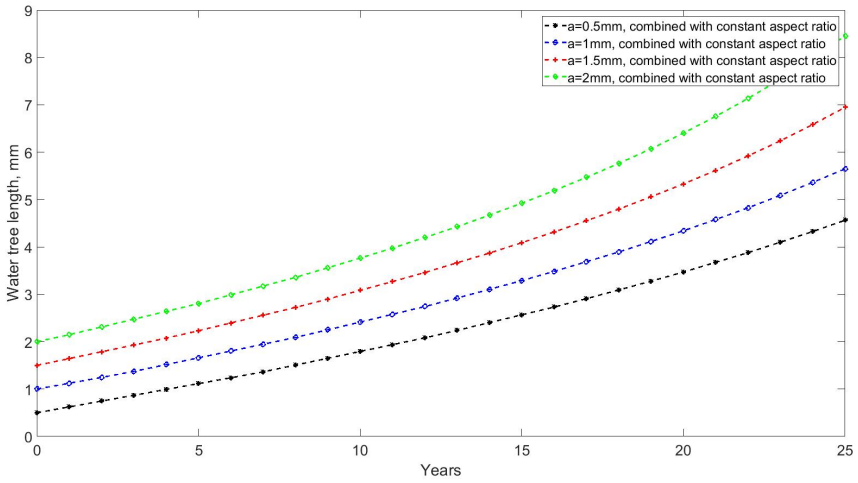

Figure 6.14: Water tree length at Location 1, after years operation in Load case 1, H_s 4.75m and T_z 7.75s with Maxwell stress applied for a constant water tree head aspect ratio of 2.

As can be seen from both Figures 6.13 and 6.14 when compared to the previous water tree propagation results by Paris Law, the water tree propagation is dominated by the monomer rupturing by the microscale Maxwell stress. The microscale monomer rupturing model predicts failure of the cable in 11 years in the maximum Maxwell stress

case, or 19 years in the constant aspect ratio case. This shows that the water tree propagation is dominated by the distortion of the electric field. This can offer an explanation as to why water trees grow parallel to the electric field lines, as they are driven by it.

The dynamic mechanical stresses have been shown to have minimal impact on the propagation of vented water trees growing from the insulation screen, matching experimental work conducted by Ilstad et al. [129]. It should noted however that Ilstad found that mechanical stresses did increase the number of vented water trees growing from the conductor screen, but had minimal impact on their length. Vented trees growing from the conductor screen are not considered in this work as they are thought of as self limiting as they propagate away from the core, and therefore unlikely to grow to cause an arc fault. Finally, this work confirms that after a water tree is initiated by means of a defect, or initial crack within the XLPE, the water tree will propagate at a rate predominantly determined by the local electric field at its tip.

An explanation as to why the mechanical stresses have minimal impact is offered in how they are applied to the XLPE. Within Paris Law the mechanical stresses are applied as far field stresses on the macroscale, and the stress intensity factor at the water tree tip is calculated ΔK. However this far field stress will be acting upon a much greater number of polymer chains. As the polymer chains in XLPE are linked by the cross linking this allows for transferring of the stress, and to accumulate the energy to break one monomer, all the monomers in this much larger area need to be subjected to this breaking force, therefore a much greater quantity of energy is required. The stresses induced by the electric field distortion are instead applied on a microscale, as the entire area the electric field distortion acts upon is approximately 3μm, and applied at the water tree tip. The electric field distortion has been shown to be a property of the distance the water tree tip is from the dynamic cable's core, and the aspect ratio of the water tree. To lean on the side of conservatism the maximum induced Maxwell stress acting on the water tree tip is chosen to determine the fatigue life of the dynamic cable's insulation, however it is likely that the true fatigue lifetime would exist above

this limit. Further to this it has been assumed that all of the energy per Maxwell stress cycle is accumulated at the water tree tip, for both constant aspect ratio and maximum Maxwell stress cases. In practise this would not be the case as there would be some dissipation of the energy, for example the semi-crystalline structure of the XLPE would allow dissipation of the energy along its crystal edges. Therefore this assumption of 100% energy accumulation would over predict the rate of the water tree propagation. However, this work did not include the thermal impacts on water tree propagation, nor the impact of the force on a water droplet in an electric field, i.e micro water jetting, both of which would accelerate water tree propagation, so assuming no energy dissipation is thought of as a means to balance this.

While the mechanical stresses have been shown to have limited impact on the propagation of water trees, this work has still assumed that the areas of highest mechanical stress would serve as initiation point for water treeing. Furthermore the mechanical stress calculation work can serve as a starting point for other components of the cable's cross section where mechanical stress is of a greater concern, for example the armouring wires and the screens.

Finally, Figure 6.15 compares the time in years for the water tree to propagate to a length to cause failure for two scenarios; the combined mechanical and maximum Maxwell stress driven water tree propagation, and the combined mechanical and Maxwell stress derived from an aspect ratio of 2 driven water tree propagation.

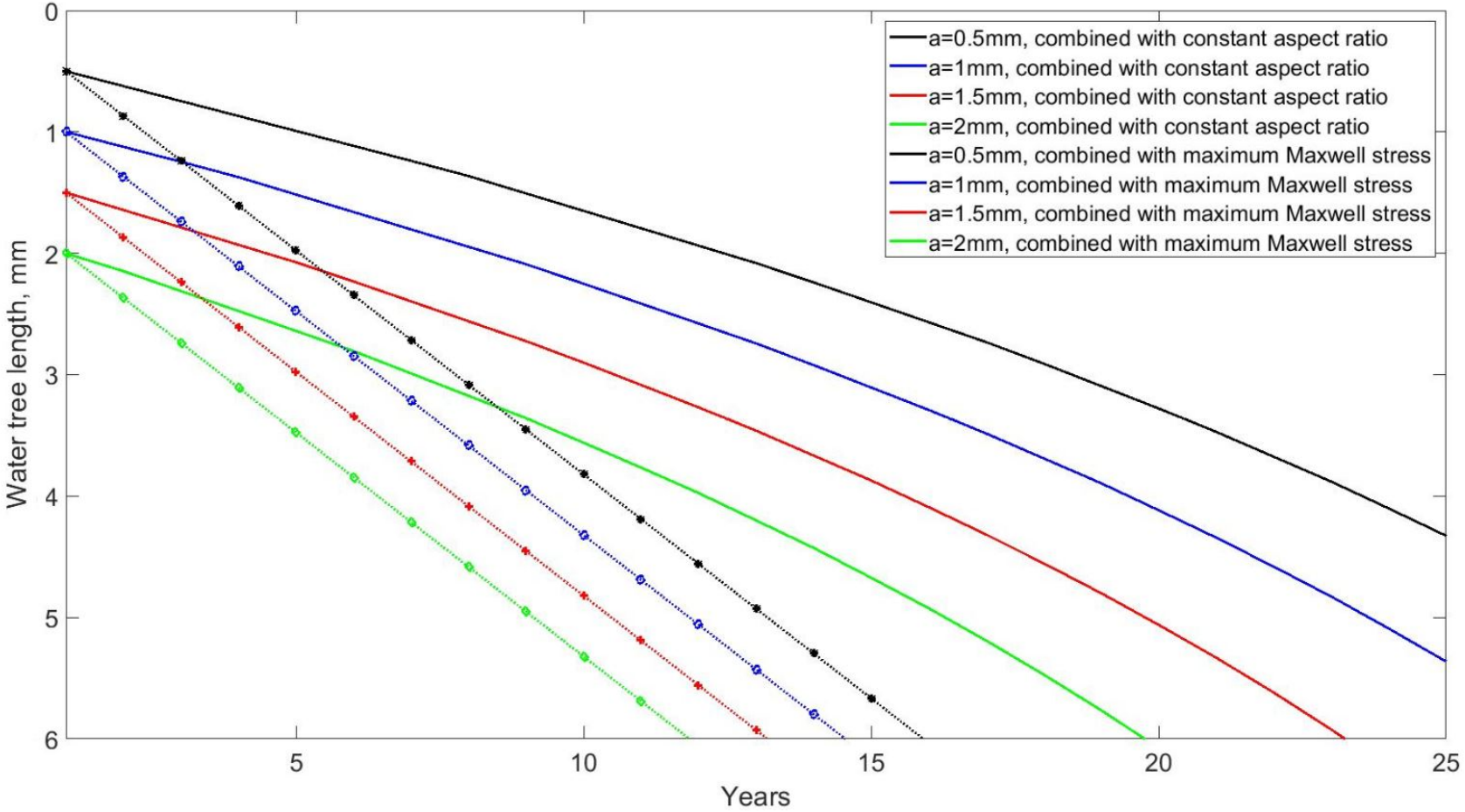

Figure 6.15: Comparison of water tree length at Location 1, after years operation in Load case 1, H_s 4.75m and T_z 7.75s with most damaging Maxwell stress applied or constant aspect ratio induced Maxwell stress applied for varying initial defect sizes.

6.4.2 Comparison of water tree propagation model to experimental data case study

The result of the water tree propagation model discussed has been compared to experimental data previously presented within literature. As an example, Figure 6.16 shows the experimental set up by Sun et al. [128], to determine the growth of water trees within XLPE of differing concentrations of water tree retardant chemicals. This work has focused on non water tree retardant XLPE, and so the results of the sample with 0% retardant shall be compared accordingly. Table 6.5 shows the testing conditions to complete the model comparison. It should be noted there are no dynamic stresses applied in this experiment and so water tree propagation was a product solely of the electric field distortion.

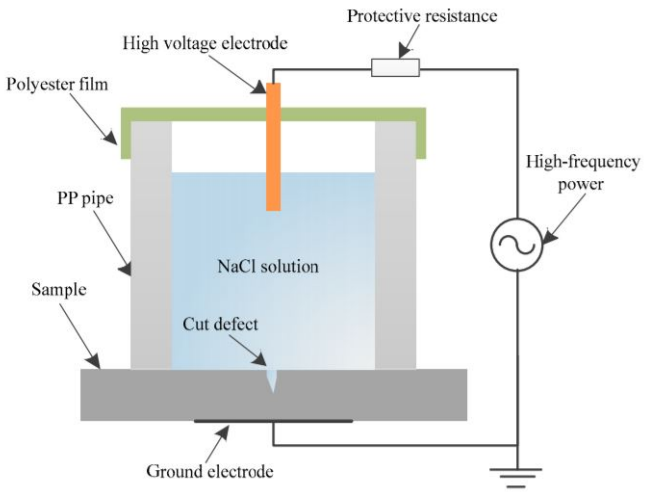

Figure 6.16: Experimental schematic of the water knife electrode system, reproduced from [128]

Table 6.5: Table of experimental conditions

Variable	Value
Frequency	3 kHz
Duration of test	7 days
Applied voltage	4 kV
XLPE sample thickness	2mm
Blade defect size	40mm x 0.03mm

The electric field distortion within the XLPE has been modelled and the peak in electric field strength at the tip of the blade defect is shown in Figure 6.17. The aspect ratio of the water tree, or the shape of the water tree head, will also have an impact on the electric field distortion [125] [121], for this the electric field strength will vary between the peak shown in Figure 6.17 of 1.5MV/m and the maximum of 22 MV/m. To match the conservatism of the model the maximum value has been chosen, and thus the corresponding maximum Maxwell stress. Table 6.6 compares the results from the experimental and those predicted by the model.

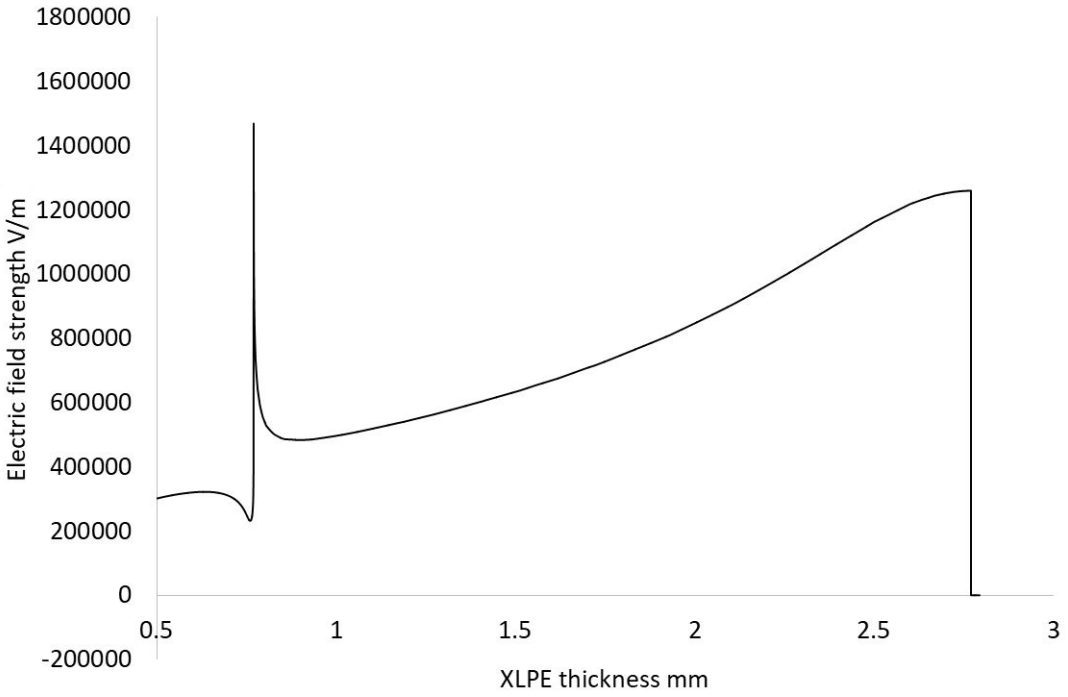

Figure 6.17: Electric field strength distortion due to blade defect, peak shown at blade defect edge face of 1.5MV/m.

Table 6.6: Comparison of experimental water tree length and model water tree length.

Source	Water tree length μm	Percentage difference
Experimental [128]	316	
Model assuming 100% energy accumulation	436	+38%
Model assuming 80% energy accumulation	349	+10%

As expected the model over predicts the propagation of water tree length by 38%. This is explained due to the assuming of the maximum electric field strength distortion at the tip of the water tree, and by having no energy dissipation within the XLPE. When 80% of the energy is assumed to accumulate the propagation over prediction reduces accordingly, to 10%.

6.5 Chapter summary

Within this chapter the previously calculated mechanical and Maxwell stress time histories were used to determine the damage on the dynamic cable's insulation layers and

to model the propagation of a water tree to the point of cable failure.

Initially the mechanical damage was used with Palmgren-Miners rule to determine the accumulated damage on each element across the cable insulation's cross section. The calculated accumulated damage was shown to be very small, leading to excessive large fatigue lives of $7x10^{11}$ years. Locations 1 and 3 were shown to experience the greatest level of damage, with Location 1 experiencing the overall greatest damage. Damage on the insulation layers was shown to increase with increasing significant wave height at the hang off point, however accumulated damage was shown to peak at the 1.25m significant wave height peak at Location 3. Finally the damage was displayed across the cable's insulation cross section to allow visualisation of which areas experience the greatest damaged. These areas were assumed as the points of water tree initiation, and the stress time history of these specific elements was then used for water tree propagation by Paris Law.

Paris Law was then used to model the water tree propagation for multiple initial defect lengths. It was shown that a water tree would not propagate using Paris Law as the maximum calculated stress intensity factor was below the threshold required for crack propagation. As a result it was decided that a macroscopic approach was not applicable, as this did not match what is found in field or experimentally. Therefore, the propagation was then considered as a microscale application of the Maxwell stress in the form of a polymer chain monomer rupture by energy accumulation model.

For multiple initial defect lengths the water tree propagation was modelled, resulting in the water tree reaching a length to cause arc failure within 11 years for an initial defect of 2mm and the maximum Maxwell stress applied. When the propagation per ten minute cycle due to monomer rupturing is added to the defect length to deduce propagation by Paris Law due to the mechanical stress, it is shown that the propagation is entirely governed by the Maxwell stress rupturing the monomers. The model result was compared with experimental work found in the literature, and was found to over predict

water tree propagation by 38%. Explanations provided for this over prediction were the assumption of 100% energy accumulation at the water tree head which would not occur in practice as some energy would dissipate. When 20% of the energy imparted by the Maxwell stress is assumed to dissipate, the over prediction reduces accordingly to 10%.

The conclusions from each chapter are then listed in Chapter 8.

Chapter 7

Discussion

7.1 Chapter introduction

In this chapter the results from the previous chapters are summarised. These results are interpreted, and some discussion is given to their academic and industrial relevance. From this discussion the conclusions of this research project are drawn.

7.2 Discussion

A reliable electrical infrastructure is essential to maximise the availability of offshore wind turbines. As the offshore wind industry continues to move towards larger turbines offshore and into deeper waters, the possibility of floating offshore wind turbines has become a reality. The failure of offshore cables has been identified as one of the greatest risks to continuing the lowering of the LCOE of offshore wind. As floating offshore wind poses new installation configurations of the cable and exposes it to the dynamics of the marine environment, there is a need to develop a better understanding of the failure mechanisms of these cables, in order to prevent and predict when failure will occur.

One of the failure mechanisms of subsea cables is a process known as water treeing. The concern with water trees is that with current technologies they are unable to be detected during the cable's lifetime, resulting in an otherwise healthy cable failing unexpectedly. In static testing water trees have been shown to propagate due to electrical

loading, with tensile mechanical loading increasing their propagation. The overarching aim of this research project was to develop an electrical-mechanical coupled model which can model and predict the growth of water trees within the insulation of a dynamic subsea cable installed in a floating wind configuration. This in turn is then used to predict when a dynamic cable will fail due to water treeing.

To achieve this aim, the work was divided into a series of objectives which were addressed in the individual chapters of this thesis. Chapter 3, the global model chapter, produced a global model of the floating wind platform with attached dynamic cable to determine the environmental forces that the marine environment would subject the dynamic cable to for a series of differing load cases. In Chapter 4, the local model, a finite element analysis of a dynamic cable's cross section was developed, and the force history output from the global model was transformed to a stress time history across the cross section of the dynamic cable's insulation layer. Within Chapter 5, the electric field model chapter, the distortion of the electric field in a 66kV AC cable's insulation in the presence of a water tree was modelled. This electric field distortion was then transformed to the Maxwell stress that would occur at the tip of a water tree. In Chapter 6, the fatigue assessment and water tree propagation chapter, the fatigue life of the insulation layer was investigated initially in terms of damage accumulation across the cross section, then in terms of the time required for a water tree to propagate to a length that would cause failure of the dynamic cable due to the applied mechanical and electrical stresses. This water tree propagation was initially investigated as a combined Paris law crack propagation of the mechanical and Maxwell stresses, then the water tree propagation was instead considered on a micro scale energy accumulation to overcome the intermolecular strength of the XLPE monomers. This model prediction of water tree growth rate was then compared to existing experimental data of water tree lengths from the literature.

Within Chapter 3, a global model of a floating offshore wind turbine and platform with its attached dynamic cable was constructed. The dynamic cable modelled was

based upon a dynamic cable from a historic oil and gas installation. The floating platform was that of a tension leg platform with the NREL 5W reference turbine installed on top. This is different to the majority of the floating offshore wind platforms currently installed. As listed in Table 2.1 the majority are semi-submersible designs, the second most common is the spary buoy design and only three projects currently utilise a TLP design. The reason why a TLP was chosen was due to it being akin to the platforms used in the oil and gas industry, where the dynamic cable modelled originates from. Further to this the TLP has some advantages over the other platform designs due to its stiffness, which results in less dynamics imposed on the cable. This work however was not designing or optimising a floating offshore wind turbine, nor was it an optimisation exercise on the installation configuration or length of the installed cable. Equation 3.15 was used to estimate the cable length in a lazy wave configuration. The environmental loads were applied in the global model to be perpendicular to the cable length trajectory to give a more damaging arrangement for conservatism. However, this was the limit of the optimisation work. This will have an impact on the results obtained; any change to the cable installation layout will change the force responses on the dynamic cable. For example, if the cable trajectory angle is changed to be in line with the current tidal stream, this will reduce the forces that the cable is subjected to. Furthermore, the choice of basing the dynamic cable on a historic oil and gas cable, due to available information, limits the results as this cable may be over-designed and differ to designs chosen for floating offshore wind. In future this work could be repeated, using the methodology described, but instead including an optimisation of the cable length and installation arrangement to reduce the forces that the cable is exposed to, based on a cable design for floating offshore wind. The results of such an optimisation exercise could be then used to make recommendations on dynamic cable installation configurations for the floating offshore wind industry.

Key assumptions made with respect to the dynamic cable were the values used for its axial and bending stiffnesses. Ideally these values would be determined experimentally for the specific cable being modelled, and supplied by the cable manufacturer. For

this work these values were not supplied, and were instead calculated and verified by methods laid out in the literature. Furthermore, the stiffnesses were assumed a property solely of the cable's armouring wire layers. These values could have been calculated experimentally, however to do so would require a commercial business need from ORE Catapult, which was absent from this work as it was deemed that calculated results would suffice for initial estimates. This is a crucial assumption of the work, and applies some constraints to the results as the stiffness values of the cable deems much of it's dynamics. In future, an improvement of this work would be to confirm experimentally the stiffness values of the dynamic cable to be used in the global model. Another assumption made for the Global model was the absence of VIV acting on the dynamic cable. In future if the dynamic cable to be modelled is not double or quad armoured then this assumption would no longer hold as the cable would not be torque balanced.

Four environmental Load Cases were developed based upon DNVGL-ST-0019 and applied to the global model. The force and bend moment outputs from the global model at four points along the dynamic cable's length were extracted. The four points being; the hang off point at the base of the turbine platform, the beginning of the Lazy-S bend configuration, the end of the Lazy-S bend configuration and the cable touch down point on the seabed. These four locations were chosen based on the work completed in Section 3.5.3 showing that these locations experience the greatest magnitude of forces and bend moments and thus accumulated damage. This section could be expanded further in future works with a greater focus on tracking down the location of potential cable failures along the installed cable length. This would benefit industry greatly as one of the current key challenges is not only identifying when a cable might fail, that the research question of this work focused on, but also where a cable might fail. This work touched lightly on addressing this "where" question, in Section 3.5.3, but there is considerable future work that could be completed here that was out of the scope of this research project.

The software OrcaFlex was used to construct the global model of the floating offshore

wind turbine and its attached dynamic cable. This proved a good decision, as not only is OrcaFlex widely used and accepted within the industry, but also for its ease of coupling with FAST; to capture the aerodynamics of the turbine and couple this with the hydrodynamics acting on the floating platform. So successful is this link, that since completion of the work on the global model, Orcina has released a latest edition, 10.3a, which has introduced a new turbine object that includes functionality to model the generator, gearbox, pitch controller and rotor. Blades can be modelled as rigid bodies or can be flexible, utilising a structural model derived from that of the line object. This allows for modelling an offshore wind turbine without the need to be coupled with FAST. Future work can take advantage of this, as one of the main challenges of this work was the computational resource that the OrcaFlex-FAST link demanded, which drastically increased modelling run times. Furthermore, it offers the opportunity for a simple verification exercise of the Global model results presented in this work.

From the Global model results, a peak in force and bend moment output was observed at a significant wave height of 1.25m. This was explained due to the wind velocity being correlated to significant wave height, and a wave height of 1.25m corresponds to the rated wind speed of the NREL 5MW reference turbine. Here the thrust force on the turbine will be greatest, causing the platform to surge to its maximum, and a corresponding peak in bend moment and force experienced by the dynamic cable. While this result can be explained, it does highlight the impact of one of the assumptions made during the construction of the global model. While environmental data could be found for wave and tidal resource at the chosen offshore site, wind data was not available. Instead wind data was then based on a hind cast model that correlated wind speed to wave height. Ideally in future works a site would be chosen where raw wind data can also be obtained.

The overall output from the global model chapter were the ten minute time histories of forces and bend moments extracted from each location on the cable's length. These were then used as inputs to the local model chapter to determine what stress the applied forces and moments induce on the cross section of the dynamic cable. While this

was the extent of the usage of the global model for this work, it does have applications in other industries. The methodology presented here can be used to construct a global model of a TLP used in the oil and gas industry, to determine the dynamic mechanical stresses on the associated umbilical cables. Further to this, any floating platform will require dynamic cables to be suspended in the water column. Therefore this work can be used as a starting point for modifications to be made to make it applicable to wave energy converters and floating tidal technologies, and determine the mechanical damage to their associated dynamic cables.

With the completion of the global model, a number of objectives of this research project are realised. Specifically, a resource assessment of the site is complete and used to develop a series of load cases for the global mode. A global model of a TLP was constructed with its attached dynamic cable, the outputs of which are the time series of forces and bend moments that the dynamic cable is subjected to. The completion of these objectives allowed for progression to the next section of this work; developing the local model of the dynamic cable's cross section.

The local model was a finite element analysis of the cable cross section built using ANSYS Mechanical software in Chapter 4. This local model was used to allow application of the F_x, F_y, F_z, M_x, M_y and M_z force/moment response output from the global model to determine the stress exerted on the insulation layers of the cross section. As this work is ultimately being used to model water tree propagation within the insulation layer, this layer of the cable cross section was the focus. However, any component of the cable's cross section can be analysed for the mechanical stresses exerted on it. Therefore, this work has wider applications outside of its original scope. If new cable designs are considered with different material choices of screens, cores or armour wires, the methodology presented here can be used as a starting point for assessment of their dynamic performance in future work.

Within the global model an assumption was made that the armour wires determined

the stiffness of the dynamic cable, as discussed before. Further to this, the armour wires were assumed to always remain within stick state and not slide over one another. The stiffnesses were calculated based on work completed by Raoff [13] and Chen [14] for bending and axial stiffness respectively. These stiffness calculations account for the helical structure of the armouring wire, which for this work the helical angle has been assumed to be 18°. For the local model this assumption that the armour wires remain within stick state was carried from the global model. The carrying of this assumption allowed for simplification of the armour layers to thin walled tubes based on work completed by [12], which again is based on the assumption that the cable armouring wires remain within stick state. These assumptions based on numerical work and assuming the cable remains within stick state, and simplifying the armouring layers to thin walled tubes limits the results obtained. In future work, the local model can be further developed to contain a level of sophistication that would also have the helical layout of the armour wires modelled. This would allow for modelling of armouring wire slipping.

A finite element analysis, FEA, of the cable cross section was constructed using ANSYS Mechanical software. This proved an effective method to determine the interactions between different components of the dynamic cable's cross section. A 0.5 metre 3D length of the dynamic cable was built within ANSYS. A length of 0.5m was chosen as this was the same length as the sections of the lumped mass model of the cable within the global model. This 3D model consisted of two equal lengths of 0.25 metres glued together at their centre. The purpose of this was to allow for a flat surface of the cable cross section exactly at its midpoint. This was done to allow for extraction of results at the cross section at the exact mid point of the cable length. As this is a 3D model, and therefore 3D elements are used in the model, the key benefit of using the glueing technique is that it allows for a flat surface that can be further refined and modelled in a 2D sub-model. If this technique is not used then sub modelling on at flat 2D surface at the midpoint is not achievable. To clarify further, the ANSYS local model was constructed using Boolean operations where the two cable lengths were "glued" together at their ends to form the overall cable volume. Using the Boolean operations within

ANSYS, when volumes are glued together they maintain their individuality, i.e they are not added, and therefore do not share nodes. They instead are joined using constraint equations and become connected at their intersection.

Submodelling uses two separate models; the previous generated 3D model of the cable 0.5m length segment, and the 2D model of the face of the cable's cross section at its midpoint. The initial 3D model was used to transform the applied loads from the global model to local deformations, the sub model in turn then included the local geometric details with the more refined mesh density. As the sub model includes the geometric details from the initial 3D model, this was an effective way to ensure materials properties including stiffness are maintained.

To save on computation expense a linear superposition of the FEA local model was completed within Matlab as opposed to completing a transient dynamic analysis with ANSYS as described in Section 4.4. Using this model the three planar and three shear stress time histories were calculated for every element of the insulation layer's cross section. These six components of the stress tensor were combined to calculate the von Mises stress time history of every element of the insulation layer's cross section. The von Mises stress is a representation of the effective stress produced by a combination of the tensile, compression, bending and shear loading, such as in this case. The von Mises stress criterion provides a viable general value of the distortional energy stored in an isotropic material before it will begin to fail at a value known as the yield strength, σ_y. The von Mises stress, σ_v, can be used to predict yielding of an isotropic material which is subjected to complex loadings, such as a dynamic cable. A disadvantage found of the linear superposition was one related to the boolean operations employed in the original ANSYS FEA model. As the two glued faces at the cable cross section mid point did not share nodes, and the two glued volumes maintained their individuality, this resulted in some interactions that were not accounted for in the linear superposition within Matlab. While it was found that the ANSYS model and the linear superposition shared the same stress distribution across their cable cross sections, it was seen that

there was the general under prediction by the linear superposition compared to the ANSYS model. The average % difference between the two was an under prediction of 9.6%. The greatest % difference of a cross section element was 12.8% under prediction. An average percentage difference of 9.6% has been accepted as reasonable to allow for use of the linear superposition within Matlab of the dynamic analysis to drastically reduce computational expense. Further reasoning allowing for acceptation of this result was that the additional interactions, generating the higher stress in the ANSYS model, caused by the boolean "glueing" is not one that would appear in practice, as the cable sample is one continuous length and not two glued together at their centre.

With the completion of the local model, and thus the generation of the mechanical stress time histories, two more objective of the research project were complete.

Chapter 5 described the work completed to produce a time history of stresses due to the distortion of the electric field within the XLPE cable insulation layer. A finite element model of the insulation layer's cross section was built using ANSYS Maxwell software. An iterative approach was taken to calculate the distortion of the electric field at the tip of a water tree head for varying lengths of water tree. This electric field distortion was then converted to a Maxwell stress by means of Maxwell equations. The electric field distortion, and thus Maxwell stress, was shown to peak at the water tree head and to increase in magnitude with increasing water tree length, i.e. when the tip of the water tree is closer to the dynamic cable's core. This Maxwell stress was shown to be considerably smaller than the previously calculated mechanical stress, but acts over a much smaller area at the water tree head. The Maxwell stress followed the same sinusoidal shape and frequency of the operating voltage.

The voltage of the cable was fixed at 66kV, and assumed to be permanently energised. In practice this would not be the case as there will be times where the turbine will be turned off for maintenance work or should a fault occur. Furthermore the 66kV assumption was made based on where the offshore wind industry is moving towards;

larger turbines offshore that require a higher voltage cable rating from the traditional 33kV. In fact, the Carbon Trust already has a floating wind joint industry project which is developing dynamic cables ranging in voltage from 130kV to 250kV for future floating wind farms with even larger wind turbines.

The aspect ratio of the water tree head was shown to act as a stress concentrator and can produce large electric field distortions, limited by the dielectric breakdown strength of the XLPE insulation, 22MV/m. The Maxwell stress was shown to vary with varying water tree head aspect ratios and a theoretical maximum Maxwell stress based on this was calculated.

The outputs of the electric field model were the Maxwell stress time histories at the tip of the water tree head. Two scenarios were taken forward to Chapter 6; firstly one where the aspect ratio of the water tree head is a constant value of 2 and secondly, the more conservative theoretical maximum Maxwell stress at the tip of the water tree head. This Maxwell stress time history is in addition to the previously calculated mechanical stress time history and is used as an input to Chapter 6 to determine the water tree propagation.

With the completion of the electric field distortion model and the generation of the electrical stress time histories, three more objectives of the research project were completed. This allowed for the final chapter to bring the work together to combine the mechanical and electrical stresses and predict their impact on the propagation of a water tree.

Within Chapter 6 the previously calculated mechanical and Maxwell stress time histories were used to determine the damage on the dynamic cable's insulation layers and to model the propagation of a water tree to the point of cable failure.

Initially the mechanical damage was used with Palmgren-Miners rule to determine the

accumulated damage on each element across the cable insulation's cross section. The calculated accumulated damage was shown to be very small, leading to excessive large fatigue lives of $7x10^{11}$ years. Locations 1 and 3 were shown to experience the greatest level of damage, with Location 1 experiencing the overall greatest damage. Damage on the insulation layers was shown to increase with increasing significant wave height at the hang off point, however accumulated damage was shown to peak at the 1.25m significant wave height peak at Location 3. Finally the damage was displayed across the cable's insulation cross section to allow visualisation of which areas experience the greatest damage. These areas were assumed as the points of water tree initiation, and the stress time history of these specific elements was then used for water tree propagation by Paris Law.

Paris Law was then used to model the water tree propagation for multiple initial defect lengths. It was shown that a water tree would not propagate using Paris Law as the maximum calculated stress intensity factor was below the threshold required for crack propagation. As a result it was decided that a macroscopic approach was not applicable, as this did not match what is found in field or experimentally. Therefore, the propagation was then considered as a microscale application of the Maxwell stress in the form of a polymer chain monomer rupture by energy accumulation model.

For multiple initial defect lengths the water tree propagation was modelled, resulting in the water tree reaching a length to cause arc failure within 11 years for an initial defect of 2mm and the maximum Maxwell stress applied. When the propagation per ten minute cycle due to monomer rupturing is added to the defect length to deduce propagation by Paris Law due to the mechanical stress, it is shown that the propagation is entirely governed by the Maxwell stress rupturing the monomers. The model result was compared with experimental work found in the literature, and was found to over predict water tree propagation by 38%. Explanations provided for this over prediction were the assumption of 100% energy accumulation at the water tree head which would not occur in practice as some energy would dissipate. When 20% of the energy imparted by the

Maxwell stress is assumed to dissipate, the over prediction reduces accordingly to 10%.

The conclusions of this research project and the proposed future works are listed in Chapter 8.

Chapter 8

Conclusions and future work

8.1 Chapter introduction

In this chapter a short summary of the work completed for each chapter is presented with the corresponding chapter conclusions listed. The limitations of the conclusions are presented and from this future works are suggested.

8.2 Conclusions

8.2.1 Global model conclusions

To determine the marine environment induced force loadings on the dynamic cable, a resource assessment of wind, wave and current data was completed from a site off the North East coast of England and a global model of the floating offshore wind turbine and platform developed. Four environmental load cases of the wind, waves and current were developed based upon DNVGL-ST-0019. Within each load case there were 87 wave conditions, a fixed wind direction and a fixed current profile. For each load case there were different misalignments between the wave and wind directions. A global model of a tension leg floating wind platform was developed, using OrcaFlex coupled with FAST, with the NREL 5MW reference turbine installed on top of the platform. To determine the magnitude of the forces on the dynamic cable, Morison's coefficients were decided upon with C_d varying from 0.6-12 in accordance with Reynolds number

to account for the angle of the dynamic cable. C_m and C_a were decided as 2 and 1 respectively. A historic dynamic cable from an oil and gas application was attached to the global model, with axial and bending stiffness calculated from methods laid out in the literature, 150MN and 500kNm^2 respectively. The magnitude of the forces and bend moments upon the dynamic cable was assessed for each load case. Based upon the magnitudes of the calculated forces and bend moments, four locations of interest along the cable length were chosen for analysis.

- In general it was found that the forces the cable experiences increase with significant wave height, with a peak force observed at 1.25m significant wave height. The reasoning for the peak being that this wave height corresponds to a wind speed where the axial thrust force on the turbine is at its maximum.

- Location 1 at the hang off is the point of the cable that experiences the greatest force, specifically tension. Location 3, at the beginning of the "S" in the "Lazy S" installation configuration, is found to be the location where the cable experiences the greatest level of bending.

8.2.2 Local model conclusions

To determine the von Mises stress time history across the cross section of the XLPE insulation an FEA of the dynamic cable was developed. A 3D finite element analysis of the dynamic cable was constructed within ANSYS, split into two distinct and equal length sections to allow extraction of stress results at the cable mid point. A submodel of the mid point cross section was constructed with an overall excellent mesh quality of 0.93. A linear superposition of the global model's force outputs onto the cross section of the dynamic cable was completed. This allowed for visualisation of the von Mises stress distributions across the cross section. A linear superposition of the forces was completed instead of a transient dynamic analysis with ANSYS to save on computational expense. Stress time histories are produced for every element of the XLPE cross section. These stress time histories are used as inputs for the fatigue and water tree propagation chapter.

- In general it was seen that maximum von Mises stress across the XLPE insulation increased with increasing significant wave height. A stress peak is observed at 1.25m significant wave height due to the peak in force and bend moments output from the global model at this significant wave height.
- The greatest von Mises stresses are recorded at Locations 1 and 3, where the cable experiences the greatest tension and bending respectively.

8.2.3 Electric field model conclusions

To determine the stresses on the XLPE caused by the distortion of the electric field in the presence of water trees, a FEA of the insulation cross section was built within ANSYS Maxwell.

- For an undisturbed scenario in the absence of water trees the electric field seen at the conductor screen side of the insulation is more than double that seen at the insulation screen side of the XLPE.
- The presence of a water filled water tree within the XLPE insulation causes distortion of the electric field.
- The electric field concentrates at the tip of the water tree, the point closest to the cable core.
- The electric field strength at the tip of the water tree is greater than the electric field strength recorded at the conductor screen. The water molecules within the water tree act as a conductor within the electric field.
- Electric field distortion due to the presence of water trees was modelled iteratively to show how the electric field strength varies as a function of the radius distance the water tree tip is from the cable core.
- Maximum Maxwell stress at the water tree tip is limited by the maximum electric field strength concentrated at the tip of the water tree, which in itself is limited by the dielectric strength of the XLPE.

- Electric field strength at the tip of the water tree is a property of the water tree length, but also the aspect ratio of the water tree.
- The maximum aspect ratio allowed before the XLPE dielectric strength is overcome is found to be 2.3.

8.2.4 Fatigue and water tree propagation conclusions

The mechanical stresses and Maxwell stresses from the Local model and Electric field distortion modelling chapters were combined. The resulting stresses were analysed to determine the fatigue life of the XLPE insulation by means of Palmgren-Miners damage accumulation, Paris Law and as a microscale function of the chemical bond breaking of the monomers by energy accumulation.

- The cable hang off point and the beginning of the "Lazy S" curve where the cable is most bent were identified as risk areas for damage to the XLPE.
- Fatigue lives calculated by the Palmgren-Miners rule gave very large fatigue lifetimes of the XLPE insulation layer of $7x10^{11}$ years.
- Areas of greatest damage on the cross section of the XLPE were identified, and considered as initiation locations of water treeing.
- The combined far field mechanical stresses modelled and Maxwell stresses were not of significant magnitude to propagate water trees as the ΔK value calculated was below the $\Delta K_threshold$ value for XLPE.
- Water tree propagation was shown to not be a macro scale crack propagation mechanism.
- When Maxwell stresses at the water tree tip are considered as a microscale issue of chemical bond breaking, this gave the much reduced fatigue lifetime of 11 years for the dynamic cable installed in the offshore environment modelled, assuming an initial defect of 2mm. It is thought that the mechanical stresses of dynamic cables can exasperate or cause this initial defect.

- After initial defect, water tree propagation was found to be governed by the energy accumulation at the tip of a water tree caused by the distortion of the local electric field.

- When compared to experimental water tree propagation the 100% energy accumulation model is overly conservative and over estimates water tree propagation by 38%. When 80% of the energy is assumed to accumulate to cause monomer rupture the model over predicts by 10%.

8.2.5 Limitations

To complete this work a number of assumptions were made which do limit the stated conclusions. When modelling the dynamic cable the stiffness of the cable was assumed a property of the armouring layers which were assumed as thin walled tubes. Further to this the armouring wires were always assumed to be in stick state and never slip. In practice this would not be the case as the armouring wires would move and slip over one another thus changing the cable stiffness. To this extent the stiffness of a dynamic cable is best determined experimentally.

In the local model a linear superposition of the time history of forces on to the cable cross section was completed as opposed to a complete transient dynamic analysis. This was done to save on computation expense, however would not be the most accurate methodology.

The fatigue life of the dynamic cable was analysed in terms of the mechanical and electric field distortion stresses only. The thermal impacts of an energised cable were not considered. It was assumed that a dynamic cable operating with a constant flow of sea water would act as an appropriate cooling agent, and thus thermal considerations were not a concern. However, a hotter cable could alter the bitumen layers between the armouring wires of the cable, allowing a greater degree of armour wire slipping and a less stiff cable, thus impacting the overall dynamics of the cable. Furthermore the thermal impacts would alter the breaking of the chemical bonds at the microscale monomer

level. The chemical impact of breaking polymer chains has not been considered nor the impact of the exposed carbonyl hydrophilic groups at the end of the polymer chain and potential release of free radicals into the water tree. As stated the water molecules within the water tree would experience an acceleration, however the force impact of these water micro jets on the polymer chains has not be considered.

For conservatism a maximum Maxwell stress was considered as a consequence of the maximum electric field strength at the water tree tip. As shown electric field strength at the tip is a function of the water tree length and the aspect ratio of the water tree. The impact of aspect ratio was acknowledged and a secondary case was considered for a constant aspect ratio. Furthermore this conservatism was continued by assuming that 100% of the energy imparted by the Maxwell stress would accumulate at the water tree tip. This however would not be the case due to the XLPE crystal edges providing a route for energy dissipation. These assumptions produce an overly conservative model. However this conservatism was deemed necessary due to the omission of the thermal effects as listed previously.

The turbine within the model was assumed to be operating constantly for the modelled fatigue lifetime of the cable. Again this would not be the case, and if the turbine is not generating there would be no electric field distortion and therefore no driving force behind the water tree propagation, thus increasing the fatigue lifetime.

8.3 Future work

The future work proposed here is a series of improvements and next steps to be taken to address the limitations identified previously:

- A level of sophistication can be added to the model to account for when the turbine is not operating, and thus not producing any electric field within the dynamic cable.
- Experimental work regarding the stiffness of the dynamic cable needs to be con-

ducted to gain a more complete understanding of the dynamics of the cable, thus impacting the mechanical stresses produced.

- A more detailed cross section FEA can be completed to model the armouring wires as distinct to one another as opposed to a thin walled tube. Further to this future work should include a technique to model the slipping of the armouring wires.

- A more complete analysis can be conducted which examines all the components of the entire dynamic cable cross section. The benefit of this would be the potential to identify cable armouring wires breaking due to the dynamics of the cable, potentially damaging the XLPE insulation layer, serving as the initiation point for the electric field distortion and water tree propagation.

- In future works the aspect ratio of the water tree needs to be better understood and investigated, as opposed to assuming worst case scenario conditions or a constant condition at the tip of the water tree. This would therefore give a more accurate time frame for the water tree propagation and thus time to arc fault estimate. A molecular dynamics investigation is suggested to complete this.

- The thermal impacts need to be considered for future works, both in terms of how a hotter operating cable would impact the stiffness of the cable and also the chemical bond breaking of the XLPE monomers.

- More work needs to be completed to better understand the energy dissipation at the water tree tip due to thermal losses, dissipation along monomer cross linking bonds and dissipation along crystal structure edges. This should provide a more accurate estimation of the energy available for bond breaking and thus water tree propagation.

- The impact force of micro jetting water molecules in an alternating electric field on the XLPE polymer chains needs to be included in future works and the impact on water tree propagation.

- Finally, more work needs to be completed to understand the sources of initial defects within the XLPE, whether this be impurities or inclusions during the manufacturing process, the impacts of poor installation potentially causing the initial crack in the insulation, or other components of the dynamic cable cross section breaking and damaging the XLPE insulation.

References

[1] European Comission. *2030 climate & energy framework.* 2014.

[2] Climate Change Act. *UK regulations: the Climate Change Act.* 2008.

[3] Department for Business National Statistics, Energy & Industrial Strategy. *Energy Trends: renewables.* 2018.

[4] Life50+. *Lifes50plus - Innovative floating offshore wind energy.* 2015.

[5] Vasilis Markatselis and al. et. 4C Offshore - Floating Wind: Changing Gear. Technical report, July 2019.

[6] DNV GL. *Offshore wind industry joins forces to reduce costs of cable failures.* April 2018.

[7] Offshore Wind Programme Board. Export Cable Reliability Description of Concerns. Technical report, July 2017.

[8] *Key project dates for London Array - 4C Offshore.*

[9] Hilary Marazzato, Ken Barber, Mark Jansen, and Barnewell Graeme. *Cable Condition Monitoring to Improve Reliability.* Olex Australia, 2004.

[10] GCube. *Down to the Wire: An Insurance Buyer's Guide to Subsea Cabling Incidents, June 2016 Report.* GCube Insurance Services, June 2016.

[11] CODAN. *Insuring offshore cables, an insurers' perspective, 6th Annual Submarine Power Cable Forum.* Berlin, June 2017.

[12] Shun-Han Yang, Jonas W. Ringsberg, and Erland Johnson. Parametric study of the dynamic motions and mechanical characteristics of power cables for wave energy converters. *Journal of Marine Science and Technology*, 2017.

[13] M. Raoof and T.J. Davies. Determination of the bending stiffness for a spiral strand. *The Journal of Strain Analysis for Engineering Design*, 39(1), 2004.

[14] Xiqia Chen, Shixiao Fu, Leijian Song, Qian Zhong, and Xiaoping Huang. Stress analysis model for un-bonded umbilical cables. *Ocean Systems Engineering*, 3(2):097–122, June 2013.

[15] 4C Offshore. *Blyth Offshore Wind Farm*. 2019.

[16] Subhamoy Bhattacharya. Challenges in Design of Foundations for Offshore Wind Turbines Professor. 2014.

[17] 4COffshore. *Hywind Scotland Pilot Park Offshore Wind Farm - 4C Offshore*. 2019.

[18] Roberts Proskovics. An introduction to Risk in Floating Wind, Key risks and how to mitigate them. Technical report, Offshore Renewable Energy Catapult, 2017.

[19] Ideol. *Ideol-offshore, floating barge technology*. 2019.

[20] International Electrotechnical Commission. IEC 61400-3-1:2019 Wind energy generation systems - Part 3-1: Design requirements for fixed offshore wind turbines. Technical report, 2019.

[21] DNVGL. *DNVGL-ST-0126 Support structures for wind turbines*. April 2016.

[22] DNVGL. *DNVGL-ST-0119 Standard, Floating wind turbine structure*. July 2018.

[23] DNVGL. *DNVGL-ST-0437 Loads and site conditions for wind turbines*. November 2016.

[24] Industrial Services Germanischer Lloyd Rules and Guidelines. *Guideline for the Certification of Wind Turbines,*. 2005.

[25] Soren Karkov. *Offshore Wind Risks - Issues and Mitigations*. 2010.

[26] Carbon Trust. *Carbon Trust's Floating Wind Joint Industry Project reveals winners of dynamic export cable competition*. 2019.

[27] Government of Japan Public relations office. The World's Largest Floating Wind Farm. Technical report, 2016.

[28] Richard Aukland and al. et. 4C Offshore - Global Market Overview Report. Technical report, May 2019.

[29] Richard Aukland and Sam Langston. Subsea Cable Report Global Forecast to 2027 - 4C Offshore. Technical report, 4C Offshore, July 2018.

[30] Şahin Tuğçe. Subsea Cable Insight Report EUROPE: Production and Installation: Supply & Demand. Technical report, 4C Offshore, April 2019.

[31] 4C Offshore. *Global Offshore Wind Database (Cable Edition)*. June 2019.

[32] Ofgem. Calculating Target Availability Figures for HVDC Interconnectors - Update. Technical report, Ofgem, 2016.

[33] National Grid. National Electricity Transmission System Performance Report 2017–2018. Technical report, 2018.

[34] Offshore Renewable Energy Catapult. Offshore Wind Subsea Power Cables, Installation and Operation Market Trends. Technical report, ORE Catapult, 2018.

[35] John Warnock, David McMillan, James Pilgrim, and Sally Shenton. Failure Rates of Offshore Wind Transmission Systems. *Energies 12*, July 2019.

[36] J Warnock, D. McMillan, J. A. Pilgrim, and S. Shenton. Review of Offshore Cable Reliability Metrics. 2018.

[37] CIGRE working group B1.10. Update of service experience of HV underground and submarine cables. Technical report, 2009.

[38] CIGRE working group B1.21. Third-Party Damage to Underground and Submarine Cables. Technical report, 2009.

[39] H Stiesdal and P. H Madsen. Design for reliability. 2005.

[40] Roman Svoma, Mark Dickinson, and Craig Brown. SUBSEA CONNECTIONS TO HIGH CAPACITY OFFSHORE WINDFARMS: ISSUES TO CONSIDER. 2007.

[41] J. C. Chan, M. D. Hartley, and L. J. Hiivala. Performance characteristics of XLPE versus EPR as insulation for high voltage cables. *IEEE Electrical Insulation Magazine*, 9(3):8–12, May 1993.

[42] Qi Chen. *Water tree modelling and detection for underground cables*. PhD Thesis, Clemson University, 2017.

[43] T. Uematsu. *Historical review of water trees in XLPE cables*. Furukawa Rev. no 10, pp. 31-48, 1992.

[44] L. A. Pruitt. Conventional and Cross-Linked Polyethylene Properties. In Johan Bellemans, Michael D. Ries, and Jan M.K. Victor, editors, *Total Knee Arthroplasty: A Guide to Get Better Performance*, pages 353–360. Springer Berlin Heidelberg, Berlin, Heidelberg, 2005.

[45] S. J. Gencur, C. M. Rimnac, and S. M. Kurtz. Failure micromechanisms during uniaxial tensile fracture of conventional and highly crosslinked ultra-high molecular weight polyethylenes used in total joint replacements. *Biomaterials*, 24(22):3947–3954, October 2003.

[46] P. Werelius, P. Tharning, R. Eriksson, B. Holmgren, and U. Gafvert. Dielectric spectroscopy for diagnosis of water tree deterioration in XLPE cables. *IEEE Transactions on Dielectrics and Electrical Insulation*, 8(1):27–42, March 2001.

[47] Qi Chen, Klaehn Burkes, Elham Makram, Ramtin Hadidi, and Xufeng Xu. Capacitance of Water Tree Modeling in Underground Cables. *Journal of Power and Energy Engineering*, 02(11):9–18, 2014.

[48] Chemistry LibreTexts. *Ethane, Ethylene, and Acetylene.* June 2019.

[49] Omnexus. *Polyethylene (PE) Plastic: Properties, Uses & Application.* 2019.

[50] Siraj M. Tamboli, Shashank T. Mhaske, and Dinar Kale. Crosslinked polyethylene. *Indian journal of Chemical Technology*, 2004.

[51] Lyondellbasel. *THE CHEMISTRY OF POLYETHYLENE INSULATION.* 2019.

[52] Skorsepova Terezia. *The Growth of Water Trees in XLPE Cable's Insulation.*

[53] T. Kurihara, T. Okamoto, M. H. Kim, N. Hozumi, T. Tsuji, and K. Uchida. Measurement of residual charge using pulse voltages for water tree degraded xLPE cables diagnosis. *IEEE Transactions on Dielectrics and Electrical Insulation*, 21(1):321–330, February 2014.

[54] S. Hvidsten, E. Ildstad, J. Sletbak, and H. Faremo. Understanding water treeing mechanisms in the development of diagnostic test methods. *IEEE Transactions on Dielectrics and Electrical Insulation*, 5(5):754–760, October 1998.

[55] Nigel Hampton, Rick Hartlein, Hakan Lennartsson, Harry Orton, and Ram Ramachandran. Long-life XLPE insulated power cable. 2007.

[56] Qi Chen, Elham Makram, and Xufeng Xu. A hybrid high frequency pulse and pattern recognition method for water tree detection in long distance underground cables. In *2015 IEEE Power & Energy Society General Meeting*, pages 1–5. IEEE, 2015.

[57] E. Ildstad, H. Bardsen, H. Faremo, and B. Knutsen. Influence of mechanical stress and frequency on water treeing in XLPE cable insulation. In *, Conference Record of the 1990 IEEE International Symposium on Electrical Insulation, 1990*, pages 165–168, June 1990.

[58] Leslie Y. Yeo, Dmitri Lastochkin, Shau-Chun Wang, and Hsueh-Chia Chang. A New ac Electrospray Mechanism by Maxwell-Wagner Polarization and Capillary Resonance. *Physical Review Letters*, 92(13), April 2004.

[59] E. F. Steennis and F. H. Kreuger. Water treeing in polyethylene cables. *IEEE Transactions on Electrical Insulation*, 25(5):989–1028, October 1990.

[60] H. Ahmad and M.H. Ahmad. Effects of acidic and salinity level to the water treeing in crosslinked polyethylene insulation material. pages 57–61. IEEE, October 2010.

[61] Tan Bao and John Tanaka. The diffusion of ions in polyethylene. In *Properties and Applications of Dielectric Materials, 1991., Proceedings of the 3rd International Conference on*, pages 236–239. IEEE, 1991.

[62] Hiroaki Uehara, Katsutoshi Kudo, Yoshihiro Ishikawa, Teruo Kanekawa, Yuichi Tsuboi, Kodai Ushiwata, and Tetsuo Yoshimitsu. A New Water Electrode Method for Short-Time Testing of Water Treeing and Consideration of Temperature Effects of Water Tree Initiation and Propagation. *Electrical Engineering in Japan*, 184(2):1–9, July 2013.

[63] Martin German-Sobek, Roman Cimbala, and Jozef Kiraly. Influence of Ageing and Water Treeing to Degradation of XLPE Insulation. 2013.

[64] Chengcheng Zhang, Chunyang Li, Linlin Nie, Ziang Jing, and Baozhong Han. Research on the water blade electrode method for assessing water tree resistance of cross-linked polyethylene. *Polymer Testing*, 50:235–240, April 2016.

[65] B. K. Hwang. A new water tree retardant XLPE. *IEEE Transactions on Power Delivery*, 5(3):1617–1627, 1990.

[66] T. Maeda, D. Kaneko, Yoshimichi Ohki, T. Konishi, Y. Nakamichi, and M. Okashita. Effect of the applied voltage frequency on the water tree shape in polyethylene. In *Solid Dielectrics, 2004. ICSD 2004. Proceedings of the 2004 IEEE International Conference on*, volume 1, pages 276–279. IEEE, 2004.

[67] I. Zamora, A. J. Mazon, K. J. Sagastabeitia, and J. J. Zamora. New Method for Detecting Low Current Faults in Electrical Distribution Systems. *IEEE Transactions on Power Delivery*, 22(4):2072–2079, October 2007.

[68] Jakov Vico, Mark Adamiak, Craig Wester, and Ashish Kulshrestha. High impedance fault detection on rural electric distribution systems. In *Rural Electric Power Conference (REPC), 2010 IEEE*, pages B3–B3. IEEE, 2010.

[69] Asmarashid Ponniran and Muhammad Saufi Kamarudin. Study on the performance of underground XLPE cables in service based on tan delta and capacitance measurements. In *Power and Energy Conference, 2008. PECon 2008. IEEE 2nd International*, pages 39–43. IEEE, 2008.

[70] Andrew J. Thomas and Tapan K. Saha. Diagnosing water tree degraded XLPE cables using Frequency Domain Spectroscopy. In *Conference Proceedings the Australasian Universities Power Engineering Conference (AUPEC), Melbourne*, 2006.

[71] *Tan Delta Test \textbarLoss Angle Test \textbar Dissipation Factor Test \textbar Electrical4u.*

[72] A. Rodrigo Mor, P. H. F. Morshuis, P. Llovera, V. Fuster, and A. Quijano. Localization techniques of partial discharges at cable ends in off-line single-sided partial discharge cable measurements. *IEEE Transactions on Dielectrics and Electrical Insulation*, 23(1):428–434, February 2016.

[73] B. Howarth, M. Coates, and L. Renforth. Fault location techniques for one of the World's longest AC interconnector cables. In *The 8th IEE International Conference on AC and DC Power Transmission, 2006. ACDC 2006*, pages 14–18, March 2006.

[74] W. Choi, J. T. Kim, I. J. Seo, J. S. Hwang, and J. Y. Koo. Development of a partial discharge detection algorithm and verification test for extra-high-voltage cable system. *IET Science, Measurement Technology*, 10(2):111–119, 2016.

[75] F. Alvarez, J. Ortego, F. Garnacho, and M. A. Sanchez-Uran. A clustering technique for partial discharge and noise sources identification in power cables by means of waveform parameters. *IEEE Transactions on Dielectrics and Electrical Insulation*, 23(1):469–481, February 2016.

[76] A. Cavallini, A. Contin, G. C. Montanari, and F. Puletti. Advanced PD inference in on-field measurements. I. Noise rejection. *IEEE Transactions on Dielectrics and Electrical Insulation*, 10(2):216–224, April 2003.

[77] Andoni Lazkano, Jesus Ruiz, Elisabete Aramendi, and Luis A. Leturiondo. Evaluation of a new proposal for an arcing fault detection method based on wavelet packet analysis. *European transactions on electrical power*, 14(3):161–174, 2004.

[78] Ibrahem Baqui, Inmaculada Zamora, Javier Mazón, and Garikoitz Buigues. High impedance fault detection methodology using wavelet transform and artificial neural networks. *Electric Power Systems Research*, 81(7):1325–1333, July 2011.

[79] Erling Ildstad. The influence of strain on water treeing in XLPE power cables. In *2010 10th IEEE International Conference on Solid Dielectrics*, pages 1–4. IEEE, 2010.

[80] E. Ildstad, H. Bardsen, H. Faremo, and B. Knutsen. Influence of mechanical stress and frequency on water treeing in XLPE cable insulation. In *, Conference Record of the 1990 IEEE International Symposium on Electrical Insulation, 1990*, pages 165–168, June 1990.

[81] Svein Helleso, Jan Tore Benjaminsen, Mildrid Selsjord, and Sverre Hvidsten. Water tree initiation and growth in XLPE cables under static and dynamic mechanical stress. pages 623–627. IEEE, June 2012.

[82] Orcina. OrcaFlex User Mnual, Line theory: Overview.

[83] Orcina. OrcaFlex User Manual, Wave theory.

[84] Bonnie Jonkman. *FAST-OrcaFlex Interface \textbar NWTC Information Portal*. 2016.

[85] K. S. Ravi Chandran. Mechanical fatigue of polymers: A new approach to characterize the SN behavior on the basis of macroscopic crack growth mechanism. *Polymer*, 91:222–238, May 2016.

[86] J. A. Sauer and G. C. Richardson. Fatigue of polymers. *International Journal of Fracture*, 16(6):499–532, December 1980.

[87] R. J. Crawford and P. P. Benham. Cyclic stress fatigue and thermal softening failure of a thermoplastic. *Journal of Materials Science*, 9(1):18–28, January 1974.

[88] Richard W. Hertzberg and John A. Manson. *Fatigue of engineering plastics*. Academic Press, 1980.

[89] M T Takemori. Polymer Fatigue. *Annual Review of Materials Science*, 14(1):171–204, 1984.

[90] W. J. Plumbridge. Review: Fatigue-crack propagation in metallic and polymeric materials. *Journal of Materials Science*, 7(8):939–962, August 1972.

[91] J. M. Schultz. Fatigue Behavior of Engineering Polymers. In J. M. Schultz, editor, *Treatise on Materials Science & Technology*, volume 10 of *Properties of Solid Polymeric Materials, Part B*, pages 599–636. Elsevier, January 1977.

[92] Arnab Ghosh, Neil Paulson, and Farshid Sadeghi. A fracture mechanics approach to simulate sub-surface initiated fretting wear. *International Journal of Solids and Structures*, 58:335–352, April 2015.

[93] J. G. Williams and P. D. Ewing. Fracture under complex stress — The angled crack problem. *International Journal of Fracture Mechanics*, 8(4):441–446, December 1972.

[94] Lahouari Fodil. Estimation of Mixed-Mode Stress Intensity Factors with Presence of the Confinement Parameters T-Stress and A3. *Advanced Engineering Forum*, 18:52–57, September 2016.

[95] Nathan L. Post. Reliability based design methodology incorporating residual strength prediction of structural fiber reinforced polymer composites under stochastic variable amplitude fatigue loading. 2008.

[96] V. R. Regel' and A. M. Leksovskii. Polymer fatigue from the standpoint of the kinetic theory of fracture. *Polymer Mechanics*, 5(1):58–78, January 1969.

[97] G. J. Lake and A. G. Thomas. The Strength of Highly Elastic Materials. *Proceedings of the Royal Society of London. Series A, Mathematical and Physical Sciences*, 300(1460):108–119, 1967.

[98] The Crown Estate. *Marine Data Exchange \|textbar\|textbar Home.* 2019.

[99] Fugro GEOS and Health & Safety Executive. Offshore Technology Report, "Wind and wave frequency distributions for sites around the British Isles". Technical report, 2001.

[100] Anna Pheonix. *Development of a tidal flow for optimisation of tidal turbine arrays.* Access to Research at NUI Galway, 2018.

[101] Claire Legrand. *Assessment of Tidal Energy Resource : EMEC: European Marine Energy Centre.* 2009.

[102] IEC 61400-1. *Wind turbines Part 1: Design requirements. 3rd edition. Geneva, Switzerland: International Electrotechnical Commision.* August 2005.

[103] IEC 61400-1. *Wind turbines Part 1: Safety requirements. 2nd edition. Geneva, Switzerland: International Electrotechnical Commision.* 1999.

[104] B.J. Jonkman and L. Kilcher. NREL National Renewable Energy Laboratory, TurbSim User's Guide: Version 1.06.00. Technical report, 2012.

[105] J Featherstone. *Dynamic Subsea Power Cables for Floating Wind & 66kV Subsea Power Cables, 6th Annual Advanced Submarine Power Cable & Interconnection Forum, Berlin.* June 2017.

[106] ABB. *XLPE Submarine Cable Systems Attachment to XLPE Land Cable Systems - User's Guide. Revision 5.* 2010.

[107] 4C Offshore. Global Offshore Wind Farms Database Database – Information & Intelligence | 4C Offshore.

[108] Hugh Martindale, Steven Rossiter, Terence Sheldrake, and Richard Langdon. Improved Dynamic Structural Modelling for Subsea Power Cables With Bitumen Coated Armour Wires. pages V05AT04A024–V05AT04A024. American Society of Mechanical Engineers, June 2017.

[109] Conseil international des grands réseaux électriques and Comité d'études B1. *Recommendations for mechanical testing of submarine cables.* CIGRÉ, Paris, 2015.

[110] Turgut "Sarp" Sarpkaya. *Wave Forces on Offshore Structures.* 2010.

[111] Shi-fu Zhang, Chen Chang, Qi-xin Zhang, Dong-mei Zhang, and Fan Zhang. Wave loads computation for offshore floating hose based on partially immersed cylinder model of improved Morison formula. 2015.

[112] H.A. Agerschou and J.J. Edens. Fifth and first order wave-force coefficients for cylindrical piles. 1965.

[113] Garbis H. Keulegan and Lloyd H. Carpenter. Forces on Cylinders and Plates in an Oscillating Fluid. May 1958.

[114] Ben Franzluebbers. *Drag Coefficients of Inclined Hollow Cylinder RANS versus LES*. PhD Thesis, Worcester Polytechnic Institute, 2013.

[115] P.R Thies, L. Johanning, and G. H. Smith. Assessing mechanical loading regimes and fatigue life of marine power cables in marine energy applications. *Proceedings of the Institution of Mechanical Engineers, Part O: Journal of Risk and Reliability*, page 1748006X11413533, October 2011.

[116] Danianderson Silva, Rosianita Balena, and Rafael Lisbôa. Methodology for Thermoplastic Umbilical Cross Section Analysis. pages 407–411, July 2012.

[117] Oleg Gaidai, Naiquan Ye, Joe Jin, Dale Reid, and Philippe Mainçon. Fatigue Analysis Methods of Dynamic Umbilicals. International Society of Offshore and Polar Engineers, July 2015.

[118] ANSYS Release 10.0. ANSYS Modeling and Meshing Guide Table of Contents (UP19980818), August 2005.

[119] K. Zhou, W. Zhao, and X. Tao. Toward understanding the relationship between insulation recovery and micro structure in water tree degraded XLPE cables. *IEEE Transactions on Dielectrics and Electrical Insulation*, 20(6):2135–2142, December 2013.

[120] W. Tao, Z. Ma, W. Wang, J. Liu, K. Zhou, T. Li, and M. Huang. The mechanism of water tree growth in XLPE cables based on the finite element method. In *2016 IEEE International Conference on High Voltage Engineering and Application (ICHVE)*, pages 1–4, September 2016.

[121] Muhatifah Mohd Salleh, Mohd Hafiez Izzwan Saad, Yanuar Z. Arief, and Nor Asiah Muhamad. Water Tree Simulation on Underground Polymeric Cable Using Finite Element Method. *Journal of Telecommunication, Electronic and Computer Engineering (JTEC)*, 10(1-12):107–112–112, March 2018.

[122] Courses.lumenlearning.com. *Conductors and Electric Fields in Static Equilibrium \textbar Physics*. 2019.

[123] J. Wang, J. Wu, Y. Li, and X. Zheng. Simulation of Electric Field Distributions in Water Treed XLPE Using Finite Element Method. In *2012 Spring Congress on Engineering and Technology*, pages 1–4, May 2012.

[124] Jean-Pierre Crine. Influence of Electro-meachanical Stress on Electrical Properties of Dielectric Polymers. *IEEE Transactions on Dielectrics and Electrical Insulation*, Vol. 12(No. 4):791, August 2005.

[125] Z. Wang, P. Marcolongo, J. A. Lemberg, B. Panganiban, J. W. Evans, R. O. Ritchie, and P. K. Wright. Mechanical fatigue as a mechanism of water tree propagation in TR-XLPE. *IEEE Transactions on Dielectrics and Electrical Insulation*, 19(1):321–330, February 2012.

[126] S. D. Downing and D. F. Socie. Simple rainflow counting algorithms. *International Journal of Fatigue*, 4(1):31–40, January 1982.

[127] J.P. Campbell and R. O. Ritchie. Mixed-mode, high-cycle fatigue-crack growth thresholds in Ti-6A-4V. A comparison of large- and short-crack behavior. *Engineering Fracture Mechanics*, 67:209–227, 2000.

[128] Kun Sun, Junqi Chen, Hong Zhao, Weifeng Sun, Yinsheng Chen, and Zhongming Luo. Dynamic Thermomechanical Analysis on Water Tree Resistance of Crosslinked Polyethylene. *Materials (Basel, Switzerland)*, 12(5), March 2019.

[129] E. ILDSTAD, S.M HELLESØ, S. HVIDSTEN, H. FAREMO, P. EGROT, J-O. BOSTRÖM, NILSSON. NILSSON, J. EEK, J. MATALLANA, and H.M. WOLNEBERG. Water Tree Ageing of High Voltage XLPE Cable Insulation System under Combined Dynamic Mechanical and AC Electrical Stress. 2014.

Appendix A

Copies of the following texts are found here for reference:

2018 **D G Young**, C Ng, S Oterkus, Q Li, L Johanning. *Assessing the mechanical stresses of dynamic cables for floating offshore wind applications.* Global Wind Summit (2018) Hamburg, Journal of Physics: Conference Series **1102** 012016. doi: 10.1088/1742-6596/1102/1/012016.

2018 **D G Young**, C Ng, S Oterkus, Q Li, L Johanning. *Predicting failure of dynamic cables for floating offshore wind.* RENEW 2018 3rd International Conference on Renewable Energies Offshore, Lisbon.

2018 **D G Young**, L Johanning. *Dynamic Cables for Floating Offshore Wind - Dynamic Mechanical Stresses on Fatigue Life of Dynamic Cables.* Windtech International November/December issues 2018.

Assessing the mechanical stresses of dynamic cables for floating offshore wind applications

IOP Conf. Series: Journal of Physics: Conf. Series **1102** (2018) 012016 doi:10.1088/1742-6596/1102/1/012016

Assessing the mechanical stresses of dynamic cables for floating offshore wind applications

D G Young[1], C Ng[1], S Oterkus[2], Q Li[3] and L Johanning[4]

[1] Offshore Renewable Energy Catapult, Blyth, UK
[2] University of Strathclyde, Naval Architecture, Ocean and Marine Engineering Glasgow, UK
[3] University of Edinburgh, School of Engineering, Edinburgh, UK
[4] University of Exeter, Offshore Renewable Energy , Exeter, UK

E-mail: david.young@ore.catapult.org.uk

Abstract. Offshore wind farms are progressing further offshore and into deeper waters, presenting the need for new substructures, including floating offshore wind turbines. These floating turbines will require dynamic cables to run through the water column, exposing them to the dynamic loadings of the marine environment. This paper presents a tool which models the stresses across a dynamic cable cross section's insulation layers when attached to a floating wind platform. Differing wave, wind and current flow conditions are applied and their impact on the stress distributions of the dynamic cable's insulation layers are presented. Finally from these stress histories, accumulated fatigue damage of the insulation is calculated and presented. The outcome of this can be used to estimate fatigue damage of a cable components cross section at any point along the cable length, and aid in cable installation configuration decisions.

1. Introduction

Offshore wind farms are progressing to having larger turbines installed as a cost effective means to reduce the cost of energy. These larger wind farms are moving further from shore and into deeper water depths. This move is presenting the need for new substructures including floating platforms for offshore turbines. Floating platform wind turbines are envisioned to be installed in water depths ranging from 50m to 200m, with the Carbon Trust estimating up to 90MW of floating wind farms are to be installed in UK waters by the end of 2018 [1].

Floating platforms will introduce new challenges for the umbilical, or array, cables that hang from the base of the platform to the seabed. This cable installation arrangement will expose the cables to the dynamic forces of the environment they would be installed in, including the actions of the waves, current flows and movement of the platform itself in response to wind/turbine interactions. Cables exposed to dynamic environmental loadings will experience dynamic mechanical stresses across their cross sections and along their length. This is a new operating consideration as traditional fixed bottom platforms have allowed cables to operate statically.

The causes of cable failures during normal operation, and excluding third party interference, can be approximately grouped into mechanical damage, water ingress and overheating which all lead to electrical failure or breakdown of the insulation layers [2]. A renewable energy insurance provider [3] highlights that most cable failure claims are related to incorrect installation, incorrect operation or electrical faults. As dynamic cables will be exposed to dynamic environments and the corresponding

force loadings, they are at higher risk of cable failure with more expected to fail during normal service lifetime.

The impact of dynamic loadings on the fatigue characteristics of dynamic cables has been investigated by [4], [5], [6] while mechanical fatigue due to environmental loadings is shown to be a concern as a propagating mechanism for water treeing in the cables insulation layers [7], [8]. The impact of differing cable bending and axial stiffness on cable fatigue damage was investigated by [9]. The axial and bending stiffness of a cable affects the cables motions in response to the dynamic environment, where having a larger stiffness reduces the cable motion. The inter-wire friction between helically wound armouring layers is found to be a determining factor in cable bending stiffness [10] while [11] investigated the impact of armouring radius reduction effects on cable axial stiffness when under tension. Similar findings are reported in [12] when comparing calculated cable axial stiffness which account for radius reduction or not.

This paper presents an assessment of the marine environment at a chosen site and presents a model which determines how the mechanical stresses across the cable cross section distribute when installed in this environment. A fatigue assessment of the cable insulation layers is completed and conclusions are drawn from the accumulated damage in differing dynamic environment loadings.

The approach presented begins with an assessment of the environment to determine the wave, wind and current loadings on the cable as detailed in section 2. An introduction to the software used and the created model is given in section 3. Section 4 provides details on how the damage is determined from the created model. Results from the model and calculated damage are presented in section 5, while section 6 gives a discussion of these results. Section 7 draws conclusions from the work, and finally section 8 highlights ongoing work.

2. Environmental Loading Assessment

Wave and current flow data from sites off the north east coast of England, as shown in Figure 1, was obtained and analysed. Wave data was obtained from a wave buoy placed at a site in 90m water depth, while current data was obtained from a 56m water depth site by an acoustic wave and current profiler, AWAC. Wind speed data correlated to wave height was obtained from two locations based in the central North Sea from the NEXT study, an extension of the North European Storm Study, NESS [13]. Briefly, NESS was initiated to produce a hind cast database of winds, waves and currents for the North European continental shelf.

Figure 1. Locations of the AWAC, 1, the wave buoy, 2, and the NEXT model locations, 3 and 4.

The locations of the wave buoy, AWAC and NEXT study sites were determined to be within the same coarse grid of the central North Sea. Therefore it was assumed the environment exhibited at each site would be similar, meaning the wave environmental data captured at the wave buoy site would be the same wave data that would be captured at the AWAC site or the NEXT sites, and vice versa. The water depths at the sites were differing, so the captured current flow speed data was fitted to the power law velocity profile using equation 1 [14] , assuming a shear profile due to seabed roughness. This was then extrapolated, allowing for current velocity calculations at other water depths:

$$\frac{U_z}{U_{max}} = (\frac{Z}{H})^{1/n} \quad (1)$$

Where U_z is the water velocity in ms^{-1} at point Z, U_{max} is the maximum water velocity in ms^{-1}. Z is the vertical position from the seabed in m, H is the full tidal depth in m and n is the power law coefficient.

To use wind data near the wave data site it was necessary to assume that the wind generated the waves and thus the wave height was directly related to the wind speed. The NEXT data sites present wave height binned with a corresponding wind speed 10m above sea level. This data was used to create a best fit curve that could be used to back calculate a corresponding wind speed for the wave heights recorded by the wave buoy. For this reason it was also assumed that the wind and waves were coming from the same general directions.

This model includes a tension legged floating wind platform incorporating the NREL 5MW turbine. This turbine has a hub height of 90m, therefore by using the equations laid out in the guidelines for the certification of offshore wind turbines [15] the wind speed at the hub height was calculated using:

$$V_z = V_{hub}(\frac{h}{h_{hub}})^{\propto} \quad (2)$$

Where V_z is the wind speed at height h in ms^{-1}, h is the height about still water line in m, h_{hub} is the hub height above still water line in m, and α is the power law exponent, [15] assumes that α is equal to 0.14 for all wind speeds.

3. Dynamic Cable Model

To understand the stresses that the loading environment would impose upon a dynamic cables cross section, the whole floating platform system needs to be analysed initially as a global model. The output from the global model can then be used to simulate the stress distributions and time history for a local mechanical model of the cable cross section.

Details of this model can be found in [16] however for clarity a condensed version of the essentials will be provided here.

3.1. Global Dynamic Model

This model was created using the proprietary marine dynamics software OrcaFlex by Orcina. OrcaFlex was used to estimate the loadings on the dynamic cables installation length in response to the actions of the waves, currents, wind and the movements of the floating platform itself. For this work the cable was split into 0.5m lengths and the software employs a lumped mass approach to solve the cables dynamic behaviour.

Required inputs for the dynamic model include the environmental loadings and properties of the cable, including its geometry, length, axial and bending stiffness's.

The MIT/NREL reference 5MW tension leg platform [17] is included in this work and its movements modelled. This is a platform of 18m waterline depth and almost 50m draft. It has four 27m long pontoons, each having two mooring lines attached to its end. Fastlink is a FAST-OrcaFlex interface package that couples the software OrcaFlex with FAST. The hydrodynamics of the cable are modelled

using OrcaFlex. The NREL 5MW reference turbine, tower, floating platform and structural dynamics, aerodynamics control and electrical drive dynamics are modelled using FAST. This allows for the coupling of the effects of the wind on the turbine with the effects of the waves and currents on the platform.

3.1.1. Dynamic Cable. The cable modelled for this work is based on 280m length of a JDR dynamic cable [18] used in previous oil and gas applications. Figure 1 gives some of the cables mechanical parameters. The cable axial stiffness was calculated using works laid out in [11], and the bending stiffness using [10].

Table 1. Mechanical Parameter of the Dynamic Cable.

Mechanical Properties	
Outer Diameter	154mm
Outer Sheath Material	Extruded Polyethylene
Cable Armouring	Galvanised Steel Wire
Minimum Bend Radius	2000mm
Safe Working Load	250kN
Diameter to Weight Ratio	4.27m^2/Te

3.2. Mechanical Model
The mechanical model is used to determine the stress time histories and distributions across the cables cross section. This local model uses the outputs of the global dynamic model to allow the user to determine the stresses acting on individual cable components, highlighting areas of greatest mechanical stress. Plane and shear stresses are calculated for each of the cables six degrees of freedom as well as combined into a von Misses stress.

3.2.1. Finite Element Analysis. A finite element analysis, FEA, of the cable cross section was constructed using ANSYS Mechanical software. This proved an effective method to determine the interactions between different components of the dynamic cables cross section. Similar works on dynamic umbilical cables [19], [20] both used an alternative FEA software called UFlex2D. This is a custom built software for umbilical cross sections however ANSYS was used here for its coupling abilities with OrcaFlex.

3.3. Model Assumptions
To balance accuracy and computational expense some assumptions were made during this analysis. The cable stiffness was assumed to come from the cable armouring layers. The armouring layers were simplified to thin walled cylinders for the mechanical model, similar to [9]. This assumption follows the thought that the armouring layers are always in stick mode rather than slip mode so that individual armouring wires do not slide over one another during operation. The cable component materials were assumed to be linear elastic and that they were glued together in the FEA, meaning they could not penetrate another components surface.

4. Fatigue Damage Calculations
An output from the mechanical model are the stress histories of the components of the dynamic cables cross section. A stress based approach to fatigue was used as the stresses exerted upon the cross section are lower than the design yield stresses of the cable component materials.

Accumulated fatigue damage of the dynamic cable insulation layers are calculated using the Palmgren-Miner linear damage rule, equation 3, and the corresponding S-N curve for that material.

$$D = \sum_{i=1}^{k} \frac{n_i}{N_i} \tag{3}$$

Where for k different stress levels and the average number of cycles to failure at the ith stress, S_i, is N_i and n_i is the number of cycles are accumulated stress S_i. No fatigue limits were set for this initial work as compression and tension are both assumed to contribute to fatigue. The S-N curve used for the XLPE insulation layers was obtained from [8].

5. Results

5.1. Environmental loading Assessment

Using the data from [13] the relationship between the significant wave height and the wind speed is plotted in Figure 2. This plot allows for the determining of the wind speed for the wave heights recorded by the buoy. Figure 3 shows a binned scatter plot of the significant heights and zero crossing period of the waves recorded by the buoy.

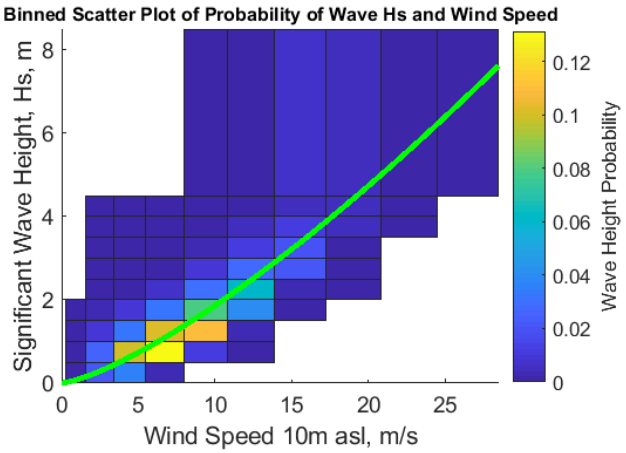

Figure 2. Relationship of wave height to wind speed.

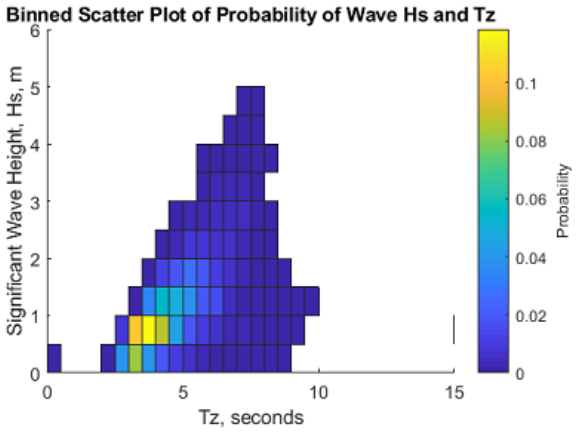

Figure 3. Binned scatter plot of significant wave height and zero crossing period.

Using the recorded wave heights from Figure 3, and equation (2), the wind speeds the turbine is exposed to are presented in table 2.

Table 2. Corresponding wave heights and wind speed.

Significant Wave Height(m)	Wind Speed 10m asl (ms^{-1})
0.25	2.2
0.75	5.1
1.25	7.4
1.75	9.5
2.25	11.5
2.75	13.4
3.25	15.1
3.75	16.8
4.25	18.5
4.75	20.1

From these results, the largest wind speed the turbine would face 10m asl is 20.1ms^{-1}, roughly corresponding to gale force winds and a Beaufort Force of 8 on the Beaufort scale.

The wave directions were also recorded by the wave buoy and are presented in a wave direction rose shown in Figure 4. As the NESS model sites did not provide much information to back calculate the wind directions, the winds and waves are assumed to come from the same direction for this work.

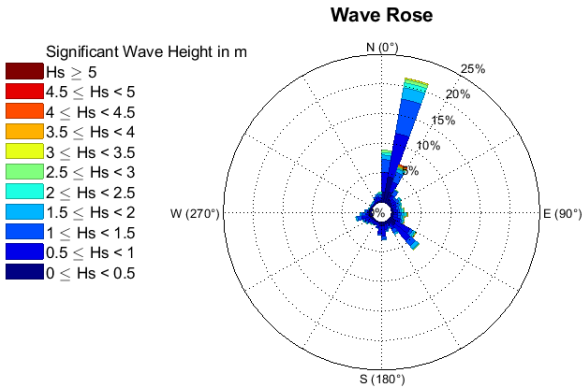

Figure 4. Wave rose of wave directions and height

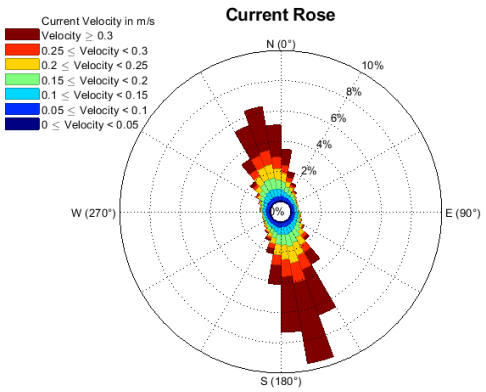

Figure 5. Current rose of current direction and speed

From figure 4 it can be seen that the wave direction is predominantly from the North, so for the model the waves and therefore wind are assumed to be coming from one direction only.

The data recorded by the AWAC was used to determine the current magnitude and direction and is presented in Figure 5. From this it can be seen that the current direction is approximately bi-directional, traversing up and down the North East of England coastline. The average current speed for each recorded water depth was calculated and extrapolated to a 200m water depth with the curve plotted in Figure 6. This curve was compared to the theoretical current profile calculated using equation (1).

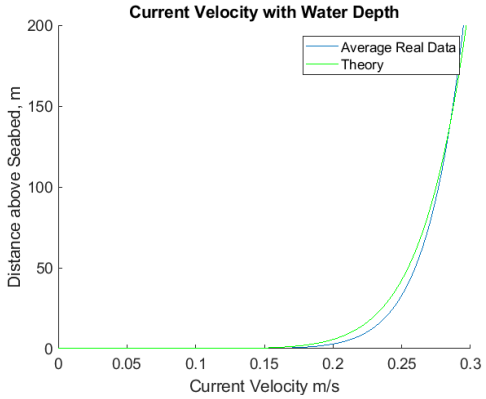

Figure 6. Current velocity profile with water depth

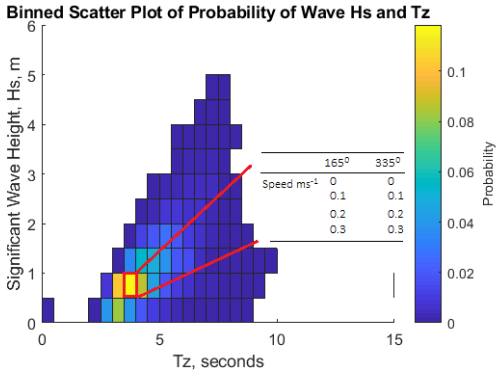

Figure 7. Subdivisions of wave loadings by current speed and direction

Figure 7 illustrates how each wave loading scenario was subdivided by current speed and directions. This plot was generated based on the assumption that the current flow is bi-directional and accelerates and decelerates from 0.3ms^{-1} in one direction to 0.3ms^{-1} in the other, similar to results found in [21]. From the calculated results the following environmental loading conditions were used for the model.

Table 3. Environmental Loadings

Environmental Loadings	
Wave height (m)	0.25 – 4.75
Wave period (s)	0.25 – 9.75
Wave direction (^{0})	15
Wind Speed (ms^{-1})	2.2 – 20.1
Wind Direction (^{0})	15
Current Speed ms^{-1}	0-0.3
Current Direction (^{0})	165 and 335

5.2. Dynamic Cable Model Output

Similar to works presented in [16] and [4], the hang off point of the cable is an area of concern for fatigue. Further investigation of the stress distributions and accumulated damage at this point specifically shall be given in these works, however it should be noted that any point along the length of the cable can be chosen.

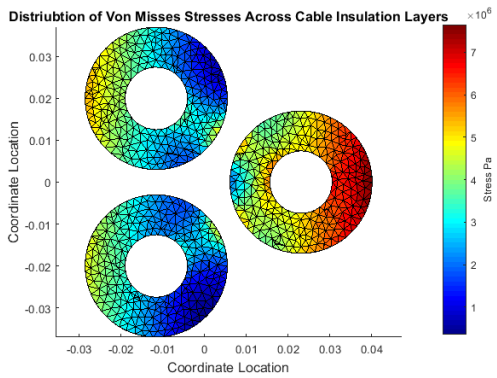

Figure 8. Stress distributions at hang off point.

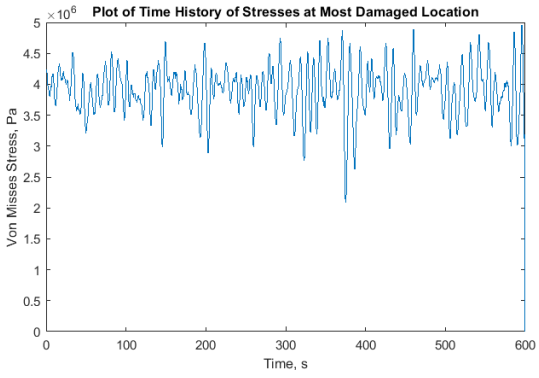

Figure 9. Stress time history at most damaged location.

Figure 8 shows the von Misses stress distributions of the cross linked polyethylene, XLPE, insulation layers at the cable hang off point. While any component of the cable cross section can be investigated, the XLPE layer shall be looked at specifically for further analysis. The stresses of the insulation layers are investigated due to concerns of water tree growth. It should be noted that for any cable component the plane or shear stresses can be deduced. Figure 8 is plotted using the outputs of the global dynamic model including, effective tension, x-bend moment, y-bend moment etc. and coupling them with the local mechanical model.

From the distribution, the stress time history of each location can be extracted. Figure 9 shows the stress time history of the XLPE location that experienced the most damage. It should be noted that the first 30 seconds of each simulation was discarded to allow for environment ramp up avoid the large stress amplitudes due to the platform moving from an initial stationary position.

5.3. Fatigue Damage

For each location the time history can be extracted, and the accumulated fatigue damage can be calculated using equation (3). This allows for the distribution of fatigue damage across the cable insulation layers to be plotted, shown in figure 10.

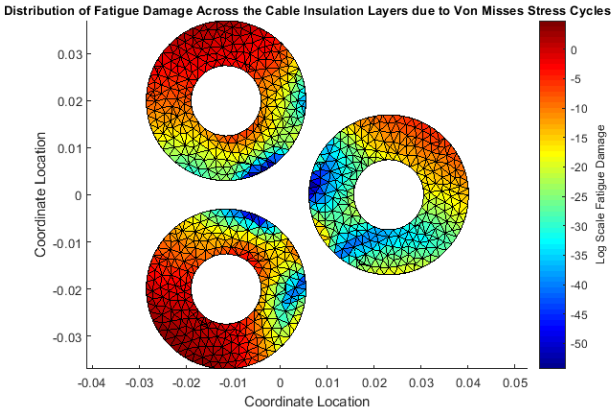

Figure 10. Log scale distribution of fatigue damage.

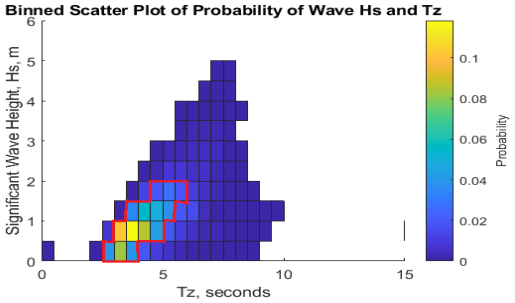

Figure 11. Wave spectrum distribution with greatest probability conditions highlighted.

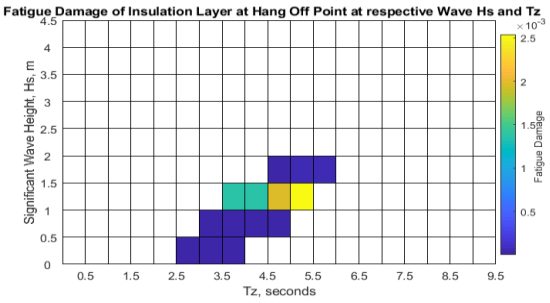

Figure 12. Calculated fatigue damage for the highlighted wave spectrum conditions.

Figure 11 shows the previously calculated wave spectrum, but with the most frequently occurring waves circled. Figure 12 shows the damage calculated for each of these wave conditions. It should be noted that these total damages incorporate the damages calculated for each of the current velocities and directions as depicted in Figure 7, but does not account for the occurrence of each wave type.

6. Discussion

The presented work can be used to give an estimation of the fatigue damage of any component of a dynamic cable's cross section. This work focused on the von Misses stress distribution, σ_{vm}, of the dynamic cable's insulation layers and assumed that in these preliminary works that both compression and tension contributed to damage within the cable insulation layers. Work was completed to deduce the impact of varying wave heights, periods and current velocities on the mechanical fatigue damage of the insulation layers of a dynamic cable. It was found that greater wave heights resulted in a greater level of fatigue damage. This could be contributed to greater wave heights causing a greater heave of the floating platform, therefore increasing the tension on the dynamic cable.

It was found that a longer wave period increases the fatigue damage calculated. This is contrary to the thought that a greater wave frequency would inhibit the platform from returning to its undisturbed position, keeping the cable in a state of stress. While wave celerity does increase with wave period, the orbital, or horizontal velocities, of the water particles decrease with wave period. These velocities can determine the force of the impact of the waves on the floating platform using Morrison's equation, where the force in the x-direction on a body in unsteady flow with velocity *U(t)* is:

$$F_x(t) = \rho C_m V \dot{U} + \frac{1}{2}\rho C_d A\,|U|U \tag{4}$$

Where V is the body volume in m^3, ρ is the mass density of the fluid in kgm^{-3}, $\dot{U}$ is the flow acceleration in ms^{-2}, A is the body reference area in m^2, C_d and C_m are the drag and momentum coefficients respectively.

Using equation 4, it can be quickly deduced that a reduction in velocity would result in a reduced force exerted on the platform from the waves, thus reducing the displacement of the platform. From figure 12 the wave periods ranging from 3.75s to 5.25s were investigated to determine the displacements of the floating platform, shown in table 4.

Table 4. Displacement of floating platform at varying wave period and wave height 1.25m

Wave Period Tz (s)	Average X displacement (m)	Average Y displacement (m)	Average Z displacement (m)	Damage
3.75	3.34	-0.081	-0.037	0.0013
4.25	3.34	-0.080	-0.037	0.0013
4.75	3.35	-0.080	-0.037	0.0019
5.25	3.34	-0.08	-0.037	0.0024

From table 4 it is seen that at varying wave periods the average platform displacement minimally changed, if at all, however the damage of the dynamic cable insulation layers increased. This increase in damage can perhaps be explained by a greater frequency of platform movement. If a closer look is taken at the stress time histories of the most damaged insulation locations, it can be seen that a wave period of 5.25s compared to a period of 3.75s, produces a stress history with more stress amplitudes, evident in the jagged plot for the 5.25s wave period shown in figure 13. This greater stress frequency can perhaps be due to the period of the waves matching the eigen period of the system, however this has not been investigated in any detail.

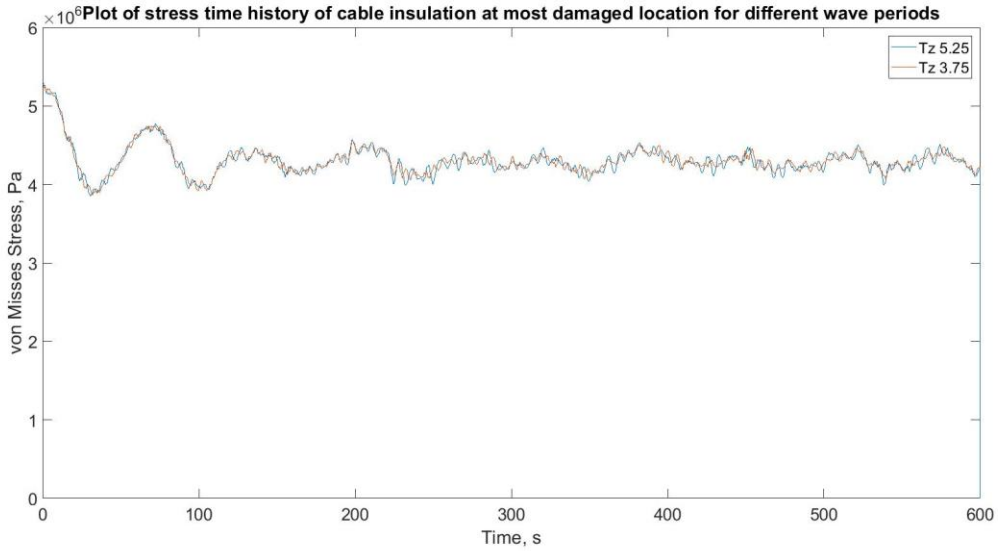

Figure 13. Stress time histories of the cable insulation at differing wave periods

It is important to note that the magnitude of the fatigue damage of the insulation layers is small. This is to be expected as the armouring layers surrounding the insulation layers are protecting them from damage. However when the extreme cases were simulated for a H_s of 4.75m and a Tz of 7.75s, the fatigue damage calculated was much larger than 1, indicating a cable failure, even of the insulation layers. Unfortunately this result was omitted from figure twelve due to its fatigue value being much larger than the others. As figure 12 shows the fatigue damages scaled to one another, this distorts the plot and results in the details of the smaller fatigue differences being lost. Furthermore as this work is the initial steps in analysing water treeing within the insulation layers, extreme wave conditions would cause a cable failure outside of that of water treeing.

When considering the impact of varying current speeds and directions it was found that when the current is travelling up the coast in Figure 1 (direction 165^0) the damage is greater than when it is travelling in the opposite direction, 335^0. It can be seen that when the current speeds are at their greatest in the tidal cycle, this also corresponds to a greater level of cable insulation fatigue damage. This output from the model could be used in the future to aid in cable installation layout and orientation decisions to reduce cable fatigue.

While this work presented von Misses stress distributions, the model allows the user to look at individual plane or shear stresses a component experiences. When these individual stresses are looked at for a particular environmental loading, it can be see that the largest contributing stress is σ_{zz} as seen in table 5.

Table 5. Magnitude of insulation fatigue damage at most damaged insulation location due to corresponding stress type.

Stress Type	Fatigue Damage
σ_{xx}	4.53e-41
σ_{yy}	5.28e-50
σ_{zz}	5.15e-06
σ_{xy}	2.74e-46
σ_{yz}	4.65e-25
σ_{xz}	3.41e-30
σ_{vm}	9.00e-06

In this case, this highlights that it is cable bending that contributes to insulation fatigue at the hang off point, rather than cable tension.

Unless in extreme storm conditions, the fatigue damage of the cable insulation calculated was very small. This could be a weakness in the model being under conservative. However it is important to note that the cable modelled was a dynamic cable used in historic oil and gas applications, and would have a much larger cable axial and bending stiffness than one that would be used for floating offshore wind applications. A further weakness of the model is that for the fatigue damage on the insulation layers, only one S-N curve could be found in previous works. To give a greater credibility to the results a larger number of S-N curves would have been desirable.

7. Conclusions

This work presents a method to determine mechanical fatigue damage across a dynamic cable's cross section, specifically the insulation layers, when exposed to a dynamic marine environment. It can be used as a tool to compare the insulation fatigue damage at differing lengths along the cables length. Individual components of the cable cross section can be investigated, giving way to a more comprehensive fatigue assessment of dynamic cables.

It was found that increasing wave height increases cable insulation fatigue damage in deep water applications. Increasing current velocities also increases cable insulation fatigue damage. Current direction plays a role in cable insulation fatigue damage, aiding in installation arrangement decisions. Finally, the works suggests that it is the stresses due to cable bending, as opposed to tension that contribute most to a dynamic cable's insulation fatigue damage.

8. Future Work

The next stages of this work is to use the most damaged cable insulation locations as initiation points of insulation water treeing. Using the stress cycles calculated within these works is hoped to allow for the modelling of cracks within the insulation as propagating mechanisms of water treeing.

The electrical stresses across the insulation layers are then to be modelled. It is envisioned this work serves at the first step in the development of a coupled mechanical and electrical fatigue model of the cable insulation which considers both mechanical stresses and electrical stresses due to the cable being energized.

9. Acknowledgements

The authors would like to thank the Energy Technology Institute and the Research Council Energy Programme for funding this research as part of the IDCORE programme (grant EP/J500847), and the Offshore Renewable Energy Catapult for providing technical assistance and equipment. A special thanks to Orcina for providing OrcaFlex software and to JDR cables for allowing presentation of cable data.

References

1. Carbon Trust. Floating Wind Joint Industry Project: Policy & Regulatory Appraisal [Internet]. 2017 [cited 2018 Mar 14]. Available from: https://www.carbontrust.com/resources/reports/technology/floating-wind-policy/

2. Marazzato H, Barber K, Jansen M, Graeme B. Cable Condition Monitoring to Improve Reliability. Olex Australia; 2004.

3. GCube. Down to the Wire: An Insurance Buyer's Guide to Subsea Cabling Incidents, June 2016 Report. GCube Insurance Services; 2016.

4. Thies PR, Johanning L, Smith GH. Assessing mechanical loading regimes and fatigue life of marine power cables in marine energy applications. Proc Inst Mech Eng Part O J Risk Reliab. 2011 Oct;1748006X11413533.

5. Buitrago J, Swearingen SF, Ahmad S, Popelar CF. Fatigue, Creep and Electrical Performance of Subsea Power Cable. In American Society of Mechanical Engineers; 2013 [cited 2018 May 23]. p. V003T03A028-V003T03A028. Available from: http://proceedings.asmedigitalcollection.asme.org/proceeding.aspx?articleid=1786236

6. Thies PR, Johanning L, Dobral C. Parametric Sensitivity Study of Submarine Power Cable Design for Marine Renewable Energy Applications. 2017 Jun 25;V03BT02A010.

7. Ildstad E, Bardsen H, Faremo H, Knutsen B. Influence of mechanical stress and frequency on water treeing in XLPE cable insulation. In: , Conference Record of the 1990 IEEE International Symposium on Electrical Insulation, 1990. 1990. p. 165–8.

8. Wang Z, Marcolongo P, Lemberg JA, Panganiban B, Evans JW, Ritchie RO, et al. Mechanical fatigue as a mechanism of water tree propagation in TR-XLPE. IEEE Trans Dielectr Electr Insul. 2012 Feb;19(1):321–30.

9. Yang S-H, Ringsberg JW, Johnson E. Parametric study of the dynamic motions and mechanical characteristics of power cables for wave energy converters. J Mar Sci Technol. 2017;

10. M. Raoof, Davies TJ. Determination of the bending stiffness for a spiral strand. J Strain Anal Eng Des. 2004;39(1).

11. Chen X, Fu S, Song L, Zhong Q, Huang X. Stress analysis model for un-bonded umbilical cables. Ocean Syst Eng. 2013;3(2):97–122.

12. Ekeberg KI, Ottesen T, Aarstein J, Saevik S, Ye N, Igland R. Predicting, Measuring and Implementing Friction and Bending Stresses in Dynamic Umbilical Design. In Offshore Technology Conference; 2006 [cited 2018 Mar 15]. Available from: https://www.onepetro.org/conference-paper/OTC-17986-MS

13. Fugro GEOS, Health & Safety Executive. Offshore Technology Report, "Wind and wave frequency distributions for sites around the British Isles." 2001.

14. Lewis M, Neill SP, Robins P, Hashemi MR, Ward S. Characteristics of the velocity profile at tidal-stream energy sites. Renew Energy. 2017 Dec 1;114:258–72.

15. Germanischer Lloyd Rules and Guidelines, Industrial Services. Guideline for the Certification of Wind Turbines,. 2005.

16. Young D, Ng C, Oterkus S, Li Q, Johanning L. Predicting failure of dynamic cables for floating offshore wind. In: 3rd International Conference on Renewable Energies Offshore. 2018.

17. Jonkman B. FAST-OrcaFlex Interface | NWTC Information Portal [Internet]. 2016 [cited 2018 Mar 15]. Available from: https://nwtc.nrel.gov/OrcaFlexInterface

18. Featherstone J. Dynamic Subsea Power Cables for Floating Wind & 66kV Subsea Power Cables, 6th Annual Advanced Submarine Power Cable & Interconnection Forum, Berlin. 2017 Jun.

19. Silva D, Balena R, Lisbôa R. Methodology for Thermoplastic Umbilical Cross Section Analysis. 2012 Jul 1;407–11.

20. Gaidai O, Ye N, Jin J, Reid D, Mainçon P. Fatigue Analysis Methods of Dynamic Umbilicals. In International Society of Offshore and Polar Engineers; 2015 [cited 2018 May 15]. Available from: https://www.onepetro.org/conference-paper/ISOPE-I-15-595

21. Pheonix A. Development of a tidal flow for optimisation of tidal turbine arrays. Access to Research at NUI Galway; 2018.

Predicting failure of dynamic cables for floating offshore wind

D.G. Young
Industrial Doctoral Centre for Offshore Renewable Energy & Offshore Renewable Energy Catapult, UK

Dr C. Ng
Offshore Renewable Energy Catapult, Blyth, UK

Dr S. Oterkus
University of Strathclyde, Glasgow, UK

Dr Q. Li
University of Edinburgh, Edinburgh, UK

Prof. L. Johanning
University of Exeter, Exeter, UK

ABSTRACT: Advancements in the offshore wind industry have increased the viability of large floating turbines. All floating structures will require cables to run through the water column, from their base at the water surface to the seabed. This exposes the cables to the dynamic forces produced by marine currents, waves and the response motions of the floating platform itself. Predicting how these cables will perform and survive offshore would prove beneficial to wind farm owners and operators.

The work presented aims to give a better understanding of how the dynamic forces the cables would be exposed to can impact the cable cross-section at a component level. How these forces produce mechanical stress across the cross-section of the dynamic cable is analyzed by finite element analysis. The outcome of this can be used to estimate fatigue damage of a cable components cross section at any point along the cable length.

1 INTRODUCTION

The UKs Climate Change Act commits the UK to reduce total carbon emissions by 80% of 1990 levels by 2050 (Climate Change Act 2008). Technological advancements in the offshore wind industry, coupled with economies of scale, has increased the viability of large scale wind turbines offshore. Wind turbines are moving further away from the shoreline to benefit from the higher wind speeds available. However moving further from shore corresponds with an increase in water depth. Traditional fixed bottom wind turbine technologies are not best able to accommodate these greater water depths; giving rise to new floating platform wind turbines. Much work has been completed in advancing floating wind technologies, including that of the LIFES50+ consortium (2015), with the Carbon Trust (2017) estimating up to 90MW of floating wind farms to be installed by the end of 2018 in the UK.

Floating platform wind turbines will require cables to run through the water column, from their platform base at the water surface to the touchdown point on the seabed. This trajectory exposes the cable to the dynamic forces of the environmental waves and currents. The platform will move in accordance with the turbines response to wind. As the cable is attached at its hang off point to the platform, it will also be subjected to these motions.

The dynamic environmental loading on the cable induces dynamic mechanical stresses across the cross section of the dynamic cable. These mechanical stresses are a new consideration in cable fatigue assessments, as traditional static cables used in fixed bottom platforms would not be exposed the dynamic environmental loadings.

Cables fail due to a number of reasons, including mechanical damage, water ingress and overheating which all lead to electrical failure or breakdown of the insulation layers (Marazzato et al. 2004). An insurance provider (GCube 2016) highlights cable faults are mostly caused by in correction installations, electrical faults and incorrect operation. Cables being exposed to more dynamic environments are expected to exasperate the number of cable failures, with more failing unexpectedly during service lifetime.

Some work has been completed on the impact of dynamic loadings on the fatigue characteristics of dynamic cables (Buitrago et al. 2013), (Thies, Johanning, and Smith 2011), (Thies, Johanning, and Dobral 2017), while similar works for dynamic environments have also been completed for mooring lines loadings assessments (Martinelli et al. 2010). Silva *et al.* (2012) used a finite element method to investigate the cable cross section regarding its allowable bend radius.

Yang *et al.* (2017) investigated the impact that varying cable bending and axials stiffness has on cable

fatigue damage for dynamic loading conditions. Axial and bending stiffness' impact cable motion, and therefore the cable stress response. Having a larger bending stiffness may be preferable in order to reduce the dynamics of the cable. Raoof has researched extensively into calculating the bending stiffness's of helically wound strands (M. Raoof and Davies 2004; M. Raoof 1990; Mohammed Raoof 1990; Mohammed Raoof and Davies 2008) and demonstrates that the inter-wire friction between helically wound armoring layers is a determining factor in bend stiffness. Chen *et al.* (2013) completed work on estimating the axial stiffness of an umbilical cable, which takes into account the radius reduction effects of the helical armoring components when under tension. Ekeberg *et al.* (2006) reports similar trends when comparing calculated axial stiffness that do and don't account for radius reduction.

Mechanical fatigue due to environmental loading is shown to be of particular concern as a starting or propagating mechanism for water treeing in cable insulation layers (Ildstad et al. 1990), (Wang et al. 2012).

This papers aims to give a better understanding of the distribution of mechanical stresses across the cable cross section, and how they will impact cable fatigue damage. Particular attention is given to areas of concern that might serve as points of water tree initiation.

The approach presented begins with a global dynamic model of a chosen dynamic cable, in a typical loading environment for a chosen site as detailed in section 2. The output cable loading history of the dynamic model, can then be used as inputs to a mechanical model of the cable cross section. The mechanical model is used to illustrate the stress distributions across the cables cross section as detailed in section 3. Finally, using the stress history from the mechanical model a fatigue analysis is conducted as detailed in section 4. Results of stress distribution and fatigue damage is given in section 5. Sections 6 gives a discussion to the results, with section 7 drawing some conclusions. Finally, section 8 highlights future work.

2 DYNAMIC MODEL

To give an understanding of the stresses that an umbilical cable would experience, the entire floating turbine system needs to be analyzed. This is necessary as the cable stresses will be sensitive to the environmental loadings, motions of the platform and the motions of the cable itself. This model couples the actions of the wind on the turbine with the action of the waves and currents on the platform, platform tendons and dynamic cable. Inputs into the dynamic model required are the environmental loadings and the properties of the cable to be modelled including length and stiffness'.

2.1 *Software Used*

For the work completed in creating the dynamic model of the cable, the proprietary marine dynamics software OrcaFlex from by Orcina was used. OrcaFlex was used to estimate the loadings on the cable in response to the wave, current, wind and therefore the movements of the floating platform. This software is a three dimensional non-linear, time domain finite element program. It splits the length of the cable into user defined lengths (0.5m for this work) and employs a lumped mass approach to solve the cables dynamic behavior.

Shown in Figure 1 (Masciola, Nahon, and Driscoll 2012) the cable is represented as a series of lines or "elements" connected by a node at each end. The line elements hold the axial and torsional characteristics while other properties such as mass, buoyancy, weight etc. are held by the nodes. Forces and moments are applied to the cable at the nodes, and line segments are weightless and straight with the axial and torsional spring damping characteristics. The segment ends hold a rotational damping term that is used to model the cable bending.

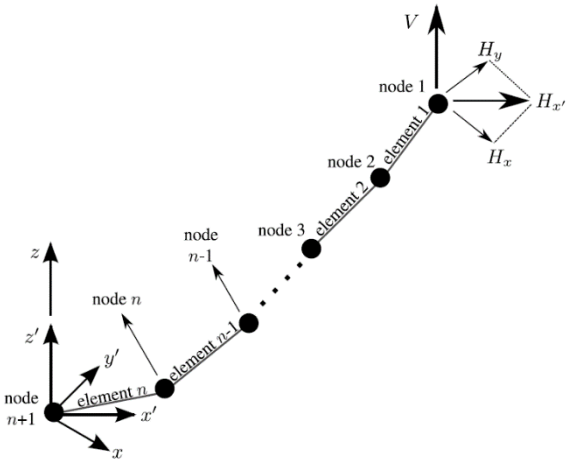

Figure 1 The cable lumped mass model arranged in the xyz frame. H_X, H_Y, and V correspond to the applied external forces. In their absence, the cable likes in the vertical x'z' reference frame.

FASTlink is a FAST-OrcaFlex interface package that was used for this work. All hydrodynamics and mooring loads on the cable are solved using OrcaFlex, while the NREL 5MW reference turbine, tower, floating platform structural dynamics, aerodynamics control and electrical drive dynamics are computed using FAST.

2.2 *MIT/NREL Tension Leg Platform Model*

This work incorporates the MIT/NREL reference 5MW tension leg platform (Jonkman 2016) and uses its modelled motions to investigate the impact on the dynamic cable stresses. This is a platform of 18m waterline diameter with a draft of almost 50m. It has four 27m long pontoons with two mooring lines attached to each pontoon.

NREL have incorporated this model into a package known as FASTLink. This allows one to combine the effects of the wind on the turbine, with the effects of the waves and currents on the platform. The turbines response to the wind loads being modelled in FAST and this response on the platform with the wave and current loads being modelled in OrcaFlex.

2.3 *Environmental Loading*

An appropriate loading environment is needed as inputs to the dynamic model. Wave buoy data located at GPS coordinates 55.23855^0 N, -1.09524. At a site 10km away, coordinates 55.850^0N, 0.911^0W, data was obtained to correlated wave height with wind speed. Based on data from a nearby acoustic doppler current profiler, current at the site is assumed bi-directional and has the same max speed in both directions. Using this has resulted in the following appropriate environment detailed in table 1.

Table 1 Environmental Loading Data for Global Cable Simulations

Environmental Conditions	
Wave Height, H_s, m	1.75
Wave Period, T_z, s	5.25
Wind Velocity, V, ms^{-1} 10m above sea level	9.5
Max Current Velocity, ms^{-1}	0.3
Current Directions, Deg	165, 335
Sea Depth, m	200

2.4 *Dynamic Cable*

The cable modelled for this work is based on 280m length of a JDR dynamic cable (Featherstone 2017) used in previous oil and gas applications. Figure 2 shows a schematic of the cable modelled, while table 2 gives some of the cables mechanical parameters.

Table 2 Mechanical Parameters of Dynamic Cable

Mechanical Properties:	
Outer Diameter	154mm
Outer Sheath Material	Extruded Polyethylene
Cable Armouring	Galvanised Steel Wire
Minimum Bend Radius	2000mm
Safe Working Load	250 kN
Diameter to Weight Ratio	4.27 m^2/Te

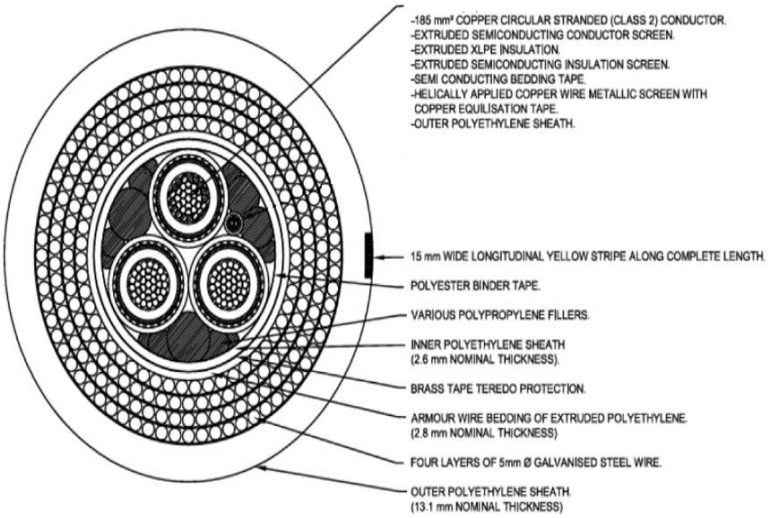

Figure 2 Schematic Overview of Dynamic Subsea Cable

2.5 *Cable Stiffness and Length*

2.5.1 *Axial Stiffness*

Axial stiffness has been calculated from the following equation (Chen et al. 2013):

$$K_a = \sum_{i=1}^{n} A_i E_i cos\alpha_i (cos^2\, a_i - v sin^2 \alpha_i) + \sum_{j=1}^{m} A_j E_j \qquad (1)$$

Where A_iE_i is the axial stiffness of the helical components, α_i is the lay angle of the helical component, n is the number of helical components, A_jE_j is the axial stiffness of any straight components and m is the number of straight components. The radius reduction ratio is the relationship between the radius reduction and the axial elongation of the helical tendon, represented by v.

2.5.2 *Bending Stiffness*

Bending stiffness has been calculated from the following equation (M. Raoof and Davies 2004):

$$EI = I \sum_{i=1}^{N} \lambda_i E_i \qquad (2)$$

Where, denoting the cable outside diameter by *d*,

$$I = \frac{\pi}{4}\left(\frac{\pi d^4}{64}\right) \qquad (3)$$

N is the number of layers of helical wires, E_i is the Young's modulus and λ_i is denoted by:

$$\lambda_i = \frac{I_{ni}}{I_0} \qquad (4)$$

Where I_{ni} is the second moment of area of each layer and I_0 is given by:

$$I_0 = \sum_{i=1}^{N} I_{ni} \quad (5)$$

2.5.3 *Cable Length*

A sea depth of 200m was chosen, which using the recommendations laid out in (CIGRÉ 2015) gives a cable length when installed in a "lazy s" arrangement of 280m using the equation for L_0.

$$L_0 = \sqrt[d]{1 + 2\,\frac{H}{w.d}} \quad (6)$$

Where d is the maximum depth, w is the submerged weight of 1m length of cable and H is the maximum expected bottom tension, which in this case is taken as 15kN.

3 MECHANICAL MODEL

For this work the mechanical model refers to the interaction of the dynamic cables individual components across its cross section. This model looks at the stresses across the cable cross sections individual components, highlighting areas of greatest mechanical stress. Stresses have been resolved into their six degrees of freedom as well as combined into Von misses stress distributions. The output of the dynamic model is coupled with the cables cross section mechanical model to produce a time history of stresses for particular cable cross section components.

3.1.1 *Finite Element Analysis*

A finite element analysis, FEA, model of the cable cross section was constructed using ANSYS Mechanical software. The finite element method is an effective option to determine the interactions between the dynamic cables internal components. Similar works by (Silva, Balena, and Lisbôa 2012) and (Gaidai et al. 2015) both used an alternative FEA software UFlex2D to investigate the stresses across an umbilical cross-section. UFlex2D is custom made FE software for umbilical cross sections however ANSYS was used due to its ability to be coupled with the outputs of the OrcaFlex software.

3.1.2 *Model Assumptions*

Some assumptions were made to perform the analysis of the dynamic cables. The cable stiffness was assumed to be a characteristic of the cable armoring layers. Similar to (Yang, Ringsberg, and Johnson 2017) the armoring layers were simplified to thin walled tubes for the local mechanical model. This assumption was made based on the principle that the cable armoring layers remain in stick state and that the individual armor wires do not slide over one another during normal operation. The cable cross section component materials were assumed to be linear elastic, and that in the local cross section model, the components are glued together, i.e. they cannot penetrate one another's interface.

4 FATIGUE ASSESSMENT

The accumulated fatigue of the dynamic cables, and their associated fatigue lives can be calculated after the stresses they experience is calculated.

Preliminary modelling of the cable showed that the stress levels it would experience to be much lower than the design yield stresses of the materials. Therefore a stress based approach for fatigue has been employed. Stress history for the cables are temporal and an output of the coupled dynamic and mechanical models. Individual stress histories can be deduced for particular components of interest of the cross sections.

The rain flow counting method is used to find the stress ranges and cycles from the stress history for the fatigue analysis. An accepted method for fatigue damage, D, analysis is the use of the Palmgren-Miner linear damage rule and the accompanying S-N curves for the material under consideration:

$$D = \sum_{i=1}^{k} \frac{n_i}{N_i} \quad (7)$$

Where for k different stress levels and the average number of cycles to failure at the ith stress, S_i, is N_i and n_i is the number of cycles are accumulated stress S_i. No fatigue damage limit has been included for this initial work, and therefore all fatigue ranges contribute to the damage. The S-N curve for the XLPE insulation layer in particular was obtained from (Wang et al. 2012).

5 RESULTS

5.1 *Dynamic Model Output*

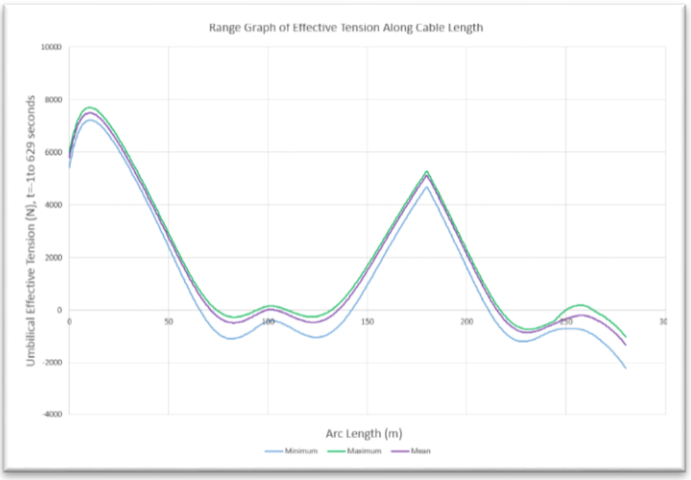

Figure 3 Plot showing Cable Effective Tension at points along the installed cable length.

On the x-axis is the cable installed length while the y-axis denotes the effective tension. The upper line on the plot is the maximum seen tension at that specific point along the cable length, the middle line is average, and the bottom is the minimum.
From the plot it can be seen greatest effective tension is found approximately 10m from the cable hang off point, with a secondary peak just after the suspended section of the "lazy s" cable installation configuration. See Figure 4 for clarity of dynamic cable installation arrangement. Similar results on this distribution of effective tension along the cable length were found by (Thies, Johanning, and Smith 2011).

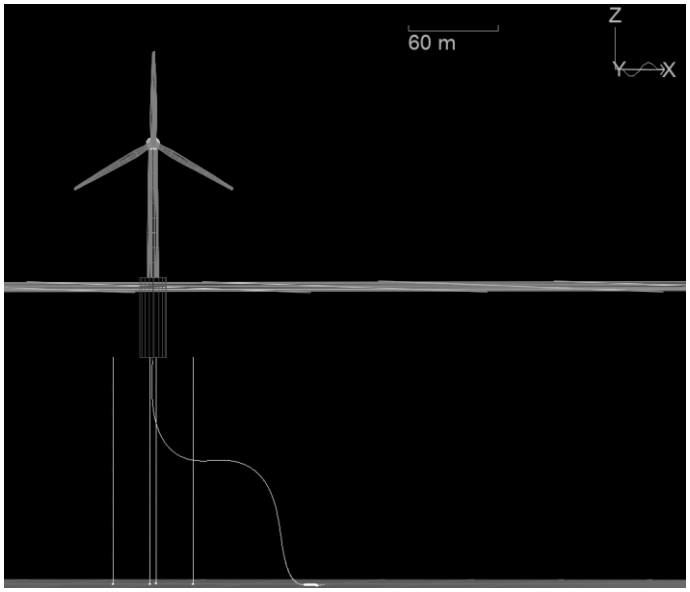

Figure 4 Dynamic Cable Installation Arrangement

This point 10m from the hang off point shall be looked at specifically now for further investigation, it should be noted that any point of interest along the cable length can be chosen.

5.2 *Stress Distribution*

While any cable component can be chosen for investigation using the presented approach, the insulation layers of XLPE shall be looked at specifically for further investigation within these works.

Outputs from the dynamic model at the chosen reference point, or node, include a time series of the torque, effective tension, x-bend moment, y-bend moment etc. This time series of various outputs can be coupled with the mechanical FE model of the cable cross section to produce an illustration showing how stresses distribute across the cable insulation layers. Figure 5 illustrates how the Von Misses stresses distribute across the cable insulation layers. It should be noted that for any component of the cable cross section, and any of the 3D plane or shear stresses can be examined using the presented approach. Purely for comparison of the stress magnitudes between the insulation and armoring layers, a plot has been included of the stress distribution at the same point across the armoring, Figure 6.

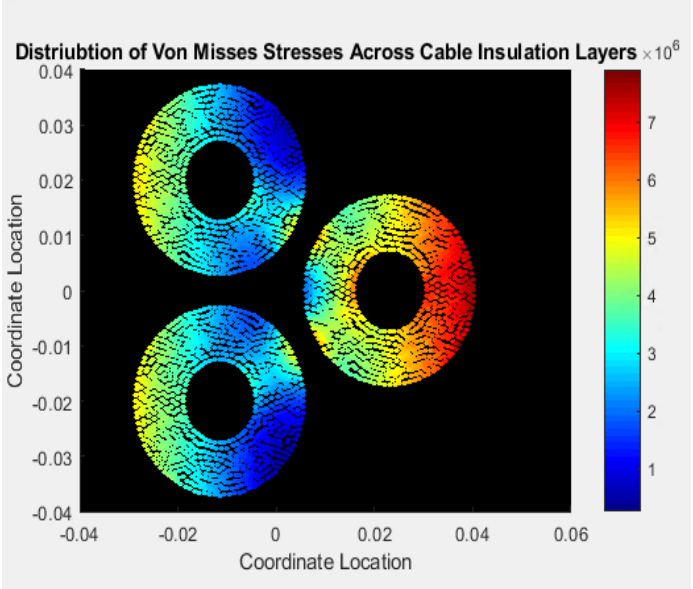

Figure 3 Von Misses Stress Distribution across Cable Insulation Layers

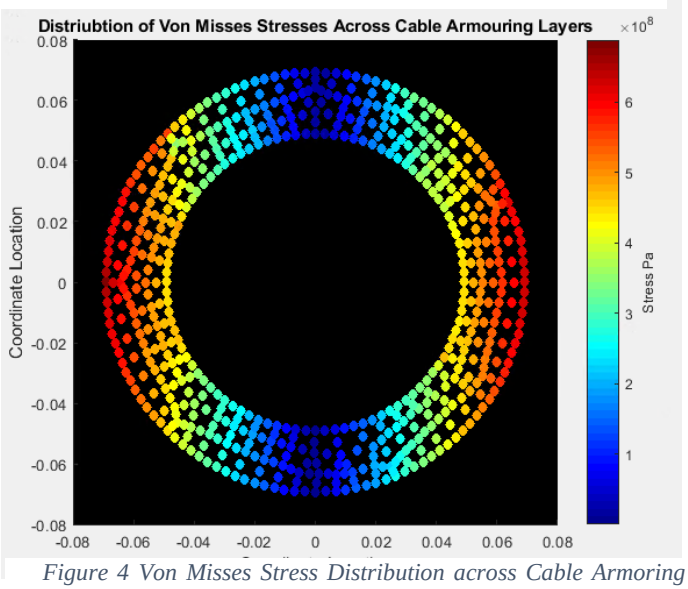

Figure 4 Von Misses Stress Distribution across Cable Armoring Layers

5.3 *Stress Cycle Generation*

The displayed stress distributions in section 5.2 are in effect a snap shot in time of the stress distribution across the cable. As the cables for floating wind will be dynamic, their corresponding stress histories will also be dynamic. It was assumed that once one location element of the cross section fails, failure of the cable has occurred. Therefore for illustration purposes the stress history of the location element that experienced the greatest damage is presented. To understand the distribution of the fatigue damage of the cable insulation layers, all location elements were analyzed.

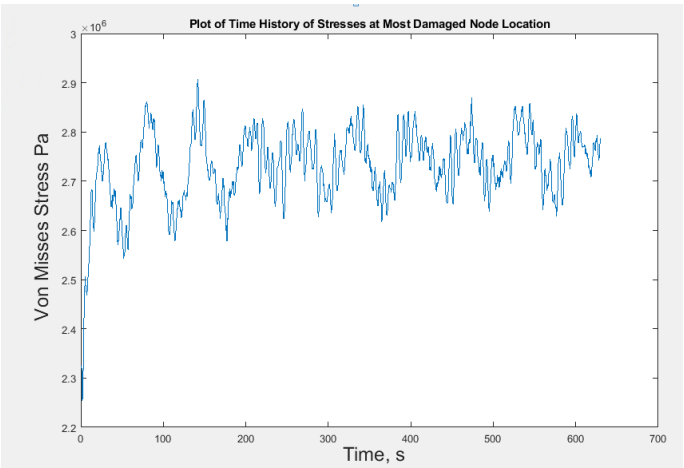

Figure 5 Stress Cycles of Most Damaged Location Element

5.4 *Fatigue Damage*

The stress cycles found in 5.3 were computed to determine the fatigue damage for each of the location elements. The corresponding damages were then plotted to illustrate the distribution of the damage to the cable insulation layers. It should be noted the use of a log scale for the damage allows for easier visualization, however once the log scale is removed it is easier to deduce the exact location to fail first, shown in figure 9. These points of highest fatigue damage would be of concern as potential initiation points of water treeing within the insulation.

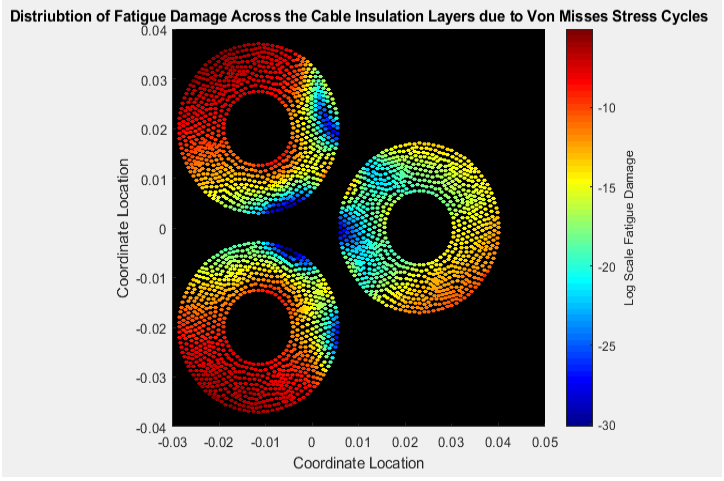

Figure 8 Log scale distribution of cable insulation layers fatigue damage

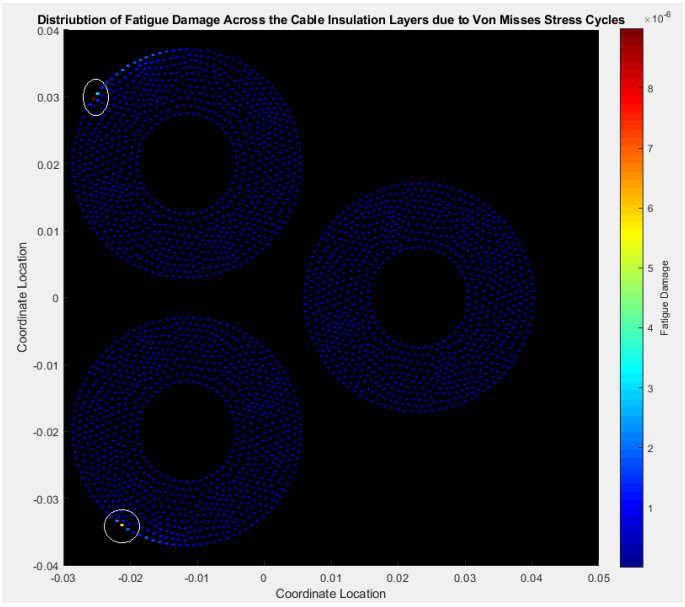

Figure 9 Cable Insulation Layers Fatigue Damage with areas of concern for water tree initiation circled

6 DISCUSSION

The presented work can be used to give an initial estimate of fatigue damage of any component of a dynamic cables cross section. The work focused on using Von Misses stresses as an initial estimate tool, where both compression and tension would contribute to damage. This work would need to be validated with laboratory experiments to conclude the effectiveness and accuracy of the developed model. Von Misses stresses can be thought of as a tool to capture the effects of both planar stresses and shear stresses, according to equation 8.

$$\sigma_v = \sqrt[2]{0.5\left[(\sigma_{xx}-\sigma_{yy})^2+(\sigma_{yy}-\sigma_{zz})^2+(\sigma_{zz}-\sigma_{xx})^2+6(\sigma_{yz}^2+\sigma_{zx}^2+\sigma_{xy}^2\right)} \quad (8)$$

Where σ_{xx}, σ_{yy}, σ_{zz}, are the planar stresses in Pa, while σ_{xy}, σ_{yz}, and σ_{xz} refer to the shear stresses in Pa, σ_v is the Von Misses stress in Pa. As the Von Misses is an amalgamation of the planar and shear stresses, a quick comparison of them can be used to determine which, if any, of the stresses is contribution most to the magnitude of the Von Misses stress. As a rudimentary estimate of their contribution, the magnitudes of the fatigue damage due to each of the stresses is given in table 3.

Table 3 Magnitude of Fatigue Damage at most damaged location due to corresponding stress type

Stress Type	Fatigue Damage
σ_{xx}	4.53e-41
σ_{yy}	5.28e-50
σ_{zz}	5.15e-06
σ_{xy}	2.74e-46
σ_{yz}	4.65e-25
σ_{xz}	3.41e-30
σ_{v}	9.00e-06

From table 3 it can be quickly deduced that the planar stress type σ_{zz} is the dominating stress contributing to the cable insulations fatigue damage. In this scenario it can be seen that it is the cable bending which dominates fatigue damage.

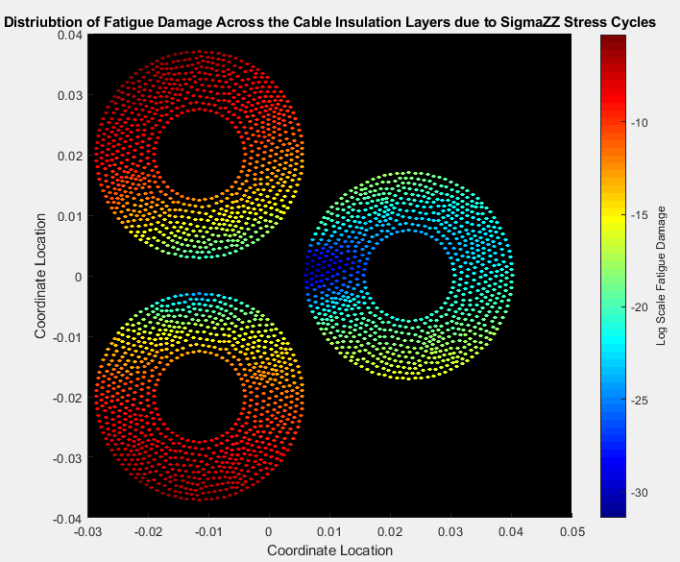

Figure 6 Fatigue Damage Distribution due to Sigma ZZ stresses

The magnitudes of the fatigue damage overall are quite small, particularly as these damages have been calculated for a cables expected life of 25 years. The simulations for the stress cycles were from a ten minute period of constant environmental scenarios. This time period would suffice to capture the stress cycles due to the higher frequency wave and wind interactions on the floating platform with a constant current, but would miss the overall much lower frequency tidal cycle stresses. It is expected that the tidal cycle would contribute stresses of much greater amplitudes, and thus contributing to a much higher fatigue damage.

7 CONCLUSIONS

This work presents a method to determine mechanical fatigue damage across a dynamic cables cross section when exposed to a dynamic marine environment. It can be used as a tool to compare the fatigue damage at differing lengths along the cables length. Individual components of the cable cross section can be investigated, giving way to a more comprehensive fatigue assessment of dynamic cables. Concerns of mechanical fatigue damage as an initiation point of water treeing within the cable insulation layers was investigated, with potential imitation points highlighted. Finally, the works suggests that it is the stresses due to cable bending, as opposed to tension that contribute most to a dynamic cables fatigue damage.

8 FUTURE WORK

Immediate future work would be to incorporate the stresses due to the tidal cycle and varying current characteristics into the model to calculate a new fatigue damage estimate. This would allow the model users to determine if the wave characteristic or current characteristics dominate cable fatigue. A statistical analysis of an environmental parametric study would follow. Finally it is envisioned this work serves at the first step in the development of a coupled mechanical and electrical fatigue model which considers both mechanical stresses and electrical stresses due to the cable being energized.

9 ACKNOWLEDGMENTS

The authors would like to thank the Energy Technology Institute and the Research Council Energy Programme for funding this research as part of the IDCORE programme (grant EP/J500847), and the Offshore Renewable Energy Catapult for providing technical assistance and equipment. A special thanks to Orcina for providing OrcaFlex software and to JDR cables for allowing presentation of cable data.

REFERENCES

Buitrago, Jaime, Sean F. Swearingen, Sana Ahmad, and Carl F. Popelar. 2013. “Fatigue, Creep and Electrical Performance of Subsea Power Cable.” In , V003T03A028-V003T03A028. American Society of Mechanical Engineers. https://doi.org/10.1115/OMAE2013-10852.

Carbon Trust. 2017. “Floating Wind Joint Industry Project: Policy & Regulatory Appraisal.” 2017. https://www.carbontrust.com/resources/reports/technology/floating-wind-policy/.

Chen, Xiqia, Shixiao Fu, Leijian Song, Qian Zhong, and Xiaoping Huang. 2013. “Stress Analysis Model for Un-Bonded Umbilical Cables.” *Ocean Systems Engineering* 3 (2): 97–122. https://doi.org/10.12989/ose.2013.3.2.097.

CIGRÉ, Conseil international des grands réseaux électriques. 2015. *Recommendations for Mechanical Testing of Submarine Cables*. Paris: CIGRÉ.

Climate Change Act. 2008. "UK Regulations: The Climate Change Act." *Committee on Climate Change* (blog). 2008. https://www.theccc.org.uk/tackling-climate-change/the-legal-landscape/the-climate-change-act/.

Ekeberg, K. I., T. Ottesen, J. Aarstein, S. Saevik, N. Ye, and R. Igland. 2006. "Predicting, Measuring and Implementing Friction and Bending Stresses in Dynamic Umbilical Design." In . Offshore Technology Conference. https://doi.org/10.4043/17986-MS.

Featherstone, Jeremy. 2017. "Dynamic Subsea Power Cables for Floating Wind & 66kV Subsea Power Cables, 6th Annual Advanced Submarine Power Cable & Interconnection Forum, Berlin." June.

Gaidai, Oleg, Naiquan Ye, Joe Jin, Dale Reid, and Philippe Mainçon. 2015. "Fatigue Analysis Methods of Dynamic Umbilicals." In . International Society of Offshore and Polar Engineers. https://www.onepetro.org/conference-paper/ISOPE-I-15-595.

GCube. 2016. *Down to the Wire: An Insurance Buyer's Guide to Subsea Cabling Incidents, June 2016 Report*. GCube Insurance Services.

Ildstad, E., H. Bardsen, H. Faremo, and B. Knutsen. 1990. "Influence of Mechanical Stress and Frequency on Water Treeing in XLPE Cable Insulation." In , *Conference Record of the 1990 IEEE International Symposium on Electrical Insulation, 1990*, 165–68. https://doi.org/10.1109/ELINSL.1990.10973 2.

Jonkman, Bonnie. 2016. "FAST-OrcaFlex Interface | NWTC Information Portal." 2016. https://nwtc.nrel.gov/OrcaFlexInterface.

"Lifes50plus - Innovative Floating Offshore Wind Energy." 2015. Lifes50+. 2015. http://lifes50plus.eu/.

M. Raoof, and T.J. Davies. 2004. "Determination of the Bending Stiffness for a Spiral Strand." *The Journal of Strain Analysis for Engineering Design* 39 (1).

Marazzato, Hilary, Ken Barber, Mark Jansen, and Barnewell Graeme. 2004. "Cable Condition Monitoring to Improve Reliability." Olex Australia.

Martinelli, L., A. Spiandorello, P. Ruol, and A. Lamberti. 2010. "Dynamic Model for Catenary Mooring: Experimental Validation of the Wave Induced Load." 2010. https://www.comsol.com/paper/dynamic-model-for-catenary-mooring-experimental-validation-of-the-wave-induced-l-8698.

Masciola, Marco D., Meyer Nahon, and Frederick R. Driscoll. 2012. "Static Analysis of the Lumped Mass Cable Model Using a Shooting Algorithm." *Journal of Waterway, Port, Coastal, and Ocean Engineering* 138 (2): 164–71. https://doi.org/10.1061/(ASCE)WW.1943-5460.0000117.

Raoof, M. 1990. "Effect of Hydrostatic Pressure on Strand Behaviour." *The Journal of Strain Analysis for Engineering Design* 25 (2): 75–84. https://doi.org/10.1243/03093247V252075.

Raoof, Mohammed. 1990. "Axial Fatigue of Multi-layered Strands." *Journal of Engineering Mechanics* 116 (10): 2083–99. https://doi.org/10.1061/(ASCE)0733-9399(1990)116:10(2083).

Raoof, Mohammed, and Timothy J. Davies. 2008. "Axial Fatigue Design of Sheathed Spiral Strands in Deep Water Applications." *International Journal of Fatigue* 30 (12): 2220–2238. https://doi.org/10.1016/j.ijfatigue.2008.05.002.

Silva, Danianderson, Rosianita Balena, and Rafael Lisbôa. 2012. "Methodology for Thermoplastic Umbilical Cross Section Analysis," July, 407–11. https://doi.org/10.1115/OMAE2012-83509.

Thies, P. R., Lars Johanning, and Corentin Dobral. 2017. "Parametric Sensitivity Study of Submarine Power Cable Design for Marine Renewable Energy Applications," June, V03BT02A010. https://doi.org/10.1115/OMAE2017-62208.

Thies, P.R, L. Johanning, and G. H. Smith. 2011. "Assessing Mechanical Loading Regimes and Fatigue Life of Marine Power Cables in Marine Energy Applications." *Proceedings of the Institution of Mechanical Engineers, Part O: Journal of Risk and Reliability*, October, 1748006X11413533. https://doi.org/10.1177/1748006X11413533.

Wang, Z., P. Marcolongo, J. A. Lemberg, B. Panganiban, J. W. Evans, R. O. Ritchie, and P. K. Wright. 2012. "Mechanical Fatigue as a Mechanism of Water Tree Propagation in TR-XLPE." *IEEE Transactions on Dielectrics and Electrical Insulation* 19 (1): 321–30. https://doi.org/10.1109/TDEI.2012.6148534.

Yang, Shun-Han, Jonas W. Ringsberg, and Erland Johnson. 2017. "Parametric Study of the Dynamic Motions and Mechanical Characteristics of Power Cables for Wave Energy Converters." *Journal of Marine Science and Technology*.

WINDTECH INTERNATIONAL

November/December 2018 Volume 14 No. 8

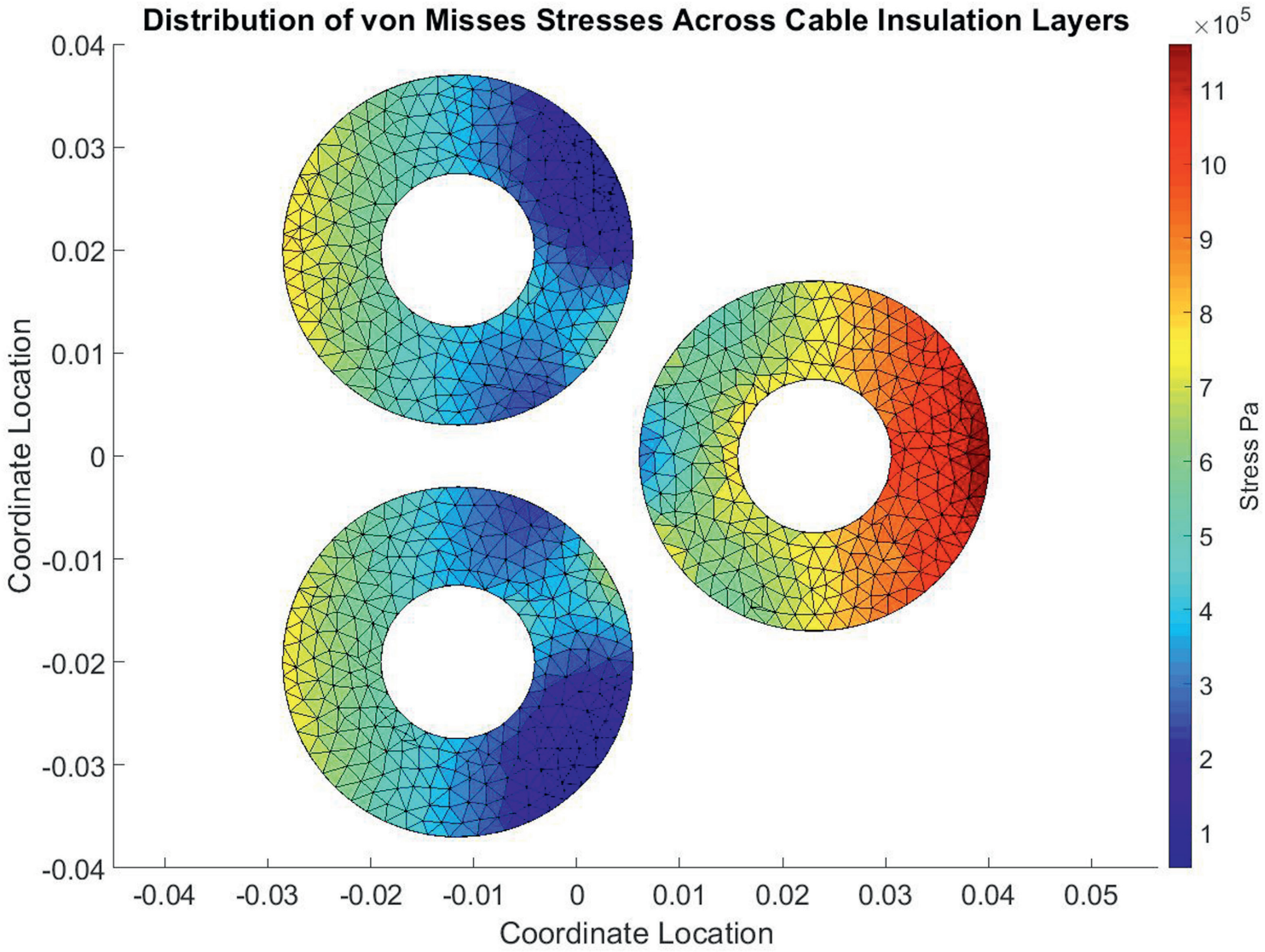

Dynamic Cables for Floating Offshore Wind

Dynamic Mechanical Stresses on Fatigue Life of Dynamic Cables

Dynamic Cables for Floating Offshore Wind

By David Young, IDCORE and ORE Catapult, and Lars Johanning, University of Exeter, UK

Floating platform wind turbines will require cables to run through the water column from their platform base at the water surface to the touchdown point on the seabed. This trajectory exposes the cable to dynamic environmental forces, such as waves and currents. The Offshore Renewable Energy Catapult (ORE Catapult) and the Industrial Doctoral Centre for Offshore Renewable Energy (IDCORE) have been investigating the impact of this dynamic marine environment on a dynamic cable's fatigue life, with the aim of reducing uncertainty and improving the reliability of dynamic cables. The aim of this project is to allow more effective planned maintenance offshore through the prediction of a failure of a dynamic cable.

Offshore wind turbines are moving into deeper waters to take advantage of the greater resource further offshore. Floating platforms provide a solution to depths previously out of reach. Approximately 80% of insurance claims in the offshore wind industry are linked to cable failures. This amounts to a cost in excess of hundreds of millions of euros annually to the industry. Despite cable costs typically only contributing up to 10% of the total initial investment in an offshore wind farm, their failures account for the longest periods of unavailability of a wind farm. Usually a single export cable repair takes from three to five months for an unexpected fault, with the average repair cost estimated to be £ 12.5 million. These factors position cable incidents as one of the main risks affecting the continued reduction of the levelised cost of electricity for offshore wind.

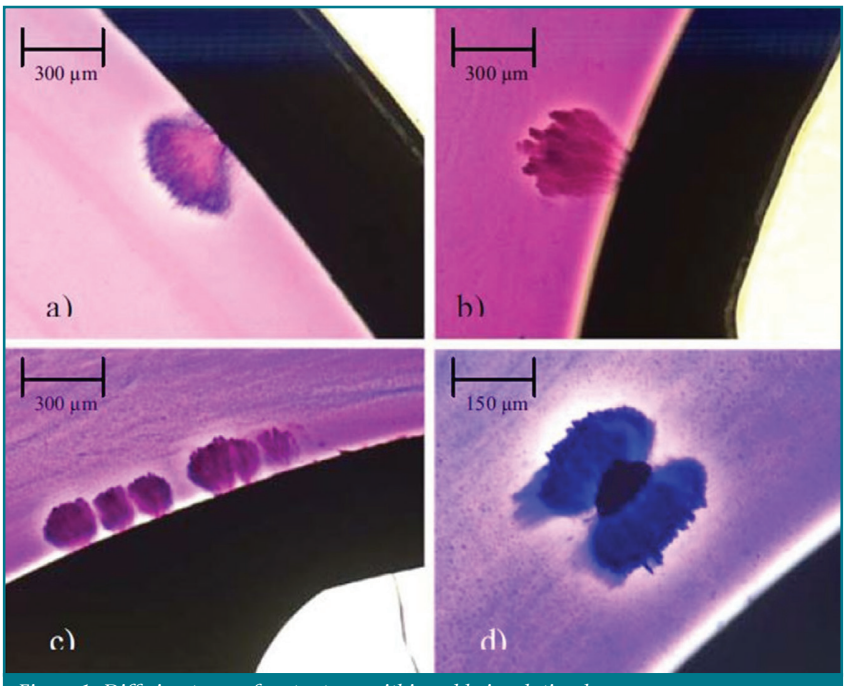

Figure 1. Differing types of water trees within cable insulation layers

Understanding how the cables attached to these floating platforms survive in a dynamic environment is crucial.

This dynamic environmental loading on the cable is a new consideration for cables that traditionally operate under static conditions. The resultant dynamic mechanical stress across the cross section of the cable is a new consideration that needs to be taken into account when conducting fatigue assessments for the dynamic cable.

Subsea cable failures can be loosely categorised into failures due to mechanical damage, water ingress and overheating. All can contribute to the breakdown of the cable insulation layers, eventually leading to an electrical fault. A failure mechanism of the insulation layers is known as water treeing, and it is thought that these slowly developing trees cause the unexpected failure of a cable that was otherwise previously healthy. There are concerns that the dynamic mechanical stresses across the dynamic cables could initiate and propagate these trees further, leading to faster and more frequent cable failures. Figure 1 gives an example of water trees in cable insulation layers found by work completed by Ståle Nordås (see further reading).

The Offshore Renewable Energy Catapult (ORE Catapult) in conjunction with the Industrial Doctoral Centre for Offshore Renewable Energy (IDCORE) has been developing methods to investigate the impacts of dynamic mechanical stresses on the fatigue life of dynamic cables. The outcome is a reduction in the uncertainty and an improved reliability of the dynamic cables for floating offshore wind turbines.

After completing an analysis of the entire floating wind turbine system, the cross sections of the cables were looked at in more detail. Figure 2 shows how stresses across a dynamic cable's cross section are distributed across the cable insulation layers.

Using the stresses shown in Figure 2, a time history can be extracted which allows a fatigue damage assessment of the insulation layers. Figure 3 shows where the most damage occurs on the cable insulation layers, and it is from these most damaged locations that the

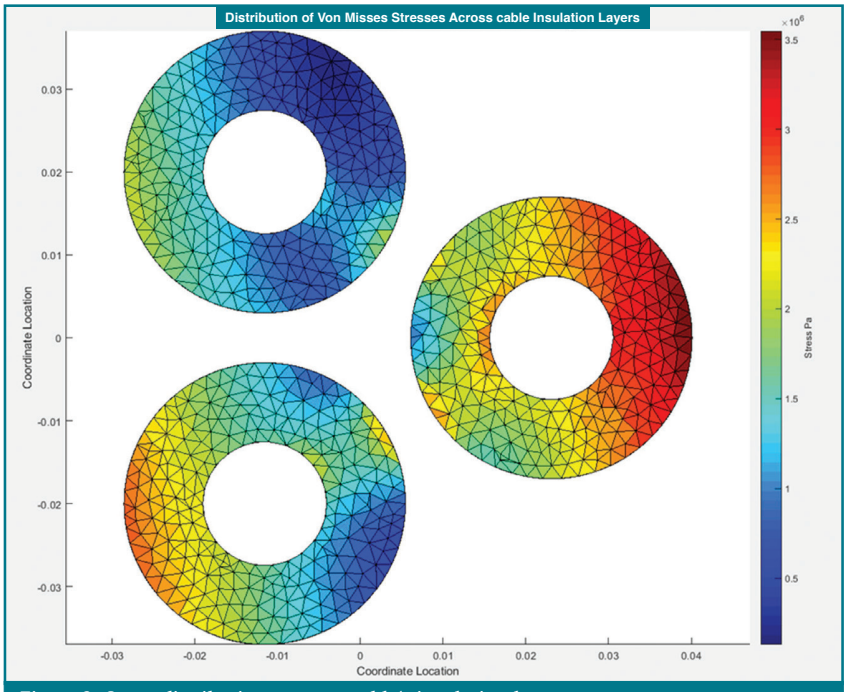

Figure 2. Stress distribution across a cable's insulation layers

areas of potential initiation for the water trees can be predicted. Further detail on this work can be found in Young et al. (2018).

Using the information from these models, the growth of the water tree lengths due to the mechanical stresses induced by a dynamic marine environment can be simulated. By simulating the time taken for a water tree to grow to a length that could cause an electrical fault, a new fatigue assessment for dynamic cables is provided. This time taken is then used to predict when a dynamic cable may start to fail, which allows planning of preventive maintenance. This can be used as a tool to compare the fatigue damage at differing lengths along the cable. Individual components of the cable cross section can be investigated, giving way to a more comprehensive fatigue assessment of dynamic cables.

This work serves as the first step in the development of a coupled mechanical and electrical fatigue model which considers both the mechanical stresses the cable is subjected to and the electrical stresses due to the electrical field distribution in an energised cable.

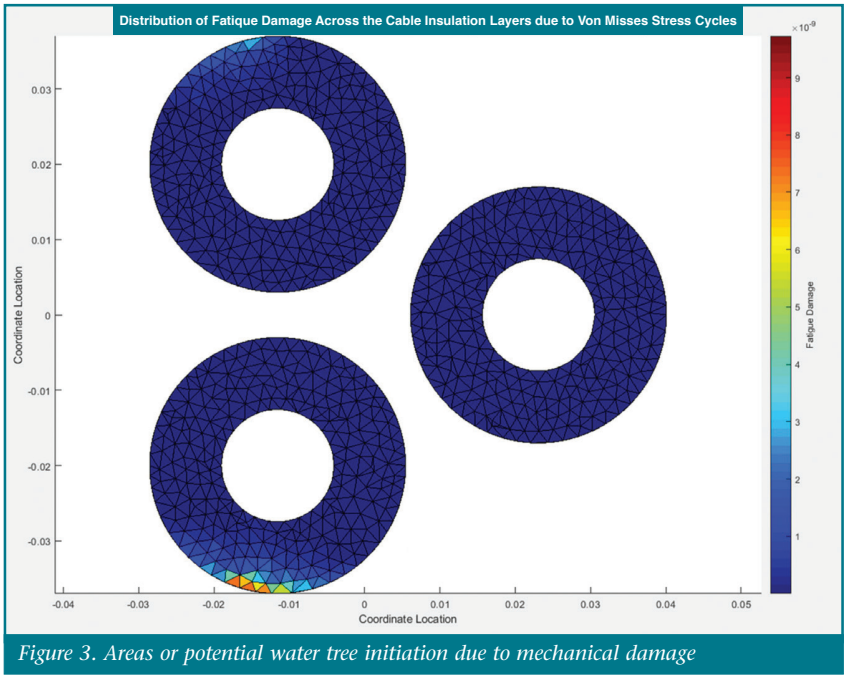

Figure 3. Areas or potential water tree initiation due to mechanical damage

Further Reading

- Young, D.G., Ng, C., Oterkus, S., Li, Q., Johanning, L. 2018, Predicting failure of dynamic cables for floating offshore wind, Proceedings of the 3rd International Conference on Renewable Energies Offshore, 8–10 October 2018, Lisbon, Portugal.
- Ståle Nordås, Erling Ildstad, The influence of strain on water treeing in XLPE power cables, 2010 10th IEEE International Conference on Solid Dielectrics (https://ieeexplore.ieee.org/document/5568215)

Websites

https://ore.catapult.org.uk
https://www.idcore.ac.uk

David Young is a research engineer completing his doctorate thesis on the prediction of dynamic cable failures in conjunction with IDCORE and ORE Catapult. He has a master's in Chemical Engineering and has previous experience working in environmental engineering and the oil and gas sector.

Professor Lars Johanning, Chair of Ocean Technology at the University of Exeter, received his PhD from Imperial College in 2003. He is a deputy manager of IDCORE and is a leading researcher with international recognition in the field of ocean energy and technology with a focus on hydrodynamics and subsea systems.

Affiliation

David Young
ORE Catapult
Offshore House, Albert Street
NE24 1LZ, Blyth, UK
david.young@ore.catapult.org.uk
https://ore.catapult.org.uk

Lars Johanning
University of Exeter
Penryn Campus
TR10 9FE, Penryn
Cornwall, UK
l.johanning@exeter.ac.uk
https://emps.exeter.ac.uk/renewable-energy/staff/lj233